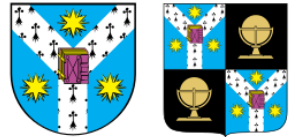


GEOMORPHOMETRY
IASI
ROMANIA

2023

10-14 JULY



Geomorphometry 2023 Proceedings

Editors:

Mihai Niculiță, Peter Guth, Hannes Reuter, Vincent Lecours, Carlos Grohmann, Samantha Arundel, Cheng-Zhi Qin

geomorphometry.org

IAȘI 2023

Department of Geography
Faculty of Geography and Geology, Alexandru Ioan Cuza
University of Iași
and
International Society for Geomorphometry

Geomorphometry 2023 Proceedings

Editors:

Mihai Niculiță, Peter Guth, Hannes Reuter, Vincent Lecours, Carlos Grohmann, Samantha Arundel, Cheng-Zhi Qin

Iași, 2023

This volume is a contribution to the 7th International Conference on Geomorphometry, Geomorphometry 2023, organized in Iași, Romania between 10 and 14 July 2023,

Department of Geography, Faculty of Geography and Geology, Alexandru Ioan Cuza University of Iași

Example reference

Fahrland E., Paschko, H., Schrader, H., Herrera, V. 2023. *Evolution of the Copernicus DEM: beyond today's elevation data with WorldDEM Neo*. In: Mihai Niculiță, Peter Guth, Hannes Reuter, Vincent Lecours, Carlos Grohmann, Samantha Arundel, Cheng-Zhi Qin (Eds) Geomorphometry 2023 Proceedings, Tehnopress, Iași, Romania.

Print
Editura Tehnopress

ISBN
978-606-687-517-2

The content of abstracts are the sole responsibility of the authors

Organizing Committee

Hannes Reuter
Peter Guth
Mihai Niculiță

Local Organising Committee

Mihai Niculiță, Ciprian Mărgărint, Nicușor Necula, Adrian Grozavu, Lilian Niacșu, Ionuț Vasiliniuc
Georgiana Văculișteanu, Denisa Ursu, Alex Cuvuliuc, Guzu Mădălină, Cioranu Ana

Scientific Committee

Alexander Brenning — Friedrich Schiller University
A-Xing Zhu — University of Wisconsin
Carlos Grohman — University of Sao Paolo
Giuseppe Amatulli — Yale School of the Environment
Hannes I. Reuter — European Commission
Helena Mitasova — North Carolina State University
Ian Evans — Durham University
Jaroslav Hofierka — Pavol Jozef Safarik University
John Gallant — CSIRO
John Lindsay — University of Guelph
Laurence Hawker — University of Bristol
Lucian Dragut — West University of Timisoara
Massimiliano Alvioli — CNR IRPI Perugia
Mihai Niculita — Alexandru Ioan Cuza University of Iași
Peter L. Guth — US Naval Academy
Qiming Zhou — Hong Kong Baptist University
Qin Cheng-Zhi — Chinese Academy of Sciences
Robert A. MacMillan — LandMapper Environmental Solutions Inc.
Samantha Arundel — USGS
Scott D. Peckham — University of Colorado
Sebastiano Trevisani — University of Venice
Steve Kopp — ESRI
Tomislav Hengl — OpenGeoHub Foundation

Table of Contents

Ernest Fahrland, Virginia Herrera, Hanne Paschko and Henning Schrader – Evolution of the Copernicus DEM: beyond today's elevation data with WorldDEM Neo	.1
Laurence Paul Hawker, Peter Uhe and Jeffrey Neal – FABDEM Updates – FABDEM VI-2	5
Peter Guth, Carlos Grohmann and Sebastiano Trevisani – Geomorphometric and Geospatial Patterns in Differences Between ALOS and COPDEM	8
Dean Gesch – Assessing Global Elevation Models for Mapping the Low Elevation Coastal Zone	11
Richard Feciskanin – DEM generalization using polygonal simplification	14
Sebastiano Trevisani and Peter L. Guth – Landscape according to surface roughness: experimenting in the Taklimakan Desert	18
Vincent Lecours, Benjamin Misiuk and Craig J. Brown – Exploring the Effects of Acoustic Frequency on Terrain Attributes and Classifications Derived from Digital Bathymetric Models at Multiple Scales	22
John Lindsay – The time-in-daylight land-surface parameter	26
Gaurav Sinha, Samantha Arundel, Romim Somadder, David Martin and Kevin McKeehan – Geomorphometric analysis of Summit and Ridge landforms in the USGS GNIS topographic database	30
Mihai Niculită – Neighborhood contextual merging of segments for landform detection and classification	34
Janusz Godziek – Application of LiDAR-based DTMs and DSMs to detect landforms created by the trees uprooting process	37
Christian Depraetere, Benoît Deffontaines and Serge Riazanoff – Hydro-geomorphometrical processing of dense Lidar/DEM: Relationships between landforms and hydrological processes	41
Bofei Zhao, Haigang Sui and Qiming Zhou – Flood inundation analysis based on SAR image and DEM: A case study of the 2021 Zhengzhou Flood in China	45
Maeve DeBuse and Peter Guth – Evaluation of elevation, slope, roughness, and vegetation type on the burn severity of the 2020 Calwood Fire in Boulder County, Colorado	49
Nicușor Necula and Mihai Niculita – Machine learning classification of geomorphometric segments for floodplain detection and delineation	53
Liyang Xiong, Jiang Yinghui and Sijin Li – Super-resolution for terrain modeling using deep learning in High Mountain Asia	57
Yu-Feng Ho, Tomislav Hengl and Leandro Parente – A Simply Updatable Cloud-based Ensemble Digital Terrain Model	60

Jun Chen, Liyang Xiong, Guanghui Hu and Guoan Tang – Integrating topographic knowledge into point cloud simplification for terrain modelling	62
Juan Francisco Reinoso-Gordo and Francisco Javier Ariza-López – A method to rank global DEMs quality focused on their horizontal accuracy	66
Adam Rusinko and Jozef Minár – The role of geomorphometric predictors in LUCC modeling	70
Xiaohui Huang and Liyang Xiong – Mapping gully affected areas based on Sentinel 2 imagery and digital elevation model	74
Tian Jia, Cheng-Zhi Qin, Ping Fu and Vladimir Brusic – Applicability of longitudinal profiles for glacial cirque classification	78
Guohua Gou, Haigang Sui, Sheng Wang, Qiming Zhou and Jianya Gong – Constructing a True 3-D Model of a Karst Cave Using an UAV	82
Carlos Grohmann, Gulherme Garcia, Camila Viana, Helen Dias and Rebeca Coelho – RPA flight pattern and GCP influence on SfM-MVS modeling of a stable landslide in SE Brazil	85
Haigang Sui, Hao Zhang, Qiming Zhou and Jianya Gong – The true 3-D surface reconstruction using a multi-UAV cooperation method	89
Ian Evans, Yingkui Li and Zhibin Zhao – Dependence of statistical results on definitions and extents of study area: examples from cirques and glaciers	93
Hannes Reuter – Applying Terrain analysis to human population?	97
Francisco Javier Ariza-López and Juan Francisco Reinoso-Gordo – Functional Quality for GDEMs Assessment	100
Francisco Javier Ariza-López, Manuel A. Ureña-Camara, Juan Francisco Reinoso-Gordo and Marcelo Antonio Nero – Proposal for a Collaborative Data Infrastructure for Control of DEMs	104
Carlos Henrique Grohmann, Carlos López-Vázquez, Peter Guth, Conrad Bielski – The DEMIX Wine Contest: a Summary	108
Carlos Henrique Grohmann – The DEMIX Wine Contest Jupyter notebook	112
Peter Guth, Carlos Henrique Grohmann and Sebastiano Trevisani – Subjective Criterion for the DEMIX Wine Contest: Hillshade Maps	115
Peter Guth, Carlos Grohmann, Sebastiano Trevisani and Conrad Bielski – Going Forward: Extending and Exploiting the DEMIX Database With MICRODEM	120

Programme

GEOMORPHOMETRY 2023 PROGRAMME									
Monday 10 th July		Tuesday 11 th July		Wednesday 12 th July		Thursday 13 th July		Friday 14 th July	
08:00-08:45	Registration	8:00-9:00	Iași-Costești	8:30-09:00		8:30-09:00		8:30-09:00	
08:45-09:00	Opening	9:00-10:00	Costești Geoarchaeosite	09:00-10:00	Keynote 1	09:00-10:00	Keynote 2	09:00-10:00	DEMIX Workshop
09:00-10:00	Award	10:00-10:40	Costești- Cotnari	10:00-10:40	ESRI RO	10:00-10:20	CEOS Terrain Mapping Sub- Group	P27 P28 P31 P32 P33	10:00-10:20 10:20-10:40 10:40-11:00 11:00-11:20 11:20-11:40
10:00-10:20	P1	10:40-11:00	Cotnari	11:00-11:20	P17	10:40-11:00			
10:20-10:40	P2	11:00-11:30	Vineyard&Winery	11:00-11:20	P18	11:00-11:20			
10:40-11:00	P19	11:20-11:40		11:20-11:40	P21	11:20-11:40			
11:00-11:20	P4								
11:20-11:40	P5								
11:40-13:00	Lunch Break	11:30-13:00	Wine tasting+ Lunch	11:40-13:00	Lunch Break	11:40-13:00	Lunch Break	11:40-13:00	Lunch Break
13:00-13:20	P6	13:00-13:20		P22	13:00-13:20	P34	13:00-13:20		
13:20-13:40	P8	13:20-13:40		P23	13:20-13:40	P36	13:20-13:40	Whitebox Workshop	
13:40-14:00	P9	13:40-14:00		P24	13:40-14:00	P37	13:40-14:00		
14:00-14:20	P10	14:00-14:20		P25	14:00-14:20	P38	14:00-14:20	Coffee Break	
14:20-14:40	P11	14:20-14:40		P26	14:20-14:40		14:20-14:40		
14:40-15:00	Coffee Break	14:40-15:00	Dragoș Vodă Bisons Reserve	14:40-15:00	Coffee Break/ DEMIX Registration	14:40-15:00	Coffee Break	14:40-15:00	Workshop
15:00-15:20	P12	15:00-15:20		P27	15:00-15:20	P39	15:00-15:20		
15:20-15:40	P13	15:20-15:40		P28	15:20-15:40	P40	15:20-15:40		
15:40-16:00	P15	15:40-16:00		P29	15:40-16:00	P41	15:40-16:00		
16:00-16:20	P16	16:00-16:20		P30	16:00-16:20	P42	16:00-16:20		
16:20-16:40	P3	16:20-16:40		P31	16:20-16:40	P43	16:20-16:40		
16:40-17:00		16:40-17:00		P32	16:40-17:00	Coffee Break			
17:00-20:00	Guided City Tour	16:30-18:00	Neamț Fortress	17:00-17:20		17:00-17:20	ISG Bussiness	17:00-22:00	Informal City Tour
		18:00-20:00	Târgu-Neamț- Iași	17:20-17:40		17:20-17:40			
				17:40-18:00	DEMIX icebreaker	17:40-18:00	DINNER		
				18:00-21:00		18:00-21:00			

Sunday (9th July)

17:30-21:00	Icebreaker meeting	Casa Universitarilor Restaurant
-------------	--------------------	---------------------------------

Monday (10th July) – Day 1

08:00-08:45	Registration	front of Aula Magna Mihai Eminescu, University Main Corp (A)
08:45-09:00	Opening & Welcome Address	Aula Magna Mihai Eminescu, University Main Corp (A)
09:00-10:00	Geomorphometry Lifetime Achievement Award Lecture:	John Wilson – “Recent Advances and Challenges in Geomorphometry”
10:00-10:20	Ernest Fahrland, Virginia Herrera, Hanne Paschko and Henning Schrader	Evolution of the Copernicus DEM: beyond today's elevation data with WorldDEM Neo
10:20-10:40	Laurence Paul Hawker, Peter Uhe and Jeffrey Neal	FABDEM Updates – FABDEM V1-2
10:40-11:00	Peter Guth, Carlos Grohmann and Sebastiano Trevisani	Geomorphometric and Geospatial Patterns in Differences Between ALOS and COPDEM

11:00-11:20	Dean Gesch	Assessing Global Elevation Models for Mapping the Low Elevation Coastal Zone
11:20-11:40	Richard Feciskanin	DEM generalization using polygonal simplification
11:40-13:00	Lunch Break	Titu Maiorescu Canteen
13:00-13:20	Fei Zhao and Liyang Xiong	A novel algorithm for calculating flow direction in multi-lake areas
13:20-13:40	Sebastiano Trevisani and Peter L. Guth	Landscape according to surface roughness: experimenting in the Taklimakan Desert
13:40-14:00	Vincent Lecours, Benjamin Misiuk and Craig J. Brown	Exploring the Effects of Acoustic Frequency on Terrain Attributes and Classifications Derived from Digital Bathymetric Models at Multiple Scales
14:00-14:20	John Lindsay	The time-in-daylight land-surface parameter
14:20-14:40	Gaurav Sinha, Samantha Arundel, Romim Somadder, David Martin and Kevin McKeehan	Geomorphometric analysis of Summit and Ridge landforms in the USGS GNIS topographic database
14:40-15:00	Coffee Break	The Hall of the Lost Steps, University Main Corp (A)
15:00-15:20	Mihai Niculită	Neighborhood contextual merging of segments for landform detection and classification
15:20-15:40	Andrei Dornik, Marinela Adriana Chețan, Lucian Dragut, Andrei Iliuță and Daniel Dorin Dicu	Delineation of mapping units for land suitability assessment using land-surface parameters
15:40-16:00	Janusz Godziek	Application of LiDAR-based DTMs and DSMs to detect landforms created by the trees uprooting process
16:00-16:20	Christian Depraetere, Benoît Deffontaines and Serge Riazanoff	Resampling and hydrogeomorphometrical processing of dense Lidar/DEM: Relationships between landforms and hydrological processes in a Mediterranean peri-alpine catchment basin
16:20-16:40	Maeve DeBuse and Peter Guth	Evaluation of elevation, slope, roughness, and vegetation type on the burn severity of the 2020 Calwood Fire in Boulder County, Colorado
17:00-20:00	Guided City Tour – Meeting point is Corp A entry	

Tuesday (11th July) – Day 2

8:00-9:00	Travel from Iași to Costești
9:00-10:00	Costești Geoarchaeosite
10:00-10:30	Travel from Costești to Cotnari
10:30-11:30	Cotnari Vineyard & Winery
11:30-13:00	Wine tasting & Lunch
13:00-14:30	Travel from Cotnari to Vânători
14:30-16:00	Visit to Dragoș Vodă Bison Reserve
16:00-16:30	Travel from Vânători to Târgu Neamț

16:30-18:00	Neamț Fortress Visit	
18:00-20:00	Travel from Târgu Neamț to Iași	

Wednesday (12th July) – Day 3

9:00-10:00	Keynote Lecture 1: John Lindsay	The case for locally scale optimized land-surface parameters
10:00-10:40	Simona Bacau - ESRI Romania	Processing Drone Imagery
10:40-11:00	Bofei Zhao, Haigang Sui and Qiming Zhou	Flood inundation analysis based on SAR image and DEM: A case study of the 2021 Zhengzhou Flood in China
11:00-11:20	Alexander Brenning	Novel approaches to spatial model assessment and interpretation: the example of landslide susceptibility modeling
11:20-11:40	Nicușor Necula and Mihai Niculita	Machine learning classification of geomorphometric segments for floodplain detection and delineation
11:40-13:00	Lunch Break	Titu Maiorescu Canteen
13:00-13:20	Liyang Xiong, Jiang Yinghui and Sijin Li	Super-resolution for terrain modeling using deep learning in High Mountain Asia
13:20-13:40	Yu-Feng Ho, Tomislav Hengl and Leandro Parente	Cloud services for ensemble global elevation data using an updatable method achieved by parallel computation
13:40-14:00	Jun Chen, Liyang Xiong, Guanghui Hu and Guoan Tang	Integrating topographic knowledge into point cloud simplification for terrain modelling
14:00-14:20	Juan Francisco Reinoso-Gordo and Francisco Javier Ariza-López	A method to rank global DEMs quality focused on their horizontal accuracy
14:20-14:40	Adam Rusinko and Jozef Minár	The role of geomorphometric predictors in LUCC modeling
14:40-15:00	Coffee Break	The Hall of the Lost Steps, University Main Corp (A)
15:00-15:20	Peter Strobl	Overview of the DEMIX Initiative
15:20-15:40	Carlos Henrique Grohmann, Carlos López-Vázquez, Peter Guth, Conrad Bielski	The DEMIX Wine Contest: a summary
15:40-16:00	Carlos Henrique Grohmann	The DEMIX Wine Contest Jupyter notebook
16:00-16:20	Peter Guth, Carlos Henrique Grohmann and Sebastiano Trevisani	Subjective Criterion for the DEMIX Wine Contest: Hillshade Maps
16:20-16:40	Guth, Peter L., Grohmann, Carlos H., Trevisani, Sebastiano, & Conrad Bielski	Going Forward: Extending and Exploiting the DEMIX Database With MICRODEM
16:40-17:00	Serge Riazanoff	SG3 events
17:00-17:40	Panel discussions with the audience	

Thursday (13th July) – Day 4

09:00-10:00	Keynote Lecture 2: Jozef Minar	“Using principles of physics in geomorphometry: moving toward hypothetico-deductive geoscience”
10:00-11:40	CEOS Terrain Mapping Sub-Group	Room 2 Casa Universitarilor Restaurant
10:00-10:20	Xiaohui Huang and Liyang Xiong	Mapping gully affected areas based on Sentinel 2 imagery and digital elevation model
10:20-10:40	Tian Jia, Cheng-Zhi Qin, Ping Fu and Vladimir Brusic	Applicability of longitudinal profiles for glacial cirque classification
10:40-11:00	Ian Evans, Yingkui Li and Zhibin Zhao	Dependence of statistical results on definitions and extents of study area: examples from cirques and glaciers
11:00-11:20	Hannes Reuter	Applying Terrain analysis to human population?
11:20-11:40	Francisco Javier Ariza- López and Juan Francisco Reinoso	Functional Quality for GDEMs Assessment
11:40-13:00	Lunch Break	Titu Maiorescu Canteen
13:00-13:20	Francisco Javier Ariza- López, Manuel A. Ureña-Camara, Juan Francisco Reinoso and Marcelo Antonio Nero	Proposal for a Collaborative Data Infrastructure for Control of DEMs
13:20-13:40	Guohua Gou, Haigang Sui, Sheng Wang, Qiming Zhou and Jianya Gong	Constructing a True 3-D Model of a Karst Cave Using an UAV
13:40-14:00	Carlos Grohmann, Gulherme Garcia, Camila Viana, Helen Dias and Rebeca Coelho	RPA flight pattern and GCP influence on SfM-MVS modeling of a stable landslide in SE Brazil
14:00-14:20	Haigang Sui, Hao Zhang, Qiming Zhou and Jianya Gong	The true 3-D surface reconstruction using a multi-UAV cooperation method
14:20-14:40	ISG Busssiness Meeting	
14:40-15:00	Coffee Break	The Hall of the Lost Steps, University Main Corp (A)
15:00-16:40	ISG Busssiness Meeting	
16:40-17:00	Coffee Break	The Hall of the Lost Steps, University Main Corp (A)
17:00-18:00	ISG Busssiness Meeting	
18:00-21:00	Dinner	Casa Universitarilor Restaurant

Friday (14th July) – Day 5

8:45-10:20	Serge Riazanoff	<p>DEMIX workshop – Department of Geography, University Corp B (1) VtWeb for DEMs and (2) DEMIX Operations Portal</p> <p>(1) How to use VtWeb to select DEMs, their various versions, visualise them, apply on-the-fly processing, compare interactively DEMs and their versions, compute statistics, compute profiles...</p> <p>See for example https://visioterra.fr/telechargement/A003_VISIOTERRA_COMMUNICATION/HYP-107-VtWeb-E_Comparison_of_Copernicus_DEM_releases_2022_vs_2021.pdf</p> <p>(2) How to use “DEMIX Operations Portal” to import candidate and VHR reference DEMs and to compute criteria.</p> <p>See https://visioterra.org/DemixOperationsPlatform/</p>
10:20-10:40	Coffee Break	Department of Geography, University Corp B, Room 658
10:40-1:40	Serge Riazanoff	<p>DEM4S2</p> <p>How to get the DEM that has been used to orthorectify the Sentinel-2 tile and how this DEM produced on the exact tile footprint can be uploaded to better photo-interpret the optical data.</p> <p>See for example https://visioterra.org/DEM4S2/?s2Id=S2A_MSIL1C_20230616T012701_N0509_R074_T54STE_20230616T045503</p>
11:40-13:00	Lunch Break	Titu Maiorescu Canteen
13:00-14:00	John Lindsay	Whitebox Workshop – Department of Geography, University Corp B
14:00-14:20	Coffee Break	Department of Geography, University Corp B
14:20-15:40	John Lindsay	Whitebox Workshop – Department of Geography, University Corp B
15:40-17:00	John Lindsay	Whitebox Workshop – Department of Geography, University Corp B
17:00-22:00	Informal City Tour	

Evolution of the Copernicus DEM: beyond today's elevation data with WorldDEM Neo

Ernest Fahrland, Hanne Paschko, Henning Schrader
 Airbus DS, SAR Programs Potsdam, Germany
ernest.fahrland@airbus.com
hanne.paschko@airbus.com
henning.schrader@airbus.com

Virginia Herrera
 Airbus DS, SAR Programs Friedrichshafen, Germany
virginia.herrera@airbus.com

Abstract— The Copernicus DEM has established a programme-level reference for Digital Elevation Models, serving all Copernicus elements (Space, Services and In-situ) over a large array of Earth- Observation based applications. Originating from the TanDEM-X SAR-mission, interferometric data have been acquired between December 2010 and January 2015 to process a global, homogenous and highly accurate Digital Surface Model (DSM), which has been made available to ESA and its partners in a 10m resolution version. The 30m and 90m resolution versions have been made available to the general public. The value-adding of the TanDEM-X DEM (removal of terrain artefacts and hydrologic editing) conducted by Airbus created the WorldDEMTM dataset, which served as input for Copernicus DEM.

Based on the source data of the Copernicus DEM (WorldDEM) and fresh data acquisitions (2017-2020), a new generation of global DEM has been developed and validated which show improvements in actuality (2017-2020) and level of detail due to its new grid spacing of 5m. The global SAR-based DSM is commercially available as “WorldDEM Neo” with fully automated production processes, so as the DTM that is currently in production. Furthermore, known deficiencies in WorldDEM Neo caused by side-looking SAR (layover, shadow, high-rise buildings) are compensated through advanced processing. This comprises the local/regional integration of high- resolution DEM data from evolving techniques such as SAR image reconstruction or from optical sensors (primarily for DSM).

This document will focus on the processes to create an up-to-date high-resolution DSM/DTM on a global scale and the prospect of serving further applications in the Copernicus / Sentinel ecosystem.

I. INTRODUCTION

Digital elevation information (DSM, DTM) are an essential information source for various scientific and commercial applications. The Copernicus DEM & WorldDEM (acquired 2010-2015), ALOS World 3D (2006-2011) and SRTM (2000) are well-established DSMs though the data is not up-to-date. As Earth’s surface is very dynamic, current height information is as important as a high degree of precision. A huge challenge for global elevation information is the transformation of

raw/unedited elevation information into edited, analysis-ready elevation information.

In section II, a fully automated production process for global DSM data starting with unedited TanDEM-X Change DEM (German Space Agency; DLR) is described. This comprises the automated compensation of artefacts as well as hydro editing to produce the global WorldDEM Neo dataset. Section III provides the results of a statistical analysis based on ICESat-2 ATL08 point data and a visual example of WorldDEM Neo. An outlook on the subsequent integration of alternate DEM data to improve WorldDEM Neo and further processing to derive global DTM data is provided in section IV.

II. METHODS

A. Input Datasets

1) WorldDEM as input for Copernicus DEM

The current version of the Copernicus DEM is primarily derived from the commercial WorldDEM offered by Airbus DS with substitutions of the nominal fill sources by national DEM data for the area of Norway and Spain. WorldDEM is based on the unedited version of the TanDEM-X DEM (DLR). The generation process and performance of the TanDEM-X DEM is described in [1]. A description of the editing process to create the WorldDEM is available in [2]. The technical specification of the WorldDEM dataset is provided hereafter.

TABLE I. WORLDDEM PARAMETERS

Acquisition timeframe		Dec. 2010 – Jan. 2015
Coverage		Global / pole-to-pole
Projection		Geographic coordinates
Data Tiling		1° x 1°
Coordinate reference system	horizontal	WGS84-G1150
	vertical	EGM2008
Pixel spacing	latitude (Y)	0.4" (~12m)
	longitude (X)	0.4" – 4.0" (~12m, dep. on latitude)

2) TanDEM-X Change rawDEM scenes

DLR and Airbus DS decided in 2016 to acquire an additional global coverage of bi-static DEM data, after finishing the TanDEM-X DEM. The looking direction of the so-called Change DEM acquisitions is opposite to the one from the nominal TanDEM-X data (acquired 2010-2015). The across-track overlap of the new DEM scenes is ~4-5 km (Figure 2) and the interferometric processing is based on the delta-phase algorithm described in [3]. Although the interferometric process is supported by WorldDEM (~30m), the new phase (height) values are independent. The ground sampling distance of the Change rawDEM scenes is 0,2" (~5-6m). To preserve the level of detail of the Change rawDEM scenes best, no additional process step is performed by DLR (mosaicking and calibration, MCP) as this would create a DEM with again 0,4" ground sampling distance (~12m). The Change raw DEM data is unedited.

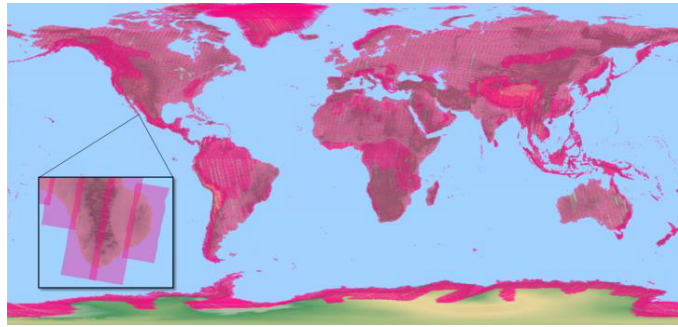


Figure 1. TanDEM-X Change DEM coverage and DEM scene overlap

B. WorldDEM Neo production process

1) Process overview

The production process creates an analysis-ready DSM dataset in a short timeframe. User interaction to mitigate artefacts in the unedited Change rawDEM data is not applied and a fully automated production process in a high performance computing environment has been established. The following Figure 2 provides a graphical overview of the process structure.

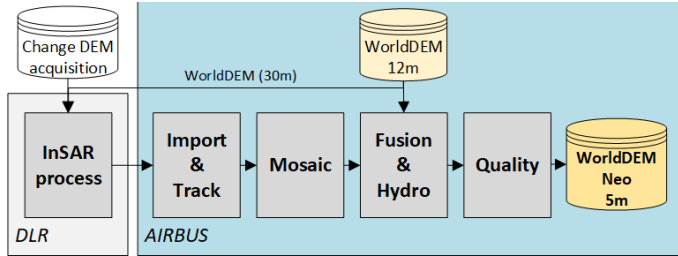


Figure 2. Global coverage of WorldDEM / Copernicus DEM

2) Mosaicking of TanDEM-X Change rawDEM scenes

After data transfer from DLR and database import at Airbus, the Change rawDEM scenes are mosaicked. Overlap regions of the scenes (see zoom caption in Figure 2) are processed with priority on the more up-to-date scene. A feathering algorithm at the scene borders for a distance of 10 pixels ensures a consistent and homogenous representation of the final WorldDEM Neo. Auxiliary information required for subsequent processes and/or the final product comprise an

incidence angle mask (IAM), height error mask (HEM), radar amplitude mosaic (AMP) and source scene mask (SCM).

3) DEM Fusion: Change rawDEM mosaic and WorldDEM

As the Change rawDEM mosaic represents unedited height information, a compensation of local artefacts based on DEM fusion has been developed. Reliable and fresh height information from the Change DEM acquisitions is preserved as much as possible, whereas unreliable height information is either compensated via alternate height information (weighted DEM fusion with WorldDEM) or edited acc. to pre-defined rules (hydro editing). A quality-based fusion principle based on the DEM height error is described in [4] and served as basis for process development. The height error is available in form of the standard deviation on a pixel basis and derived from the radar coherence and geometrical considerations. The weight of the Change rawDEM mosaic is derived with the following procedure.

$$w_{CD} = \frac{\frac{1}{\sigma_{HEMCD}^{4/\sqrt{|\Delta Z|}}}}{\frac{1}{\sigma_{HEMCD}^{4/\sqrt{|\Delta Z|}}} + \frac{1}{(s \times \sigma_{HEMWD})^{4/\sqrt{|\Delta Z|}}}} \quad \text{Eq. 1}$$

The pixel-based height errors for the Change rawDEM and WorldDEM are represented by σ_{HEMCD} resp. σ_{HEMWD} . The absolute height difference between both DEMs is represented by $|\Delta Z|$. The stretch factor s for σ_{HEMWD} is based on geometrical considerations (local slope gradient, incidence angle (IAM) incl. variable margin), the absolute height difference $|\Delta Z|$ and three additional parameters. The following Figure 3 displays the stretch factor scenario for a sample incidence angle of 40°.

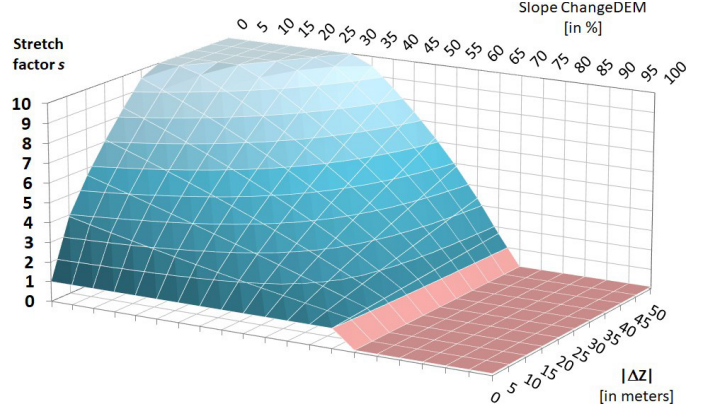


Figure 3. Stretch factor for σ_{HEMWD} with a radar incidence angle of 40°

For steep terrain in combination with a steep incidence angle, the stretch factor reduces the height error of WorldDEM, i.e. this height information is superior to the one from Change DEM. For moderate to plain terrain in combination with a low absolute height difference, the stretch factor is almost 1 and the weighting between the two DEMs is balanced. With an increasing absolute height difference, the height error of WorldDEM is raised, i.e. the Change DEM gains increasing superiority compared to WorldDEM. The final weighting is integrated in the final WorldDEM Neo product (in percent, weighted combination mask, WCM).

4) Editing of fused DEM

Hydrological features are subject to changes in extent as well as water level throughout time. For instance, ocean shoreline can change due to coastal erosion or harbor construction. Lakes and reservoirs can have different water extent/level. River courses can have changed. An automated process for delineation and vertical levelling process has been developed with the support of the hydrological information created during the WorldDEM editing process [2]. The editing information is integrated in the final WorldDEM Neo product (editing mask, EDM).

5) Statistical analysis based on ICESat-2 ATL08

A global statistical analysis using ICESat-2 laser altimetry data (ATL08, [5]) was applied on WorldDEM Neo. A filtering of the (reference) point data is based on the following attributes:

- Sole h_te_best_fit_20m elevation without parallel presence of canopy height information
- h_te_uncertainty < 7.5m
- No hydro editing during production process

Regions with permanent snow/ice cover (Antarctica, Greenland) have been excluded. The generalized slope gradient of WorldDEM Neo (~30m) is used to categorize the ICESat-2 ATL08 point data. The point count for slopes of 0°-10° is significantly higher compared to slopes >10°.

TABLE II. STATISTICAL RESULTS FOR WORLDDEM NEO BASED ON ICESAT-2 ATL08 TERRAIN POINTS (H_TE_BEST_FIT_20M)

Slope	LE90	RMSE	ATL08 point count	
0°-10°	1.350 m	0.961 m	2'553'468'984	99.404 %
10°-20°	4.979 m	3.122 m	14'201'213	0.553 %
20°-30°	11.110 m	7.315 m	961'622	0.037 %
30°-40°	16.882 m	12.695 m	125'519	0.005 %
40+ °	29.211 m	22.636 m	15'511	0.001%
TOTAL	1.375 m	0.976 m	2'568'772'849	100 %

III. RESULTS

A. Visual example

The following Figure 4 provides a visual comparison of WorldDEM and WorldDEM Neo for an area North of the city of Lanzhou in China (36,45°N, 103,75°E; incl. radar image overlay).

B. WorldDEM Neo Technical Specification

WorldDEM Neo is compliant to independent DEM standards (DGED Level 4b, INSPIRE Level 17) and is specified according to the table below.

IV. DISCUSSION AND FUTURE DEVELOPMENTS

WorldDEM Neo represents the most up-to-date global Digital Surface Model with a high level of detail and accuracy. The production is based on a fully automated and parameterizable python process, which allows easy adaptation and fast WorldDEM Neo re-processing to encompass future user requirements (e.g. new timestamp based on additional future acquisitions).

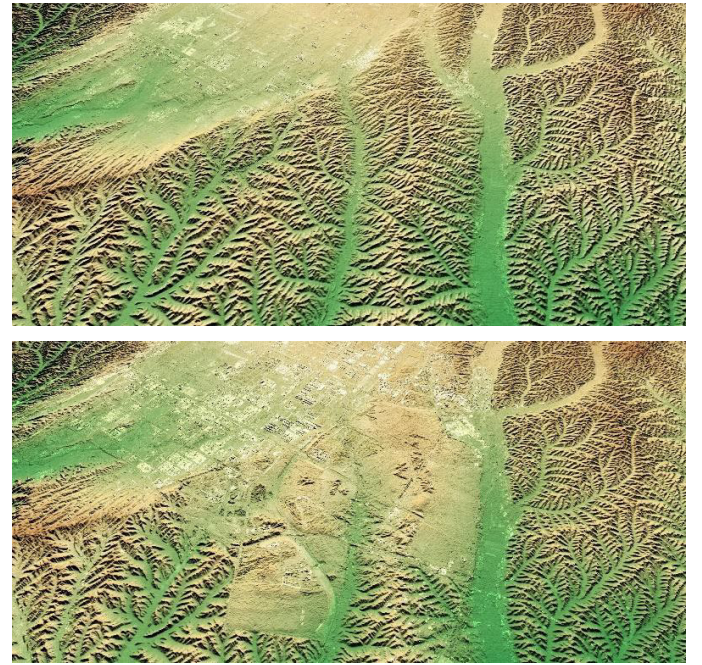


Figure 4. Comparison display of WorldDEM (top) and WorldDEM Neo (bottom) for an area North of Lanzhou (China)

TABLE III. WORLDDEM NEO PARAMETERS

Acquisition timeframe	2017 - 2020	
Coverage	Global / pole-to-pole	
Projection	Geographic coordinates	
Data Tiling	0,5° x 0,5°	
Coordinate reference system	horizontal	WGS84-G1150
	vertical	EGM2008
Pixel spacing	latitude (Y)	0,15" (~5m)
	longitude (X)	0,15" – 1,5" (~5m, dep. on latitude)

A. Global DTM with new temporal footprint

A wide range of DEM applications (e.g. hydrology, risk management, geology) require bare ground elevation information with vegetation, buildings, etc. removed. WorldDEM Neo opens the possibility for an improved global Digital Terrain Model (DTM) due to the higher level of detail and the fresh data acquisition compared to current DTMs originating from TanDEM-X (WorldDEM DTM LITE, FABDEM [6]). WorldDEM Neo

DTM will close the gap of providing a global coverage while offering more detailed terrain structure and time update.

The WorldDEM Neo DTM production process (knowledge-based set of rules) is based on the identification and description of surface objects within the DSM followed by a transformation of the surface heights into terrain heights while conserving the characteristics of the underlying terrain. The fully automated and parameterizable process is closed by an automated quality control and a visual check (if required).

B. Local/regional quality improvement of WorldDEM Neo

Side looking radar technology can cause deficiencies in a DSM that can be isolated to specific regions of the Earth, e.g. urban areas and regions with very steep slopes.

C. Regional updates of WorldDEM Neo beyond 2020

The on-going bistatic orbit configuration of TerraSAR-X and TanDEM-X and the available satellite resources allow

additional DEM acquisitions, which can be used to further update the current version of WorldDEM Neo.

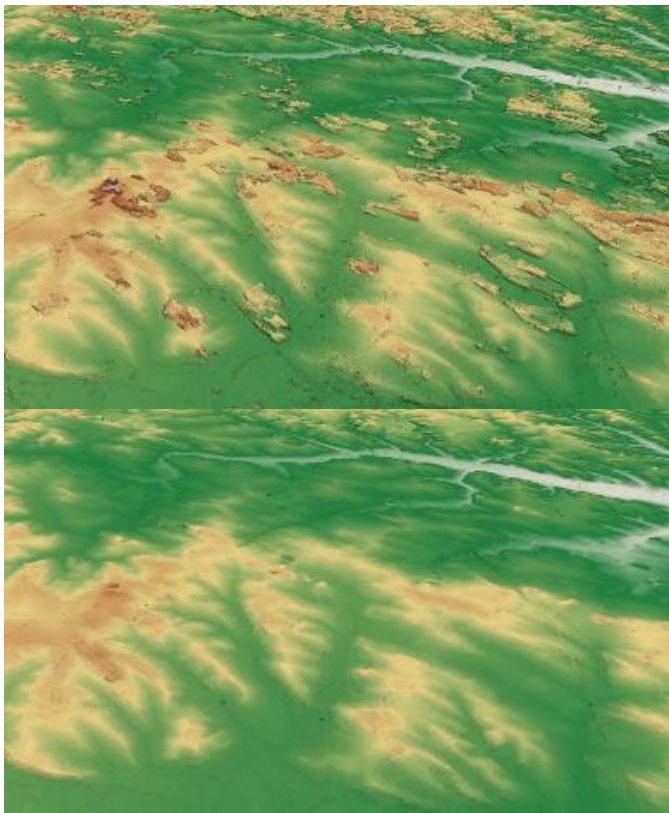


Figure 5. Example of WorldDEM Neo DSM and WorldDEM Neo DTM for an area West of Munich (Germany; 48,25°N, 11,25°E))

V. ACKNOWLEDGMENT

Airbus would like to thank DLR for their continuous support during the Change rawDEM production.

REFERENCES

- [1] Rizzoli, P. & Martone, M. & Gonzalez, C. & Wecklich, C. & Tridon, D.B. & Bräutigam, B. & Bachmann, M. & Schulze, D. & Fritz, T. & Huber, M. & Wessel, B. & Krieger, G. & Zink, M. & Moreira, A. (2017). "Generation and performance assessment of the global TanDEM-X digital elevation model", ISPRS Journal of Photogrammetry and Remote Sensing, Volume 132, 2017, Pages 119-139, ISSN 0924-2716. <https://doi.org/10.1016/j.isprsjprs.2017.08.008>
- [2] Collins, J. & Riegler, G. & Schrader, H. & Tinz, M. (2015). „Applying terrain and hydrological editing to TanDEM-X data to create a consumer-ready WorldDEM product”, ISPRS - International Archives of the Photogrammetry, Remote Sensing and Spatial Information Sciences. XL-7/W3. 1149-1154. <https://doi.org/10.5194/isprsarchives-XL-7-W3-1149-2015>
- [3] Lachaise, M. & Schweisshelm, B. & Fritz, T. (2020), „The new TanDEM-X Change DEM: Specifications and Interferometric Processing, ISPRS Annals of Photogrammetry, Remote Sensing and Spatial Information Sciences. IV-3/W2-2020. 143-148. <https://doi.org/10.5194/isprs-annals-IV-3-W2-2020-143-2020>
- [4] Wessel, B. (2018) “TanDEM-X Ground Segment – DEM Products Specification Document”, EOC, DLR, Oberpfaffenhofen, Germany, Public Document TD-GS-PS-0021, Issue 3.2, 2018. [Online]. Available: <https://tandemx-science.dlr.de/>
- [5] Neuenschwander, A. & Pitts, K. & Jelley, B. & Robbins, J. & Markel, J., & Popescu, S. & Nelson, R. & Harding, D. & Pederson, D. & Klotz, B. & Sheridan, R. (2022). “ICESat-2 Algorithm Theoretical Basis Document for the Land - Vegetation Along-Track Products (ATL08)”, Version 5.0, April 5, 2022. NASA ICESat-2 Project. 144p.
- [6] Hawker, L. & Uhe, P. & Paulo, L. & Sosa, J. & Savage, J. & Sampson, C. & Neal, J. (2022). “A 30m global map of elevation with forests and

buildings removed”. Environmental Research Letters. 17. <https://doi.org/10.1088/1748-9326/ac4d4f>

- [7] Grohman, G. & Kroenung, G. & Streckeck, J. (2006). “Filling SRTM voids: The delta surface fill method”, Photogrammetric Engineering and Remote Sensing. 72. 213-216.

FABDEM Updates - FABDEM V1-2

Laurence Hawker

School of Geographical Sciences
 University of Bristol
 Bristol, UK
laurence.hawker@bristol.ac.uk

Peter Uhe

Fathom
 Square Works, 17-18 Berkeley
 Square,
 Bristol, UK
p.uhe@fathom.global

Jeffrey Neal

School of Geographical Sciences
 University of Bristol
 Bristol, UK
j.neal@bristol.ac.uk

Abstract—FABDEM (Forest And Building removed copernicus Digital Elevation Model) is a global 1 arc second grid spacing Digital Terrain Model. Trees and buildings are removed from Copernicus GLO30 DEM using a novel machine learning approach. Since FABDEM’s release it has been widely used by the community in a variety of geoscience applications.

In this paper, we outline the latest updates to FABDEM (V1-2). Improvements to FABDEM include updating the baseline Digital Surface Model and methodological tweaks to fix discontinuities at some tile edges and artifacts caused by resampling at higher latitudes.

I. INTRODUCTION

FABDEM (Forest And Building removed copernicus Digital Elevation Model) is a global 1 arc second grid spacing Digital Terrain Model that removes buildings and trees from the Copernicus GLO30 DEM using a random forest based machine learning technique [1]. Since FABDEM V1.0 was released in December 2021, there have been numerous applications of FABDEM ranging from flooding [2,3] to road network extraction [4]. Users have provided invaluable feedback, and based on this, we introduce an update of FABDEM called FABDEM V1-2. FABDEM V1-2 is available from data.bris.ac.uk [5]. Note that FABDEM V1-1 was created but never publicly released and is not discussed in this article.

There are five changes in FABDEM V1-2 compared to FABDEM V1-0, with the changes outlined below:

- Discontinuities fixed at the edge of tiles covering large homogeneous forests
- The underlying Copernicus DEM has been updated to Copernicus 2021_1. Details on the updates to the Copernicus GLO30 DEM can be found on the [Copernicus website](#) [6].
- Copernicus GLO30 DEM has variable grid spacing in high latitudes (50°N/S). This results in grids not being aligned across the interface where different resolutions are used, resulting in some artifacts being introduced. For FABDEM, Copernicus DEM was first resampled to a 1 arcsecond grid, however for V1.0, the alignment of high latitude tiles was not matched to the low latitude tiles. The pre-

processing of the Copernicus DEM was updated for FABDEM V1.2 to align all tiles consistently.

- File format: changed to Cloud Optimized Geotiff, with updated compression options (DEFLATE with PREDICTOR=2). This reduces file size by ~40%
- File metadata: AREA_OR_POINT label changed to Point. Previously incorrectly labelled as Area.

Further details on some of the fixes are given in the following subsections, as well as comments on accuracy metrics to compare FABDEM V1-2 to FABDEM V1-0.

II. IMPROVEMENTS

A. Discontinuities

Discontinuities were first reported in the Amazon rainforest. In FABDEM V1-0 post-processing, a 5 pixel buffer was added to the corrected DEM for each 1 degree tile, before the post-processing stage. This buffer was taken from the Copernicus GLO30 DEM, without forests removed. The inconsistency between the corrected DEM and buffer resulted in incorrect depression filling during the post-processing step for densely forested areas (Fig. 1). The uncorrected buffer would typically be the height of the forest, usually ~20m, resulting in depression filling from the edge of the tile. This happened in large forests as these are areas where corrections are applied over wide areas.

The discontinuities were fixed by extending the buffer to 0.1 degrees and using a corrected buffer (FABDEM). This avoids using the uncorrected elevations which falsely filled in the depressions. The result of the fix can be seen in Fig. 2.

B. Artifacts in high latitude tiles

Copernicus DEM has variable grid spacing in high latitudes (50°N/S), which FABDEM resampled to 1 arc second to create a consistent grid that is more compatible to models typically used in the geosciences. However, the alignment of the lower latitude tiles did not match the higher latitude tiles, creating a slight offset. A result of this were artifacts being introduced in some tiles due to resampling and processing errors, such as an extreme example in Fig. 3. Note most of the changes are minimal (e.g. Fig. 4).

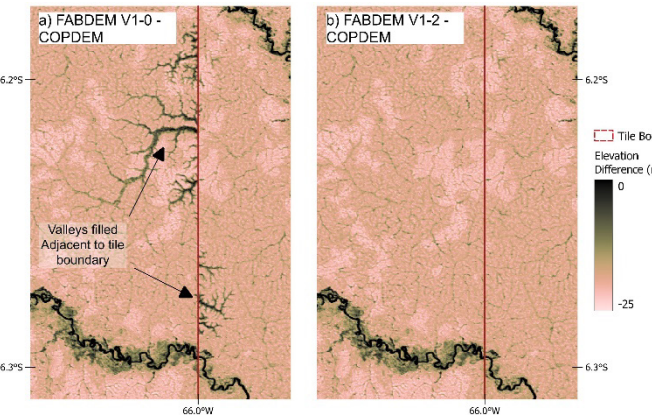


Figure 1. FABDEM V1-0 with valleys incorrectly filled (a), compared to FABDEM V1-2 (b). Difference to Copernicus DEM. Note the valleys incorrectly filled on FABDEM V1-0. Colour Maps for Figures are the Scientific color maps [7]

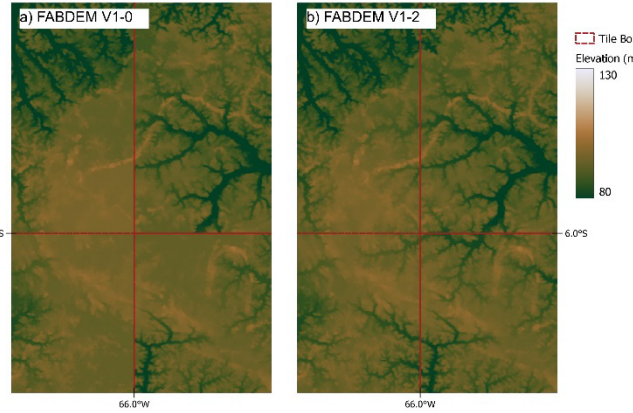


Figure 2. FABDEM V1-0 (a) compared to FABDEM V1-2 (b). Note the lack of discontinuities at tile boundaries in FABDEM V1-2.

C. Error Metrics

Reprocessing error metrics for FABDEM V1-2 yields mild improvements over FABDEM V1-0, with improvements in the order of 1-10cm (e.g. tiles in Germany and Poland not shown). However, for some applications, particularly hydrological applications, the improvements in FABDEM V1-2 can be significant, especially where discontinuities and artifacts have been removed.

D. Other changes

The file format of FABDEM V1-2 has been changed to Cloud Optimized Geotiff, with updated compression options (DEFLATE with PREDICTOR=2). This has helped reduce the size of the entire dataset to less than 300Gb, from ~450Gb of FABDEM V1-0. The new data record also includes a geoJSON of the tile extents (i.e. FABDEM in 1x1 degree tiles) to add usability.

Finally, the file metadata AREA_OR_POINT label has been changed to Point. Previously this was incorrectly labelled as Area.

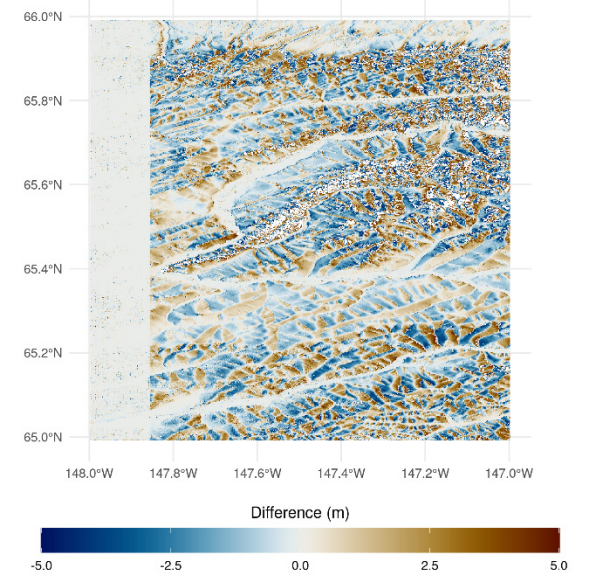


Figure 3. Difference between FABDEM V1-2 and FABDEM V1-0 for a high latitude tile.

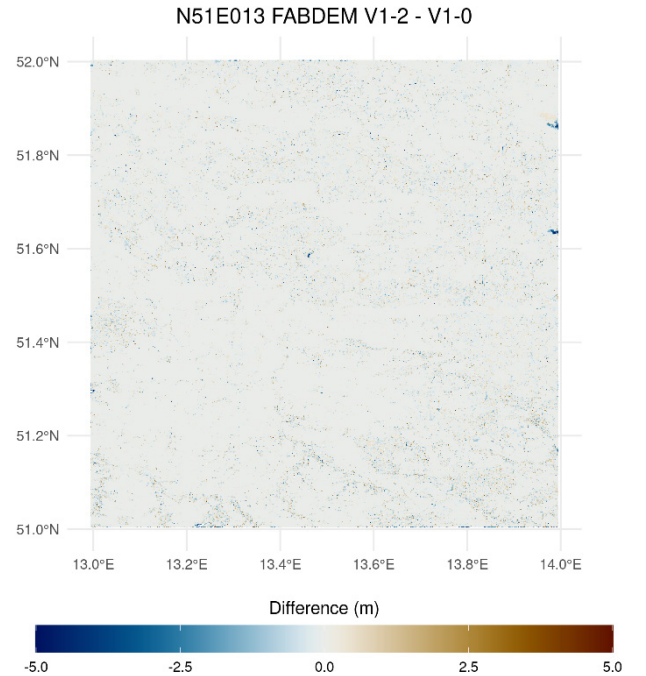


Figure 4. Difference between FABDEM V1-2 and FABDEM V1-0 for a high latitude tile (less extreme example)

E. Future Outlook

FABDEM will be continuously improved with the addition of improved covariates, more (in both quantity and diversity) training reference elevation data and the refinement of the machine learning method. As a result, the development team will cease incremental updates to the FABDEM V1.X family of DEMs and focus on a more major development. Besides improving the quality of the corrections, other noteworthy developments that need to be addressed include filling in the missing tiles covering Armenia and Azerbaijan (not available in Copernicus GLO-30 DEM), making FABDEM easier to

download, and working with groups to develop datasets that commensurate FABDEM such as a hydrography.

III. ACKNOWLEDGMENTS

We would like to thank all the FABDEM users who have contacted us with their feedback. In particular, we would like to thank Kevin Gross and Dr Anderson Ruhoff who gave us detailed feedback that helped identify the areas to improve. LH is funded by the Natural Environment Research Council (NERC) EvoFLOOD Project (NE/S015795/1).

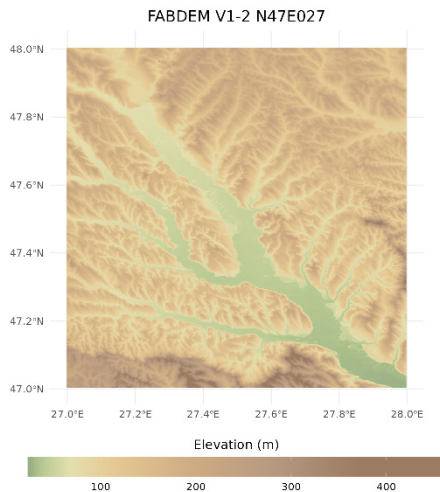


Figure 5. Terrain containing Iasi, Romania

REFERENCES

- [1] Hawker, L., Uhe, P., Paulo, L., Sosa, J., Savage, J., Sampson, C. and Neal, J., 2022. A 30 m global map of elevation with forests and buildings removed. *Environmental Research Letters*, 17(2), p.024016. <https://dx.doi.org/10.1088/1748-9326/ac4d4f>
- [2] Loli, M., Kefalas, G., Dafis, S., Mitoulis, S.A. and Schmidt, F., 2022. Bridge-specific flood risk assessment of transport networks using GIS and remotely sensed data. *Science of the Total Environment*, 850, p.157976. <https://doi.org/10.1016/j.scitotenv.2022.157976>
- [3] Teng, J., Penton, D.J., Ticehurst, C., Sengupta, A., Freebairn, A., Marvanek, S., Vaze, J., Gibbs, M., Streeton, N., Karim, F. and Morton, S., 2022. A Comprehensive Assessment of Floodwater Depth Estimation Models in Semiarid Regions. *Water Resources Research*, 58(11), p.e2022WR032031. <https://doi.org/10.1029/2022WR032031>
- [4] Chen, Y., Yang, X., Yang, L. and Feng, J., 2022. An Automatic Approach to Extracting Large-Scale Three-Dimensional Road Networks Using Open-Source Data. *Remote Sensing*, 14(22), p.5746. <https://doi.org/10.3390/rs14225746>
- [5] Hawker, L., Uhe, P., Paulo, L., Sosa, J., Savage, J., Sampson, C. and Neal, J., 2022. FABDEM V1-2. <https://doi.org/10.5523/bris.s5hqmjcdj8yo2ibzi9b4ew3sn>
- [6] Copernicus DEM, ESA 2022. <https://doi.org/10.5270/ESA-c5d3d65>
- [7] Cramer, Fabio. (2021). Scientific colour maps (7.0.1). Zenodo. <https://doi.org/10.5281/zenodo.5501399>

Geomorphometric and Geospatial Patterns in Differences Between ALOS and COPDEM

Peter L. Guth

Ocean & Atmospheric Sciences Dept
 United States Naval Academy
 Annapolis, MD, USA
pguth@usna.edu

Carlos H. Grohmann

Institute of Energy and Environment
 Universidade de São Paulo
 São Paulo 05508-010, Brazil
guano@usp.br

Sebastiano Trevisani

Culture del Progetto Dept
 University IUAV of Venice
 Venice 30123, Italy
strevisani@iuav.it

Abstract—We proposed three new criteria to use in addition to those presented in the DEMIX wine contest for evaluating 1 arc second global DEMs. We use the criteria to compare the COPDEM and ALOS DEMs. These criteria use a pairwise, pixel by pixel comparison of the candidate DEM to a reference DEM for elevation, slope, and roughness. With two candidate DEMs and a tolerance for differences not considered significant, we can score each pixel as a tie or win for COPDEM or ALOS. The method allows us to map the differences, and shows that the terrain has a major impact on the errors in these DEMs.

I. INTRODUCTION

DEMs represent a fundamental building block for work in science, engineering, social science, government, and the military. DEMs at 1 arc second (~30 m) provide the best resolution freely available globally. The DEMIX group is working to compare and rank those DEMs [1]. We use their database [2] to show the geomorphometric and geospatial patterns of the differences. While we performed this analysis for 6 DEMs, space restricts us to concentrate only on COPDEM and ALOS which are demonstrably much better than SRTM, NASADEM, and ASTER [3]. We also limit consideration of FABDEM, which attempts to approximate a DTM but only improves on COPDEM for some landscapes, so that we can look at the simpler case of only two DEMs.

II. METHODS

The wine contest [1] uses geomorphometric criteria to rank DEMs. The criteria must allow numerical ranking, which means the evaluations must be unsigned, and the method requires at least 3 DEMs for the statistical significance to be valid. While the criteria must be unsigned, the signed parameters like the mean and median differences provide important auxiliary information.

We use $\frac{1}{2}$ arc sec grids (Fig. 1), so that COPDEM and ALOS are equally affected by interpolation. We create the reference DTM and DSM where available by aggregation from high resolution source data. For ALOS and COPDEM the points in the original DEM are in their positions within the $\frac{1}{2}$ sec grid, and they are surrounded by points from bilinear interpolation. This allows direct difference maps between COPDEM and ALOS, and shows the geometric pattern of the differences, without introducing variable interpolation effects between the DEMs. We consider elevation, slope, and roughness defined as the standard deviation of slope in a 5x5 window [3]. We make pixel

by pixel comparisons for approximately 520,000 pixels in each DEMIX tile which covers approximately 100 km². The difference grids allow us to map the differences. We must set tolerances for what we consider significant differences before creating some grids, because the grids classify the map area into categories using the tolerances (Fig. 2).

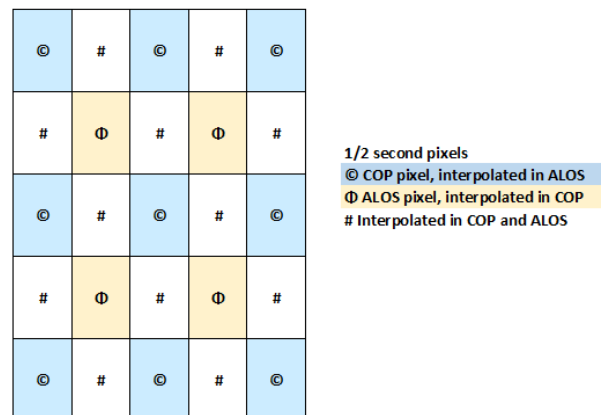


Figure 1. $\frac{1}{2}$ second resampling for arc second DEMs with rectangular pixels.

We will show two representations of the results (Figures 2 and 3), and the summary statistics for 20 test areas with over 200 100 km² tiles (Figure 4 and Table 1). Figure 3 considers the pixel a tie if both COPDEM and ALOS are within the tolerance of the reference DTM; otherwise the DEM closer in absolute value to the reference DTM is the best.

III. RESULTS

Figure 2 shows the largest differences from the reference DEM occur in steeper terrain. The computation has nine categories (each test DEM can be high, equal within tolerance, or low). The complex category lumps 6 categories.

The elevation bias in this tile is not representative of all tiles; the lack of bias for the slope and roughness are representative. The very small standard deviations are characteristic of COPDEM and FABDEM, as is the greater dispersion for ALOS, and the large dispersion for the other DEMs with a poorly defined mode.

Despite the negative overall bias for slope difference, the distribution skews toward less steep slopes. This results from

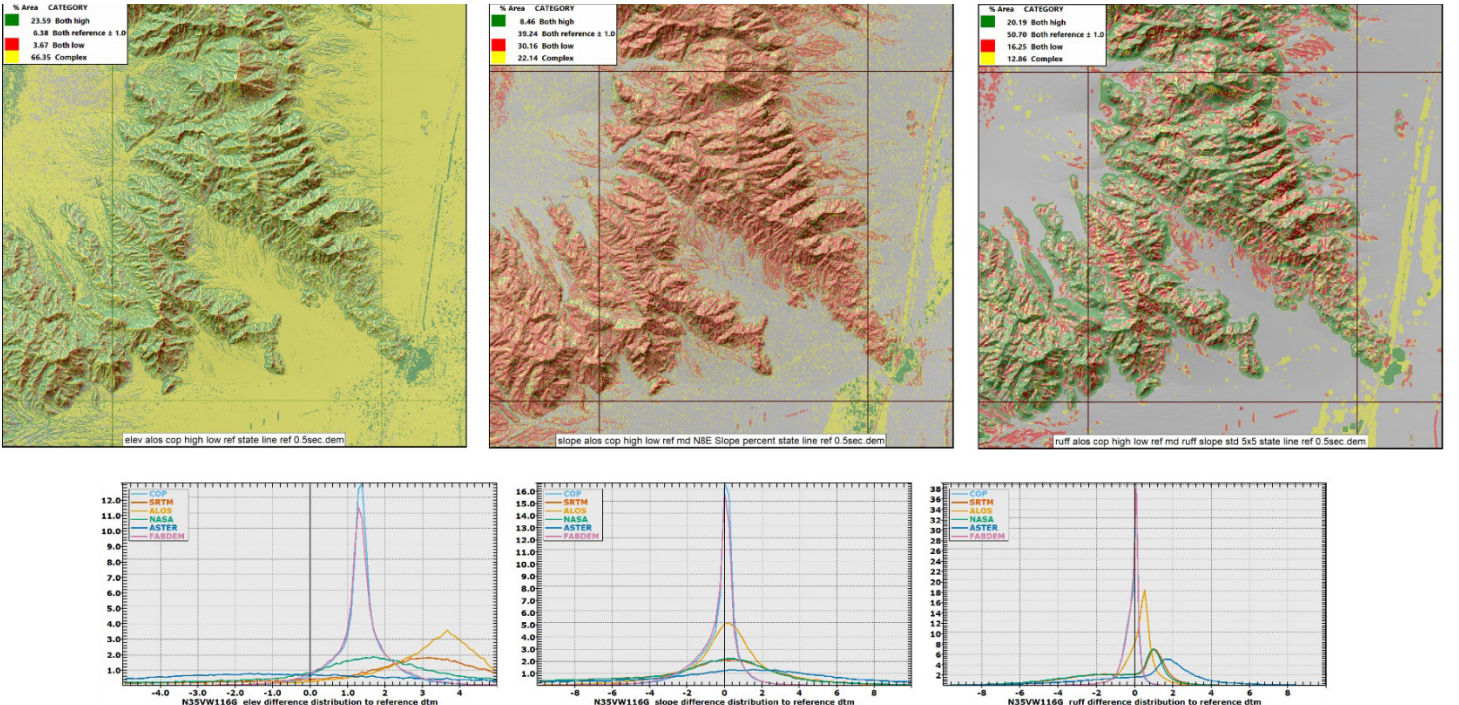


Figure 2. Comparison of COPDEM and ALOS to the reference half second DTM for DEMIX tile N35VW116G in the center of the map. Difference maps above and difference histograms below. Instate 15 on the right side of the map shows up difference appearance in the three DEMs.

comparing the $\frac{1}{2}$ second reference DEM with an interpolated test DEM which has lower average slopes.

Figure 5 shows roughness differences for a tile in the Canary Islands. The volcanic cones show the effect of trying to compare a pixel-is-area DEM and a pixel-is-point. The half pixel offset means that peaks, ridge crests, and valley bottoms in ALOS and COPDEM occur at different locations, and each is “better” compared to the reference DEM about half the time and the map pattern closely mimics the topography.

IV. DISCUSSION AND CONCLUSIONS

The wine contest criteria used in by DEMIX [1] use 5 metrics for the unsigned difference distribution. For each parameter (elevation slope, roughness), the 5 metrics are highly correlated and do not provide greatly different results. The 5 metrics

progressively get larger as they factor in increasingly extreme values in the tails of the distribution, but the global DEMs generally follow the same ranking. Beyond the evaluation numbers and rankings the criteria do not provide a simple, visual and intuitive way to assess the results.

Our three new criteria for elevation, slope, and roughness take the percentage of points in the DEM where each DEM is closest to the reference DEM, and ranks the DEMs. As designed these criteria have less influence from the tails of the difference distribution. With only two DEMs in our test, we can create maps showing the spatial patterns, and relate them to the characteristics of the region and see how slope, roughness, and aspect affect where ALOS and COPDEM diverge from the reference DEM.

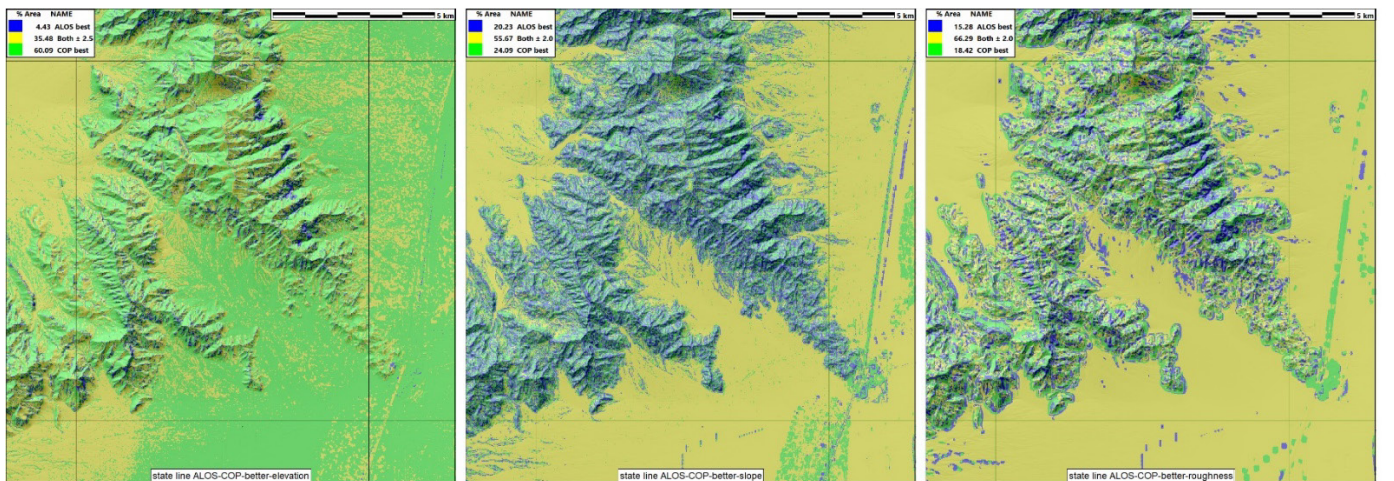


Figure 3. Comparison of COPDEM and ALOS to the reference half second DTM for DEMIX tile N35VW116G. Difference maps above and difference histograms below.

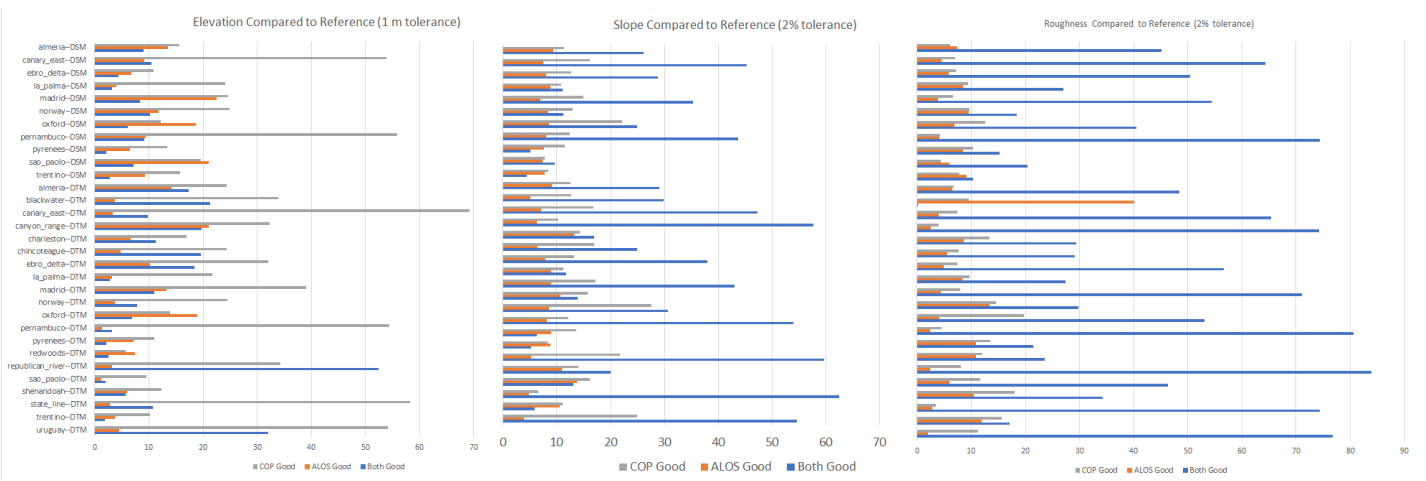


Figure 4. COPDEM and ALOS comparisons to the reference half second DTM and DSM where available for 20 test areas.

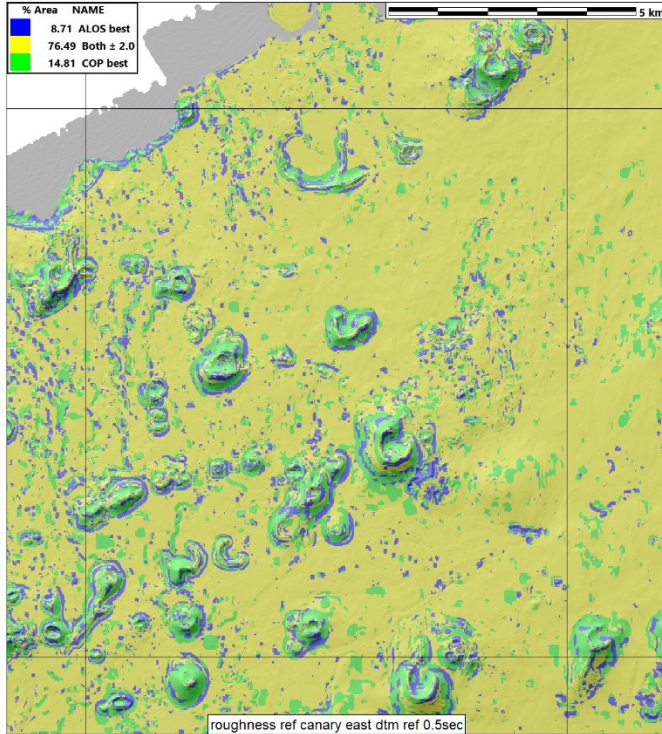


Figure 5. Roughness differences between COPDEM and ALOS from a reference DTM for DEMIX tiles N29MW014D. Supplementary figure 2 shows maps for elevation and slope, and both the DTM and DSM.

TABLE I. BEST DEM BY AREA

	DTM		DSM	
	ALOS	COPDEM	ALOS	COPDEM
Elevation	2	18	2	8
Slope	1	19	0	10
Roughness	1	19	3	7

The maps allow a subjective assessment of DEM quality that adds to the quantitative results; as one example, we have noted that ALOS frequently has small anomalies tracking the satellite's orbit path where different images were merged, something we did not observe with COPDEM.

We assume that the reference DEM is the closest to a true value of what the elevation should be for a 1 arc second pixel. Aggregating the high resolution DEM to 1 arc second necessarily loses detail, and the largest differences to the global

DEMs occur in steep terrain. In these pixels there is a large variation in elevation, and picking a single value to represent the pixel presents a challenge. We must consider the possibility that the choice for the elevations in the reference DEM has much more uncertainty in steep areas than in flat areas.

These comparisons (Table I) show that COPDEM is clearly better than ALOS, but the differences are generally small. COPDEM is better in the most heavily forested areas, reinforcing the suggestion that the radar sensor has greater penetration in the canopy compared to an optical sensor as suggested in evaluating the positions of the global DEMs in lidar point clouds [7].

Using $\frac{1}{2}$ grids allows direct comparison of ALOS and COPDEM, but does affect the slope differences and clearly shows the $\frac{1}{2}$ pixel difference between the two DEMs.

V. ACKNOWLEDGMENTS

All work done in the open source MICRODEM [5], which has source code and a 64 bit Windows executable. Larger figures and Supplementary figures available on zenodo. We thank our collaborators on the DEMIX group for stimulating discussions.

REFERENCES

- [1] Bielski, C.; López-Vázquez, C.; Guth, P.L.; Grohmann, C.H. and the TMSG DEMIX Working Group, 2023. DEMIX Wine Contest Method Ranks ALOS AW3D30, COPDEM, and FABDEM as Top 1" Global DEMs: <https://arxiv.org/pdf/2302.08425.pdf>
- [2] Guth, P.L. (2022). DEMIX GIS Database (1.0) [Data set]. Zenodo. <https://doi.org/10.5281/zenodo.7402618>. We used version 2, to be posted soon.
- [3] Grohmann, C. H., Smith M. J., and Riccomini, C, 2011, Multiscale Analysis of Topographic Surface Roughness in the Midland Valley, Scotland, IEEE Transactions on Geoscience and Remote Sensing, vol. 49, no. 4, pp. 1200-1213. <https://doi.org/10.1109/TGRS.2010.2053546>
- [4] Guth, P. L., & Geoffroy, T. M. (2021). LiDAR point cloud and ICESat-2 evaluation of 1 second global digital elevation models: COPDEMernicus wins. Transactions in GIS, 25, 2245– 2261. <https://doi.org/10.1111/tgis.12825>
- [5] Guth, P.L., 2023, git-microdem: https://github.com/prof-pguth/git_microdem, accessed 5 Feb 2023.

Assessing Global Elevation Models for Mapping the Low Elevation Coastal Zone

Dean Gesch

U.S. Geological Survey
 Earth Resources Observation and Science Center
 Sioux Falls, South Dakota, USA
gesch@usgs.gov

Abstract— Elevation data are critical for assessments of coastal hazards, including sea-level rise (SLR), flooding, storm surge, tsunami impacts, and wave run-up. Previous research has demonstrated that the quality of data used in elevation-based hazard assessments must be well documented and applied properly to assess potential impacts. Global digital elevation models (DEMs), at 30- to 90-meter resolution, have been used extensively to map and characterize coastal environments and the at-risk resources (population and built structures) contained therein. The inherent absolute vertical accuracy of global DEMs precludes their usefulness for assessing exposure to fine increments (< 1 meter) of coastal inundation at high confidence levels. However, global DEMs are highly suitable for delineation of the global low elevation coastal zone (LE CZ) (elevation < 10 meters). An accuracy evaluation of global DEMs over the United States has been conducted to quantify their performance in correctly mapping the LE CZ, namely in terms of vertical uncertainty and corresponding confidence levels for several representations of the coastal zone. The evaluation approach includes comparison of the DEMs with an extensive set of high-accuracy geodetic control points as the independent reference data covering a variety of coastal relief settings. The 1-arc-second (30-meter) global DEMs evaluated include ALOS World 3D, ASTER GDEM, Copernicus, FABDEM, and NASADEM, and the 3-arc-second (90-meter) global DEMs include CoastalDEM, Copernicus, MERIT, and TanDEM-X. Additionally, lower resolution (1-kilometer) global DEMs were also assessed, namely the Global Lidar Lowland DTM (derived from ICESat-2) and the GEDI 1-km DEM. The results of the accuracy characterization show that FABDEM performs the best (minimal vertical bias and lowest vertical root mean square error) for high-confidence mapping of the LE CZ. Among 90-m DEMs, CoastalDEM performs best, although the differences across datasets are minimal. The results also demonstrate the importance of rigorously accounting for elevation uncertainty when applying global DEMs for coastal mapping applications.

I. INTRODUCTION

Due to the low-lying nature of many coastal lands, the topography, or elevation in relation to sea level, largely controls their exposure to adverse effects of increased water levels, both chronic conditions (sea-level rise) and episodic events (storm surge inundation or king tide flooding). Elevation data, notably in the form of digital elevation models (DEMs), are therefore critical for assessing exposure to permanent or

temporary flooding and other effects of increased water levels along the coast.

Previous research has demonstrated that the quality of data used in elevation-based coastal hazard assessments must be well documented and applied properly to assess potential impacts [1-2]. The vertical uncertainty of the input elevation data substantially controls the minimum increments of inundation that can be effectively used in coastal hazard assessments. When properly characterized, the vertical accuracy of the DEM can be used to report assessment results with the uncertainty stated in terms of a specific confidence level.

Global DEMs, at 30- to 90-meter resolution, have been used extensively to map and characterize coastal environments and the at-risk resources (population and built structures) contained therein. However, in most cases, uncertainty has not been considered. An accuracy evaluation of global DEMs has been conducted to quantify their performance in mapping the global low elevation coastal zone (LE CZ), namely in terms of vertical uncertainty and corresponding confidence levels for several delineations of the coastal zone.

II. DATA AND METHODS

A. Data

The 1-arc-second (30-meter) global DEMs evaluated include ALOS World 3D (AW3D30) [3], ASTER GDEM [4], Copernicus (COP30) [5], FABDEM [6], and NASADEM [7], and the 3-arc-second (90-meter) global DEMs include CoastalDEM [8], Copernicus (COP90) [5], MERIT [9], and TanDEM-X [10]. Additionally, lower resolution (1-kilometer) global DEMs were also assessed, namely the Global Lidar Lowland DTM (GLL DTM) (derived from ICESat-2) [11] and the GEDI 1-km DEM (https://daac.ornl.gov/GEDI/guides/GEDI_L3_LandSurface_Metrics_V2.html).

The global DEMs were assessed by comparison with an extensive set of high-accuracy geodetic control points as the independent reference data covering a variety of coastal relief settings in the conterminous United States (CONUS). The control points are a product of the U.S. National Geodetic Survey (NGS) and are known as “GPS on Bench Marks” (<https://www.ngdc.noaa.gov/access/metadata/landing-page/bin/iso?id=gov.noaa.ngdc:0209231>). These points are

considered to be NGS's best control points, with millimeter- to centimeter-level accuracies, used in development of hybrid geoid models, so they are an excellent reference dataset for comparing with DEMs for accuracy assessment purposes. The points have been used extensively for such analyses [12-13]. For the study area of the CONUS coast, a subset of 3,713 points (with elevation < 10 meters) were extracted from the full GPS on Bench Marks dataset of more than 37,000 points.

B. Methods

To calculate the absolute vertical accuracy for each global DEM, the elevation value at every reference point is compared to the corresponding DEM elevation (extracted via bilinear interpolation at the exact point location) and the difference in elevations is recorded. The difference represents the DEM error at that point. The differencing operation is done by subtracting the reference point elevation from the DEM elevation. In this way, the difference statistics from the point comparisons are easy to interpret; that is, a positive mean error indicates that on average the DEM is too high (the DEM has a positive bias). Conversely, a negative mean error indicates that on average the DEM is too low (a negative bias). Prior to comparison of the DEMs and the reference data, the control points were transformed to be in the same horizontal coordinate system and vertical reference frame (vertical datum) of each of the DEMs, so the difference statistics do not contain any artificial biases.

For inundation modeling, a specific case of coastal hazard assessment, the DEM is the base data on which the water level is raised to delineate the land area subject to inundation under the selected water level (i.e., areas with an elevation less than the water level). Such a procedure is essentially an elevation contouring process whereby a line of constant elevation at the selected water level is derived from the elevation data. It is easy to define such an elevation contour, especially in a geographic information system, and the vertical increment between adjacent contours (or the contour interval) must be specified. A small interval can be applied to any DEM but doing so does not imply that the derived contours automatically meet published accuracy standards. The interval must not be so small that it falls within the bounds of vertical error of the DEM, as such an operation would place the measurement (elevation increment) "in the noise" of the underlying elevation data.

Based on the concept of elevation contour line accuracy, a method has been developed [1] to determine the minimum contour interval (or in the case of inundation modeling, the minimum increment of water level increase) that should be used to meet a specified confidence level. Using that minimum interval ensures that the contours are truly supported by the DEM given its inherent vertical uncertainty. In the United States, legacy national map accuracy standards applied to topographic contour maps specify that 90% of tested elevations should fall within one-half of the map contour interval [14], and this has been called the vertical map accuracy standard (VMAS) with a 90% confidence level, or alternatively "linear error at 90% confidence" (LE90). Based on the contour accuracy standard, it has been demonstrated [15] that the contour interval (CI) can be expressed directly as a factor of the elevation data accuracy, as in $CI = LE90 \times 2$. Two of the most commonly used DEM error metrics are root mean square error (RMSE) and LE95, and direct translations among RMSE, LE90, and LE95 are available [14], assuming the errors are from an unbiased normal distribution. Because the error metrics represent a portion of the cumulative probability distribution of errors, a confidence level can be stated for the minimum increment, for example 68% confidence for RMSE (equivalent to the "one sigma" error, or standard

deviation of the errors for an unbiased normal distribution), 90% confidence for LE90, and 95% confidence for LE95.

By applying the concept of contour line accuracy, or alternatively, minimum inundation increment, (as a function of DEM accuracy), it has been documented that global DEMs are not suitable for modeling exposure to fine increments (< 1 meter) of coastal inundation at high confidence levels [15]. However, given their range of inherent vertical accuracy, global DEMs are suitable for general delineation of the LECZ (areas with elevations < 10 meters above sea level), a commonly used elevation threshold to delimit coastal zones [16-18]. The vertical accuracy statistics calculated in the accuracy assessment reported here are applied in the contour accuracy approach to quantify the performance of the free and open global DEMs for mapping the LECZ, including stating the confidence level.

III. RESULTS AND DISCUSSION

Results of the accuracy assessment are shown in Table I. The results are grouped by sets of rows for the 30-m DEMs (FABDEM, COP30, AW3D30, NASADEM, ASTER GDEM) (rows 2-6), 90-m DEMs (CoastalDEM, COP90, TanDEM-X, MERIT) (rows 7-10), and 1-km DEMs (GLL DTM, GEDI) (rows 11-12).

TABLE II. ACCURACY ASSESSMENT RESULTS

DEM	DEM grid spacing	No. of ref. points	Mean error (m)	RMSE (m)	Min. interval (m) at 68% conf.	Min. interval (m) at 95% conf.
FABDEM	30 m	3696	-0.055	1.231	2.463	4.827
COP30	30 m	3676	0.401	1.570	3.140	6.154
AW3D30	30 m	3578	1.029	2.809	5.617	11.010
NASADEM	30 m	3641	0.638	3.090	6.180	12.113
ASTER GDEM	30 m	3646	5.874	7.199	14.398	28.219
CoastalDEM	90 m	3696	-0.810	2.092	4.183	8.199
COP90	90 m	3678	0.786	2.110	4.221	8.273
TanDEM-X	90 m	3733	0.942	2.324	4.648	9.111
MERIT	90 m	3594	1.104	2.338	4.676	9.166
GLL DTM	1 km	2116	-0.734	1.528	3.056	5.990
GEDI	1 km	3099	-0.234	2.608	5.217	10.224

Among the 30-m DEMs, FABDEM performs the best, exhibiting the lowest vertical RMSE (1.23 m) and minimal vertical bias (about -6 cm). This translates into a contour interval of 2.46 m at 68% confidence, and a contour interval of 4.83 m at 95% confidence. Thus, FABDEM is very suitable for extremely high-confidence delineation of the LECZ (i.e., the 10-m contour). In fact, FABDEM could be used to delineate a 5-m "shoreline zone" at better than 95% confidence, and even a very low elevation coastal zone of 2.5 meters at 68% confidence. COP30 is also appropriate for very high-confidence mapping of the 10-m LECZ. AW3D30 and NASADEM could also be used for such LECZ delineation, albeit at lesser confidence levels. ASTER GDEM is not appropriate for accurate mapping of the LECZ.

Among the 90-m DEMs, CoastalDEM performs the best, although the performance differences across the 90-m DEMs is minimal. CoastalDEM, COP90, TanDEM-X, and MERIT are suitable for high-confidence mapping (better than 95%

confidence) of the 10-m LECZ, and each could be used to delineate a 5-m shoreline zone at about 68% confidence. Although GLL DTM is at a much reduced spatial resolution of 1-km (compared to other global DEMs), this DEM is also found to be suitable for very high-confidence mapping of the 10-m LECZ.

It is important to note that the calculation of the minimum interval is based solely on the RMSE. In selection of a DEM for coastal zone mapping, users should also note the mean error (vertical bias) of the DEMs, which is fairly substantial in some cases. In terms of inundation modeling, the mean error can indicate whether use of the DEM will on average overpredict or underpredict areas subject to inundation.

IV. CONCLUSION

Numerous medium resolution global DEMs are available for regional, continental, and global coastal hazard assessment. Rigorous accuracy assessment of the DEMs provides quantitative information about which DEM could perform the best for high-confidence mapping of the global low elevation coastal zone. The results of the assessment reported here show that FABDEM is the most accurate and is quite well suited for high-confidence delineation of 5-m and 10-m coastal zones.

V. ACKNOWLEDGMENTS

Any use of trade, firm, or product names is for descriptive purposes only and does not imply endorsement by the U.S. Government.

REFERENCES

- [1] Gesch, D.B., 2013. Consideration of vertical uncertainty in elevation-based sea-level rise assessments: Mobile Bay, Alabama case study. *Journal of Coastal Research*, SI(63), p. 197-210. <https://doi.org/10.2112/SI63-016.1>
- [2] West, H., Horswell, M., and Quinn, N., 2018. Exploring the sensitivity of coastal inundation modelling to DEM vertical error. *International Journal of Geographical Information Science*, 1-22. <https://doi.org/10.1080/13658816.2018.1444165>
- [3] Tadono, T., Nagai, H., Ishida, H., Oda, F., Naito, S., Minakawa, K., and Iwamoto, H., 2016. Generation of the 30 m-mesh global digital surface model by ALOS PRISM. *ISPRS - International Archives of the Photogrammetry, Remote Sensing and Spatial Information Sciences* XLI-B4, 157-162. <https://doi.org/10.5194/isprarchives-XLI-B4-157-2016>
- [4] Abrams, M., Crippen, R., and Fujisada, H., 2020. ASTER Global Digital Elevation Model (GDEM) and ASTER Global Water Body Dataset (ASTWBD). *Remote Sensing* 12, no. 7: 1156. <https://doi.org/10.3390/rs12071156>
- [5] Copernicus Global Digital Elevation Model (COP-DEM). <https://doi.org/10.5270/ESA-c5d3d65>
- [6] Hawker, L., Uhe, P., Paulo, L., Sosa, J., Savage, J., Sampson, C., and Neal, J., 2022. A 30 m global map of elevation with forests and buildings removed. *Environmental Research Letters*, 17, 024016. <https://doi.org/10.1088/1748-9326/ac4d4f>
- [7] Crippen, R., Buckley, S., Agram, P., Belz, E., Gurrola, E., Hensley, S., Kobrick, M., Lavalle, M., Martin, J., Neumann, M., Nguyen, Q., Rosen, P., Shimada, J., Simard, M., and Tung, W., 2016. NASADEM Global Elevation Model: Methods and progress. *Int. Arch. Photogramm. Remote Sens. Spatial Inf. Sci.* XLI-B4, 125-128. <https://doi.org/10.5194/isprarchives-XLI-B4-125-2016>
- [8] Kulp, S.A., and Strauss, B.H., 2018. CoastalDEM: A global coastal digital elevation model improved from SRTM using a neural network. *Remote Sensing of Environment* 206, 231-239. <https://doi.org/10.1016/j.rse.2017.12.026>
- [9] Yamazaki, D., Ikeshima, D., Tawatari, R., Yamaguchi, T., O'Loughlin, F., Neal, J.C., Sampson, C.C., Kanae, S., and Bates, P.D., 2017. A high accuracy map of global terrain elevations. *Geophysical Research Letters* 44, 5844-5853. <https://doi.org/10.1002/2017gl072874>
- [10] Rizzoli, P., Martone, M., Gonzalez, C., Wecklich, C., Borla Tridon, D., Bräutigam, B., Bachmann, M., Schulze, D., Fritz, T., Huber, M., Wessel, B., Krieger, G., Zink, M., and Moreira, A., 2017. Generation and performance assessment of the global TanDEM-X digital elevation model. *ISPRS Journal of Photogrammetry and Remote Sensing*, Vol 132, pp. 119-139. <https://doi.org/10.1016/j.isprsjprs.2017.08.008>
- [11] Vernimmen, R., and Hooijer, A., 2023. New LiDAR-based elevation model shows greatest increase in global coastal exposure to flooding to be caused by early-stage sea-level rise. *Earth's Future*, 11, e2022EF002880. <https://doi.org/10.1029/2022EF002880>
- [12] Gesch, D.B., Omoen, M.J., and Evans, G.A., 2014. "Accuracy assessment of the U.S. Geological Survey National Elevation Dataset, and comparison with other large-area elevation datasets: SRTM and ASTER". USGS Open-File Report 2014-1008. <https://doi.org/10.3133/ofr20141008>
- [13] Wessel, B., Huber, M., Wohlfart, C., Marschalk, U., Kosmann, D., and Roth, A., 2018. Accuracy assessment of the global TanDEM-X Digital Elevation Model with GPS data. *ISPRS Journal of Photogrammetry and Remote Sensing* 139, 171-182. <https://doi.org/10.1016/j.isprsjprs.2018.02.017>
- [14] Maune, D.F., Maitra, J.B., and McKay, E.J., 2007. "Accuracy Standards & Guidelines," in *Digital Elevation Model Technologies and Applications: The DEM Users Manual*, 2nd Edition, ed. D.F. Maune. (Bethesda, Maryland: American Society for Photogrammetry and Remote Sensing), p. 65-97.
- [15] Gesch, D.B., 2018. Best practices for elevation-based assessments of sea-level rise and coastal flooding exposure. *Frontiers in Earth Science*, 6:230. <https://doi.org/10.3389/feart.2018.00230>
- [16] McGranahan, G., Balk, D., and Anderson, B., 2007. The rising tide: assessing the risks of climate change and human settlements in low elevation coastal zones. *Environment and Urbanization* 19, 17-37. <https://doi.org/10.1177/0956247807076960>
- [17] Licher, M., Vafeidis, A.T., Nicholls, R.J., and Kaiser, G., 2011. Exploring data-related uncertainties in analyses of land area and population in the "Low-Elevation Coastal Zone" (LEZ). *Journal of Coastal Research* 274, 757-768. <https://doi.org/10.2112/jcoastres-d-10-00072.1>
- [18] Neumann, B., Vafeidis, A.T., Zimmermann, J., and Nicholls, R.J., 2015. Future coastal population growth and exposure to sea-level rise and coastal flooding--a global assessment. *PLoS One* 10, e0118571. <https://doi.org/10.1371/journal.pone.0118571>

DEM generalization using polygonal simplification

Richard Feciskanin

Dept. of Physical Geography and Geoinformatics Faculty of Natural Sciences,

Comenius University Bratislava, Slovakia

richard.feciskanin@uniba.sk

Abstract— Generalization methods and their quality is a very important element of geomorphometric research. Polygonal simplification methods in generalization can generally preserve the basic shapes well even at a higher level of generalization. The limited suitability for subsequent mathematical modeling is a major limitation of the use of TIN-based generalization (polygonal simplification) in geomorphometry. Our main goal was to build a method for generalizing the DEM of the land surface using polygonal simplification and to create a generalized model at any level of generalization suitable for further analysis. This involves converting the resulting coarse TIN to a smooth grid. We have created an algorithm that combines well-known algorithms for individual stages of the generalization process with a new method of anisotropic subdivision that increases the quality of the process. The algorithm consists of three main parts: generalization, skeletonization, and smoothing. The main generalization procedure uses Quadratic Error Metric Simplification (QEMS) on the polyhedral model. A smooth surface is created by Laplacian smoothing and Loop subdivision methods. With a greatly simplified model, the level of smoothing required to mitigate the triangular structure is high and thus has the undesirable effect of smoothing the actual edges. We improved the algorithm by using an additional step between generalization and smoothing. The algorithm creates a detailed triangular skeleton using our new anisotropic subdividing triangles based on QEMS quadrics at the vertices. The result shows that the algorithm can successfully progressively remove small features, but also preserve the basic shapes of the landscape surface. The output mesh is also sufficiently smooth without triangular artifacts from the polyhedral TIN model.

I. INTRODUCTION

With highly detailed and accurate LiDAR DEMs now widely available, the problems of geomorphometric investigation have shifted from data error and sampling adequacy to how the surface is actually defined [1]. Research has demonstrated that neither the data's initial scale, nor the highest resolution, guarantee the best representation, suggesting that scale optimization is a complex but necessary problem [2]. This confirms that generalization methods and their quality is a very important element of geomorphometric research.

The use of grid-based generalization methods predominates in geomorphometry, although many generalization methods have been developed for TIN-based DEMs [3]. Polygonal simplification methods (a group of TIN-based generalization methods) can generally preserve basic shapes well at a higher degree of generalization [4].

The limited suitability for subsequent mathematical modeling is the main limitation of the use of TIN-based generalization in geomorphometry. Land surface curvatures and other higher order parameters are calculated almost exclusively from grids. Therefore, conversion of the resulting TIN to a smooth grid is necessary. Generalization methods used in landscape modeling skip this phase. Separate conversion methods to create a raster grid from a TIN are not very common. If available, they are very basic using linear or simple interpolation, e.g. TIN To Raster in ArcGIS [5]. This is not suitable for generating a grid from a highly generalized TIN, as triangle artifacts remain visible.

Our main goal was to compose a method to generalize the DEM of the land surface using polygonal simplification and create a generalized model at an arbitrary level of generalization suitable for further analysis. This means that the key is to find a balance between preserving the characteristic shapes of the land surface and smoothing it enough for calculations without triangular artifacts.

The construction of a smooth surface over a triangular mesh is an important topic in geometric modeling, and various techniques have been proposed for this problem [6]. They used either triangular patches or refinement schemes. It has been proven that patches with smooth interpolation schemes often generate extraneous folds [7]. In connection with the properties of the generalized model, the used polygonal simplification is better complemented with the approximating subdivision surfaces. This combination can be supplemented and refined, and then forms the integrated generalization algorithm that we present below.

II. METHOD

A. Quadric Error Metric Simplification

The Quadric Error Metric Simplification (QEMS) method [8] is a well-known method for simplifying a polyhedral surface. It was developed primarily for computer graphics; however, it is universal and suitable for use in land surface modeling too [3]. It uses the edge contraction procedure to simplify the model geometry.

QEMS uses the same metric to calculate the weight of edge contraction and optimal vertex placement. This metric is based on the quadratic distances of the new vertex from the individual planes of the triangles with the original merged vertices. An isosurface of constant distance is a quadric (which gives the method its name) and its parameters are stored in the vertices in

the form of a 4×4 matrix. A quadric is an ellipsoid if not degenerate. The resulting quadric after edge collapse is the sum of the quadrics of the merged vertices and therefore preserves information about the shape of the surrounding surface [9]. Visualized quadrics on a simplified model are shown in Fig. 1.

B. Quadric Error Subdivision

To preserve as much shape information as possible from the simplified model from the QEMS method, we created the Quadric Error Subdivision (QES) method. It enables the creation of a significantly simplified model by QEMS, but prepares a detailed skeleton for subsequent operations on the polyhedral model (e.g. smoothing). The main idea is to reuse the surface shape information stored in the vertices during QEMS.

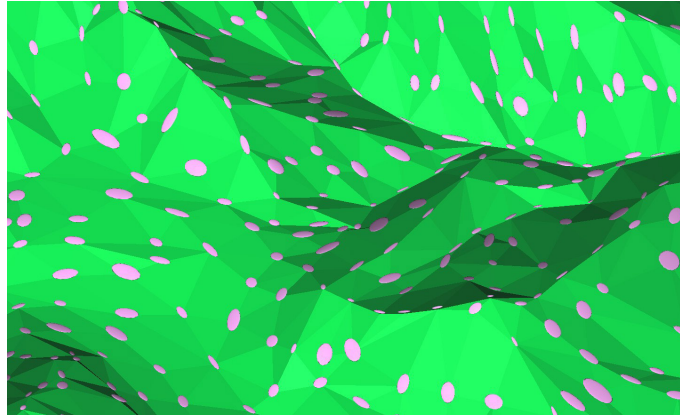


Figure 1. Quadric isosurfaces of the simplified model vertices

QES uses a triadic subdivision where each original triangle is replaced by 9 new ones. The basic division uses the PN triangle subdivision presented in [7]. The difference is that the new vertices along the edges are not in the tangent plane of the original vertex (since they are not patch control points and lie on the surface instead) but at a distance of $\frac{1}{3}$ between the tangent plane and the edge of the triangle (Fig. 2).

This is anisotropic subdivision, the new vertices along the edges of the triangle are not evenly spaced but are shifted towards the nearest original vertex based on the shape of the QEMS quadrics at that vertex. The ratio of the shift is equal to the contraction of the quadric from the normalized sphere in the direction from the vertex to the new vertex (Fig. 3). The calculation of the central control point is based on the position of the other new vertices along the edges, so the shift is used without changing the referenced equation. The shape of the created triangles follows the shape of the representing surface.

C. Laplacian smoothing

Laplacian smoothing is a simple, yet effective technique for polyhedral surface smoothing. For each vertex in a mesh, a new position is chosen based on local information (the position of neighbors) and the vertex is moved there. This displacement can be written as the Laplacian operator $U(P)$ for the point. Local update rule

$$P \leftarrow P + \lambda U(P) \quad (2)$$

applied to each point of a polyhedral surface is called Laplacian surface smoothing. The factor λ is typically a small positive number and the process (2) is performed repeatedly [10]. With more iterations and higher λ , the smoothed surface has a strong degree of shrinkage.

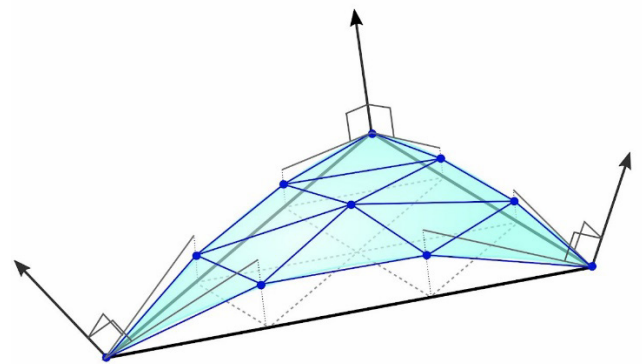


Figure 2. Basic localization of subdivision vertices - modified PN triangle subdivision.

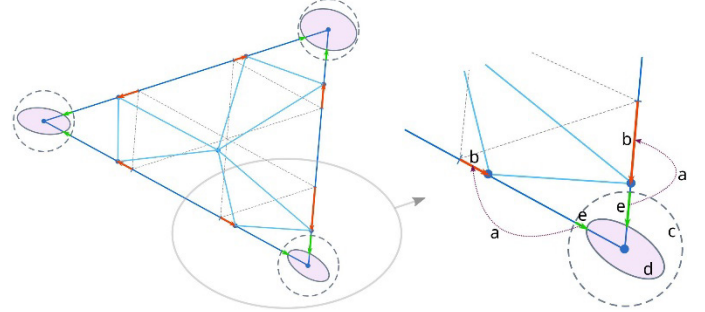


Figure 3. Anisotropic triadic subdivision using the shape of quadric isosurfaces in vertices (2D view). Arrows (a) show a vertex shift (b) dependent on the shape change of the sphere (c) to the quadric (d) direction of the triangle edge (e).

D. Loop subdividing

A subdivision surface algorithms use a recursive refinement scheme to better approximate the underlying curved surface. The Loop method for subdivision surfaces [11] is an approximating subdivision scheme for triangular meshes. It is based on iterative refinement of the triangular mesh using dyadic split operation – each edge of the triangular mesh is split into two, and new vertices are reconnected to form 4 new triangles.

The position of new, but also original vertices, is calculated based on a three-directional quartic box spline. This spline basis function is C2-continuous. The Loop scheme produces surfaces that are C2-continuous everywhere except at extraordinary vertices (whose valence $N \neq 6$), where they are C1-continuous.

III. ALGORITHM DESCRIPTION

A. Overview

The presented algorithm contains procedures for generalizing the DEM of the land surface up to a very high level of generalization and creates a smooth generalized model suitable for further analysis. The algorithm consists of three main parts:

1. Generalization
2. Skeletonization
3. Smoothing

The main generalization procedure uses the QEMS on a polyhedral model as presented in [3]. The input and output of the algorithm is a raster DEM, therefore a data structure conversion is required. However, converting a generalized triangular mesh to a raster grid (calculated from a smooth and curved surface) is a challenge. The smooth surface is created by Laplacian

smoothing and Loop subdivision methods. When targeting a highly simplified model, the level of smoothing required to mitigate the triangular structure is high and thus has the undesirable effect of smoothing the actual edges. We improved the algorithm by creating a detailed triangular skeleton using our novel anisotropic subdividing triangles based on QEMS quadrics at the vertices. The result of smoothing after anisotropic subdividing significantly better represents the original land surface.

B. Generalization

The Quadric Error Metric Simplification (QEMS) method [8] is a well-known method for simplifying a polyhedral surface. It was developed primarily for computer graphics; however, it is universal and suitable for use in land surface modeling too [3]. It uses the edge contraction procedure to simplify the model geometry.

C. Skeletonization

The Quadric Error Metric Simplification (QEMS) method [8] is a well-known method for simplifying a polyhedral surface. It was developed primarily for computer graphics; however, it is universal and suitable for use in land surface modeling too [3]. It uses the edge contraction procedure to simplify the model geometry.

D. Smoothing

The Quadric Error Metric Simplification (QEMS) method [8] is a well-known method for simplifying a polyhedral surface. It was developed primarily for computer graphics; however, it is universal and suitable for use in land surface modeling too [3]. It uses the edge contraction procedure to simplify the model geometry.

IV. RESULTS

As an input for generalization testing, we utilized aerial LiDAR raster DEM products with a resolution of 1 meter, obtained from various regions of Slovakia and different types of land surfaces. Each of the research areas selected for this study, covering several square kilometers, were primarily located in regions where previous geomorphological research had been conducted. The initial grids were generalized to many levels to confirm the applicability of the algorithm in different conditions. The individual phases of the algorithm (intermediate results) are presented on the model of the high mountain landscape in the Tatras (the vicinity of Skalné vráta hill - the terrain comprising rocky formations along the ridge at an altitude above 1,600 meters), generalized to level 75 in Fig. 4.

A comparison of the results of different levels of generalization is shown in Fig. 5. It depicts a model of Devínska Kobyla hill, located in the western region of Bratislava, which has a vertical range of 150 to 514 meters above sea level. The model includes anthropogenic elements such as quarries, and has been generalized with a ratio of 20, 60, and 150.

V. CONCLUSION

We have created an algorithm that combines well-known algorithms for individual stages of the generalization process with a novel anisotropic division method that increases the quality of the process. The results of the algorithm are now tested and compared with the results of different generalization methods and the comparison will be presented soon.

The software is developed to run in Node.js and relies on external libraries to perform partial tasks. Once the production quality of the software is ensured, the generalization tool will be made available to the public.

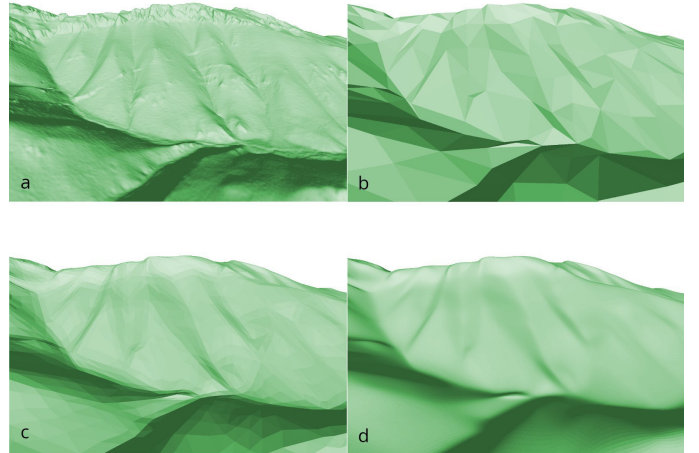


Figure 4. Algorithm stages: a) initial model, b) QEMS generalization, c) skeleton using QES, d) smoothed model to create grid

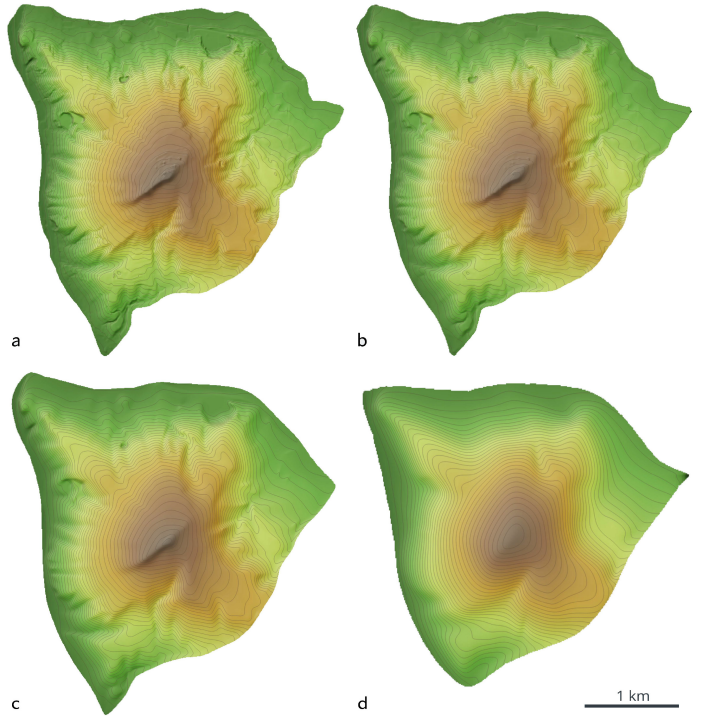


Figure 5. Generalization levels: a) initial model, b) 20, c) 60, d) 150.

VI. ACKNOWLEDGMENT

This work was supported by the Slovak Research and Development Agency under the contracts No. APVV-15-0054 and APVV-22-0024.

REFERENCES

- [1] Minár, J., Krcho, J., & Evans, I. S. (2016). Geomorphometry: Quantitative Land-Surface Analysis. In *Reference Module in Earth Systems and Environmental Sciences*. Elsevier. <https://doi.org/10.1016/b978-0-12-409548-9.10260-x>
- [2] Newman, D. R., Cockburn, J. M. H., Drăguț, L., & Lindsay, J. B. (2022). Local scale optimization of geomorphometric land surface parameters using scale-standardized Gaussian scale-space. *Computers & Geosciences*, 165, 105144. <https://doi.org/10.1016/j.cageo.2022.105144>.

- [3] Feciskanin, R., & Minár, J. (2021). Polygonal simplification and its use in DEM generalization for land surface segmentation. *Transactions in GIS*. <https://doi.org/10.1111/TGIS.12796>.
- [4] Luebke, D. P. (2001). A developer's survey of polygonal simplification algorithms. *IEEE Computer Graphics and Applications*, 21(3), 24–35. <https://doi.org/10.1109/38.920624>.
- [5] ESRI, (2022). ArcGIS Pro Documentation: How TIN To Raster works, <https://pro.arcgis.com/en/pro-app/latest/tool-reference/3d-analyst/how-tin-to-raster-3d-analyst-tools.htm>.
- [6] Lee, C.-K., Hwang, H.-D., & Yoon, S.-H. (2016). Bézier Triangles with G2 Continuity across Boundaries. *Symmetry*, 8(3) 13. <https://doi.org/10.3390/sym8030013>.
- [7] Vlachos, A., Peters, J., Boyd, C., & Mitchell, J. L. (2001). Curved PN triangles. *Proceedings of the Symposium on Interactive 3D Graphics*, 159–166. <https://doi.org/10.1145/364338.364387>.
- [8] Garland, M., & Heckbert, P. S. (1997). Surface simplification using quadric error metrics. *Proceedings of the 24th Annual Conference on Computer Graphics and Interactive Techniques*, SIGGRAPH 1997, 209–216. <https://doi.org/10.1145/258734.258849>
- [9] Garland, M. (1999). *Quadric-Based Polygonal Surface Simplification*. Dissertation, Carnegie Mellon University.
- [10] Belyaev, A. (2006). Mesh smoothing and enhancing curvature estimation. *Mpi-Inf. Mpg. De.*, 1-2.
- [11] Loop C. T. (1987). *Smooth subdivision surfaces based on triangles*. Master's thesis, Department of Mathematics, University of Utah.

Landscape according to surface roughness: experimenting in the Taklimakan Desert

Sebastiano Trevisani

University IUAV of Venice
Venice, Italy
strevisani@iuav.it

Peter L. Guth

Ocean and Atmospheric Sciences Department
United States Naval Academy
Annapolis, MD, USA
pguth@usna.edu

Abstract—Surface roughness, interpreted in the wide sense of surface texture, is a generic term referring to a variety of aspects and scales of the spatial variability structure of surface morphology. Even when the interest is limited to short-range roughness, relative to the resolution considered, various aspects of surface roughness can be characterized, such as omnidirectional roughness and roughness anisotropy. Adopting smoothing and/or upscaling approaches it is possible to perform a multiscale analysis of the selected roughness indexes. In this case study, a simplified geostatistical-based algorithm for surface/image texture analysis is adopted for the multiscale analysis. The proposed roughness algorithm is designed to offer a balance between the flexibility and complexity of geostatistical approaches, providing an easy yet informative approach for roughness analysis. Differently from conventional geostatistical approaches, it bypasses the detrending step to reduce at a minimum the user selected computational parameters. The algorithm is capable to partition roughness according to specific lag distances and to roughness anisotropy; moreover, ad hoc roughness indexes can be developed from the basic implementation. The multiscale analysis is based on a simple iterative approach, according to which the short-range roughness indexes are calculated from multiple upscaled versions of a source DEM. The DEM adopted is the 30 m resolution Copernicus DEM, representing a portion of the Taklimakan Desert, China. Despite the simplicity of the approach, the informative content extraction potential is very high, as confirmed by the unsupervised clustering of the landscape based on multiscale roughness indexes.

I. INTRODUCTION

This case study explores the potentialities of a simplified geostatistical algorithm for the multiscale analysis of surface roughness or, more generally, surface texture. The algorithm [1] is designed for the analysis of surface roughness and image texture, with some basic implementations coded in R as well as in Python for ArcMap [2]. The algorithm has been devised to provide an easy to use yet powerful geostatistical approach for the spatial variability analysis, reducing at a minimum level the user-dependent choices. Differently from conventional geostatistical approaches [3-4], it bypasses the detrending procedure; the effect of local slope is filtered out exploiting the geostatistical approach based on increments of order k [5]. The algorithm permits to calculate short-range roughness indexes, where short-range means that the spatial variability of surface is computed considering differences in elevation or in band intensity, in the case of imagery, comparing locations at a small distance (e.g., lags of 1 or 2 pixels). The current implementation,

which can be easily modified to compute ad hoc roughness indexes [6], permits to calculate two key factors of short-range roughness: omnidirectional roughness and roughness anisotropy (strength and direction). With this kind of algorithm, it is possible to perform a multiscale analysis of roughness indexes by means of a simple approach based on DEM/image upscaling [7-11]. It should be highlighted that the present implementation is conceived for the analysis of DEMs and imagery on a projected system. For working in geographical coordinates systems custom kernels can be defined, if one wants to derive the roughness considering lags with projected distances.

II. METHODS

A. Study area and Digital Elevation Model

In order to highlight the potential of the approach, the Taklimakan Desert (Fig. 1) China has been selected as study site. This kind of landscape is well suited to outline the potential of the proposed approach. In fact, it is characterized by the widespread presence of complex morphological features [12-13], with multiple wavelengths and anisotropies (Fig. 2), such as in correspondence of the network of complex/compound mega dunes. The analysis is performed on a digital elevation model (DEM) at 30 m resolution (5000 x 5000 pixels), derived by means of UTM projection of the Copernicus DEM, at 1 arc-second resolution [14]. For supporting the morphological interpretation, Sentinel 2 imagery at 10 m resolution (ESA, Copernicus) has been considered; however, the absence of vegetation and of anthropic land cover enhance the correlation between image texture and surface roughness (e.g., Fig. 2).

B. The multiscale approach

The multiscale approach followed is relatively simple: the short-range roughness analysis is performed iteratively on multiple coarser resolution versions of the original DEM. It is an approach that exploits the dispersion variance and sampling frequency to filter out specific wavelengths [7].

The short-range roughness is analyzed considering the MAD (Median Absolute Differences) estimator of spatial variability [6], which represents a robust version of the usual geostatistical estimators such as the variogram and the madogram [5]. The adopted geostatistical approach bypasses the detrending step considering differences of differences (i.e. increments of order 2); the implemented algorithm permits to compute roughness for

lag distances of 0.5, 1 and 2 pixels. For this case study a lag distance of 2 pixels has been considered both to highlight better the anisotropy as well as to filter out some fine-grain noise of the DEM. A circular search window with a 3-pixel radius has been used for MAD estimations. Two basic short-range roughness indexes have been selected: omnidirectional roughness (units in m) and anisotropy strength (ranging from 0, isotropy, to 1, maximum anisotropy). The anisotropy direction (a further index provided by the algorithm) has not been considered for the landscape classification, being here interested in rotation invariant metrics.

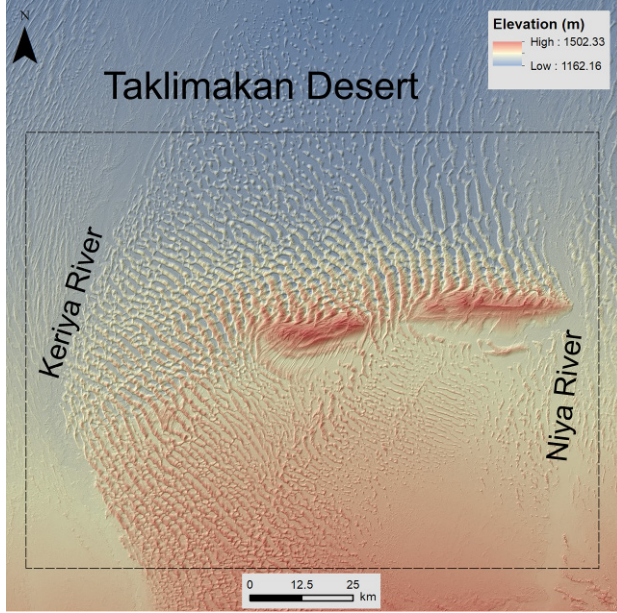


Figure 1. Study site location highlighting the morphology of the portion of the Taklimakan desert considered.

The coarsening of the original DEM resolution has been conducted via simple pixel aggregation, using the mean as estimator. The following coarsening factors of the original pixel (30 m) have been selected: 1, 2, 4, 8, 16, 32. Accordingly the DEMs' resolution ranges from 30 m to 960 m (further referred as levels L1-L32) and the lag distance from 60 m to 1920 m. Clearly a smoother transition and a narrower/wider range of variation can be selected. For each of the 6 levels L1-L32 the short-range roughness indexes, omnidirectional roughness (Fig. 3) and anisotropy (Fig. 4), have been calculated and then resampled via bilinear interpolation to the original resolution at 30 m.

Most of the computations have been computed in the R statistical programming environment. Saga Gis 8.3 has been adopted for the classification of landscape according to roughness indexes by means of the Isodata clustering method. Arcmap 10.8.2 (Esri) has been deployed for data management and the creation of the maps presented here.

III. RESULTS

The landscape classification (Fig.5), for a portion of COP DEM tile, has been conducted with the Isodata method (variables normalized, number of clusters tested from 5 to 16), using the 12 multiscale roughness indexes computed above (6 omnidirectional roughness indexes and 6 anisotropy indexes). This should be considered a preliminary classification and a more in-depth analysis on the classification approaches and selection of input features should be carried out. Nevertheless, the derived 8-clusters classification is satisfactory for providing

a glance of the rich informative content of the basic short-range roughness indexes computed. The spatial assemblage of clusters (Fig. 5, left) and the mean values of roughness indexes for clusters centers (Fig. 5, right) are quite distinctive of the different morphologies.

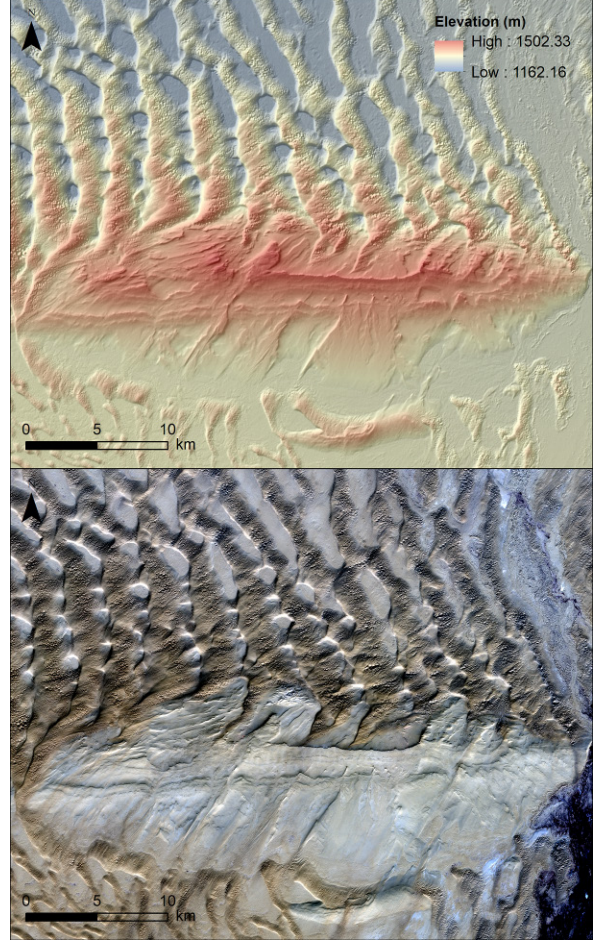


Figure 2. A detail of the study area: top, Copernicus DEM at 30 m resolution (ESA - Copernicus); bottom, Sentinel 2 imagery at 10 m resolution (Sentinel 2 color composite, ESA - Copernicus). It is evident the transition between the complex sand dune system and the mountain area with outcropping bedrock.

For example, the classes 3 (yellow), 7 (orange) and 8 (red) distinguish specific morphologies of the complex dunal system. Class 3 is characterized by low omnidirectional roughness at levels L1 and L2, but very high, as class 7, at levels L16 and L32; it has a relatively high anisotropy at levels L4, L8 and L16. This class essentially represents long wavelength dunal system with a smooth surface in the short-range. Class 7 is like class 3, but it is characterized by a higher roughness at levels L1 and L2, indicating a rougher morphology at short range, related to presence of short wavelength dunes. Class 8 is different, because it is characterized by the highest omnidirectional roughness at all scales and the highest anisotropy in the levels L1, L2 and L4. Class 8 essentially detects the steep scarps of mega-dunes facing south-west direction. The assemblage of clusters changes evidently in the two central mountains, where the bedrock is shallow or outcropping and there are some elongated ghost dunes, with a prevalence of classes 2 (green), 4 (pink) and 5 (dark green). Class 4 is characterized by low anisotropy at all scales and often represents areas with star shaped dunes. Class 5, with the lowest omnidirectional roughness at all scales, is representative of the alluvial deposits

of Keriya and Niya rivers and interdunal flat and smooth surfaces.

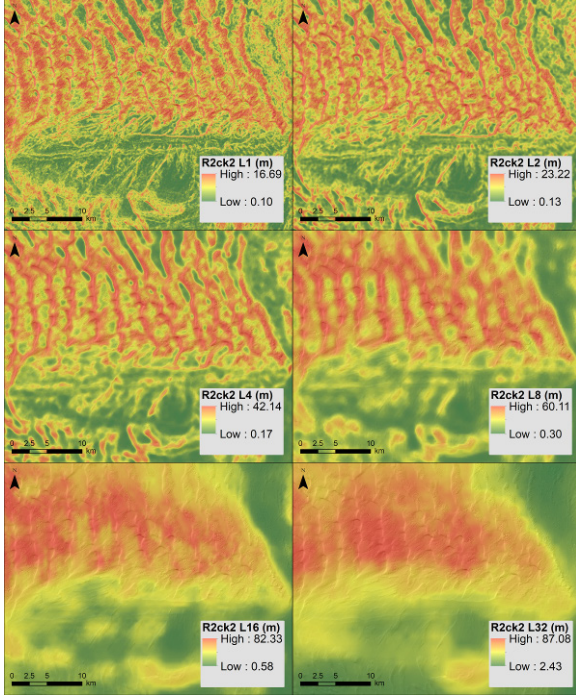


Figure 3. For the area of Fig. 2, short-range omnidirectional roughness computed on the multiresolution DEMs (levels L1-L32, from 30 to 960 m resolution). Increasing the pixel size, longer wavelengths contribute to the computed roughness indexes. The separation between the desert, the mountain with shallow bedrock and the alluvial deposits is particularly evident at levels L16 and L32. Color scales histogram equalized.

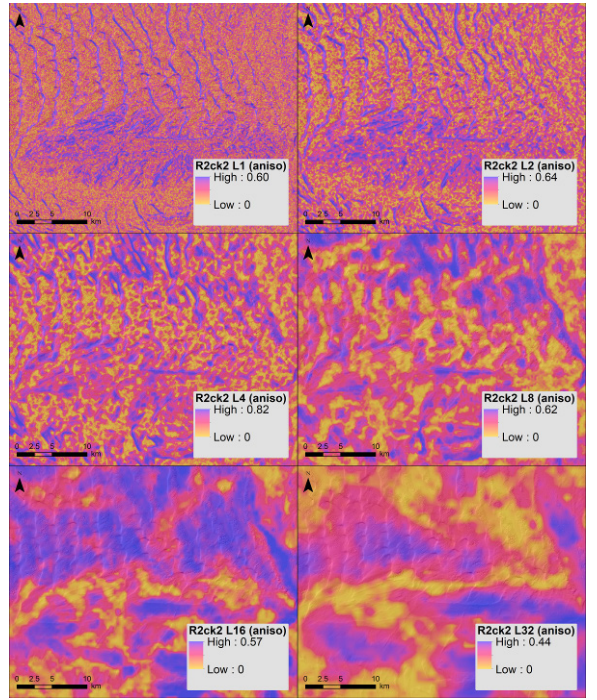


Figure 4. For the area of Fig. 2, short-range roughness anisotropy computed on the multiresolution DEMs (levels L1-L32, from 30 to 960 m resolution). Increasing the pixel size the roughness anisotropy related to longer wavelengths is enhanced. Color scales histogram equalized.

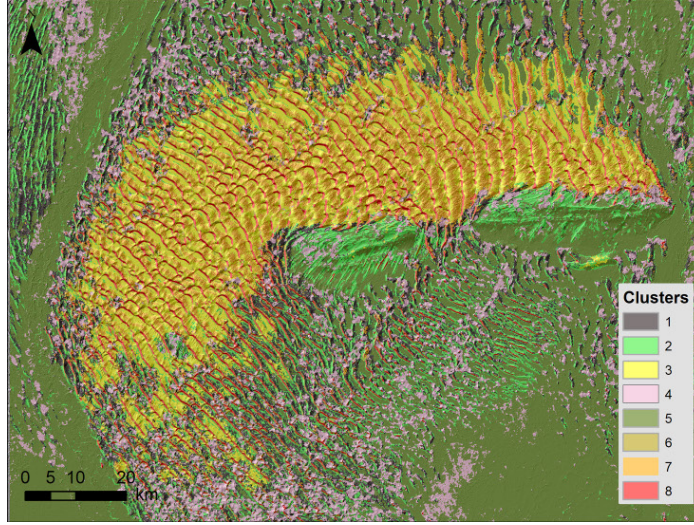


Figure 5. Isodata classification according to surface roughness indexes (on the left) and clusters centers in terms of omnidirectional roughness and anisotropy (on the right, hillshade on the background).

From the graphs of cluster centers (Fig. 5) it is also evident that anisotropy is a distinctive feature. For example, classes 1, 2 and 4 (black, light green and pink) have almost identical omnidirectional roughness at all scales and their differences are mainly related to anisotropy.

IV. CONCLUSIONS

The results of this explorative analysis are promising and demonstrate the applicability of the approach. Notwithstanding, multiple aspects require further investigation, both from the perspective of the computational details as well as from the

interpretative point of view. Regarding the geomorphological interpretation it should be admitted that the study site has been selected as a “toy example”, and the interpretation of computed indexes is quite naïve from the geomorphological and geological point of view. The interpretation of this kind of analysis from the perspective of geomorphic processes analysis and modelling is promising (e.g., [12] and [13]). Accordingly, collaboration with experts on the Taklimakan desert geology and geomorphology would be surely an added value.

REFERENCES

- [1] Trevisani, S., Teza, G. & Guth, P., 2023. A Simplified Geostatistical Approach for Characterizing Key Aspects of Short-Range Roughness. *CATENA*, Volume 223, <https://doi.org/10.1016/j.catena.2023.106927>.
- [2] Trevisani, S., 2023. <https://doi.org/10.5281/zenodo.7132160>.
- [3] Herzfeld, U.C., Higginson, C.A., 1996. Automated geostatistical seafloor classification - Principles, parameters, feature vectors, and discrimination criteria. *Computers and Geosciences*, 22 (1), pp. 35-52.
- [4] Trevisani, S., Cavalli, M., Marchi, L., 2009. Variogram maps from LiDAR data as fingerprints of surface morphology on scree slopes. *Natural Hazards and Earth System Sciences* 9, 129–133.
- [5] Chilès, J.-P., Delfiner, P., 2012. *Geostatistics - Modeling Spatial Uncertainty*. John Wiley & Sons, Inc., New Jersey.
- [6] Trevisani, S. & Rocca, M., 2015. MAD: Robust image texture analysis for applications in high resolution geomorphometry. *Computers and Geosciences*, vol. 81, pp. 78-92.
- [7] Woodcock, C.E. & Strahler, A.H., 1987. The factor of scale in remote sensing. *Remote Sensing of Environment*, vol. 21, no. 3, pp. 311-332.
- [8] Trevisani, S., Cavalli, M. & Marchi, L. 2010. Reading the bed morphology of a mountain stream: A geomorphometric study on high-resolution topographic data. *Hydrology and Earth System Sciences*, vol. 14, no. 2, pp. 393-405.
- [9] Grohmann, C.H., Smith, M.J., Riccomini, C., 2011. Multiscale Analysis of Topographic Surface Roughness in the Midland Valley, Scotland. *IEEE Transactions on Geoscience and Remote Sensing* 49, 1220-1213.
- [10] Newman, D.R., Lindsay, J.B. & Cockburn, J.M.H., 2018. Measuring hyperscale topographic anisotropy as a continuous landscape property, *Geosciences (Switzerland)*, vol. 8, no. 8.
- [11] Wilson, M.F.J., O'Connell, B., Brown, C., Guinan, J.C. & Grehan, A.J., 2007. Multiscale terrain analysis of multibeam bathymetry data for habitat mapping on the continental slope. *Marine Geodesy*, vol. 30, no. 1-2, pp. 3-35.
- [12] Wang, X., Dong, Z., Zhang, J. & Chen, G., 2002. Geomorphology of sand dunes in the Northeast Taklimakan Desert. *Geomorphology*, vol. 42, no. 3-4, pp. 183-195.
- [13] Sun, W., Gao, X., 2022. Geomorphology of sand dunes in the Taklamakan Desert based on ERA5 reanalysis data. *Journal of Arid Environments*, Volume 207. <https://doi.org/10.1016/j.jaridenv.2022.104848>
- [14] Airbus, 2020. Copernicus DEM: Copernicus digital elevation model product handbook. Report AO/1-9422/18/I-LG. Taufkirchen, Germany: Airbus Defence and Space GmbH.

Exploring the Effects of Acoustic Frequency on Terrain Attributes and Classifications Derived from Digital Bathymetric Models at Multiple Scales

Vincent Lecours

Université du Québec à Chicoutimi
Chicoutimi, Québec, Canada
vlecour@uqac.ca

Benjamin Misiuk

Department of Oceanography
Dalhousie University
Halifax, Nova Scotia, Canada
ben.misiuk@dal.ca

Craig J. Brown

Department of Oceanography
Dalhousie University
Halifax, Nova Scotia, Canada
craig.brown@dal.ca

Abstract—In recent years, new multibeam echosounders that can simultaneously collect data at multiple frequencies have become available. However, the effects of acoustic frequency on bathymetric data have yet to be characterized, as early research on these new systems has instead focused on backscatter data. Here we explore such effects by deriving terrain attributes and classifications from bathymetric data from Head Harbour, Nova Scotia, Canada, that were collected at five different operating frequencies. The geomorphometric analyses were conducted on bathymetric surfaces generated from data collected at each operating frequency using four scales of analysis. Results show that bathymetry, its derived terrain attributes, and terrain classifications produced with them are all dependent on the acoustic frequency used to collect bathymetric data. While the observed effects on the regional bathymetry were relatively minor, local bathymetry, terrain attributes and terrain classifications were highly impacted by the frequency used when collecting data. The impacts were less important when the terrain attributes and classifications were generated using broader scales of analysis. These results raise questions about how bathymetry is measured and defined and how we should interpret the outcomes of marine geomorphometric analyses. This is particularly relevant as such analyses have become a key component of marine habitat mapping and submarine geomorphology mapping.

I. INTRODUCTION

Multibeam echosounders (MBES) remain the most effective instruments for collecting continuous, high-resolution bathymetric data in waters where light cannot penetrate. They are active remote sensors that function by transmitting acoustic waves at a given frequency and measuring the return time of the signal after reflecting off the seafloor – much like LiDAR systems do with light. This produces a point cloud that can be used to generate a digital surface model (DSM) of the seafloor, commonly referred to as a bathymetric surface. The intensity of the return is also measured to produce backscatter data that can be used as a proxy for surficial geology. MBES typically produce sound at a single frequency, which is often less than 70 kHz for deep-water systems (deeper than 200 m) and up to 500 kHz for shallow-water systems (less than 200 m). The frequency at which a sonar operates is at the discretion of its manufacturer,

and no standards exist to guide that choice. Bathymetric data collected by different systems at different frequencies are almost always considered comparable as it is assumed that all systems capture the top of the seafloor accurately regardless of frequency.

In the past few years, however, a new generation of MBES systems that can collect data using multiple frequencies simultaneously has become available [1]. Research on new opportunities provided by this technology is still in its infancy, but to date, has focused mostly on backscatter data; backscatter was shown to vary significantly with frequency as a function of the interactions between acoustic wavelength and the substrate [2,3]. This may have potential implications for how bathymetry is interpreted, but they have yet to be explored. These implications can be far-reaching as bathymetry is the primary input for marine geomorphometric analyses that have become common in disciplines like marine habitat mapping, hydrodynamic modelling, and submarine geomorphology [4].

The goal of this work was to evaluate the effects of acoustic frequency on bathymetric data and terrain attributes, and on classifications that can be derived from them at multiple scales of analysis.

II. METHODS

Acoustic data were collected from Head Harbour, Nova Scotia, Canada, in October 2021, using an R2Sonic 2026 MBES. The sonar was mounted on the M/V *Eastcom* and operated at 90, 180, 270, 360, and 450 kHz frequencies simultaneously. Positioning and motion compensations were recorded with an Applanix WaveMaster GPS and IMU, respectively. Raw soundings from each frequency were processed separately in QPS Qimera, including data cleaning, and sound velocity, motion, and tidal corrections, to produce five bathymetric surfaces at 1 m horizontal resolution (Fig. 1). The cleaned acoustic data for each frequency were also imported to QPS FMGT for backscatter processing, and five surfaces were produced, also at 1 m horizontal resolution.

Areas with higher backscatter values usually had smaller differences.

TABLE I. STATISTICAL DISTRIBUTION OF ABSOLUTE DIFFERENCES IN DEPTH BETWEEN PAIRS OF DSMs FROM DIFFERENT FREQUENCIES

DSMs Compared	Absolute Differences (cm)					
	0	0-1	1-2	2-5	5-10	> 10
90-180 kHz	0.05%	1.99%	1.89%	5.49%	14.88%	75.71%
90-270 kHz	0.03%	1.18%	1.28%	4.26%	5.24%	88.01%
90-360 kHz	0.02%	0.71%	0.88%	3.87%	4.77%	89.75%
90-450 kHz	0.02%	0.71%	0.86%	3.57%	4.70%	90.14%
180-270 kHz	0.16%	6.87%	9.20%	50.68%	32.01%	1.08%
180-360 kHz	0.06%	2.48%	3.28%	19.60%	64.21%	10.38%
180-450 kHz	0.05%	2.10%	2.59%	12.57%	60.32%	22.38%
270-360 kHz	0.36%	15.33%	20.96%	54.98%	8.19%	0.17%
270-450 kHz	0.19%	8.11%	11.03%	54.73%	24.89%	1.05%
360-450 kHz	0.94%	36.46%	30.47%	29.82%	2.19%	0.12%

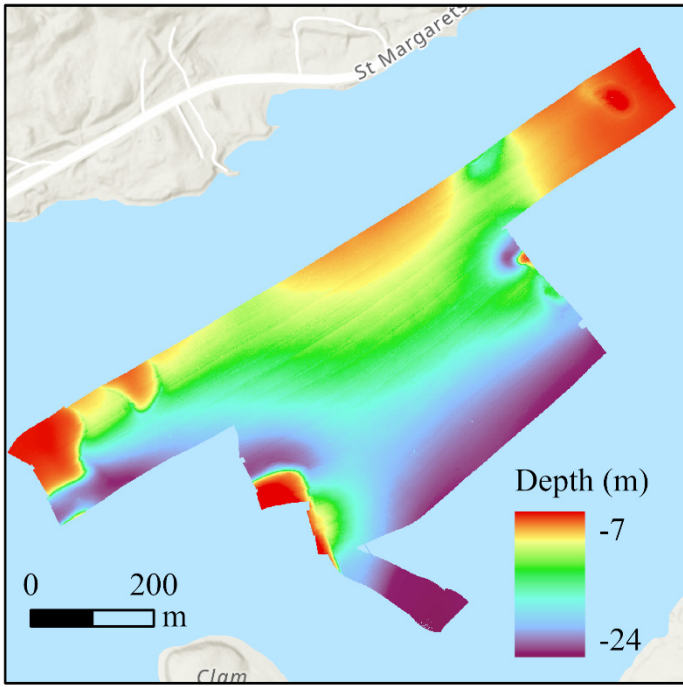


Figure 1. Multibeam bathymetric data in Head Harbour, Nova Scotia, Canada, collected at a 450 kHz frequency.

The five bathymetric datasets were used to generate 15 terrain attributes: slope, easterness and northerness, maximum, minimum and mean curvatures, planform and profile curvatures, twisting curvature [5], a topographic position index [6], the relative difference from mean value [7], a vector ruggedness measure [8], a surface area to planar area ratio [9], an adjusted standard deviation metric [10], and the roughness index-elevation [11]. In addition, the datasets were used to classify the study area into seven morphometric features [12]: channels, passes, peaks, pits, planar flat areas, planar slope areas, and ridges. All terrain attributes and classifications were performed using 3x3, 9x9, 27x27, and 81x81 windows of analysis, resulting in 325 surfaces to compare. All calculations were performed using the “MultiscaleDTM” package [10] in R v. 4.2.2. The surfaces produced were first compared in terms of their descriptive statistics (minimum, maximum, mean, standard deviation, range, excess kurtosis, and skewness). Correlation matrices (Pearson’s coefficients) and difference maps were also built to explore variations in spatial distribution, and frequency distributions were compared for the terrain classifications.

III. RESULTS

A. Bathymetric data

The descriptive statistics of the five bathymetric datasets were very similar, yet all difference maps between pairs of datasets show that less than 1% of pixels had identical depth values (Table I). As expected, the closer the frequencies of two datasets, the smaller their differences. In general, DSMs were shallower, less variable, and had a narrower range of depths with increasing operating frequency. Correlations between all DSMs were very high, the lowest being 0.989 between the 90 kHz and the 360 kHz DSMs. The absolute maximum difference in depths between two DSMs ranged from 42 cm (between the 270 and 450 kHz DSMs) to 1 m (between the 90 and 360 kHz DSMs). The absolute average differences between pairs of DSMs ranged from 2 to 21 cm. The absolute differences in depths, summarized in Table I, were highly spatially correlated with backscatter.

B. Terrain Attributes

Terrain attributes demonstrated much greater differences among frequencies than bathymetry. For example, the average of the pairwise coefficients of correlation for twisting curvature generated using a 3x3 window of analysis was 0.151 (Table II). Slope was the least affected variable with an average correlation of 0.894 among all frequencies (3x3 window). Others at this window size ranged from 0.204 (relative deviation from mean value) to 0.655 (vector ruggedness measure). Descriptive statistics confirm the high variability of terrain attributes at different frequencies. Roughness metrics were generally higher on average at lower frequencies. This was also true for slope but only when it was computed with a 3x3 or a 9x9 window of analysis; at broader scales, the average of slope was higher at higher frequencies (270 kHz with a 27x27 window, and 360 kHz with a 81x81 window).

In general, using a broader window of analysis to generate the terrain attributes increased the correlations among the different frequencies and thus reduced the differences (Table II), yet there was no consistent linear relationship observed between frequency and correlation strength. For example, many measures of curvatures had lower average correlations at a window of 27x27 than at windows of 9x9 and 81x81.

TABLE II. RANGE OF AVERAGE PAIRWISE CORRELATIONS AMONG THE SAME TERRAIN ATTRIBUTE GENERATED FROM BATHYMETRIC DATASETS OF DIFFERENT FREQUENCY, ACROSS SCALES OF ANALYSIS

Scale	Lowest \bar{x} Correlation	Attribute	Highest \bar{x} Correlation	Attribute
3x3	0.151	Twisting Curvature	0.894	Slope
9x9	0.333	Relative Deviation from Mean Value	0.984	
27x27	0.553	Adjusted Standard Deviation	0.944	Adjusted Standard Deviation
81x81	0.410	Roughness Index-Elevation	0.953	Northerness

C. Terrain Classification

As with the terrain attributes, the terrain classifications were considerably affected by the frequency of the input data. At the 3x3 scale of analysis, the morphological maps produced with

360 and 450 kHz data were the most similar, yet 53% of the study area was classified differently in the two maps. This increased to 71% between the maps produced with 90 kHz and 360 kHz. These differences among frequencies decreased when broader scales of analysis were used, ranging from 42 to 57% at 9x9, from 22 to 78% at 27x27, and between 1 and 6% at 81x81.

The differences are also reflected in the relative coverage of the different morphological features. For example, the finer-scale analysis of the 90 kHz data indicated that 30% of the study area was channels, 29% ridges, and 25% passes. When the analysis was repeated using the 450 kHz bathymetric data as input, these numbers changed respectively to 16%, 16%, and 42%. These three feature types were the most variable with changing frequency, followed by pits and peaks. The relative coverage confirms the previous observation that the variability is smaller when the analysis is performed at broader spatial scales.

IV. DISCUSSION

While the differences among bathymetric surfaces were widespread and could reach up to 1 m in places (Table 1), the high correlations among DSMs indicate that the spatial distribution of depth values remains relatively similar. This suggests that the effects of frequency on bathymetric data are primarily local, with low impact on the regional representation of the seafloor. The fact that higher frequencies produced generally shallower depths aligns with the theory behind signal penetration.

Terrain attributes were highly frequency-dependent, yet little consistency was observed in the relationships between frequencies and the statistical and spatial distributions of terrain attribute values. The results for both bathymetry and the terrain attributes raise questions about what is measured by the acoustic signal, and about how fine-scale interactions between the acoustic signal and the composition of the seafloor affect the response. This has implications for how these datasets can be used in subsequent analyses in various contexts. While additional field experiments are necessary to answer these questions, the seafloor is largely inaccessible to broad-scale and detailed ground-truthing. Additionally, it is virtually impossible to fully replicate complex field conditions in experimental tanks due to spatiotemporal variability in oceanographic conditions that may affect the interactions between the mechanical acoustic waves and the components of the transmission medium and the target. A bathymetric lidar dataset could be used as a comparison, but water conditions in this study area (*i.e.*, turbidity) are not suitable for bathymetric lidar data collection. In addition, it may be difficult to align what is measured by sound at given frequencies with what is measured by light at a given frequency.

While this work does not address the theoretical questions surrounding marine acoustic-sediment interactions, it demonstrates important effects of acoustic frequency on recorded depth values. This has implications for multi-source datasets of multiple frequencies. Artefacts are likely where datasets of differing frequency overlap, which can then influence subsequent analyses like terrain classification. We also found that the effects on terrain attributes were amplified compared to the bathymetry. Terrain attributes may vary considerably based on the frequency at which the bathymetric data were collected, however these impacts are unpredictable as no consistent patterns could be established. A similar conclusion was reached in previous work when looking at how various artefacts in digital bathymetric models impact terrain attributes [13], raising questions about whether artefacts in the data are influencing the

geomorphometric analyses. The observed frequency dependence highlights the importance of critically evaluating the fitness for use of datasets. However, despite increased awareness in the community of how sensitive bathymetry can be to survey parameters and conditions, most marine research does not have the benefit of bathymetric data at multiple frequencies, which enables comparison, validation, and multiple redundancies (and therefore, reduces data uncertainty). It also remains unclear whether generalizations can be made, as results may be dependent on the characteristics of the local seafloor.

The variability of terrain classification with acoustic frequency was higher than initially expected, but this result aligns with the observation that frequency impacts local variability more than regional variability. When the morphological features were delineated using terrain attributes that were computed over analysis distances of 3 and 9 m, they were thus more affected by the local variability of the bathymetry. The effect decreased when characterizing morphological features at greater analysis distances (*i.e.*, 27 and 81 m). This highlights the need to match the scale of analysis with the scale of local morphological features and indicates that the quantification of finer-scale morphological patterns may be highly variable and inconsistent, especially if the geomorphometric analyses capture artefacts in the bathymetric data caused by the operating frequencies, the angular dependence of seafloor detection, or platform motion.

Future work should continue looking for patterns between acoustic frequency, bathymetry, and terrain attributes – for example by quantifying variations in spatial autocorrelation. Testing multiscale terrain attributes to identify whether they can help differentiate artefacts from real fine-scale variability, and therefore capture the relevant characteristics at broader scales regardless of frequency would also be interesting. In terms of terrain classification, we should explore how combining terrain attributes with backscatter data, which are also known to vary significantly with acoustic frequency, may impact seafloor classification. Given the low correlations observed between some of the terrain attributes that were calculated at different frequencies, it may be fair to assume that they provide different information on the first few centimetres of seafloor, and they could be considered as independent variables. This may enable testing whether combinations of terrain attributes from different frequencies allows for a better discrimination of seafloor features and characteristics than single-frequency data.

V. CONCLUSION

The ability to collect multibeam bathymetric data simultaneously at different acoustic frequencies is new, and much remains to be understood about these data's characteristics and uses. Here we compared five bathymetric datasets collected between 90 and 450 kHz, and derived 15 terrain attributes and a classification of morphological features from each. This analysis was repeated at four different spatial scales of analysis. Results show that acoustic frequency alters measured bathymetry, and that the effect is amplified for all derivatives of bathymetry. Few consistent patterns between frequency, terrain attributes, and spatial scale could be established. This work is a first step in trying to understand the utility, differences, and potential pitfalls of quantitatively characterizing the morphology of the seafloor at different acoustic frequencies.

VI. ACKNOWLEDGMENTS

This research is part of the Ocean Frontier Institute/Canada First Research Excellence Fund - Benthic Ecosystem Mapping

and Engagement (BEcoME) Project. Data collection was completed in partnership with R2Sonic LLC, USA, and Quality Positioning Services (QPS) Canada. Funding through institutional support programs was also provided by the Université du Québec à Chicoutimi.

REFERENCES

- [1] Brown, C.J., J. Beaudoin, M. Brissette, and V. Gazzola, 2017. "Setting the stage for multispectral acoustic backscatter research". Proceedings of the United States Hydrographic Conference, Galveston, USA, 20 March 2017.
- [2] Brown, C.J., J. Beaudoin, M. Brissette, and V. Gazzola, 2019. "Multispectral multibeam echo sounder backscatter as a tool for improved seafloor characterization". *Geosciences*, 9(3), 126, 1-19. <https://doi.org/10.3390/geosciences9030126>
- [3] Gaida, T.C., T.A.T. Ali, M. Snellen, A. Amiri-Simkooei, T.A.G.P. van Dijk, and D.G. Simons, 2018. "A multispectral Bayesian classification method for increased acoustic discrimination of seabed sediments using multi-frequency multibeam backscatter data". *Geosciences*, 8, 455, 1-25. <https://doi.org/10.3390/geosciences8120455>
- [4] Lecours, V., M.F.J. Dolan, A. Micallef, and V.L. Lucieer, 2016. "A review of marine geomorphometry, the quantitative study of the seafloor". *Hydrology and Earth System Sciences*, 20, 3207-3244. <https://doi.org/10.5194/hess-20-3207-2016>
- [5] Minár, J. I.S. Evans, and M. Jenčo, 2020. "A comprehensive system of definitions of land surface (topographic) curvatures, with implications for their application in geoscience modelling and prediction". *Earth-Science Reviews*, 211, 103414, 1-24. <https://doi.org/10.1016/j.earscirev.2020.103414>
- [6] Weiss, A., 2001. "Topographic position and landforms analysis". ESRI User Conference, San Diego CA, USA.
- [7] Lecours, V., R. Devillers, A.E. Simms, V.L. Lucieer, and C.J. Brown, 2017. "Towards a framework for terrain attribute selection in environmental studies". *Environmental Modelling & Software*, 89, 19-30. <https://doi.org/10.1016/j.envsoft.2016.11.027>
- [8] Sappington, J.M., K.M. Longshore, and D.B. Thompson, 2007. "Quantifying landscape ruggedness for animal habitat analysis: a case study using bighorn sheep in the Mojave desert". *The Journal of Wildlife Management*, 71, 1419-1426. <https://doi.org/10.2193/2005-723>
- [9] Du Preez, C., 2015. "A new arc-chord ratio (ACR) rugosity index for quantifying three-dimensional landscape structural complexity". *Landscape Ecology*, 30, 181-192. <https://doi.org/10.1007/s10980-014-0118-8>
- [10] Illich, A.R., B. Misiuk, V. Lecours, and S.A. Murawski, 2023. "MultiscaleDTM: An open-source R package for multiscale geomorphometric analysis". *Transactions in GIS*, *in press*. <https://doi.org/10.1111/tgis.13067>
- [11] Cavalli, M., P. Tarolli, L. Marchi, and G.D. Fontana, 2008. "The effectiveness of airborne LiDAR data in the recognition of channel-bed morphology". *CATENA*, 73(3), 249-260. <https://doi.org/10.1016/j.catena.2007.11.001>
- [12] Wood, J., 1996. "The geomorphological characterization of digital elevation models". PhD thesis, University of Leicester.
- [13] Lecours, V., R. Devillers, V.L. Lucieer, and C.J. Brown, 2017. "Artefacts in marine digital terrain models: a multiscale analysis of their impact on the derivation of terrain attributes". *IEEE Transactions on Geoscience and Remote Sensing*, 55(9), 5391-5406. <https://doi.org/10.1109/TGRS.2017.2707303>

The time-in-daylight land-surface parameter

John B. Lindsay

Department of Geography, Environment & Geomatics

The University of Guelph, Guelph, Canada

jlindsay@uoguelph.ca

Abstract— Time-in-Daylight (TiD) estimates the portion of total daylight over a time span that a location experiences direct radiation. This paper describes a method for estimating TiD using horizon angle maps derived in a range of azimuths and information about the sun’s position during the time span. TiD is evaluated as a potential land-surface parameter (LSP) for relief mapping and solar radiation modelling applications. The use of horizon angle to map shadow areas in calculating TiD makes this LSP conceptually similar to both openness and sky-view factor (SVF). However, TiD differs most significantly in the pairing of horizon angle maps with a dynamic model of sun position. The findings showed that TiD is well suited to applications in relief visualization, particularly with digital surface models (DSMs) in urban areas. The ability to estimate TiD with specific date/time ranges also makes it better suited for solar radiation modelling applications than either openness or SVF.

I. INTRODUCTION

Shaded-relief mapping, or analytical hillshading [1], is one of the most common land-surface parameters (LSP) derived from digital elevation models (DEMs). Hillshading is often used for topographic visualization and as a predictor in environmental modelling applications involving solar radiation [2]. Despite its widespread use, there are issues with the application of hillshade maps in both of these areas. Interpretation of the terrain is highly sensitive to the light-source-viewer orientation—under some conditions, relief can appear inverted, with elevated sites appearing to be low-lying and vice versa, a phenomenon known as the pseudoscopic illusion [3]. Furthermore, the degree to which topographic features are apparent in hillshade maps is very dependent upon their orientation relative to the light source. Some researchers have also argued that the use of a single light-source direction with the traditional hillshade method results in near-complete loss of detail both within the darkened areas sloping away from the light source and in over-exposed areas directly facing the light, although this deficit can be addressed by applying a weighted average of multiple light-source directions in a multi-directional hillshade [4]. Lastly, because hillshading is based solely on the local topographic properties of slope gradient and orientation, it cannot account for shadowing from distant terrain [5].

These issues have led some researchers to develop alternative LSPs that overcome the limitations of hillshading, including the openness index [6] and the sky-view factor (SVF) [2,5]. Both of these alternatives have found broad application, particularly in archeological surveying [7]. This paper describes a new LSP, called Time-in-Daylight (TiD), that can be used as

an alternative to hillshade maps in relief visualization and solar modelling applications.

II. TIME-IN-DAYLIGHT (TiD)

A. Definition

TiD is defined as the portion of the total daylight period over a span of time that a location experiences direct radiation. TiD ranges from 0 (full shadow) to 1 (full sun). Thus, it is effectively the result of the integration through time of a dynamic Boolean shadow/sunlight model. Fig. 1 shows an example of a TiD map derived from a 10-m lidar DEM of an area south of Brantford, Canada. TiD has been calculated in this example using the full day and full year. Darker areas represent sites that experience more shadowing throughout the year.

B. Estimation and implementation of TiD

Whether or not a site is contained within a shadow area at a particular time is determined by the sun’s position (altitude and azimuth, θ and ϕ respectively) and the horizon angle (μ) in the direction of ϕ [5]. μ is the maximum vertical angle between the horizontal plane and the topography (i.e., the horizon) in a direction. When θ is lower than the local horizon angle, the site is within a shadow cast by a distant object. Thus, thresholding a μ -map for a particular sun position will produce a shadow model for an instant in time. TiD can be estimated by deriving a series of μ -maps from a DEM corresponding to the sun positions for a specified time span and then, for each grid cell, determining the portion of maps (or duration) the cell is in sunlight. We only consider times when the sun is above the nominal horizon, i.e., $\theta > 0$, which ensures that TiD ranges from 0 to 1.

Because it is impractical to sample time continuously, there are two approaches to estimating TiD. A TiD implementation may either discretize time, sampling at regular intervals and estimating the μ -maps at each individual time stamp, or ϕ may be discretized, i.e., sampling at a constant azimuth interval and then calculating the times at which the sun is located at each ϕ value for each day in the time span (if the span includes multiple days, there will be multiple times). The first approach has the advantage that, because each sampled time is of equal duration, one merely needs to count the portion of μ maps in sunlight to estimate TiD. However, each sampled time is likely to have a unique ϕ , and because μ must be calculated to correspond to ϕ , potentially a very large number of μ -maps will need to be estimated (one for each sampled time over the span).

The second approach offers the main advantage that there are significantly fewer μ -maps that must be calculated (360 divided by the ϕ -interval minus the ϕ -intervals for which the sun is never above the horizon during the time span). However, because the rate of change in ϕ is not constant during the day, each sampled ϕ -interval represents a varying duration, and a time-weighted sum must be used to estimate TiD. Ultimately, of the two main computational tasks involved in measuring TiD, i.e., tracking the change in solar position during the time span and calculating μ -maps, the latter is by far the more computationally intensive. Thus, the second approach is recommended, and it is this method that is used in the TiD tool implemented in the WhiteboxTools open-source GIS software [8].

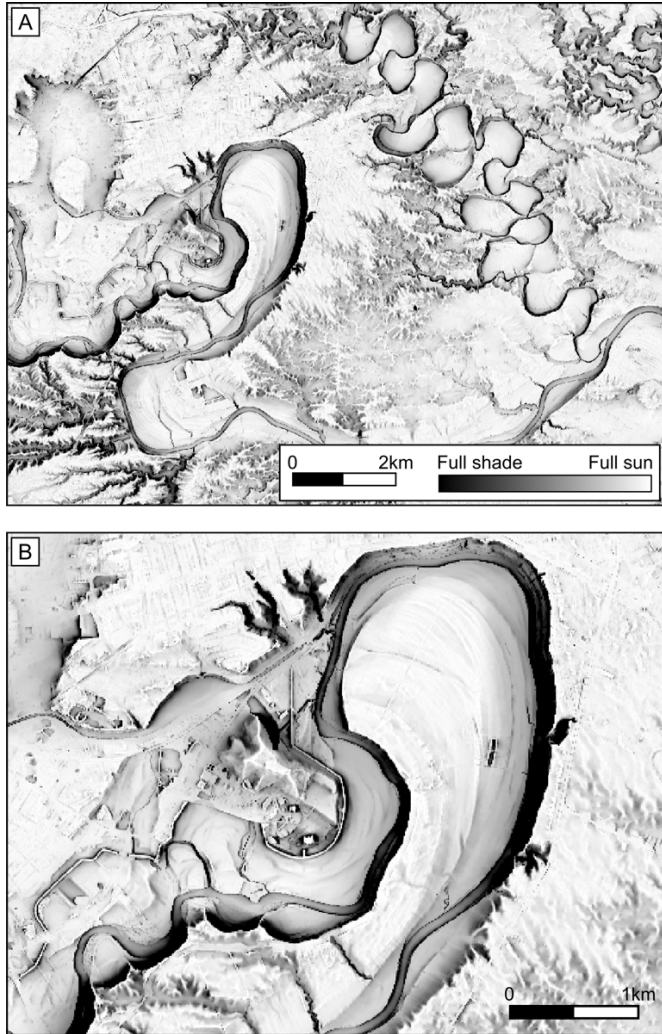


Figure 1. TiD for a site south of Brantford, Canada. TiD should be displayed using a greyscale with lighter colors associated with brighter areas.

In applying the WhiteboxTools TiD tool, the user must specify the ϕ -interval, the maximum search distance used for calculating μ , the location (latitude and longitude) of the mid-point of the input DEM (used to calculate sun positions), and the time span. The search distance and ϕ -interval parameters both impact processing times, although performance is more sensitive to the later parameter (Table I). The span is provided as starting/ending days of the year and starting/ending times of day. Therefore, TiD can be estimated for a range of days, e.g., a season or the whole year, or for specific times of day, e.g., mornings or afternoons. For instance, Fig. 2 shows TiD maps for different time spans derived from the same 0.5-m lidar digital surface model (DSM) of a suburban neighborhood in

Guelph, Canada. The WhiteboxTools TiD tool is currently limited to application with projected DEMs and does not account for Earth's curvature. It is therefore best applied to surface models with less than regional-scale spatial extents.

TABLE I. PROCESSING TIME ON M1-MAX PROCESSOR TO CALCULATE TiD WITH VARYING PARAMETER VALUES FOR A 47.5 MILLION GRID CELL DEM.

Parameter Values	Time (mm:ss)
100-m search distance, 15° ϕ -interval	03:46
50-m search distance, 15° ϕ -interval	03:13
10-m search distance, 15° ϕ -interval	02:32
50-m search distance, 5° ϕ -interval	09:20
50-m search distance, 10° ϕ -interval	04:46
50-m search distance, 30° ϕ -interval	01:42
50-m search distance, 45° ϕ -interval	01:16

The tool has been implemented using the Rust programming language and uses parallelized code for calculating χ_0 -maps to improve computational performance. The use of a maximum search distance parameter (also used in the calculation of openness and sky-view factor) improves the performance of the tool. The χ_0 algorithm also only estimates the slope between the source grid cell and cells along the search line when a new maximum elevation is detected, since comparing elevations is faster. Lastly, the search for χ_0 for a grid cell can be cut short before the maximum distance is reached if a χ_0 -value greater than a threshold (set to 80-degrees) is encountered. Such high slopes can only typically occur when the obstruction cell (horizon) is located near the query cell and a substantial increase in elevation would be necessary for a more distant grid cell to form the actual horizon. This short-circuiting can improve algorithm performance, particularly when applied to DSMs in urban areas containing numerous buildings and vegetation.

C. Comparison with hillshade, openness, and SVF

The WhiteboxTools TiD algorithm was found to be faster than the Saga GIS SVF tool when applied with similar parameter values, although both LSPs took considerably longer to process a 47.5 million grid cell test DSM of the Guelph area than either hillshade or positive openness (Table II).

TABLE III. PROCESSING TIME ON M1-MAX PROCESSOR TO CALCULATE VARIOUS LSPS FOR A 47.5 MILLION GRID CELL TEST DEM.

LSP	Parameters	Time (mm:ss)
Hillshade	$\theta = 30^\circ, \phi = 270^\circ$	00:01
Openness	100-m search distance	00:12
SVF	100-m search distance, 10° ϕ -interval	10:33
TiD	100-m search distance, 10° ϕ -interval	05:58

Fig. 3 compares hillshade, positive openness, SVF, and TiD for an area of the University of Guelph campus. It is evident that as a relief visualization technique, hillshade is less satisfactory than the other LSPs for this dataset; it appears flat by comparison and its basis on local 3x3 neighborhoods makes it unable to capture the relative height differences among the

many off-terrain objects in the DSM. Positive openness, SVF and TiD appear similar, although TiD is most like openness (Figs. 3D and 3B). TiD does appears smoother than openness, but this is solely due to the finer ϕ -interval used in its calculation, which is also the primary reason why openness is faster to estimate (Table II). Unlike openness and SVF, TiD appears less omni-direction in illumination, which is apparent where one side of buildings is more brightly lit than the reverse side. The SVF raster has a strong dependency on local slope, which is something that has been previously observed about the LSP [7].

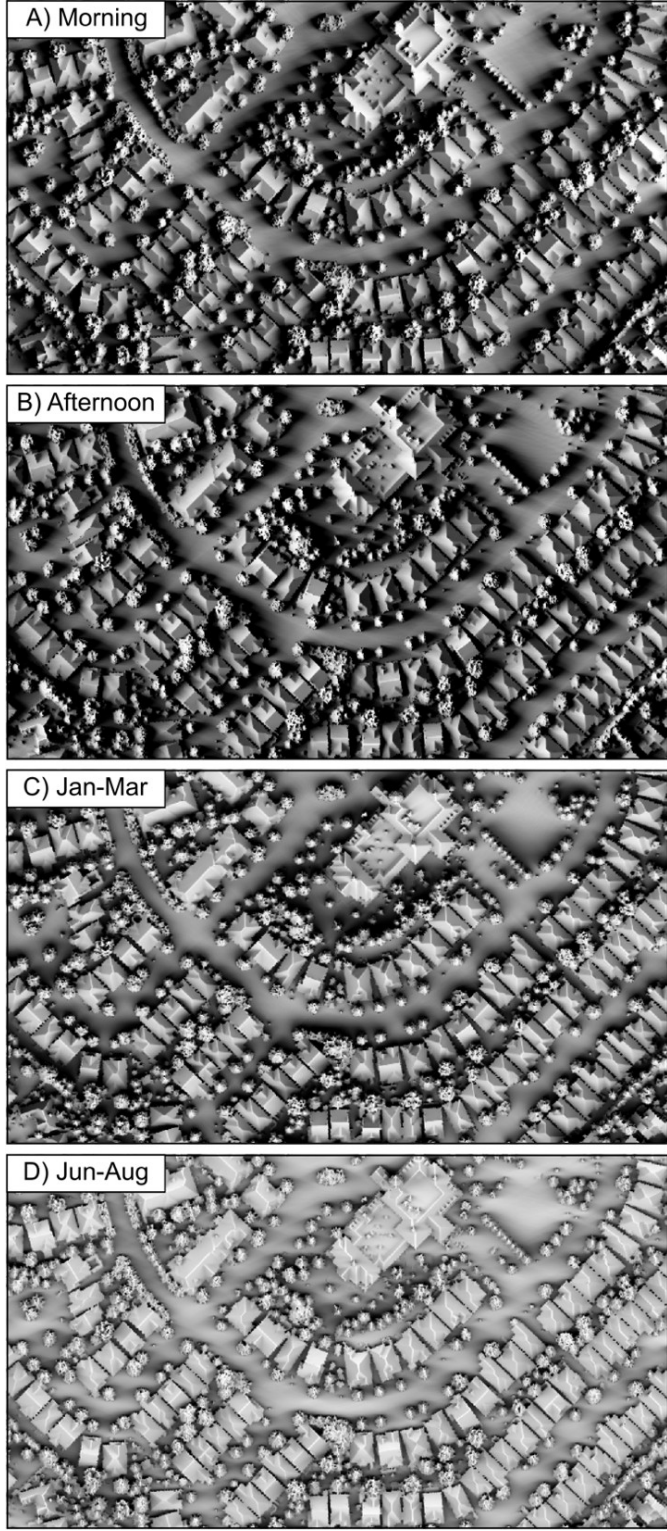


Figure 2. TiD calculated for A) sunrise to 09:30 (full year), B) 15:30 to sunset (full year), C) January to March (full day), and D) June to August (full day). In each image, lighter colors indicate fuller sunlight.



Figure 3. Hillshade (A), positive openness (B), SVF (C), and full-year TiD (D) for an area of the University of Guelph campus. In each image, lighter colors indicate higher LSP values.

III. DISCUSSION AND CONCLUSIONS

For relief visualization mapping, positive openness, SVF, and TiD are each better suited than traditional hillshading for application to DSMs in complex urban settings. The extended

neighborhoods used to calculate distant horizons can encode information about the relative heights of buildings and vegetation, which means that they generally appear less flat than hillshade maps (Fig. 3). Full-year TiD has a directional lighting that is dictated by the local solar almanac and, therefore, has less omni-directional illumination than either openness or SVF. Whether or not this property provides advantages for relief mapping visualization is debatable and in practice all three LSPs (openness, SVF, and TiD) provide similar looking relief maps.

TiD has advantages over similar LSPs, however, for modelling the spatial pattern of solar energy potential. TiD is a measure of the direct solar radiation potential while openness and SVF are more related to diffuse radiation. The ability to restrict TiD calculation to specific day ranges (Fig. 2) could be useful for crop growth modelling, where TiD could be calculated over the growing season for specific crops in a region. Similarly, the ability to restrict TiD to certain times of day (Fig. 2A) could be useful for power utility companies engaged in residential rooftop solar-panel installation. For example, it would be possible to estimate TiD from lidar DSMs of residential neighborhoods during peak- demand times to help utilities target residences with suitably exposed properties for rooftop solar panel installation.

IV. ACKNOWLEDGMENT

Funding has been provided by the Natural Sciences and Engineering Research Council of Canada (NSERC).

REFERENCES

- [1] Horn, B. 1981. Hill shading and the reflectance map. Proc. IEEE, 69, 14-47.
- [2] Zakšek, K., Oštir, K. and Kokalj, Ž., 2011. Sky-view factor as a relief visualization technique. Remote Sensing, 3(2), pp. 398-415.
- [3] Conklin, H.C. and Pinther, M., 1976. Pseudoscopic illusion. Science, 194(4263), pp. 374-374.
- [4] Mark, R.K., 1992. Multidirectional, oblique-weighted, shaded-relief image of the Island of Hawaii (No. 92-422). US Geological Survey.
- [5] Böhner, J. and Antonić, O., 2009. Land-surface parameters specific to topo-climatology. Developments in soil science, 33, pp. 195-226.
- [6] Yokoyama, R., Shirasawa, M. and Pike, R.J., 2002. Visualizing topography by openness: A new application of image processing to digital elevation models. Photogrammetric engineering and remote sensing, 68(3), pp. 257- 266.
- [7] Doneus, M. 2013. "Openness as visualization technique for interpretative mapping of airborne lidar derived digital terrain models." Remote Sensing 5:12, pp. 6427-6442.
- [8] Lindsay, J.B. 2022. WhiteboxTools User Manual v.2.2. Available online: https://www.whiteboxgeo.com/manual/wbt_book/preface.html

Geomorphometric analysis of the *Summit* and *Ridge* classes of the Geographic Names Information System

Gaurav Sinha
Department of Geography
Ohio University
Athens, OH, USA
snhag@ohio.edu

Samantha T. Arundel
U.S. Geological Survey
Center of Excellence for
Geospatial Information
Science, Rolla, MO, USA
sarundel@usgs.gov

Romim Somadder
Department of Geography
Ohio University
Athens, OH, USA
rs829222@ohio.edu

David P. Martin
Charlotte, NC
david.martin.3234@gmail.com
m

Kevin G. McKeehan
U.S. Geological Survey
Center of Excellence for
Geospatial Information
Science
Rolla, MO, USA
kmckeehan@usgs.gov

Abstract—This paper reports results from a geosemantic comparison of landforms classified in the *Summit* and *Ridge* feature classes in the Geographic Names Information System (GNIS). The comparison is based on a 2D shape analysis of manually delineated polygons produced by USGS staff to correspond to 33,304 *Summit* and 8,006 *Ridge* features. Five shape measures were chosen for this specific geomorphometry-based analysis. Univariate and bivariate statistics are first calculated to compare the two feature classes. This is followed by unsupervised learning with k-means cluster analysis to identify two major geomorphometric clusters corresponding to *Summit* and *Ridge* features. Although this supports sufficient internal homogeneity to have stable *Summit* and *Ridge* feature classes, more than 7,500 (18%) special features were also identified, which were assigned by k-means to the cluster not corresponding to their given GNIS class. These features remain to be analyzed further to decide if GNIS features should be reclassified based on geomorphometric analysis of available polygonal representations.

I. INTRODUCTION

Landforms are dependent features of terrestrial planetary surfaces and are incredibly challenging to delineate because of their indeterminate and vague extents. Delineation of landform objects is intrinsically linked to how they are conceptualized and categorized (especially into linguistic categories) [3,4]. In geosciences, general geomorphometric methods for land surface segmentation are preferred. However, the specific geomorphometry approach is preferable for cartographic representation and natural language applications because it can support the naïve (commonsense) geography-based description and characterization of terrain in terms of cognitively and culturally salient landform objects.

Research in specific geomorphometry on automated mapping and geospatial and geomorphological characterization of popularly recognized landforms shown on topographic maps is quite limited. Macroscale landforms are important to people and recognized as individual entities, even if their spatial extents are not explicit. In the United States, all such named landforms are found recorded in the Geographic Names Information System (GNIS), the official topographic gazetteer database developed by the U.S. Geological Survey (USGS) in cooperation with the U.S. Board on Geographic Names (BGN) [9]. However, more than 2.28 million GNIS features are

classified into 63 non-hierarchical, mutually exclusive, broadly scoped feature classes, which were created based on generic terms of the feature names, such as Mount or Canyon, and not as a definitive or scientific classification system [5].

There are two major limitations of most topographic gazetteers, including GNIS. First, they are limited to point feature representation of all features—including landforms. Thus, the two lead authors have established a long-term research collaboration for automating the extraction of cognitively plausible and scale-sensitive areal representations of landforms [1-2,6-7]. Adapting such methods for national-scale automated mapping of GNIS landform features is one of the top objectives of this collaboration.

The second problem of gazetteers is due to basing the classes on name generics, lack of a formal specification of class semantics, and issues of semantic overlap between classes. In the case of landforms within GNIS, there has never been a formal investigation into whether the chosen landform categories make semantic sense or whether features are classified correctly. A visual scan of topographic map labels for specific landforms and nearby contour patterns reveals cases where the GNIS classification fails to correspond to the type of landform people would identify in that area. A formal, large-area study is only possible if mapped boundaries for landform features are available. However, no existing general or even specific geomorphometric methods yield a cognitively plausible agreement between named landforms as would be visually perceived by people and algorithmically extracted objects.

Fortunately, the authors now have access to a database of manually delineated 2D polygons corresponding to 89,100 GNIS landform features across the US. These polygons were digitized by USGS staff members of the US Topo program [8] for a different project related to the automated placement of feature labels on topographic maps. A small subset of the manually delineated polygons has already been successfully used to identify limitations and suggest improvements for the core-eminence method of mapping salient topographic eminences (a subset of convex landforms) [6].

The discussion here is limited to the semantic comparison of the *Summit* and *Ridge* feature classes based on the 2D shape

analysis of manually delineated polygons corresponding to GNIS landform features from the classes. *Summit* and *Ridge* features correspond, respectively, to non-linear and linear topographic eminences, which are cognitively salient convex landforms [7].

II. METHODOLOGY

GNIS point feature data are freely available as a text file from the USGS [9]. Manually digitized GNIS landform polygons were obtained internally by the second author by virtue of her status as a USGS employee. This dataset is not available publicly. Of the 89,100 landform polygons, 33,304 correspond to *Summit* and 8,006 to *Ridge* GNIS landform features. The 2D shape analysis of these *Summit* and *Ridge* landform polygons relied on five popular 2D shape measures summarized in Table 1. For the *elongation* measure, the width and length of the oriented bounding box for each GNIS feature were generated with the help of the *Minimum Bounding Geometry* tool available in ArcGIS Pro GIS software. All other shape measures were calculated with the help of the Python *shapely* package, widely used for the manipulation and analysis of planar geometric objects.

Univariate statistics, box plots, and frequency distribution histograms were generated for each shape measure to summarize shape measure statistics. Next, a bivariate scatterplot and correlation matrix was generated for all pairs of shape measures to thoroughly analyze the shape differences between features within and across the *Summit* and *Ridge* classes.

TABLE I. 2D OBJECT SHAPE MEASURES

2D Shape Measure	Shape Description	
	Formula	Definition
Compactness (Com)	$(4\pi \cdot \text{area}) / (\text{perimeter})^2$	Ratio of the area of an object to the area of a circle with the same perimeter. <i>Max value of 1 is achieved for circular objects.</i>
Roundness (Rou)	$(4\pi \cdot \text{area}) / (\text{convex perimeter})^2$	Ratio of the area of an object to the area of a circle with the same perimeter as the object's convex hull. <i>Max value of 1 is achieved for circular objects.</i>
Elongation (Elo)	$(\text{width} / \text{length})_{\text{bb}}$	The width-to-length ratio of the object's bounding box is oriented parallel to the object's major axis.
Convexity (Con)	$(\text{convex perimeter}) / (\text{object perimeter})$	Ratio of the perimeter of an object's convex hull to the perimeter of the object itself. <i>A value of 1 signifies a perfectly convex object, and a value less than one signifies an object having an irregular boundary or containing holes.</i>
Solidity (Sol)	$(\text{object area}) / (\text{convex area})$	Ratio of the perimeter of an object's convex hull to the perimeter of the object itself. <i>A value of 1 signifies a solid object, and a value less than one signifies an object having an irregular boundary or containing holes.</i>

Finally, all 41,310 features were input into the unsupervised machine learning method of K-means cluster analysis to test if 2D shape measures segregated the features into only two or more statistically significant clusters. Testing was done by deriving up to 10 clusters to check for the existence of additional transitional classes in addition to the expected two primary clusters corresponding to *Summit* and *Ridge* classes. Features (mis)classified by the K-means method such that *Summit* (*Ridge*) features assigned to the cluster corresponding to the other *Ridge*

(*Summit*) feature class were identified and analyzed for more insights.

All data analysis and K-means cluster analysis were automated with a Python script using typically used Python data analysis and visualization libraries.

III. RESULTS

A. Geomorphometric analysis based on exploratory statistics

As evident from summary statistics (Table 1) and the frequency distributions (Figure 1), the shape measures help capture differences between the shapes of polygons digitized for the GNIS *Summit* and *Ridge* feature classes. Note that because *compactness* and *roundness* are strongly positively correlated (Figure 2) and have nearly identical frequency distributions, only the frequency distribution for *Roundness* is included in Figure 1. *Ridge* shape measure distributions are close to normal, but *Summit* shape measures are all left-skewed, with extremely skewed solidity and convexity. Based on the mean values of shape measures and distribution shapes, the digitized polygons would lead us to believe that. In contrast, there is substantial overlap between shape-measure frequency distributions; non-linear *Summit* features are more rounded, less elongated, and exhibit a higher degree of solidity/convexity than *Ridge* features. Box plots (not presented here for lack of space) also complemented these observations.

The correlation matrix in Figure 2 shows the direction and strength of correlation between all five shape measures. As expected, *compactness* is significantly positively correlated with *roundness*. But they still differ appreciably in the power of their correlations with other variables. Both *compactness* and *roundness* are positively correlated with all other measures as well, but most positively with *solidity*. In contrast, *elongation* exhibits its weakest correlations with *convexity*, followed by *solidity*, with these correlations being appreciably lower for the *Ridge* feature class compared to the *Summit* class. For only *Ridge* features, there is also an interesting lack of correlation between *roundness* and *convexity* (but not *solidity*). Scatter plots of all variable pairs (not shown here) confirmed insights already gained.

B. Geomorphometric analysis based on K-Means clusters

The K-means unsupervised method was chosen because this project aimed to identify clusters representing *Summit* and *Ridge* objects. When the five shape measures for the 41,310 features were input into the k-means algorithm, it predicted only two primary clusters. A sharp elbow (inflection point) was observed after two clusters in the inertia plot. Due to the predominance of *Summit* features in one cluster and *Ridge* features in another, the clusters can also be confidently assumed to correspond mainly to GNIS *Summit* and *Ridge* feature classes.

Table II reports the means for all shape measures for the four sets of features derived from a combination of two original GNIS feature classes and two predicted clusters. It seems clear that *Summit* or *Ridge* features assigned to the corresponding majority *Summit* or *Ridge* cluster, respectively, are characterized by substantially larger shape measure values than features assigned to the non-corresponding (*Summit* to *Ridge*, *Ridge* to *Summit*) cluster.

The K-means clustering accuracy analysis presented in Table III reveals that 98% of features in one cluster are *Summit* and 94% in another are *Ridge* features, indicating that data-driven clusters correspond strongly to GNIS *Summit* and *Ridge* feature classes. The most interesting finding from K-means analysis is the identification of 7,171 (21.5%) GNIS *Summit* and 475 (6%) GNIS *Ridge* features that were morphometrically more similar to features in the *Ridge* and *Summit* cluster, respectively.

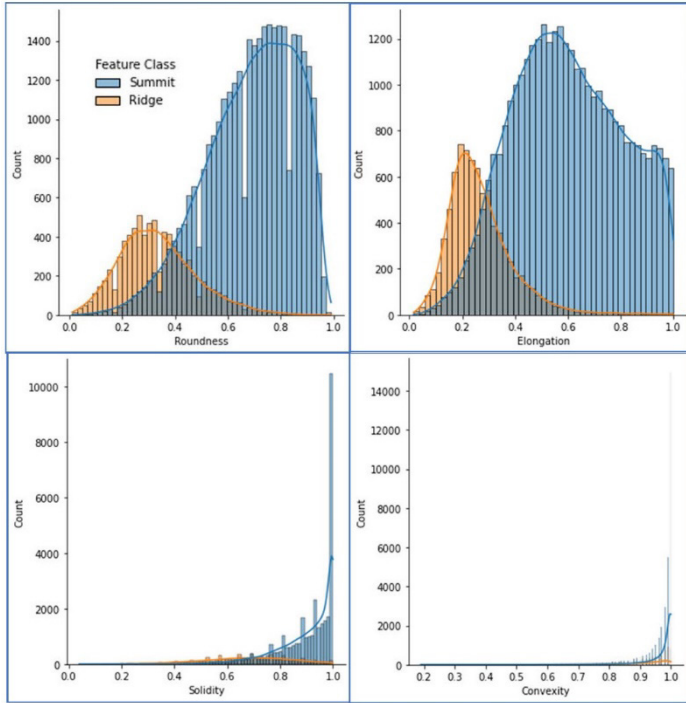


Figure 1. Frequency distributions for *roundness*, *elongation*, *solidity*, and *convexity* shape measures for *Summit* and *Ridge* classes.

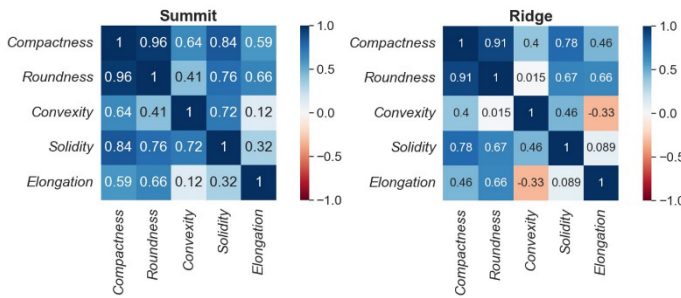


Figure 2. Correlation matrix summarizing correlations between shape measures for *Summit* and *Ridge* feature classes.

As mentioned above, the means of shape measures are already much smaller for these minority features. The reason became apparent when the manually digitized polygons for these minority *Summit* and *Ridge* features were overlaid on USGS topographic maps (available as a basemap in ArcGIS Pro). Figure 3 shows example polygons for each type of minority feature. Whereas the minority *Summit* features are long and narrow, the minority *Ridge* features are not linear but shaped more like rounded/compact *Summit* features. The manual polygons are digitized based on labels found on topographic maps. The importance of generic parts of feature names played a vital role in originally classifying GNIS features. Still, the analysis here reveals that the choice of generic terms

is not always reliable as an indicator of the geomorphometric characteristics of a feature. This will always present challenges in determining the semantic scope of GNIS feature classes. Indeed, the k-means algorithm performed admirably to isolate more than 7,500 of such specialized cases requiring more careful analysis of their shapes and possible reassignment to the other feature classes.

IV. CONCLUSION

This analysis clearly shows that the specific geomorphometry approach to GNIS enhancement can help guide the automation of feature extraction for both named and unnamed prominent landforms in the United States and other countries. Although descriptive statistics and K-means cluster analysis confirmed the usefulness of the chosen shape measures, the analysis presented herein is still limited and exploratory. Future work could reduce the correlation between shape measures and test transformations to reduce the skewness of some shape measures before statistically valid hypotheses about if and how GNIS features could be reclassified based on geomorphometric analysis of available polygonal representations, especially to use as training data in deep learning. The authors have also initiated work to understand whether (dis)similarities in shapes of features can be related to the generic terms in their names. A more comprehensive set of findings will be presented in a forthcoming journal paper, including more robust evidence based on inferential statistics.

TABLE II. MEAN STATISTICS FOR SHAPE MEASURES

GNIS	Count	Mean statistics for Shape measures				
		Com	Rou	Sol	Con	Elo
Summit	33,304	0.66	0.69	0.91	0.97	0.60
Ridge	8,006	0.28	0.34	0.67	0.91	0.27

GNIS	K-means	Summit	Ridge	Summit	Ridge	
Summit	Summit	26,133	0.73	0.75	0.95	0.99
Summit	Ridge	7,171	0.37	0.46	0.75	0.90
Ridge	Ridge	7,531	0.26	0.32	0.66	0.91
Ridge	Summit	475	0.61	0.64	0.92	0.97

TABLE III. K-MEANS CLUSTER ANALYSIS RESULTS

GNIS	Confusion Matrix		Accuracy Analysis		
	K-Means Cluster	(Summit) Cluster	(Ridge) Cluster	TP = True positive TN = True negative	FP = False positive FN = False negative
Summit	26,133	7,171	0.98	0.78	33,304
Ridge	475	7,531	0.51	0.94	8,006
Overall Accuracy: 0.81					41,310

V. ACKNOWLEDGMENTS

The authors sincerely appreciate the USGS staff at the US Topo program for sharing the manually delineated polygons. Any use of trade, firm, or product names is for descriptive purposes only and does not imply endorsement by the U. S. Government.

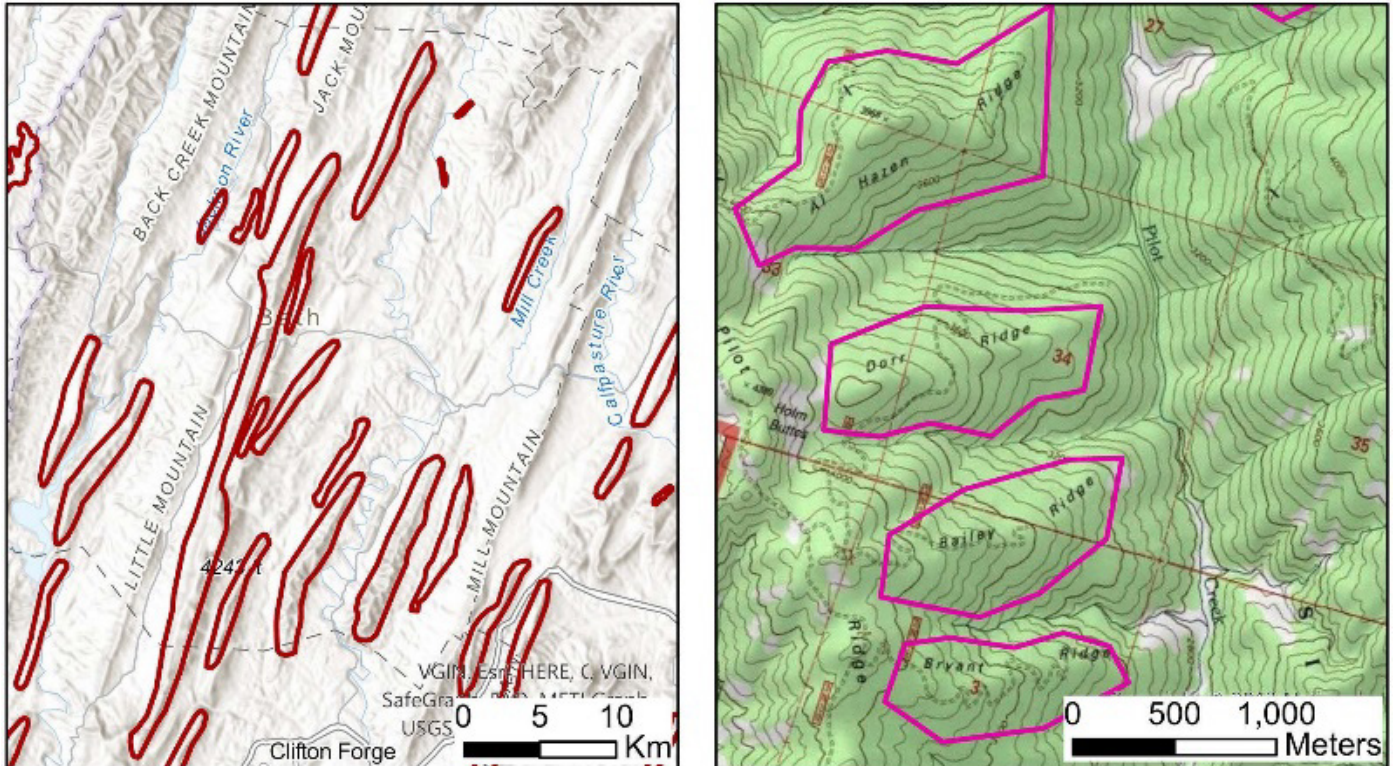


Figure 3. (Left) Examples of *Summit* features assigned by K-means to the cluster mostly dominated by *Ridge* features. (Right) Examples of *Ridge* features assigned by K-means to the cluster dominated by *Summit* features.

REFERENCES

- [1] Arundel, S. T., Sinha, G., 2019. Validating the use of object-based image analysis to map commonly recognized landform features in the United States. *Cartography and Geographic Information Science*, 46(5), 441–455.
- [2] Joly, G., Sinha, G., Hassan, W., 2022. Evaluating methods for automated mapping of apexes of non-linear eminences. *Proceedings of the AutoCarto 2022 – 24th International Research Symposium on Cartography and GIScience*.
- [3] Mark, D. M., and Smith, B., 2002. Do mountains exist? Towards an ontology of landforms. *Environment and Planning B: Planning and Design*, 30(3), 411–427.
- [4] Minár, J., and Evans, I. S., 2008. Elementary forms for land surface segmentation: the theoretical basis of terrain analysis and geomorphological mapping. *Geomorphology* 95 (3–4): 236–59.
- [5] Orth, D. J., and Payne, R. L., 1987. The National Geographic Names Data Base: Phase II Instructions. *US Geological Survey Circular* 1011.
- [6] Sinha G., and Arundel, S. T., 2021. Automated extraction of areal extents for GNIS Summit features using the Eminence-Core Method. *Proceedings of the Geomorphometry 2020 Conference*.
- [7] Sinha, G., Arundel S. T., Hahmann, T., Stewart, K., Usery, E. L., and Mark, D. M., 2018. The Landform Reference Ontology (LFRO): A foundation for exploring linguistic and geospatial conceptualization of landforms. In: *Proceedings of the 10th International Conference on Geographic Information Science (GIScience 2018)*, LIPIcs Vol. 114.
- [8] USGS 2023a. US Topo: Maps for America. <https://www.usgs.gov/programs/national-geospatial-program/us-topo-maps-america>. Last accessed April 28, 2023.
- USGS 2023b. Geographic Names Information System (GNIS). <https://www.usgs.gov/tools/geographic-names-information-system-gnis>. Last accessed April 28, 2023.

Neighborhood contextual merging of segments for landform detection and classification

Mihai Niculiță

Department of Geography, Faculty of Geography and Geology
 Alexandru Ioan Cuza University of Iași
 Iași, Romania
mihai.niculita@uaic.ro

Abstract— Contextual merging of segments using spatial relations of the neighborhood and the geomorphometric variable of the neighbor segments is introduced as a method to improve the over-segmentation of object-based analysis. The scope of the approach is to provide better candidates for the detection and delineation of landforms with simple geomorphometric signatures like sinkholes and aeolian closed depressions. The approach is simple and effective and can be implemented in many GIS software. We exemplify it for the aeolian closed depression from a part of the Romanian Plain by using elevation standard deviation to merge the segments of such closed depressions. While generally, these can be considered as concave features; actually, these have multiple shapes: a flat bottom surrounded by concave, straight, and convex parts. The results are promising, but the approach needs to be better framed in a GUI GIS environment to be implemented for specific landforms detection and delineation tasks.

I. INTRODUCTION

Contextual spatial context is inherent in image classification and pattern recognition [1,2] and becomes essential in Object-based image analysis for remote sensing [3-5]. Contextual merging of segmentation results is a well-known approach in geomorphometry [6,7], although yet with limited applicability (pixel proximity and hierarchical clustering).

The present paper aims to assess the usability of the contextual merging of segments using the neighbors and their geomorphometric variables. The approach is considered useful because over-segmentation often happens when segments are obtained, and thus the geomorphometric signature is degraded. Or naturally, the shape is degraded by erosion or deposition. The method's main strength is the ability to use geomorphometrical data of the segments as criteria to decide the merge, compared to only shape, texture, or distance. To exemplify the method's usability, we use the case of closed depressions of aeolian nature that, despite being seen as concave in shape, actually have multiple forms: a flat bottom surrounded by concave, straight, and convex parts while incised in the flat plateau. This was investigated already as a reality for concave and convex features like sinkholes and aeolian closed depressions (deflation depressions or blowouts) [8].

II. MATERIAL AND METHODS

A. Materials

The DEM used for testing the proposed approach is a Copernicus DEM (COP-DEM30) crop at 20 m resolution covering the Găvanu-Burdea Plain in Southern Romania (Fig. 1).

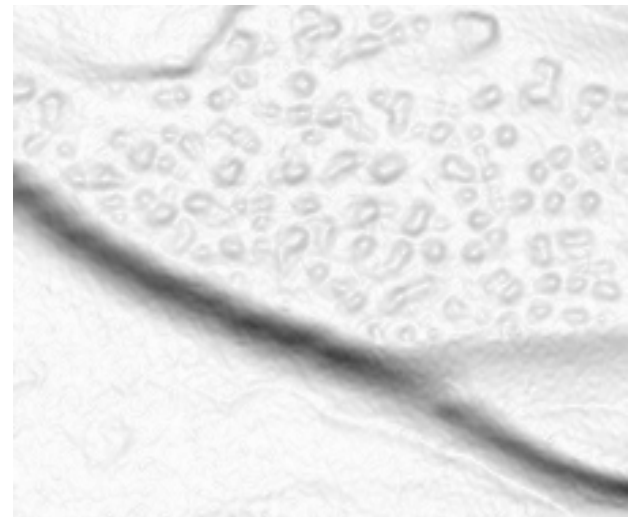


Figure 1. COPDEM at 30 m resolution for the study area.

B. Methods

While segmentation and polygon manipulation can be implemented in many software, I have used SAGA GIS [9] and R stat [10] because they are open source, and the reproducibility and readability is assured.

SAGA GIS watershed segmentation is a simple approach based on the ViGrA - Vision with Generic Algorithms (<http://hci.iwr.uni-heidelberg.de>) library [11] and is known to produce over-segmentation. Our objective here is different from dealing with these aspects here.

The *sf* package [12] representation of spatial geometry allows the integration with other R stat packages for straight manipulation of statistical methods and implementing machine learning algorithms. The spatial geometry analysis functions of *sf* package are also used for neighborhood identification and merging.

The neighbors are found with *poly2nb* function (<https://r-spatial.github.io/spdep/reference/poly2nb.html>) and stored as a list of vector IDs.

The descriptive statistics of the geomorphometric variables (minimum, mean, maximum, range, variance, standard deviation, percentiles) for every segment are computed in SAGA GIS with the tool and stored as attributes in the segments file. Additionally, shape attributes could be computed and used

if a certain shape is in the geomorphometric signature. I used only the descriptive statistics of altitude for the sample shown here. If the target landforms are influenced by various agents (water, air, ice), variables related to these agents could also be used (topographic wetness, drainage area, openness).

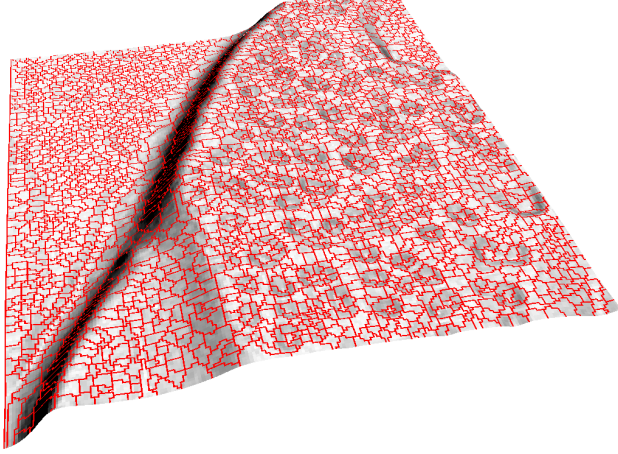


Figure 2. 3D view of the shaded surface and the segments of slope (x10).

Polygons are read and stored as an attribute table with a geometry column (“sf” and “data.frame” class in R). IDs are assigned in a new column starting from 1 to n.

Every neighbor segment geomorphometric values are stored as table columns (1 to m, where m is the maximum number of neighbors), and indexes can also be computed.

The neighbor IDs list of vectors is filtered by the condition of geomorphometric variables, and only those fulfilling the condition will have the ID in the list. The rest of the IDs are set up to zero.

The neighbors that have IDs in the list will be merged with the `st_union` function (https://r-spatial.github.io/sf/reference/geos_combine.html).

Duplicated geometries are then removed, and all the polygons that intersect each other are combined. Another filter can be set up during the final union.

III. RESULTS

In Figures 3 to 5, I show a closed depression formed by the segment with ID 1605 and its seven neighbors. Using the mean, standard deviation elevation values of all the neighbors, the segments that have neighbors with values bigger than 1 m are merged. In the case of the closed depression shown in Figure 3, the merging is performed as shown in Figure 5.

In Figure 6, I show a zoom 3D perspective view of the closed depression represented in Figures 3-5.

In the test, there was no further filtering based on geomorphometric variables. This would require the computation of the altitude statistics for the merged polygons. All the polygons that have intersections with other polygons are merged.

IV. DISCUSSIONS

The OBIA (Object-Based Image Analysis) literature showed that objects (superpixels, segments) are better candidates for performing land-cover classifications. For DEMs, this should also be true [13].

In multiscale situations, the object delineation might need a scalar approach, but the process is straightforward for specific “simple” shapes.

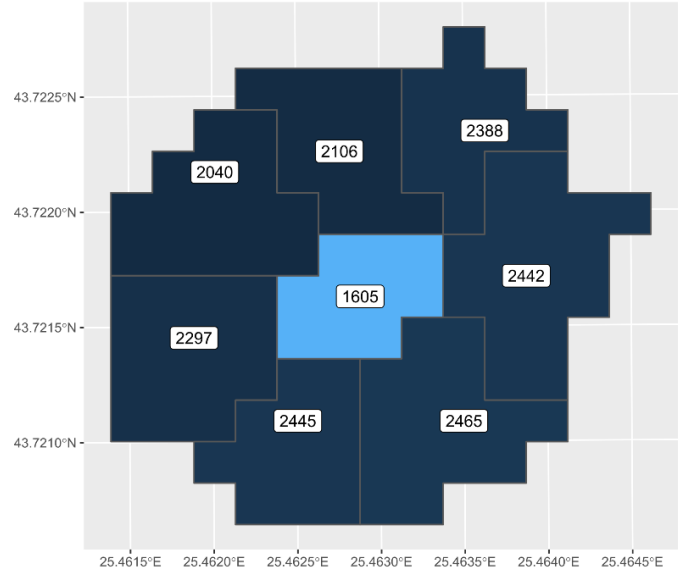


Figure 3. Example of a polygon and its identified neighbors.

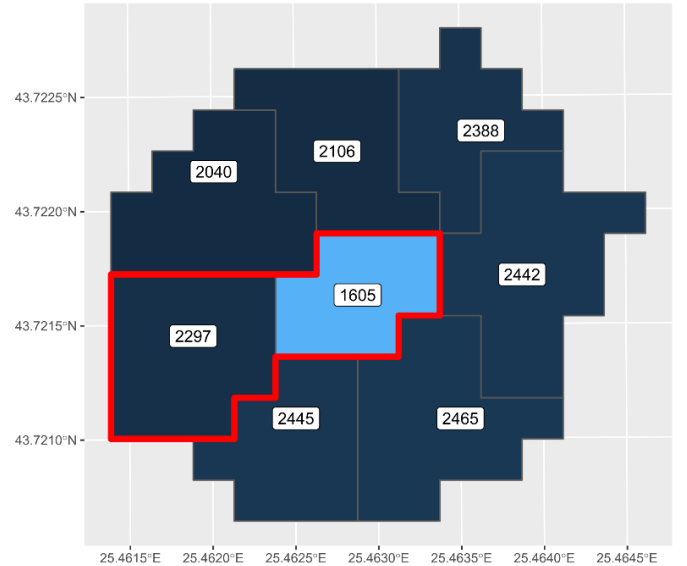


Figure 4. Example of a polygon merging with a single neighbor.

The limitations of object-based approaches are given by the over- or under-segmentation, so assessing these aspects is needed when using segments for classifications. Our objective here is to avoid dealing with the algorithmic aspects of these issues. Instead, the focus is on the ability to contextually merge adjacent segments based on their geomorphometric variables regarding the neighbors.

The eCognition software has similar abilities to merge or grow neighbor segments. Still, it is limited to a single class and spectral values or segments shape characteristics (https://docs.ecognition.com/v9.5.0/eCognition_documentation/User%20Guide%20Developer/4%20Basic%20Rule%20Set%20Editing.htm). The algorithms implemented in eCognition are closer to the post-segmentation or semi-automatic/manual refinement.

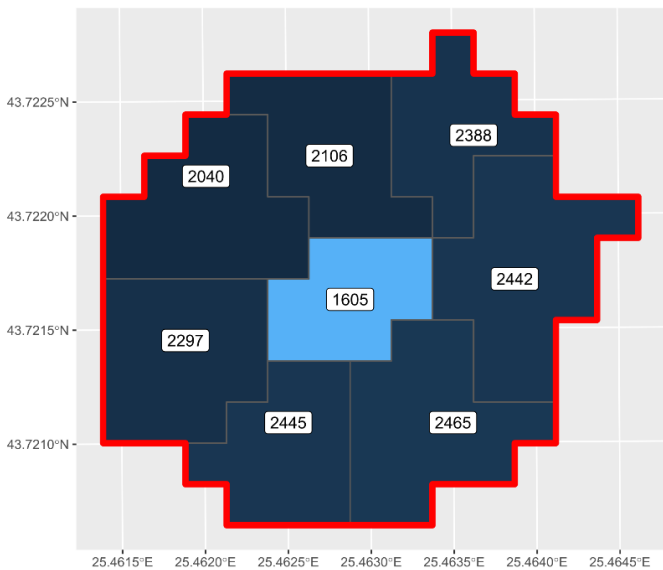


Figure 5. Example of a polygon merging with all the neighbors.

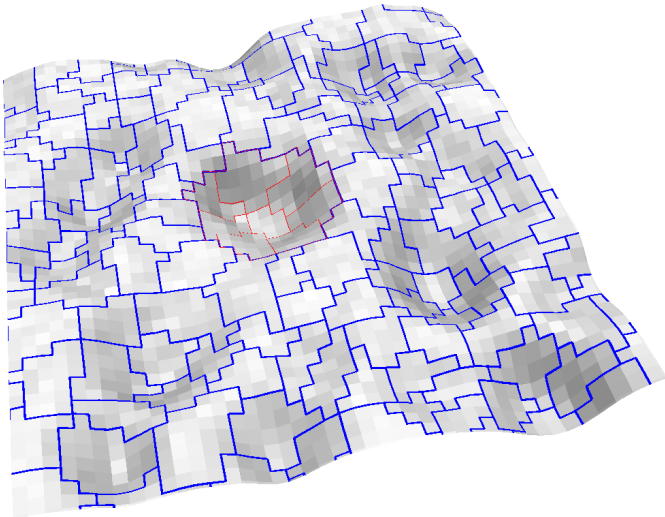


Figure 6. Example of the closed depression (segments with boundaries in red) formed by the polygon with ID 1605 and its seven neighbors.

Our approach is still straightforward in one iteration, but in this specific example can merge the segments of closed depressions pretty well. From this point on, new iterations can be used, or statistical models can be fitted to train a model for detecting and delineating closed depressions. The other merged features will need to be labeled in other classes.

V. CONCLUSIONS

The results are promising for the aeolian closed depression as a landform with a clear geomorphometric signature. For complex signatures, the complexity of the approach needs to be increased by adding iteration and other rules, but we are confident that this is achievable. The approach needs to be better framed in a GUI GIS environment to be implemented for specific landforms detection and delineation tasks.

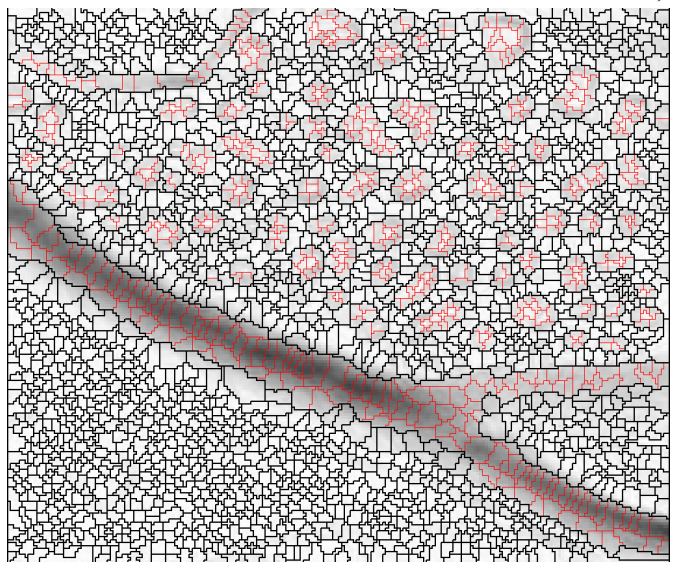


Figure 7. The merged polygons (in red) after a first iteration for neighbors that have a mean, standard deviation of altitude bigger than 1.5 m.

REFERENCES

- [1] Kettig, R., & Landgrebe, D. (1976). Classification of Multispectral Image Data by Extraction and Classification of Homogeneous Objects. *IEEE Transactions on Geoscience Electronics*, 14(1), 19–26. <https://doi.org/10.1109/tge.1976.294460>
- [2] Toussaint, G.T. 1977. The Use of Context in Pattern Recognition," *Pattern Recognition*. 10(3):189–204. [https://doi.org/10.1016/0031-3203\(78\)90027-4](https://doi.org/10.1016/0031-3203(78)90027-4)
- [3] Blaschke, T., Burnett, C., & Pekkarinen, A. (2004). Image Segmentation Methods for Object-based Analysis and Classification. in, F. De Meir, S. de Jong (Eds.), *Remote Sensing Image Analysis: Including the spatial domain*, Kluwer Academic Publishers, Dordrecht (2004), pp. 211-236. https://doi.org/10.1007/978-1-4020-2560-0_12
- [4] Blaschke, T. (2010). Object-based image analysis for remote sensing. *ISPRS Journal of Photogrammetry and Remote Sensing*, 65(1), 2–16. <https://doi.org/10.1016/j.isprsjprs.2009.06.004>
- [5] O’Neil-Dunne, J.P.M. 2010. Incorporating contextual information into object-based image analysis workflows. <https://www.asprs.org/wp-content/uploads/2010/12/ONEILDUNNE.pdf>
- [6] Bue, B. D., & Stepinski, T. F. (2006). Automated classification of landforms on Mars. *Computers & Geosciences*, 32(5), 604–614. <https://doi.org/10.1016/j.cageo.2005.09.004>
- [7] Jasiewicz, J., & Stepinski, T. F. (2013). Geomorphons — a pattern recognition approach to classification and mapping of landforms. *Geomorphology*, 182, 147–156. <https://doi.org/10.1016/j.geomorph.2012.11.005>
- [8] Niculaia, M. 2022. Machine learning and geomorphometrical objects for convex and concave geomorphological features detection, EGU General Assembly 2022, Vienna, Austria, 23–27 May 2022, EGU22-1853, <https://doi.org/10.5194/egusphere-egu22-1853>, 2022.
- [9] Conrad, O., Bechtel, B., Bock, M., Dietrich, H., Fischer, E., Gerlitz, L., Wehberg, J., Wichmann, V., and Böhner, J. (2015): System for Automated Geoscientific Analyses (SAGA) v. 2.1.4, Geosci. Model Dev., 8, 1991–2007. <https://doi.org/10.5194/gmd-8-1991-2015>
- [10] R Core Team (2022). R: A language and environment for statistical computing. R Foundation for Statistical Computing, Vienna, Austria. <https://www.R-project.org/>.
- [11] Köthe U., 1999, “Reusable Software in Computer Vision” in B. Jähne, H. Haußecker and P. Geißler, *Handbook of Computer Vision and Applications*. Academic Press, 103-132.
- [12] Pebesma, E. (2018). “Simple Features for R: Standardized Support for Spatial Vector Data.” *The R Journal*, 10(1), 439–446. doi:10.32614/RJ-2018-009, <https://doi.org/10.32614/RJ-2018-009>.
- [13] Stepinski, T.F., Ghosh, S., Vilalta, R. 2007. Machine Learning for Automatic Mapping of Planetary Surfaces. *Nineteenth Innovative Applications of Artificial Intelligence Conference*, July 2007

Application of LiDAR-based DTMs and DSMs to detect landforms created by the tree uprooting process

Janusz Godziek

Institute of Earth Sciences, Faculty of Natural Sciences
 University of Silesia in Katowice
 Sosnowiec, Poland
janusz.godziek@us.edu.pl

Abstract— Tree uprooting plays a significant role in shaping the microtopography in forested areas. This process leads to the formation of 1) pit-mound topography (with adjacent pit and mound forms being a result of the tree uprooting) and 2) root plates (with undecomposed root systems and soil material attached to them). The increasing availability and accuracy of LiDAR point clouds enable producing high-resolution DTMs and DSMs. Such models can be applied to detect even small forms with a diameter below 3 meters.

In the present project DTMs and DSMs were used to detect the location of 1) treethrow pit-mound pairs and 2) root plates of uprooted trees. Analysis was performed for selected 100x100 m research plots situated within the Babia Góra National Park (BgNP; Western Carpathians, Southern Poland). We used an open-source point cloud from the Polish Institute of Geodesy and Cartography (density: 20 pts/m²). All steps of the analysis were automated with the use of R programming language. Closed contour lines can be used to detect both types of forms. For pit-mound pairs detection, we tested different DTM resolutions and contour line intervals to achieve the best accuracy of the proposed contour method (CM). In the case of root plate detection, the point cloud was reduced to the points of the last return of the laser beam to maximize the chances of catching the points that actually reflect the locations of root plates and trunks. A differential model (DM) was produced by applying double classification of ground reflections with the use of a cloth simulation function algorithm (CSF). A contour line of the height of 1 m calculated from the DM was used to extract the potential locations of root plates.

The study has been supported by the Polish National Science Centre (project no 2019/35/O/ST10/00032).

I. INTRODUCTION

Tree uprooting is one of the main processes shaping the forest floor microrelief [12] (Fig. 1). This process is driven mainly by hurricane-force winds, which cause the trees to fall. Trees may be damaged in two ways, i.e. 1) by stem breakage and 2) by uprooting. The stem breakage does not have an impact on the forest floor microtopography, while during uprooting, the soil and bedrock material attached to roots is

uplifted in the root system [11]. The root plates formed in this way consist of *i*) undecomposed root systems and *ii*) soil and bedrock material. The subsequent process of the root system decomposition causes the soil and bedrock material to move down. This leads to a gradual disintegration of a root plate, which may last from several years to several decades. The disintegration process is controlled by climate, soil properties, and root plate volume [10]. Finally, a treethrow mound forms as a remnant of the root plate. In most cases, a treethrow mound has an adjacent pit, which was created during tree uprooting in the place previously occupied by the tree root system. Such neighboring convex and concave forms indicate the place, where the tree was uprooted and create the so-called pit-mound topography [8]. The entire process of pit-mound topography formation can be considered an example of hillslope biomorphodynamics, i.e. the impact of living organisms on the creation and evolution of landforms and soils [11, 13].

Currently, the availability of accurate Light Detection and Ranging (LiDAR) data is growing. Hence, Digital Terrain Models (DTMs) and Digital Surface Models (DSMs) can be produced with very fine, submeter resolution. This allows the application of this data to detect small microtopography forms with diameters below 3 m. Therefore LiDAR data may be an excellent source of information about the landforms resulting from the tree uprooting process.

Under the present project, we investigated the application of DTMs and DSMs to detect the location of 1) pit-mound pairs and 2) root plates of uprooted trees. We made an attempt to automate the detection process with the use of R programming language. Analysis was conducted for selected 100x100 m research plots located within the Babia Góra National Park (BgNP; Western Carpathians, Southern Poland). We applied open-source point cloud data from the Polish Head Office of Geodesy and Cartography (density: 20 points/m²). We used a closed contour lines approach to extract the location of forms. This approach was previously applied to detect karst landforms [4] and surface depressions [14].

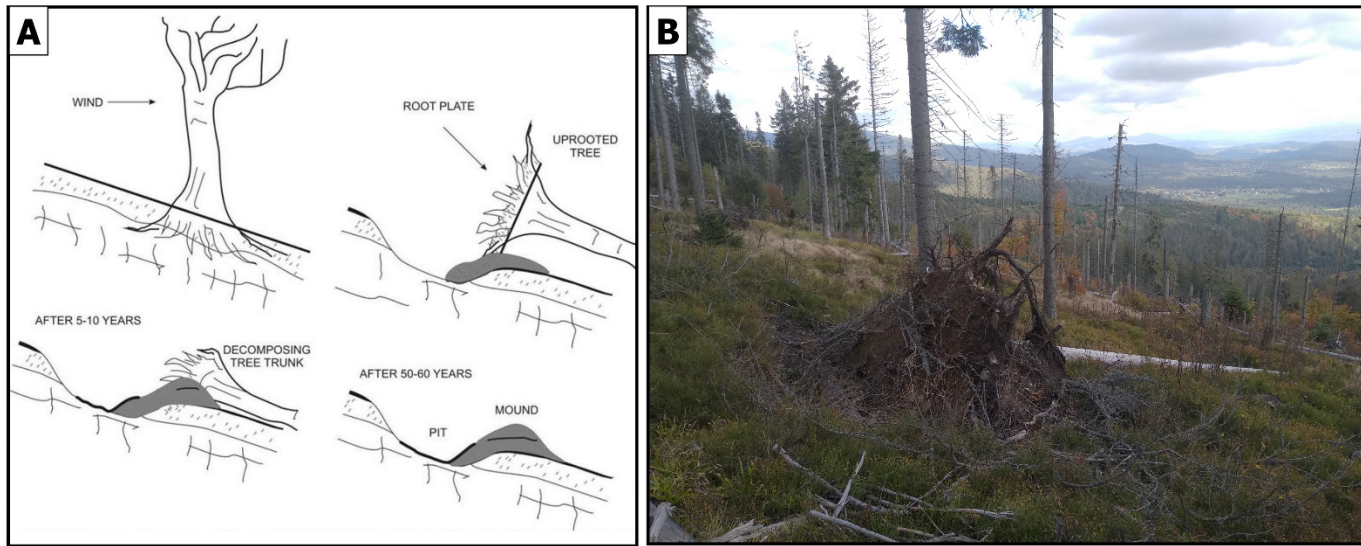


Figure 1. A – The process of tree uprooting and pit-mound topography formation (after [7]). B – Uprooted tree with a root plate and stem (Photo. J. Godziek 2022).

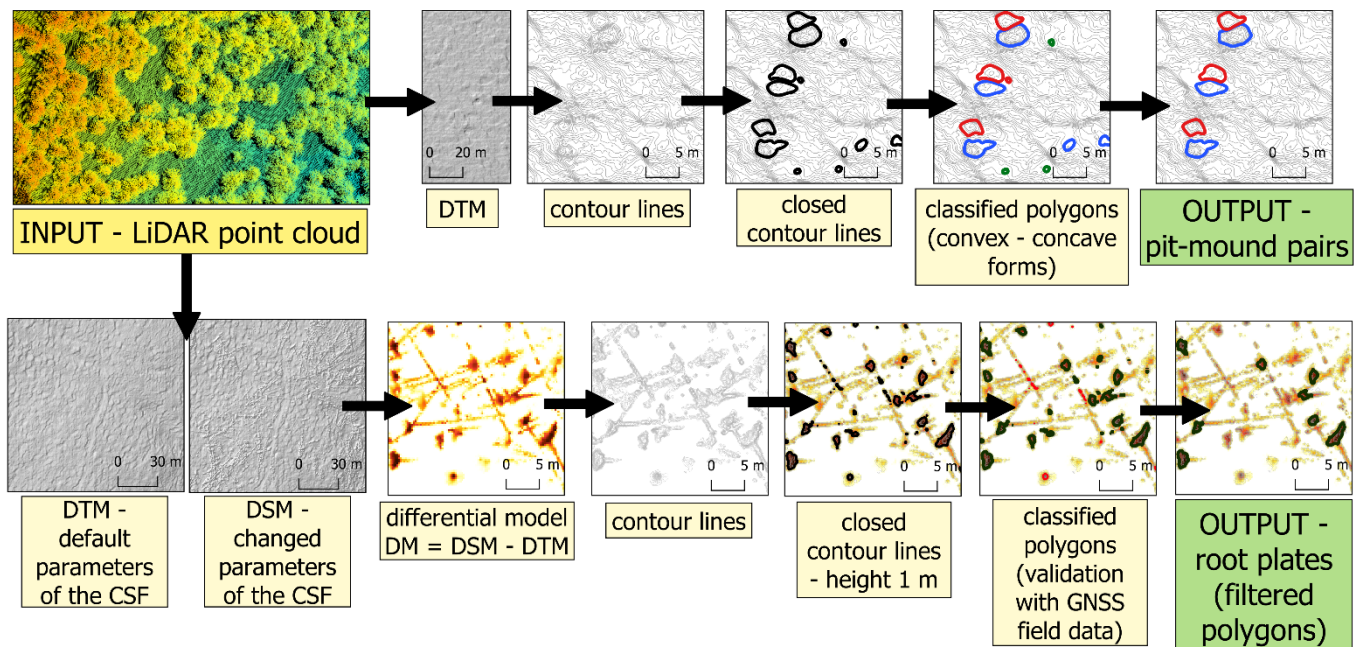


Fig. 2. Workflow of the pit-mound topography and root plates detection methods.

II. DETECTION METHODS AND RESULTS

A. Pit-mound topography

For pit-mound topography detection, we proposed the contour method (CM) allowing extraction of the location of individual pit-mound pairs [3] (Fig. 2). We produced DTM from LiDAR data. We tested three DTM resolutions: 0.5 m, 0.25 m, and 0.1 m. After that, we delineated contour lines and computed the length of each contour line. Three contour line intervals were tested: 0.25 m, 0.1 m, and 0.05 m. Then we filtered contour lines by selecting only those with the length within a particular interval. We checked three length intervals: 1.5 – 25 m, 2.5 – 20 m, and 3.5 – 15 m. In the next step, we converted selected contour lines into polygons. Finally, we classified these polygons into objects representing convex and concave forms by analyzing the location of the maximum and minimum elevation within the polygon.

We prepared the validation dataset by recognizing pit and mound forms manually, „on-screen”. The recognition was based on several criteria, i.e. 1) the values of the Topographic Position Index (TPI), 2) the characteristic shape of contour lines between adjacent pits and mounds, indicating the formation of both forms as a result of a single tree uprooting. We marked 74 pit-mound pairs in two research areas.

The next step was to compare the results of the CM with the validation dataset. Out of 27 tested variants of the CM, the best one (1st) reached accuracies around 95% for pits, 90-93% for mounds, and 85-90% for pit-mound pairs. For the 1st variant, we performed additional computations. We selected adjacent pits and mounds, located at a distance below 1.5 m. This enabled the assignment of a single pit to a single mound. Then we plotted the probable locations of pit-mound pairs on the map. The entire analysis described above was automated with the R script.

B. Root plates of uprooted trees

To obtain validation data on root plates location, measurements were carried out in the area of a forest stand damaged by the windstorm in November 2004 and strictly protected since 2005 [15]. On two research plots, we measured the location of 205 root plates using a GNSS receiver with an accuracy of 0.05 m. These measurements enabled us to estimate the accuracy of the proposed detection method.

We observed that the root plates of uprooted trees are visible in the LiDAR point clouds. To maximize the chances of catching the points that actually reflect the locations of root plates and trunks, we selected only the points marking the last return of the laser beam. To extract the location of root plates we performed double classification of ground reflections using the cloth simulation function (CSF) available in the lidR package [16] (Fig. 2). In the first classification we applied default parameters of the CSF algorithm and as a result we obtained DTM. In the second classification, we changed the parameters of the CSF algorithm (`sloop_smooth = T`, `class_threshold = 3`). The outcome of the computation was the DSM representing terrain surface, root plates, fallen trunks, and dense understory vegetation. Then we produced the differential model (DM) using the formula: $DM = DSM - DTM$. All computations were performed in a spatial resolution of 0.25 m.

We computed the contour lines of the DM in the interval of 0.1 m. Then we visually inspected the shape and layout of the contour lines of the root plates. We observed, that the contour line of the height of 1 m closes on the majority of root plates. We decided to use this contour line to extract the location of root plates. We converted the contour of the height of 1 m into polygons. We excluded from further analysis small polygons of the area below 0.2 m². Then we classified polygons into „root plates” and „false positives” using GNSS field measurements. The next step was to filter polygons to decrease the number of false positives. Therefore for each polygon, we calculated the following parameters: area, perimeter, the distance between the outermost vertices of the polygon boundary, polygon compactness index [1], zonal statistics of the DM (maximum, minimum, average, range, standard deviation), and morphometric indices (circulatory ratio [6], elongation ratio [2], hypsometric integral [9], and relief ratio [13]). For morphometric indices, we used values of the DM as height and the distance between the outermost vertices of the polygon boundary as „catchment” length. Then we analyzed the distribution of values of the above-mentioned parameters on the box plots. For each parameter, we produced two box plots considering two groups of features: root plates and false positives. We performed also visual, „on-screen” analysis of the values of particular polygons. Finally, we decided to select only polygons of area greater than 1 m² and polygon compactness index smaller than 1.9 (Fig. 3).

Accurate boundaries of root plates are required to extract the volume of these forms. To delineate boundaries, we created a 1 m buffer along the selected polygons representing the contour lines of the height of 1 m. Then we reclassified the DM. We assigned the value „1” to all pixels greater or equal to 0.2 m and the value „0” to all other pixels. We polygonized such reclassified raster and removed all polygons located below 0.2 m (with value „0”). Then we performed an intersection between 1 m buffers and polygons with value „1”. Finally, we simplified and smoothed the shape of the resulting polygons.

Initial results indicate quite a high accuracy of the proposed root plate detection method for the selected area of interest. Out of all 90 finally selected polygons, 60 were marked in the field

as root plates and 30 are false positives. Hence the accuracy of the proposed method can be estimated at 66%.

III. CONCLUSIONS

Both proposed methods achieved an accuracy above 60%. The methods perform well in the selected study area, however concerning the concept of the area of applicability [5] they are spatially limited. Therefore further testing on other areas and with different datasets is required. The results are strongly impacted by the quality of the point cloud data used in the study. The point cloud density of 20 pts/m² enables the recognition of microforms of diameter 1-3 m created due to the tree uprooting. Presumably point clouds of smaller densities do not enable such detection. The DTM resolution does not exert a significant impact on the detection outputs. To detect microforms, the contour line interval should be significantly smaller than the height of the forms. The methods presented in this paper may be applied to assess the scale and impact of the tree uprooting process in mid-latitudes forests and can be used in research in geomorphology, soil science, and forest ecology.

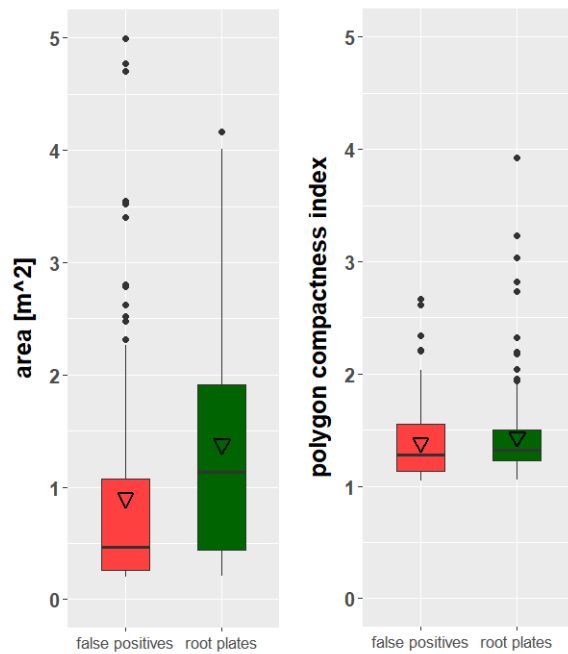


Fig. 3. Distribution of the values of area and polygon compactness index – data for polygons extracted from the contour line of the height of 1 m. Mean value marked by a triangle.

IV. ACKNOWLEDGMENTS

The study has been supported by the Polish National Science Centre (project no 2019/35/O/ST10/00032).

REFERENCES

- [1] Brinkhoff, T., Kriegel, H. P., Schneider, R., & Braun, A., 1995. Measuring the Complexity of Polygonal Objects. In: ACM-GIS, p. 109.
- [2] Eagleson, P.S., 1970. Dynamic Hydrology. McGraw-Hill Book Company, New York, 462.
- [3] Godziek, J., Pawlik, Ł., 2023. Indicators of wind-driven forest disturbances – pit-mound topography, its automatic detection and significance. CATENA 221, 106757. <https://doi.org/10.1016/j.catena.2022.106757>
- [4] Liang, F., Du, Y., Ge, Y., Li, C., 2014. A quantitative morphometric comparison of cockpit and doline karst landforms. J. Geogr. Sci. 24, 1069–1082. <https://doi.org/10.1007/s11442-0141139-6>

- [5] Meyer, H., Pebesma, E., 2021. Predicting into unknown space? Estimating the area of applicability of spatial prediction models. *Methods Ecol Evol* 12, 1620–1633. <https://doi.org/10.1111/2041-210X.13650>
- [6] Miller, V.C., 1953. Quantitative geomorphic study of drainage basin characteristics in the Clinch Mountain area, Virginia and Tennessee. Technical report (Columbia University. Department of Geology), 3.
- [7] Pawlik, Ł., 2013. The role of trees in the geomorphic system of forested hillslopes — A review. *Earth-Science Reviews* 126, 250–265. <https://doi.org/10.1016/j.earscirev.2013.08.007>
- [8] Pawlik, Ł., Migoń, P., Owczarek, P., Kacprzak, A., 2013. Surface processes and interactions with forest vegetation on a steep mudstone slope, Stołowe Mountains, SW Poland. *CATENA* 109, 203–216. <https://doi.org/10.1016/j.catena.2013.03.011>
- [9] Pike, R.I., Wilson, S.E., 1971. Elevation relief ratio, Hypsometric integral and geomorphic area altitude analysis. *Geol. Soc. Am. Bull.* 82: 1079–1084.
- [10] Šamonil, P., Antolík, L., Svoboda, M., Adam, D., 2009. Dynamics of windthrow events in a natural fir-beech forest in the Carpathian mountains. *Forest Ecology and Management* 257, 1148–1156. <https://doi.org/10.1016/j.foreco.2008.11.024>
- [11] Šamonil, P., Daněk, P., Schaeztl, R.J., Vašíčková, I., Valterová, M., 2015. Soil mixing and genesis as affected by tree uprooting in three temperate forests. *European Journal of Soil Science* 66, 589–603. <https://doi.org/10.1111/ejss.12245>
- [12] Schaeztl, R.J., Burns, S.F., Small, T.W., Johnson, D.L., 1990. Tree Uprooting: Review of Types and Patterns of Soil Disturbance. *Physical Geography* 11, 277–291. <https://doi.org/10.1080/02723646.1990.10642407>
- [13] Strahler, A.N., 1964 Quantitative geomorphology of drainage basin and channel networks. In: Chow, V.T., (Ed.) *Handbook of Applied Hydrology*. McGraw-Hill, New York. pp 439–476.
- [14] Wu, Q., Liu, H., Wang, S., Yu, B., Beck, R., Hinkel, K., 2015. A localized contour tree method for deriving geometric and topological properties of complex surface depressions based on high-resolution topographical data. *International Journal of Geographical Information Science* 29, 2041–2060. <https://doi.org/10.1080/13658816.2015.1038719>
- [15] Zadrożny, P., Krużel, J., Lamorski, T., Nicia, P., Kozina, P., 2017. Changes of the monitoring windfallen area on the Babia Góra mountain. *J. Ecol. Eng.* 18, 193–199. <https://doi.org/10.12911/22998993/67097>
- [16] Zhang, W., Qi, J., Wan, P., Wang, H., Xie, D., Wang, X., Yan, G., 2016. An Easy-to-Use Airborne LiDAR Data Filtering Method Based on Cloth Simulation. *Remote Sensing* 8, 501. <https://doi.org/10.3390/rs8060501>

Resampling and hydrogeomorphometrical processing of dense Lidar/DEM: Relationships between landforms and hydrological processes in a Mediterranean peri-alpine catchment basin

Christian Depraetere

Institut de Recherche pour le Développement, UMR Espace-DEV,
Maison de la Télédétection
500, rue Jean-François Breton
38000, Montpellier, France
christian.depraetere@ird.fr

Serge Riazanoff

VisioTerra, Scientific consulting for Earth observation, 14 rue Albert Einstein, 77420 Champs-sur-Marne, France

Benoît Deffontaines

Université Gustave Eiffel (ex UPEM / UMLV),
5 Bd Descartes, 77454 Marne-la-Vallée, Cedex 2, France

I. INTRODUCTION

Dense DEM/DTM from LIDAR tend to become an overarching data for environmental sciences particularly those requiring an accurate knowledge of the relationships between landforms and hydrological, so to say hydrogeomorphology. Herein, the focus is on a specific hydrogeomorphological processing of the forthcoming EEA-10 Copernicus DTM covering all EU (Figure 1). For testing purpose, a "pseudo" EEA-10 DTM was generated by undersampling at 10 meters resolution from the RGE ALTI® at 1 meter resolution available all over France (® Institut Géographique National, IGN).

An *ad hoc* method (SEAD) is tested to minimize the smoothing effect of undersampling on the landforms especially along the crest and the talweg lines. Then, an innovative sub surface percolation algorithm (DRAMP) derived from Beven's index is tested with this "RGEALti-SEAD-10m" on the peri alpine Mediterranean catchment basin of the Duyes in the Southern Alps. A study of the sensitivity of hydrogeomorphological landform depictions (i.e. alluvial fans, gullies, anastomosing channels, scree slopes, etc.) according to resolution shows that 10-meters resolution with decimeter precision suggesting that the forthcoming EEA-10 DTM should be a promising and more accurate product for various environmental issues along the river beds and hazards such as floods and landslides.

II. THE DTM DATA

The DTM under-sampling method SEAD (*Sous Echantillonnage ADaptatif* [5], adaptative undersampling) from dense to coarser resolution is purposely suitable for hydrogeomorphological applications. Taken a given spatial resolution of $\mu=1$ meter of the RGEALTI® DTM, the aim is to resampled it with $\mu=10$ meters to simulate a surrogate EEA-10 DTM. Instead of usual resampling methods based on averaging elevations and therefore smoothing the topography, SEAD is "adapting" the elevation at coarse resolution taking into account the topographic pattern at fine resolution. For instance, a summit or a crest should remain as such in the undersampled topography

with high elevation compare to their surrounding points and vice-versa for pit, talwags and valley. This means that it preserve better the major orographic patterns such as crest and talweg lines as well as it minimize the smoothing of hillslopes.

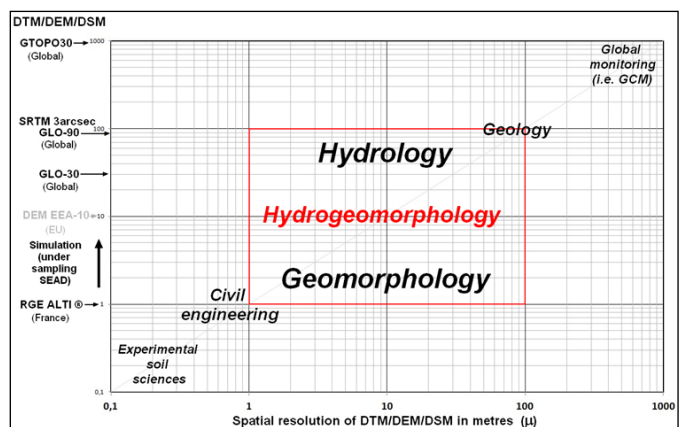


Figure 1

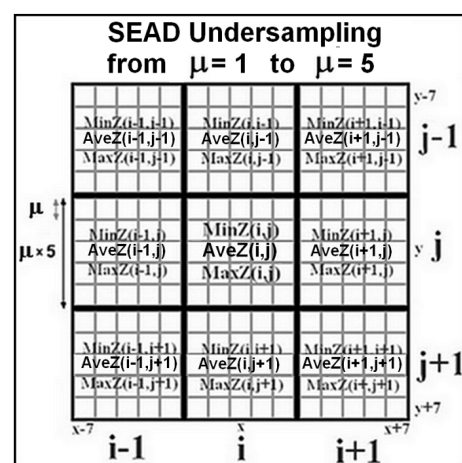


Figure 2

Taking the example of a subset of 15 by 15 meshes ($\mu=1$) in Figure 2, the objective is to compute the elevation on the central

meshes of a 3×3 undersampled window with ($\mu=5$). For the nine 5μ meshes, the min, average and max elevation are calculated from the 15×15 1μ meshes.

A score S_z is computed according to the relative elevations of min, average and max of the neighboring meshes compared to the central one.

$$S_z = S_{minz} + S_{averz} + S_{maxz} \text{ with } S_z \in [0..24] \quad \text{Eq. 1}$$

If $S_z = 0$, the central part corresponds to a well defined summit and the elevation Z for mesh(i,j) will be equal to $\text{MaxZ}(i,j)$. Conversely, a value of 24 for S_z means that it is clearly a depression area (pit, deep valley, etc.) with elevation Z for mesh(i,j) equal to $\text{MaxZ}(i,j)$. In other cases, it comes:

$$Z[i,j] = \text{MaxZ}(i,j) - (S_z/24) \cdot (\text{MaxZ}(i,j) - \text{MinZ}(i,j))$$

$$\text{with } Z[i,j] \in [\text{MinZ}(i,j).. \text{MaxZ}(i,j)] \quad \text{Eq. 2}$$

For instance on the example in Figure 3 corresponding to a valley, the score S_z is equal to 18. Therefore, the elevation $Z[i,j]$ between $\text{MinZ}(i,j)$ and $\text{MaxZ}(i,j)$ but closer to the minimum value ($Z[i,j] = \text{MaxZ}(i,j) - (18/24) \cdot (\text{MaxZ}(i,j) - \text{MinZ}(i,j))$).

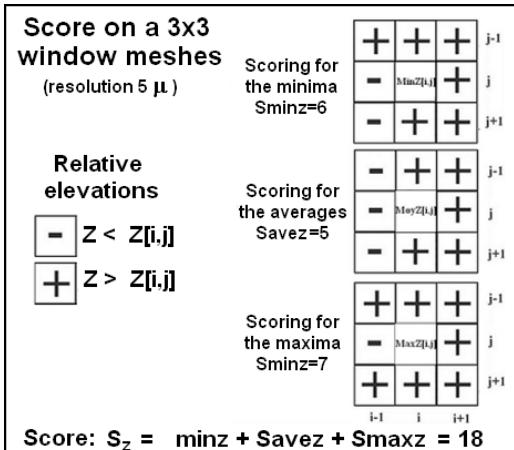


Figure 3

For comparison purposes, two DTM at 5 metres resolution ($\mu=5$ m) are undersampled with two methods: Z_{aver} with the averaged value ($\text{AveZ}(i,j)$), Z_{seed} with the method SEAD explained before. The differences of elevation (ΔZ) are given on Map 1B (Resolution 5 m) in the downstream part of the Riou torrent with various hydrogeomorphological landforms as shown on Map 1A (REGALTI® full resolution 1 m).

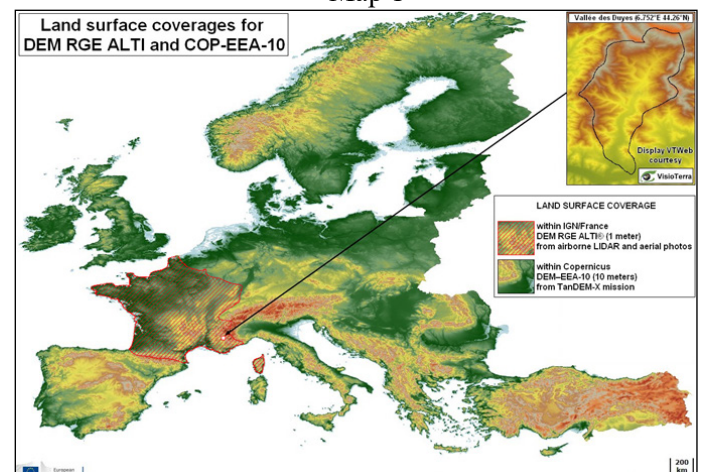
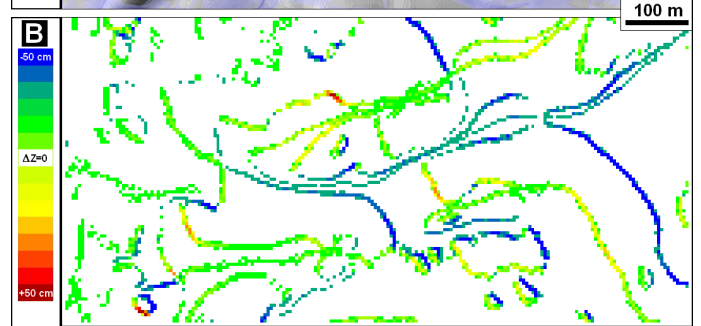
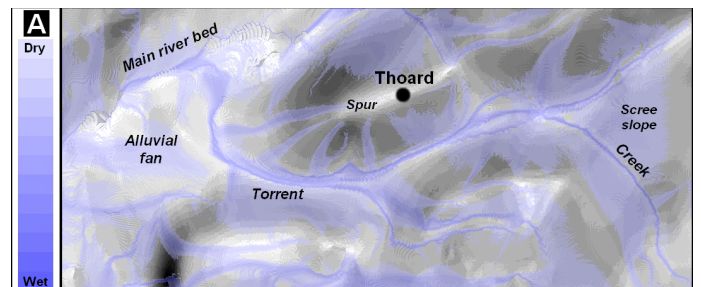
$$\Delta Z = Z_{\text{seed}} - Z_{\text{aver}}$$

Purposefully with the SEAD method, the elevations of crest and summit tend to be “positively” preserved while the elevation for talweg, creeks and river bed are instead “negatively” maintained.

III. SIMULATION OF SUB SURFACE PERCOLATION

The method that is presented is a simplified variant of the Beven's Index [1][2][9] and applied on the catchment basin of the Duyes valley (150 km^2 , sedimentary rocks and alluvial deposits, peri alpine Mediterranean climate, Map 2).

This catchment offers a large palette of hydrodynamic landforms such as glacis, upstream reception basins, gullies, alluvial fans, fluvial terraces, scree slopes, stony river beds, etc. developed on geological structural features of the Digne thrust sheet (Map 3).



Map 2

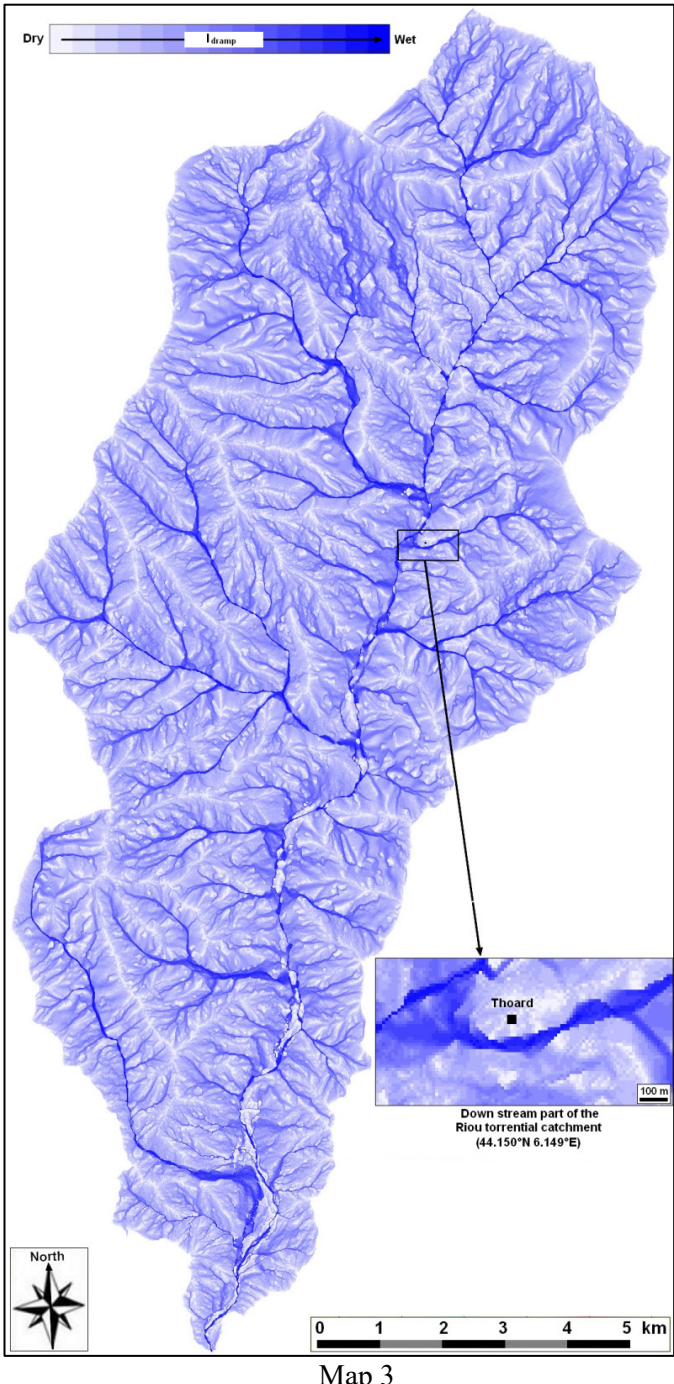
The Beven's index, also known as the Topographic wetness index ($I_{tw}=\text{Log}(\alpha)/\text{Tan}(\beta)$), states two basic assumptions about sub-surface percolation within pervious substrates:

- It is proportional to the drained surface $\text{Ln}(\alpha)$ in the sense of multidirectional drainage weighted for each direction according to the difference in level. It is an estimate of the probability of water flowing through a specific point;

- It is contrary wise proportional to the local slope $\text{Tan}(\beta)$.

In this study, the parameter α will be used without β because the present purpose is the multidirectional sub-surface percolation mapping for hydrogeomorphological applications (Cf. Map 3 with RGEAlti-SEAD-10m DTM) and not for the parametrization of potential saturation of soil (or “source area”) as I_{tw} is usually used for distributed and physical based hydrological modelling like TOPMODEL and its variants.

This simplified variant of the Beven's index is called the DRAMP method (*DRAinage Multidirectionnel Probabiliste* [5], Probabilistic multidirectional drainage). Thus, $I_{dramp} = \text{Log}(a)$.



Map 3

The computation of α can be explained on the example of Figure 4A. It is more complex than the usual "mono directional" surface flow D8 based on steepest descent as shown in Figure 4B or purpose like methods [3][7][8][11]. This "oil cloth" D8 flow routing generates only one drainage line from a given point, for instance from the "source" point at 105 m down to the "outlet" point at 1 m. From the same source point with the DRAMP method, many drainage lines are possible as shown on Figure 4C and depending of the slope gradient pattern. This corresponds to a "multi directional" sub-surface flow routing that could be assimilated as a "sponge" like superficial reservoir. The amount of water percolating down to the outlet point has a strong probability to be inferior to the infiltrated water into the source point.

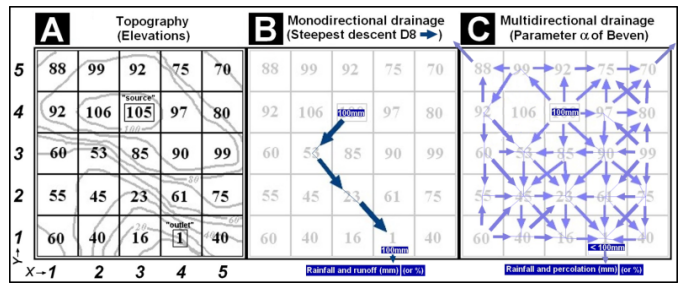


Figure 4

The Figure 5 detailed the probability of percolation from the source point to the outlet point along the steepest descent line as defined in Figure 4B. It comes that only 16 % percolates from the source down to the outlet. The other 84 % follow others multiple diverging flow lines, some of them not flowing through the outlet. On this example, the value of α will be superior to 16% and inferior to 100 mm. The overall computation with a shifting 3x3 window consider each point as a source and an outlet.

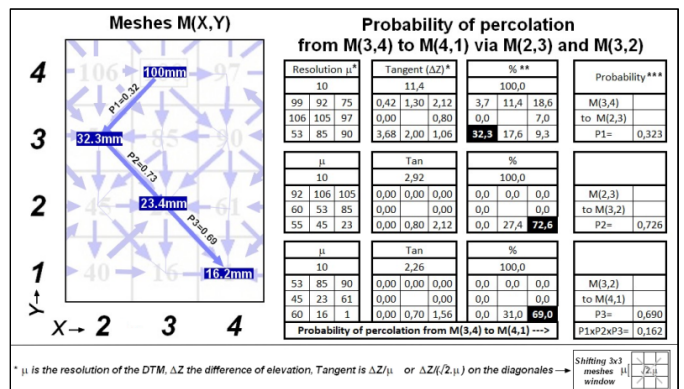


Figure 5

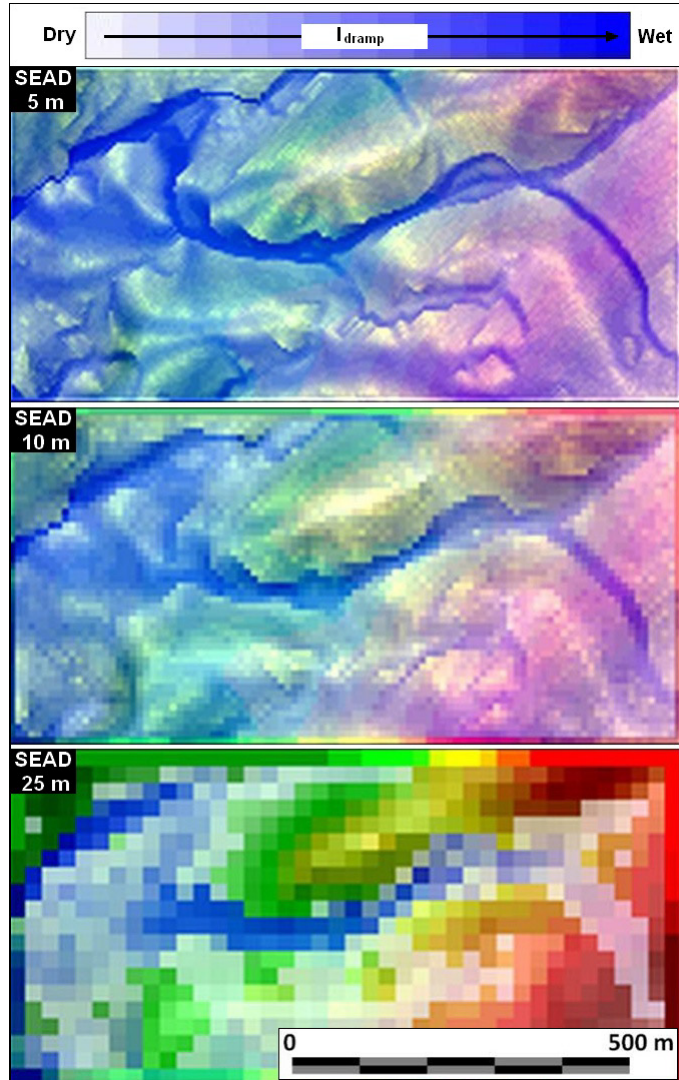
Starting from the RGE ALTI®, this allows comparing the effect of SEAD undersampling 5, 10 ("pseudo" DEM EEA-10) and 25 meters resolution on sub-surface percolation simulation with the DRAMP algorithm [5]. A sensitivity analysis of hydrogeomorphometric patterns and textures rendering from the DRAMP method is given in Map 4 on the same area of the lower part of the Riou catchment (cf. Map 1A and Map 3). The percolation patterns are clear at 5 and 10 meters resolution with well-depicted divergent percolations on the alluvial fan and in the torrential river bed. Conversely, the rendering becomes fuzzy at 25 meters resolution with not so well depiction of landform units such as the limit between the main river bed of the Duyes and the alluvial fan of the Riou.

The Map 5 gives a more detailed hydrogeomorphological analysis of the various landforms unit identifiable at 5 meters resolution and still detectable at 10 meters resolution with the "pseudo" COP-EEA-10.

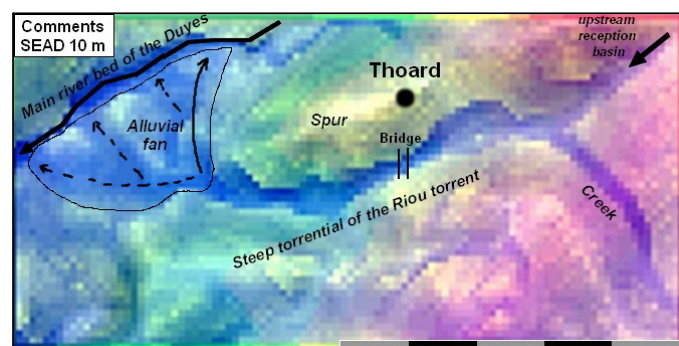
IV. CONCLUSIONS

The previous simulation and analysis suggests that the forthcoming Copernicus DEM COP-EEA-10 covering 29 countries of Europe (cf. Map 1) should be an accurate product for mapping and semi-automatic detection of fluvial and torrential landform. This should contribute to a standardization of hydro-geomorphological mapping and parametrization of risk evaluation and mitigation for flooding and landslides hazards at the European scale.

In France, the undersampling of the RGE ALTI® (or LITTO3D on some overseas territories) at 5 or even 10 meters with appropriate method such as SEAD could back up the steady national policy on the integrated management of rivers following the Water Framework Directive (WFD 2000) and its translation into French law (Law on Water and Aquatic Environments, LEMA, 2006).



Map 4



Map 5

In the regions of the French Southern Alps, Haute Provence and probably other Mediterranean mountainous area, the ongoing impact of river beds incision due to reforestation and abandonment of agricultural land since many decades [6-7] is manifold: lowering of alluvial water table, erosion of alluvial terraces and undermining of dykes and bridge piers. These facts

Depraetere, Riazanoff & Deffontaines pledge for an accurate and continuous GIS monitoring of the "The green and blue network" (*trames verte et bleue*) with Lidar data.

The DRAMP method could be one asset for those actions.

V. ACKNOWLEDGMENTS

The study and field works in the Duyes Valley were conducted in collaboration with the UNESCO Geopark of Haute Provence and the National Taiwan University in Taipei.

The scientific and technical support of VisioTerra, contributed to this work with expertise and remote sensing data. <https://www.visioterra.fr>

REFERENCES

- [1] Beven, K. J. and Kirkby, M.J. 1979. A physically-based variable contributing area model of basin hydrology. *Hydrol. Sci. Bull.*, 24, 43–69, 1979.
- [2] Beven, K., and Germann, P. 1982. Macropores and water flow in soils. *Water Resour. Res.*, Volume 18, Issue 5, pages 1311–1325, October 1982.
- [3] Chorowicz J., Ichoku C., Riazanoff S., Youn-Jong Kim and Cervelle B. 1992. A Combined Algorithm for Automated Drainage Network Extraction in Water Resources Research, vol.28, n°5, pp.1293-1302. American Geophysical Union.
- [4] Depraetere C. and Riazanoff S. 2004. The new Digital Elevation Model data set from the Shuttle Radar Topography Mission: Hydrogeomorphological applications in the Ohrid region Albania, Greece and Macedonia. Conf. on Water Observation and Information System for the Balkans Countries BALWOIS, Ohrid, North Macedonia, 25-29 Mai 2004. https://igm.univ-mly.fr/~riazano/publications/20040525_BALWOIS_Conference.pdf.
- [5] Depraetere, C. 2013. Introduction à l'hydro-géomorphométrie : études des relations entre le modélisé des formes de terrain et les processus hydrologiques dans des contextes insulaires. Document inédit d'Habilitation à Diriger des Recherches HDR, 8 novembre 2013 à l'Université Paris-Diderot VII, 249 pages. https://www.espace-dev.fr/wp-content/uploads/2022/03/HDR_01_Hydroge%CC%81omorphome%CC%81trie_Partie-1-Historique.pdf
- [6] Descroix L. 1998. L'érosion hydrique dans les terrains peu résistants des Préalpes françaises du sud : mesures et variables explicatives sur parcelles et bassins versants. In : Recherches dans les Alpes françaises du sud : bocages du Champsaur, cartographie des alpages, érosion et mouvements de terrain; tourisme en haute montagne. *Revue de Géographie Alpine*, 1, p. 43-58.
- [7] Descroix L., Gauthier E., Olivry J-C. (2002). « L'influence de la végétation et de son évolution dans les processus d'érosion dans les Alpes du Sud ». In: Roose Eric (ed.), Sabir M. (ed.), De Noni Georges (ed.). Techniques traditionnelles de GCES en milieu méditerranéen. Bulletin - Réseau Erosion, (21), p. 346-357. La Gestion Traditionnelle de l'Eau, de la Biomasse et de la Fertilité des Sols, Base d'une Nouvelle Approche de la Lutte Antiérosive dans les Montagnes Marocaines : Journées Scientifiques, Salé (MAR), 2002/02/08-09.
- [8] Dupéret A., Deffontaines B. and Passalacqua O., 2003. Critères géomorphométriques issus des modèles numériques de terrain au service des applications hydrologiques. *Bulletin de la Société française de photogrammétrie et de télédétection* 2003, n°172, pp. 107-121.
- [9] Fairfield, J., & Leymarie, P. 1991. Drainage networks from grid digital elevation models. *Water resources research*, 27(5), 709-717.
- [10] Merot P., Ezzahar B., Walter C. and Aurousseau P. 1995. Mapping water logging of soils using digital terrain models. *Hydrol. Process* 1995; 9:27–34.

Flood inundation analysis based on SAR image and DEM: A case study of the 2021 Zhengzhou Flood in China

Bofei Zhao, Haigang Sui
The State Key Laboratory of Information Engineering in Surveying, Mapping and Remote Sensing, Wuhan University, Wuhan, China
haigang_sui@263.net

Abstract— In recent years, flood disasters have become more frequent all over the world. It is of great importance to analyze flood disasters by remote sensing image and topographic data. Space-based synthetic aperture radar (SAR) is a powerful tool for monitoring flood conditions over large areas without the influence of clouds and daylight, but it cannot reflect the cause and trend of flood formation. The combination of terrain data and remote sensing data has potential utility in mapping and analyzing large-scale surface floods caused by heavy rainfall. Taking the flood disaster in Zhengzhou, China in 2021 as an example, this paper attempts to analyze the topographic and hydrological characteristics based on the Gaofen-3 (GF3) SAR image and FABDEM data, so as to understand the trend of flood inundation. The experiment demonstrates that combining digital elevation model (DEM) data can facilitate mutual validation of remote sensing image flood monitoring and analysis of urban water flow mechanisms.

I. INTRODUCTION

Due to climate change and urbanization, natural disasters are occurring more frequently and affecting more people. A report published in 2020 by the United Nations Office for Disaster Risk Reduction (UNDRR) confirms that extreme weather events will dominate the disaster landscape of the 21st century [1]. Between 2000 and 2018, the world experienced 913 major flood disasters [2]. How to realize pre-disaster warning and post-disaster rapid detection of floods is very important.

An accurate mapping of the disaster situation can be achieved by extracting flooded areas, and the results combined with pre disaster geographic data can be used to evaluate the post-disaster damage losses.

Flood disasters are often widespread and associated with cloudy weather. Synthetic aperture radar (SAR) is one of the most effective tools for flood emergency monitoring due to its all-day, all-weather earth observation capability. And SAR is very sensitive to surface roughness and other characteristics, so it has high accuracy to extract water extent and to obtain flood range by comparing changes between water bodies before and after disasters.

Li Hua
College of Resources & Environment, Huazhong Agriculture University, Wuhan, China

Qiming Zhou
Department of Geography, Hong Kong Baptist University, Hong Kong, China

Jiansi Yang
School of Urban Design, Wuhan University, Wuhan, China

The most basic water extraction method is image classification. Sui et al. adopted multi-scale level set segmentation and OTSU thresholding method to realize automatic water extraction of SAR image, effectively improving the detection accuracy of flood inundation area [3]. In addition, because the electromagnetic waves generated by the radar are reflected from the water by the mirror, the water body has low brightness in SAR images. This is reversed in forested areas, where the electromagnetic waves emitted by the radar are reflected off the water surface and hit tree trunks and canopies, increasing the backscatter strength.

Flooding is a complex process involving meteorological precipitation, hydrology, topography and other factors. Although the remote sensing image has the characteristics of large coverage and fast data collection in flood disaster monitoring, the development of flood is closely related to topography and geomorphic information, while the remote sensing image only focuses on surface distribution characteristics.

It is very important to utilize the topographic and geomorphic features for flood hazard risk assessment. By using DEMs to analyze hydrological features and hydrodynamic model, flood simulation can be realized to evaluate the possibility of flood disaster [4]. Compared with only relying on remote sensing image to obtain water distribution information, DEM and other data fusion methods can effectively improve the accuracy of large-scale water identification. Li et al. effectively combined DEM, Landsat, MODIS and water occurrence data to observe surface water changes with finer spatial-temporal resolution [5].

This paper combines SAR and DEM data to analyses the distribution of flood water bodies, and taking the flood disaster in Zhengzhou, China in 2021 as an example. We use the flood area extracted from the Gaofen-3 (GF3) SAR images and the hydrological features extracted from the FABDEM to try to analyses the distribution of the flood inundation.

II. METHODS

The study area is located in Zhengzhou City, Henan Province, China. Most of this area is in the plain, the Yellow River is in the north of the Zhengzhou city, and the southwest corner of the city is a high mountain (Figure 1). On 20 July 2021, Zhengzhou experienced severe flooding due to several days of heavy precipitation. The long-term rainfall weather caused the optical images to be severely obscured by clouds. Therefore, China's disaster reduction department urgently programmed GF3 satellite to obtain the time-series SAR images of the affected areas in time.

The GF3 satellite is a multi-modal imaging SAR sensor, launched in 2016, with single-polarization, dual-polarization and full-polarization modes. The GF3 data used in this paper are dual-polarization (FSII mode) images on July 24, 2021, HV polarization channels, and the spatial resolution is 10m. Image segmentation [3] is used to extract the water range of SAR images, and the results are shown in Figure 2. The GF3 SAR image was used to extract the pre-disaster and post-disaster water body areas in the study area, and the flood distribution areas could be identified through comparative analysis.

Multi-temporal SAR images can be used to monitor the flood range, but there are some errors in the extraction results of urban water bodies, because they are interfered by SAR image noise, and the distribution of surface water caused by rainfall cannot be analyzed only depending on the flood extent.

In order to analyze the topographic and hydrological features of the study area, the river network and basin features were extracted using FABDEM DEM data [6]. This data is a global map of elevation with buildings and forests removed at 1 arc second grid spacing. The hydrological analysis module of ArcGIS software was adopted for the hydrological characteristics.

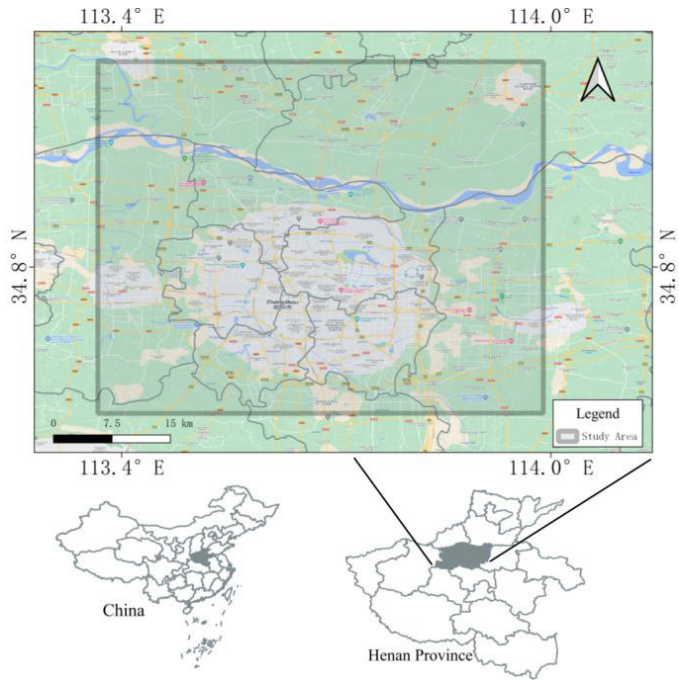


Figure 1. Location map of the study area in Henan Province, China.

The distribution of water network and watershed is obtained by calculating the flow direction and flow accumulation data of the study area. Then, the hydrological characteristics and inundation range are combined to analyze the flood distribution.

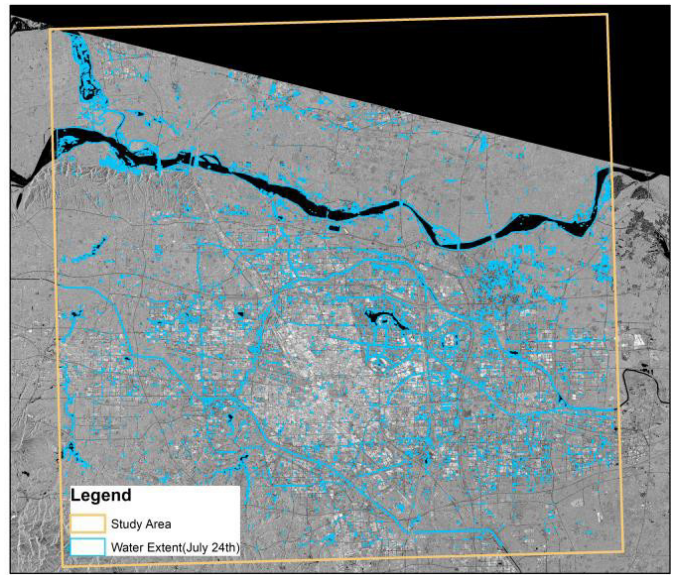


Figure 2. Water extraction results of GF3 image.

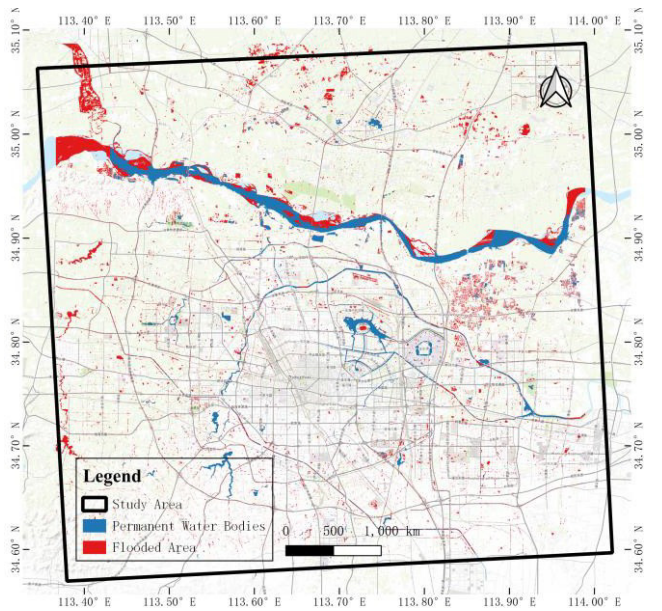


Figure 3. Flood distribution map of the study area.

III. RESULTS AND DISCUSSION

In the way of post-classification comparison, multi-temporal SAR was used to extract the flood range, as shown in Figure 3. The blue area is the distribution range of water before the disaster, and the red area is the flood water bodies on July 24, 2021. There are more flood water bodies on both sides of the Yellow River, and the width of the river surface increases significantly due to the flood. A large area of flood water bodies has appeared in the north-east of Zhengzhou. Flood water bodies are also widely distributed around the Zhengzhou city, showing that urban waterlogging is very serious.

Figure 4 is the DEM elevation map of the study area. The terrain of the study area slopes gradually from southwest to northeast, and flooding occurs on both sides of rivers in the southwest region. A large area of flooding and waterlogging occurred in urban areas with relatively flat terrain, and water on urban roads is shown as a linear red area in the image. The city of Zhengzhou, which is located in the plain area, experienced a large area of urban waterlogging after heavy rainfall.

Based on the 30m resolution DEM data of the study area, the river distribution obtained from the flow direction and flow accumulation is shown in Figure 5. Light blue is calculated to get the distribution of the river network in the study area, the dark blue area is permanent water and the red area is flood water. It can be seen that the surface stream in the study area mainly originates from the mountainous areas in the southwest and west of the city, and most of the rivers flow into the southeast of the low terrain after passing through the city.

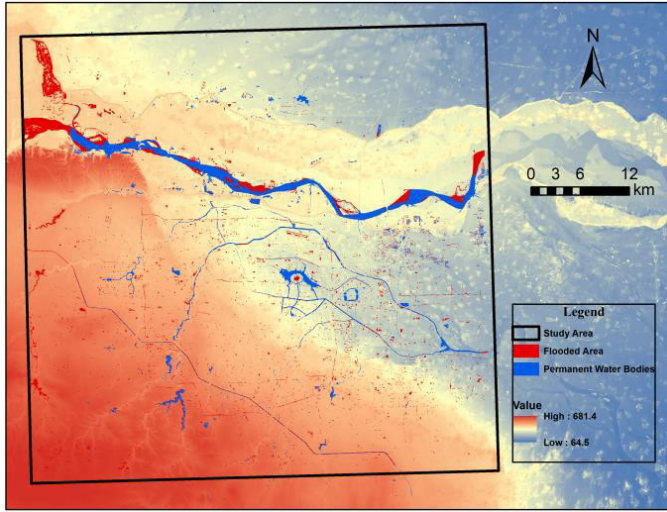


Figure 4. The elevation of the study area.

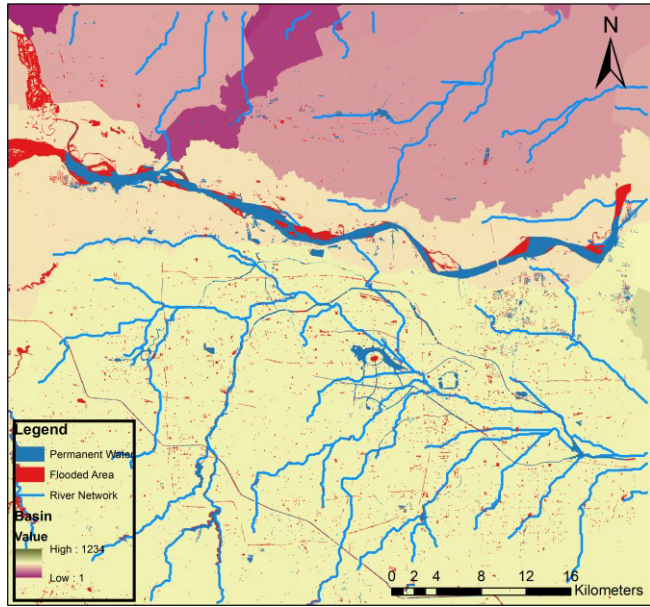


Figure 5. River networks and drainage basins in the study area.

Most of the flood water flows to the southeast of the study area after the rainfall, which is consistent with the remote sensing detection results, and most of the flood water is distributed in the eastern part of the city. By extracting the drainage basin of the study area (Figure 5), it can be seen that the flood extent is concentrated in the drainage basin mainly in the urban plain. The eastern part of the city is dominated by agricultural land and these areas have experienced extensive flooding. The combination of geomorphic data and flood data can be used to preliminarily analyze the development state of the flood after the rainfall, which is of practical value in understanding the development of the flood disaster.

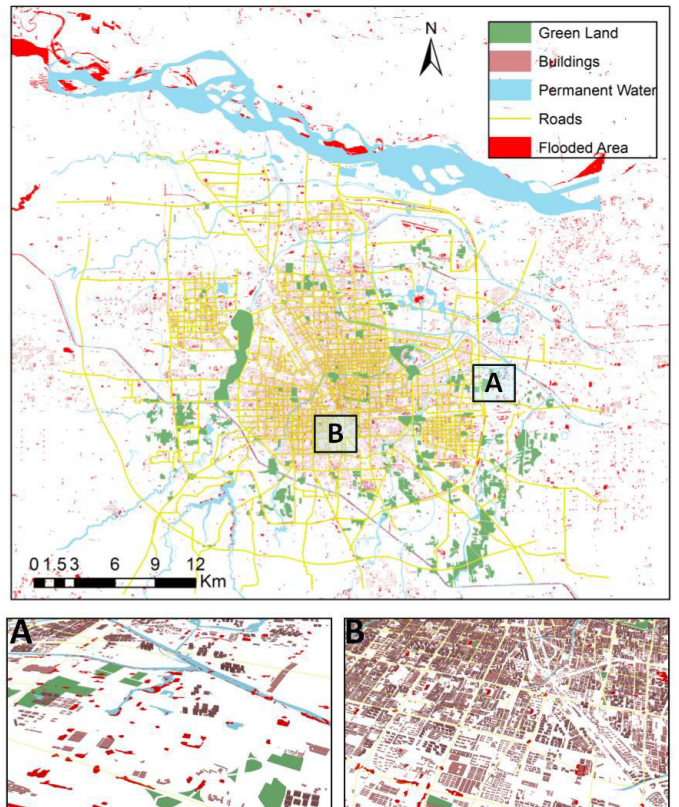


Figure 6. The basin of the study area

In 2006 researchers conducted a project to predict surface water pooling under different rainfall in Edmonton, Canada. In this work, the urban elevation is modeled with high precision, and the urban surface water pooling under different rainfall conditions is simulated very well based on the hydrology corrected DEM [7]. The report divides flood flow in urban environments into two mechanisms: one is when river water overflows from river channels and accumulates in low-lying areas, and the other is when surface water accumulates in low-lying areas from upland area.

In order to analyze the mechanisms of water flow in the study area, we combined flood inundation data and urban geographic data (such as buildings, green space, rivers, etc.) to analyze the location relationship between the inundation area and surrounding geographic elements (Fig.6). It can be found that the inundation in the study area is mainly caused by surface water pooling in low-lying areas (Figure 6.B), and the inundation area caused by river overflow is mainly distributed in the southwest area of the city (Figure 6.A).

However, there are still some problems to be solved in the evolution process of urban waterlogging based on remote sensing images and DEM data. Due to the complexity of the surface of urban areas, SAR image cannot meet the requirements of fine extraction of urban inundation area. In addition, the combination of remote sensing images and topographic data has not been able to achieve a more objective and automated analysis of urban area flooding mechanism.

IV. CONCLUSION

In this paper, SAR image and DEM data are used to analyze the geomorphic features of the flood inundation area in Zhengzhou, Henan, China in 2021. The results show that heavy rainfall causes severe waterlogging in the urban areas and tends to flow southeast of the city. In the future, it is necessary to use

topographic data with higher resolution remote sensing images to realize more accurate analysis of urban flood inundation.

V. ACKNOWLEDGMENT

This study was supported by the Guangxi Science and Technology Major Project (No. AA22068072), the Natural Science Foundation of China (NSFC) General Program (41971386 and 42271416) and Hong Kong Research Grant Council (RGC) General Research Fund (HKBU 12301820). We acknowledge the University of Bristol and Fathom for FABDEM data-set.

REFERENCES

- [1] UNDRR, 2020, "The human cost of disasters: an overview of the last 20 years (2000-2019)".
- [2] Tellman, et al., 2021, "Satellite imaging reveals increased proportion of population exposed to floods". *Nature*, 5870, p. 80-86. <https://doi.org/10.1038/s41586-021-03695-w>
- [3] Sui and Xu, 2012, "Automatic extraction of water in high-resolution sar images based on multi-scale level set method and otsu algorithm". *ISPRS - International Archives of the Photogrammetry Remote Sensing and Spatial Information Sciences*, 39, p. 453-457. <http://dx.doi.org/10.5194/isprsarchives-XXXIX-B7-453-2012>
- [4] Zhang, et al., 2019, "Accuracy assessment of ASTER, SRTM, ALOS, and TDX DEMs for Hispaniola and implications for mapping vulnerability to coastal flooding". *Remote Sensing of Environment*, p. 290-306. <https://doi.org/10.1016/j.rse.2019.02.028>
- [5] Li, et al., 2021, "Monitoring high spatiotemporal water dynamics by fusing MODIS, Landsat, water occurrence data and DEM". *Remote Sensing of Environment*, p. 112680. <https://doi.org/10.1016/j.rse.2021.112680>
- [6] Hawker, et al., 2022, "A 30 m global map of elevation with forests and buildings removed". *Environmental Research Letters*, 2, p. 024016. <https://doi.org/10.1088/1748-9326/ac4d4f>
- [7] Macmillan, City of Edmonton Drainage Study: Final Report on a project to locate, map and characterize all sags, or depressions, within the City of Edmonton. 2006.

Evaluation of elevation, slope, roughness, and vegetation type on the burn severity of the 2020 Calwood Fire in Boulder County, Colorado

Maeve L. DeBuse and Peter L. Guth

Department of Oceanography
 United States Naval Academy
 572C Holloway Road
 Annapolis MD 21402 USA
maeve@usna.edu, pguth@usna.edu

Abstract— The Calwood Fire burned in Boulder County, Colorado from October 17 through November 14 2020. The vegetation types in the area greatly influenced the spread and severity of the fire. The conifer forests burned most severely and the fire died when it ran out of fuel in the grasslands. The elevation of the land had very little effect over initial burn severity but the areas of lower elevation recovered faster than the areas of higher elevation. The areas of high slope burned less severely but recovered slower than areas of low slope. The areas of high roughness burned less severely in the initial fire than the areas of low roughness but did very little to affect the regrowth in the area.

I. INTRODUCTION

From October 17, 2020 to November 14, 2020 the Calwood Fire burned 40.9 km² in Boulder County, Colorado (Figure 1). The ignition source of the fire is unknown and strong winds at the time of the fire allowed it to spread rapidly across the landscape [1]. The fire began near the Cal-Wood Education center and spread east towards Boulder and U.S. Route 36 [2]. This study analyzes how topographical features like slope, roughness and elevation and the existing vegetation types in the area affect the severity of the initial burn and the regrowth rate.

II. DATA & METHODS

LandFire [3] provided the existing vegetation types of the affected area (Figure 2). The difference normalized burn ratio (dNBR) images are made with imagery from the Sentinel-2 satellites. NBRs [4] were created for 4 dates spanning the duration of the fire and the regrowth over the next two years. Each of the three NBRs from after the fire's ignition were subtracted from a control NBR from, 28 September 2020, before the fire started (fig. 3, 4).

The elevation, slope and roughness figures were created from a 1m digital terrain model (DTM). A hillshade map (fig. 5A), aspect map fig. 5B, using symbology after [5], and a roughness grid (fig. 5C) using a 3x3 window with the standard deviation of the slope [6].

The 1-meter DTM was masked to match the individual burn categories of the dNBRs and the data was compiled into histograms for corresponding to the elevation, slope, and roughness of the Calwood fire area (Figure 6)

III. RESULTS

Over half of the area is covered by two vegetation types: southern Rocky Mountain ponderosa pine, 49.9%, and the southern Rocky Mountain dry-mesic montane mixed conifer forest and woodland, 13.44% (Figure 2). The eastern border and southernmost point of the burn area are covered mainly in four types of grasslands and shrublands which cover 21.98% of the burn area (Figure 2).

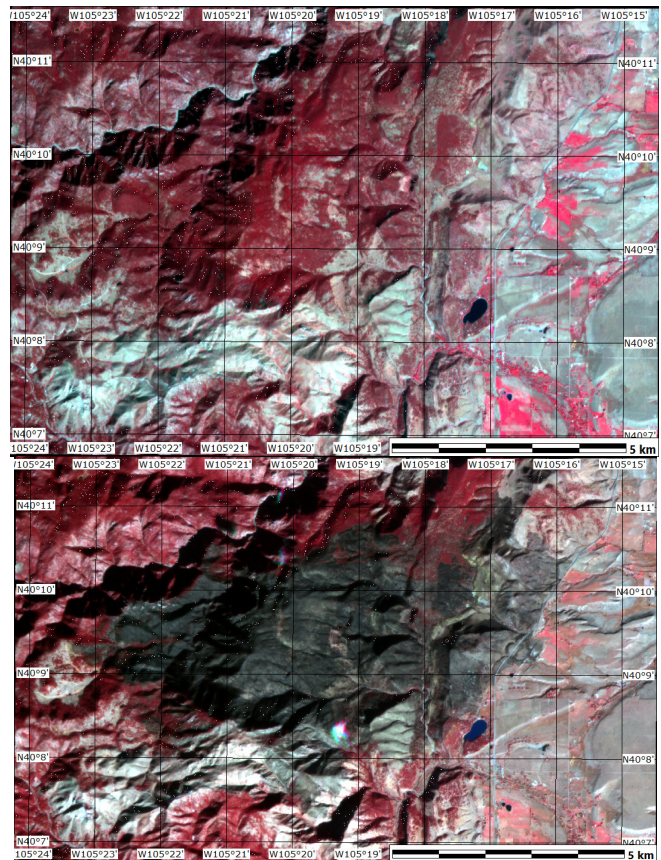


Figure 1. NIR images of the Calwood Fire burn area on 01 Oct 2020 (top) and 23 Nov 2020 (bottom). (Planet Imagery's Super Dove satellites with 3m resolution)

Over the two-year regrowth period the reduction in the high severity burn area goes from 38.4 km² in 2020, to 16.5 km² in 2021, and 4.3 km² in 2022 (Figure 3). The apparent unburned area actually decreases from 41.4 km² in 2021 to 17.7 km² in 2022 (fig. 4) which also happens with the moderate high severity burn and the unburned area from 2021 to 2022 (fig. 3). The reduction in the healed land areas as the land recovers could be a result of the bin sizes used to process the data and create the dNBRs or a less productive spring and summer and therefore less vegetation than the reference NBR in September 2020.

The areas of high severity burn in 2020 occur most prevalently in the center and western side of the area. The areas of lower severity burn in 2020 occur around the southern and eastern sides of the burn area (fig. 3a). The regrowth occurs faster in areas where the burning was less severe with few areas of high severity burn remaining in the western half of the burn area by 2022.

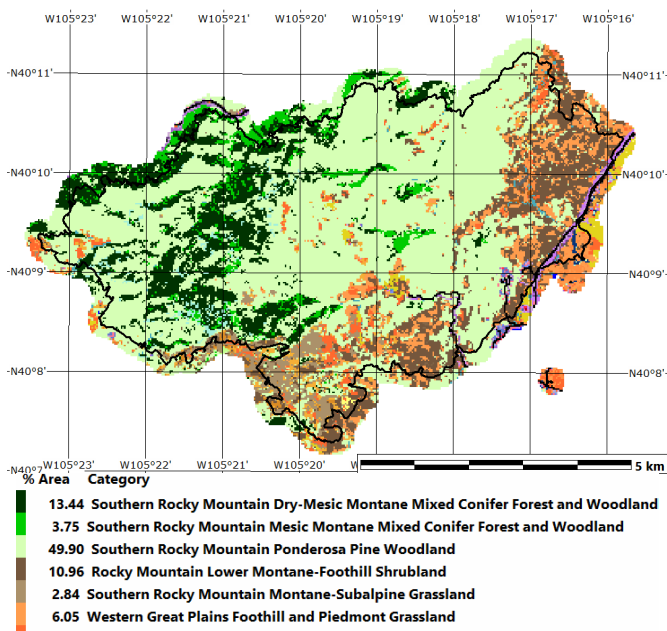


Figure 2. LandFire 2020 existing vegetation with categories over 2% labelled.

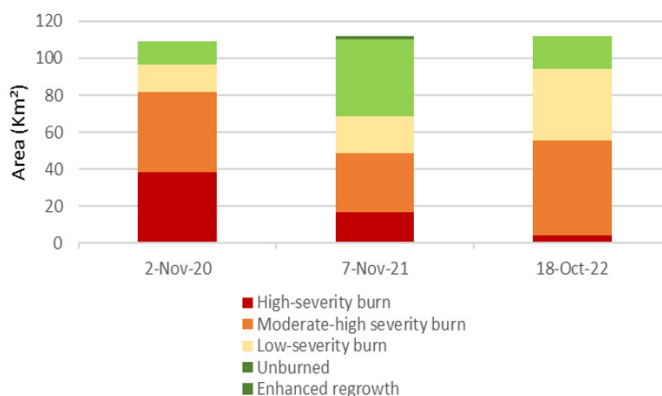


Figure 3. Calculated burn area and recovery in km² from dNBR maps in Figure 4.

The elevation of the area is higher in the west with values around 2600m and lower in the east with values closer to 1800m (fig. 5A). The Colorado flatirons lie in the areas of lower elevation in the east (fig. 5A). The roughness identifies the location of prominent ridges and valleys throughout the burn area, the majority of which fall in the western half of the area

(fig. 5C). The highest roughness values are around 25% and are located along the valleys between the mountains in the western section of the burn area and just north of where the fire originated (fig. 1 and 5C).

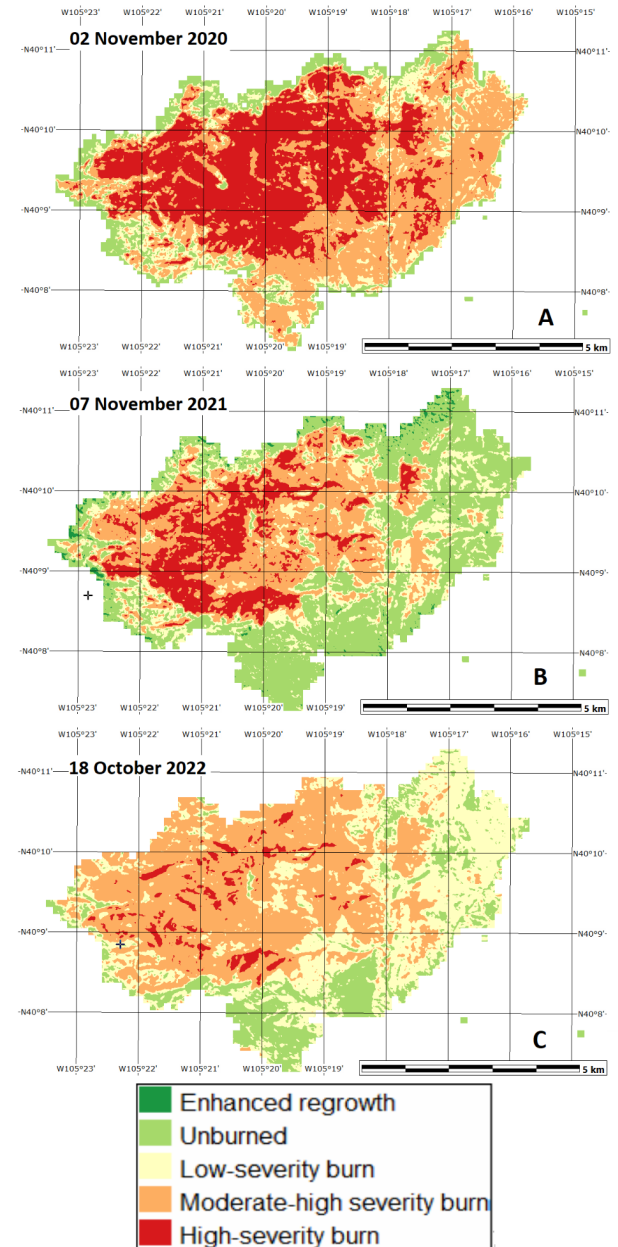


Figure 4. dNBRs created from Sentinel-2 images. All images were subtracted from an NBR of the area from 28 September, 2020.

Figure 6 shows the geomorphometric characteristics of the burn and recovery areas immediately after the fire and the next two years. The elevation data show very little difference between the categories in 2020 when the fire burned; the areas of high severity burn averaging to 2183.2m and the unburned areas averaging to 2148.8m. In 2022 after almost two years of regrowth the average elevations get further from each other with the remaining areas of high severity burn averaging 2250.7 m, the areas of low severity burn averaging 1990.6m and unburned areas averaging 2025m. Aspect shows that the strong peaks with easterly aspect (Figure 6) corresponding with the preferred habitat of the Ponderosa Pines (Figure 7).

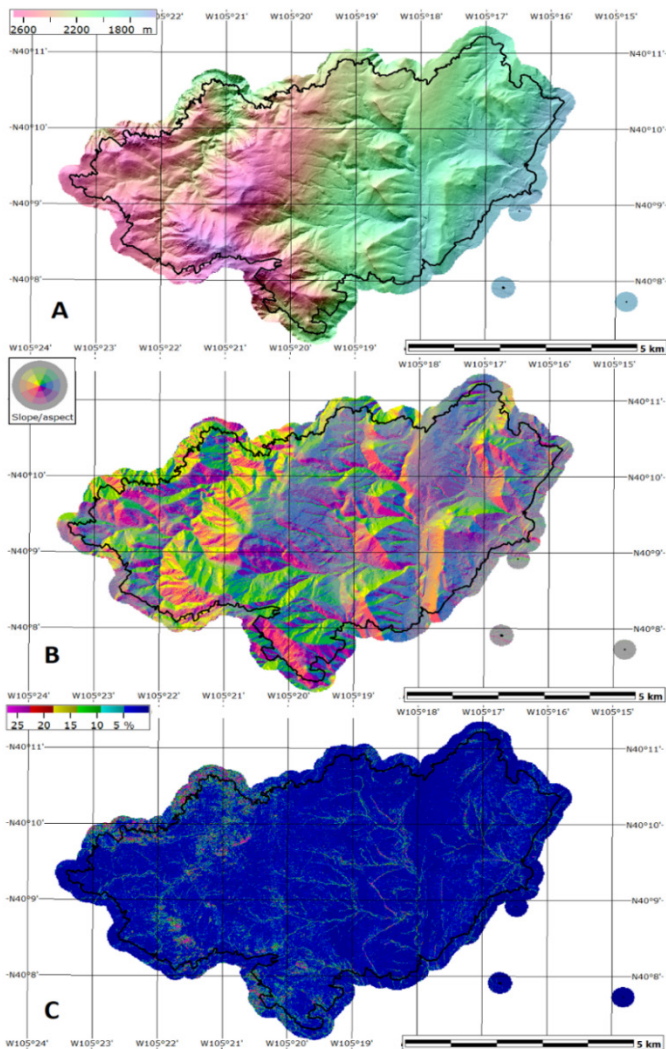


Figure 5. USGS 3DEP DTM data: (A) hillshade, (B) combined aspect and slope, (C) roughness computed from standard deviation of slope in a 3×3 window.

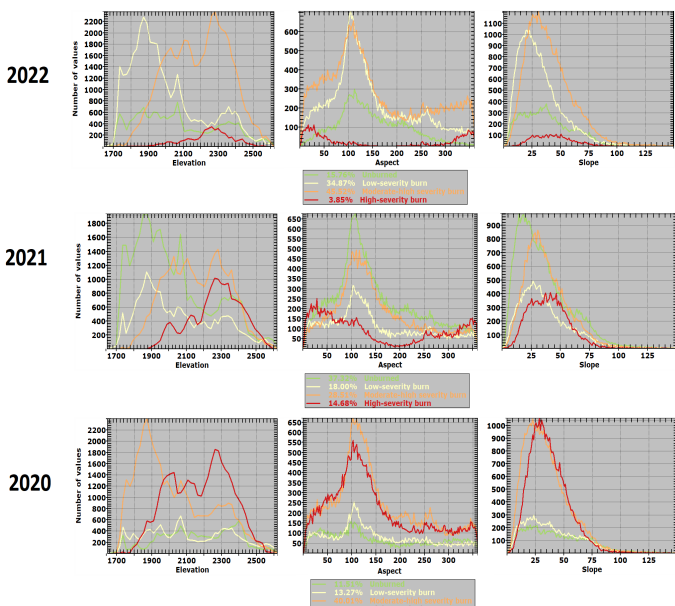


Figure 6. Elevation, slope and aspect histograms for the post fire dNBRs for four categories describing the areas of high severity burn, moderate high severity burn, low severity burn, and unburned.

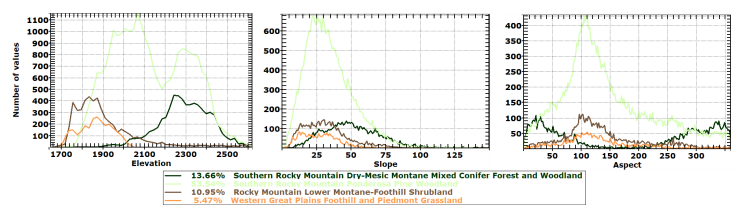


Figure 7. Elevation, slope and aspect histograms for the vegetation types found in the burn area in 2020 (from Landfire EVT).

The slope data shows lower slopes in the more severely burned categories in 2020 (37.3% and 35.57%), 41.7% in areas of low severity burn, and 45.3% in the unburned areas. In 2022 the slope values of the high severity burn areas averaged to 44.5% and the unburned areas 39.78%. The roughness of the area affected the severity of the burning similarly to the slope in 2020: high severity 3.95% and unburned 6.3%. As the two years passed the range lessened and in 2022 the roughness values vary less; high severity burn averaging 4.1% and the unburned averaging 4.9%, so the rougher areas recovered.

IV. DISCUSSION AND CONCLUSIONS

Vegetation type had the most effect on the burn severity of the Calwood Fire. The ponderosa pines and southern Rocky Mountain dry-mesic montane mixed conifer forest covered a large majority of the area and sustained the highest severity burns (fig. 2 and 4). The dry-mesic montane conifer forests grew on the uphill slopes and remained the most severely burned in 2022 (fig 2, 3, and 4). Both types of trees are most susceptible to burning in the spring and fall when their needles are the driest, with the Calwood Fire in October 2020.

The shrub and grasslands sustained less severe fire damage and regenerated more quickly than the forested area. The vegetation regrowth was observed in the dNBRs however these do not identify the type of vegetation that has returned to the highly burned areas and is not an indicator of the health of the ponderosa pine forests. The early regrowth could be grasses and; restoration efforts in the Calwood burn scar have already begun in an effort to replenish the ponderosa pines [1].

The analysis of the burn severity in the dNBRs when linked to the elevation, slope, and roughness maps allows consideration for the relationship between the factors. Elevation had little effect during the initial burn, and the lower elevation areas regrew faster. The areas of lower elevation were able to recover more quickly than those of higher elevation, likely because the grasses that inhabit the lower elevation areas can regrow faster than the trees found at the higher elevations.

Initially areas of lower average slope were more severely burned than areas of higher average slope but regrowth occurred faster in areas of lower average elevation. The fire was likely able to spread easier through the forest in areas where the trees were on even ground and their flammable foliage was at the same height. Additionally, it is likely that there was less vegetation on the areas of higher slope even before the fire as the conditions are more competitive [7]. On slopes the fire would have had a harder time jumping from tree to tree. During regrowth it was likely easier for the vegetation to regrow in flatter areas of less stress where there was less erosion or chance of landslides [7].

The roughness data in 2020 from the initial fire shows that the areas of higher burn severity had much lower roughness. The areas with lower roughness were affected more greatly during the initial burn than the areas with larger roughness. When the

data from 2022 is considered there is virtually no difference in the average roughness showing that it has little to no effect on the regrowth of vegetation.

V. ACKNOWLEDGMENTS

We thank Planet imagery for their satellite data. This project would not have been possible without discussions with MIDN 1/C Charles Dunn. All data was processed using MICRODEM [8].

REFERENCES

- [1] Pineda, Mykael, 2022, [Regeneration of Ponderosa pine within the Southern Rocky Mountains](#).
- [2] Cal-wood Education Center, The Calwood Fire: <https://www.calwood.org/about-the-fire>, accessed 9 December 2022.
- [3] Landfire, LANDFIRE, Existing Vegetation Type: <https://landfire.gov/evt.php>, accessed 9 December 2022.
- [4] USGS, Landsat Normalized Burn Ratio 2: <https://www.usgs.gov/landsat-missions/landsat-normalized-burn-ratio-2>, accessed 9 December 2022.
- [5] Brewer, C.A. and Marlow, K.A., 1993, Color Representation of Aspect and Slope Simultaneously, in Proceedings, Eleventh International Symposium on Computer-Assisted Cartography (Auto-Carto-11), Minneapolis, October/November 1993, pp. 328-337.
- [6] Grohmann, C. H., Smith M. J., and Riccomini, C, 2011, Multiscale Analysis of Topographic Surface Roughness in the Midland Valley, Scotland, *IEEE Transactions on Geoscience and Remote Sensing*, vol. 49, no. 4, pp. 1200-1213.
- [7] Arianoutsou, M., Koukoulas, S. & Kazanis, D., 2011, Evaluating Post-Fire Forest Resilience Using GIS and Multi-Criteria Analysis: An Example from Cape Sounion National Park, Greece. *Environmental Management* 47, 384-397. <https://doi.org/10.1007/s00267-011-9614-7>.
- [8] Guth, P.L., 2009, Geomorphometry in MICRODEM, In Hengl, T., Reuter, H.I. (eds), *Geomorphometry: concepts, software, applications*. Developments in Soil Science Series, Elsevier, ISBN-13: 978-0-12-374345-9, p.351-366.

Machine learning classification of geomorphometric segments for floodplain detection and delineation

Nicușor Necula
 Tulnici Research Station
 Alexandru Ioan Cuza University of Iași
 Iași, Romania
nicusor.necula@uaic.ro

Mihai Niculiță
 Department of Geography
 Alexandru Ioan Cuza University of Iași
 Iași, Romania
mihai.niculita@uaic.ro

Abstract—We propose a floodplain detection and delineation workflow based on the Copernicus DEM. It involves watershed segmentation of slope and a machine learning algorithm – Multilayer Perceptron (MLP) model, for the geomorphometrical variables of the segments. For the method's accuracy, spatially separated training and testing areas were used to assess the generalization power. Seven classes of landforms were labeled to allow the MLP model to statistically identify the flat floodplain class in the feature space compared to the adjacent channels, hillslopes, and levees. The confusion matrix data shows good generalization power with 94% accuracy for the floodplain class detection. The results show promising perspectives to solve the problem of quaternary deposits mapping and flood risk assessment.

I. INTRODUCTION

Floodplains and their morphology, including river channels and fluvial terraces, are important landforms with practical implications from many perspectives: quaternary geology/geomorphological mapping, flood risks, and planning.

The availability of a medium-resolution Digital Elevation Model (DEM) like Copernicus DEM opens up the possibility of delineating channels and floodplains with better accuracy than with SRTM or other similar DEMs.

We used a machine learning approach to classify the floodplain slope segments. Specifically, we used Multilayer Perceptron (MLP), a feedforward artificial neural network (ANN) algorithm that relies on changing the weights of the morphometric variables after each process to determine the landform type based on the amount of error in the output compared to the expected result.

II. MATERIAL AND METHODS

A. Materials

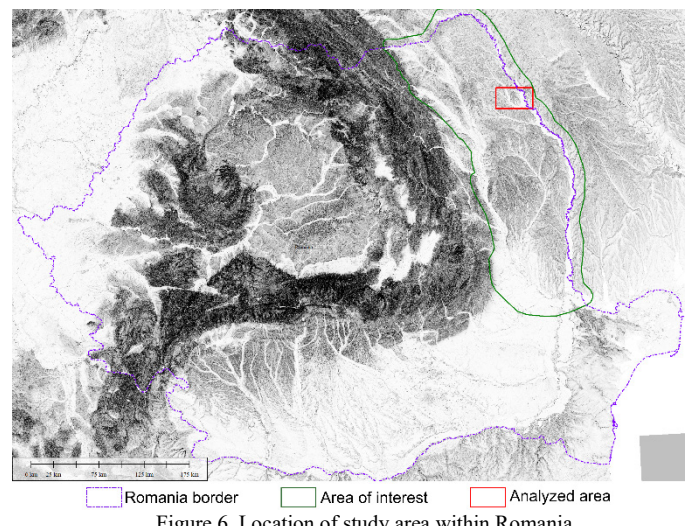
The DEM used for testing the proposed approach is a crop of the worldwide Copernicus DEM (GLO30), which was resampled to a 20 m resolution in EPSG: 3844 projection for the Eastern part of Romania (Fig. 1). The 20 m resolution is a natural choice since the pixel size in EPSG: 4326 projection is roughly

a rectangle of 60 by 20 meters at the latitude and longitude of Romania. The choice of the study area is related to the low forest coverage.

Since the elevation data comes from radar measurements, the landform shape in non-vegetated areas is well-constrained. The Copernicus DEM has low noise in flat areas and excellent precision, similar to LiDAR data (Fig. 2). At the 20 m spatial resolution, the channel and floodplain of rivers up to the third Strahler order are recognizable.

B. Methods

The segments used to delineate the landforms in the study area were generated by the watershed segmentation in SAGA GIS [1]. ViGRA implementation [2] in SAGA GIS was used on



the slope morphometrical variable. This approach generates segments that adequately describe the landforms by producing sharp boundaries between hillslopes and channels/floodplains (Fig. 3). Segments cover well even the burial mounds and levees.

For reference to estimate the accuracy of the approach, we have classified the segments into seven classes: channels, floodplains, gentle and steep hillslopes, plateaus, terraces, and

ridges (Fig. 4). We excluded the areas where there is forest cover or edited reservoir mask (non-colored areas in Fig. 4).

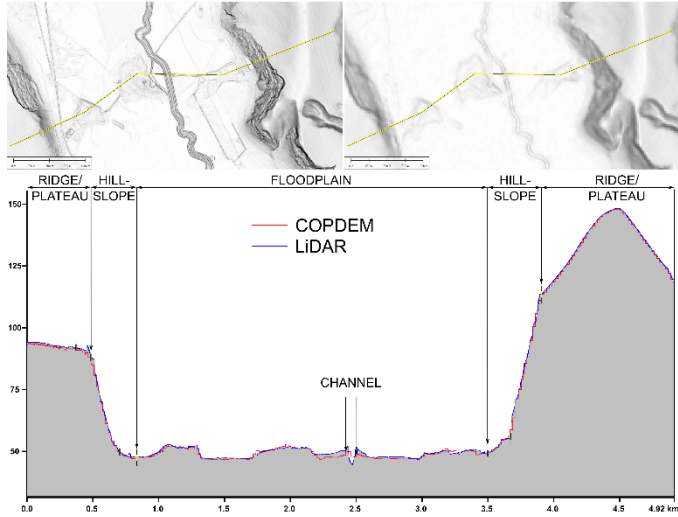


Figure 7. Topographic cross-section through the Jijia floodplain (bottom) and the LiDAR (top left) and COPDEM (top right) data associated with it.

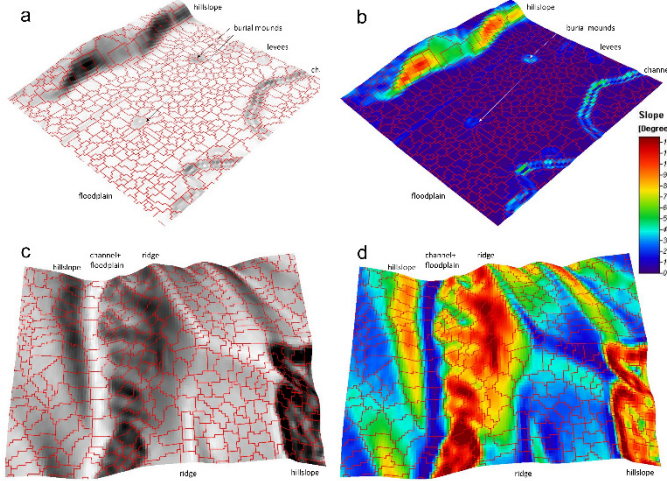


Figure 8. Examples of watershed slope segmentation results overlayed on the shaded dem (a,c) or slope (b,d) for a floodplain sector (a,b) and a hillslope sector (c, d).

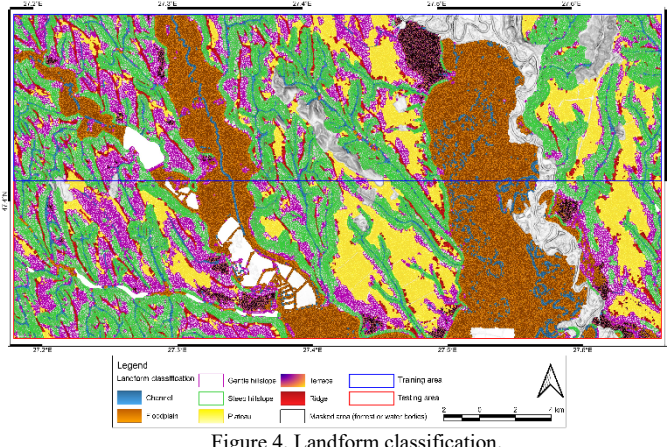


Figure 4. Landform classification.

For the segments, descriptive statistics (minimum, maximum, mean, range, variance, standard deviation) of various geomorphometric variables (elevation, index of convergence, openness, slope, full set of curvatures, flow length measures, TWI, texture, roughness, altitude relative to local channels) were generated to train a neural network, specifically Multilayer Perceptron (MLP). MLP is a deep feedforward neural network/multilayer perceptron method that uses the neuron

model, of acyclic networks, in layers that use connected functions as vector nodes to fit linear functions for an overall non-linear classification or regression. R stat [3] and kerasR package [4,5] were used for the MLP implementation.

In Figure 5, we show by color the landforms class in the statistic space defined by the mean values of segment slope and flow path length. It can be observed that floodplains and gentle and steep slopes have an excellent definition in the feature space, while the other landforms classes spread all over. This situation reflects the geomorphometric characteristics of the segmentation: channel segments also spread on the bottom of the hillslopes, while the plateaus and ridges spread on the hillslope's upper part.

In order to test the generalization power of the MLP model, we split the study area into two rectangular parts, the northern one for training and the southern one for testing.

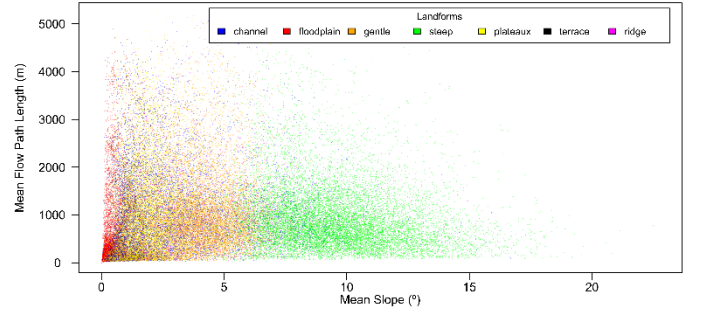


Figure 5. Landform distribution in the statistical space of mean flow path length and mean slope of the segments.

III. RESULTS

The results of the MLP fitting show that with at least 50 epochs, the accuracy is relatively stable (Fig. 6). Similar results are obtained while tuning various parameters of the MLP.

The confusion matrices and their statistics (Tables I-IV) show a good power of generalization, especially for floodplains, gentle and steep hillslopes, and plateaus and ridges. Channels and terraces are the landform types that show the lowest.

The true positive of floodplain class segments (Fig. 7) covers the floodplains in the study area very well. Looking at the false positives and false negatives of the floodplain class (Fig. 7), which is the one that interests us, it can be observed that these segments either are scattered and can be easily filtered, or they are well-delineated from the floodplain and again can be easily identified and eventually filtered.

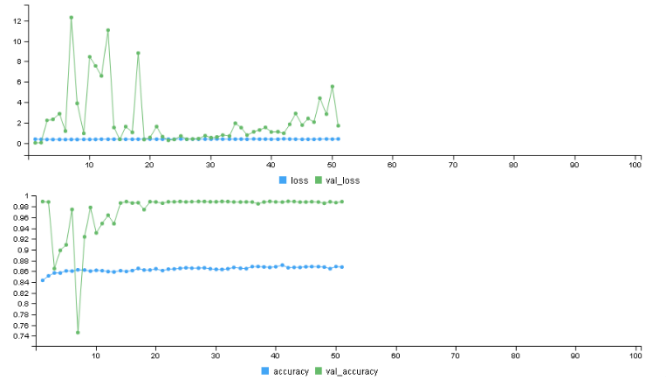


Figure 9. Line plots of learning curves for the MLP model: cross-entropy loss (top), classification accuracy (bottom).

TABLE I. CONFUSION MATRIX OF THE TRAINING AREA.

Predicted Landforms	Reference Landforms						
	C	F	G	S	P	T	R
C	2585	65	199	140	1 ^a	4	13
F	1238	10383	399	4	0	24	0
G	83	10	3789	694	621	110	50
S	82	0	37	11014	1	0	27
P	3	0	561	12	3972	7	52
T	25	0	100	2	19	1210	0
R	1	0	311	142	676	9	957

C – channels, F – floodplains, G – gentle hillslopes, S – steep hillslopes, P – plateaus, T – terraces, R – ridges

TABLE II. CONFUSION MATRIX FOR THE TESTING AREA.

Prediction	Landforms						
	C	F	G	S	P	T	R
C	2656	96	212	48	17	27	31
F	1643	9286	870	11	16	346	0
G	138	9	4545	648	670	321	75
S	134	0	58	8431	2	0	31
P	27	0	537	5	5395	430	69
T	3	1	198	0	204	812	1
R	37	0	159	39	471	99	773

C – channels, F – floodplains, G – gentle hillslopes, S – steep hillslopes, P – plateaus, T – terraces, R - ridges

TABLE III. STATISTICS OF CONFUSION MATRIX IN THE TRAINING AREA.

	Landforms						
	C	F	G	S	P	T	R
Sensitivity	0.64	0.99	0.70	0.92	0.75	0.89	0.87
Specificity	0.99	0.94	0.95	0.99	0.98	0.97	0.97
Pos Pred Value	0.86	0.86	0.71	0.99	0.86	0.89	0.46
Neg Pred Value	0.96	0.99	0.95	0.97	0.96	0.99	0.99
Prevalence	0.10	0.26	0.14	0.30	0.13	0.03	0.03
Detection Rate	0.07	0.26	0.1	0.28	0.1	0.03	0.02
Detection Prevalence	0.08	0.30	0.14	0.28	0.11	0.03	0.05
Balanced Accuracy	0.82	0.97	0.83	0.96	0.87	0.94	0.92

C – channels, F – floodplains, G – gentle hillslopes, S – steep hillslopes, P – plateaus, T – terraces, R – ridges

TABLE IV. STATISTICS OF CONFUSION MATRIX IN THE TESTING AREA.

	Landforms						
	C	F	G	S	P	T	R
Sensitivity	0.57	0.99	0.70	0.92	0.80	0.40	0.79
Specificity	0.99	0.90	0.94	0.99	0.97	0.99	0.98
Pos Pred Value	0.86	0.76	0.71	0.97	0.83	0.67	0.49
Neg Pred Value	0.95	0.99	0.94	0.98	0.96	0.97	0.99
Prevalence	0.12	0.24	0.17	0.23	0.17	0.05	0.02
Detection Rate	0.07	0.023	0.11	0.21	0.14	0.02	0.02
Detection Prevalence	0.08	0.31	0.16	0.22	0.16	0.03	0.04

	Landforms						
	C	F	G	S	P	T	R
Balanced Accuracy	0.78	0.95	0.82	0.96	0.88	0.70	0.88

a. C – channels, F – floodplains, G – gentle hillslopes, S – steep hillslopes, P – plateaus, T – terraces, R – ridges

IV. DISCUSSIONS

The main objective of this research approach is detecting and delineating floodplain areas from medium-resolution DEMs on large areas. The proposed method is to use segments in order to have crisp borders for the delineation. The watershed segmentation of the slope delineates very well the border between the flat floodplain and the adjacent hillslopes and the levees inside the floodplain. A wide range of geomorphometrical variables are used as input for training an MLP model, and the results are good enough for this research stage. More variables could be tested in a tuning approach, and some class accuracy might be improved. Although terraces are well delineated from the floodplains, some terrace levels are still mapped as floodplains. These issues will be solved in the next steps of the analysis, during which the results will be used to derive the extension of the floodplain through merging and filtering.

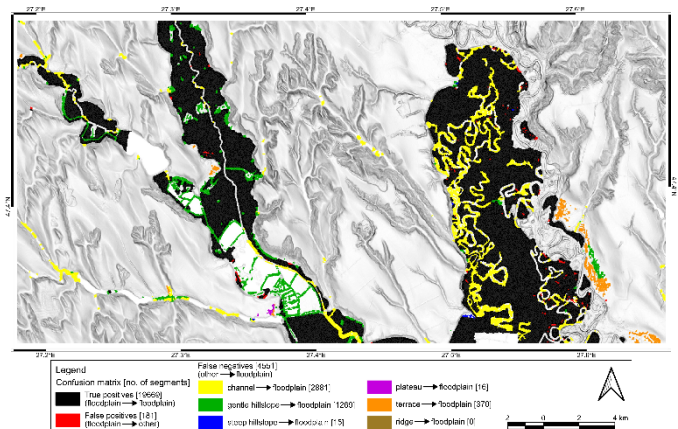


Figure 10. Predicted floodplain class according to the confusion matrix categories (False positives and false negatives).

V. CONCLUSIONS

The proposed approach of machine learning classification of landform segments proved helpful in detecting and delineating some landform types. Not all the landform types have the same accuracy, but using them allows the model to discriminate them geomorphometrically and better describe the other classes. This case is specific to floodplains and channels, which are very well-identified and can be easily delineated by simply merging and filtering polygon islands or visual inspection. Also, the delineation accuracy between floodplain and hillslope segments is well-defined.

Considering the Quaternary age of the floodplains and terraces, with most of the floodplains dating as Holocene, their geomorphometric delineation can be used as the base of their mapping. Geologic maps can be updated to incorporate this information to characterize Quaternary deposits better. As dating information improves and significantly better geological or geophysical data piles up, surface landform delineation will also be essential for the depth and volume prediction of these deposits.

VI. ACKNOWLEDGMENTS

Nicușor Necula has used the computational facilities given by the infrastructure support from the Operational Program Competitiveness 2014–2020, Axis 1, under POC/448/1/1 Research infrastructure projects for public R&D institutions/Sections F 2018, through the Research Center with Integrated Techniques for Atmospheric Aerosol Investigation in Romania (RECENT AIR) project, under grant agreement MySMIS no. 12732.

REFERENCES

- [1] Conrad, O., Bechtel, B., Bock, M., Dietrich, H., Fischer, E., Gerlitz, L., Wehberg, J., Wichmann, V., and Böhner, J. (2015): System for Automated Geoscientific Analyses (SAGA) v. 2.1.4, Geosci. Model Dev., 8, 1991–2007, doi:10.5194/gmd-8-1991-2015
- [2] Köthe U., 1999, “Reusable Software in Computer Vision” in B. Jähne, H. Haußecker and P. Geißler, Handbook of Computer Vision and Applications. Academic Press, 103-132.
- [3] R Core Team (2022). R: A language and environment for statistical computing. R Foundation for Statistical Computing, Vienna, Austria. <https://www.R-project.org/>.
- [4] Chollet F., & others. (2023). Keras. Github. Retrieved from <https://github.com/fchollet/keras>
- [5] Chollet F., Allaire JJ & others. (2023). R Interface to Keras. Github. <https://github.com/rstudio/keras>

Super-resolution for terrain modeling using deep learning in High Mountain Asia

Xiong Liyang

Key Laboratory of Virtual Geographic Environment, Ministry of Education Nanjing Normal University Nanjing, China
xiongliyang@njnu.edu.cn

Jiang Yinghui

Key Laboratory of Virtual Geographic Environment, Ministry of Education Nanjing Normal University Nanjing, China
jiangyinghui@njnu.edu.cn

Li Sijin

Key Laboratory of Virtual Geographic Environment, Ministry of Education Nanjing Normal University Nanjing, China
sijin.li@njnu.edu.cn

Abstract— High Mountain Asia (HMA) has the most complex and rugged terrain in the world. However, the high-resolution terrain data in HMA is not easy to acquire. A modified super-resolution residual network in the study is trained, in order to develop super-resolution DEMs in the HMA. Limited high resolution (HR) DEMs from other areas and freely available DEM data from the HMA is used to train the model. We constructed a new loss function which constrains the network learning and convergence by using the terrain parameters of slope and curvature. A comparative analysis between the proposed method and existing methods was conducted. The results demonstrate that MSRResNet can achieve highly accurate terrain data in the process of downscaling DEMs in HMA.

I. INTRODUCTION

Terrain is a key component in the processes that occur at the landscape [1]. The High Mountain Asia (HMA) area should be given more attention, which is characterized by some of the most complex and highest terrain conditions in the world. Digital elevation models (DEMs) are widely used to represent terrain [2]. In HMA areas, the popular DEMs used is usually global free access elevation data, such as ASTER GDEM, SRTM [3-4], which are freely available with a resolution of 1 arc-second. However, higher resolution DEMs are still needed in this area, and many earth science studies require finer scale elevation data [5-6].

Deep learning (DL)-based methods have also been proposed for the development of super-resolution DEMs from existing elevation data. These studies transferred the frameworks of EDSR [7], SRGAN [8] and ESRGAN [9] from images to DEMs and then obtain the super-resolution DEMs. However, the DL methods mostly ignore terrain knowledge in the process of super-resolution. Terrain parameters are usually used to express terrain characteristics [10], and they can be divided into types, i.e., first- and second-order terrain parameters. Thus, the integration of DL and terrain parameters is promising for improving the accuracy of generated HR DEMs.

In this paper, a modified super-resolution residual network (MSRResNet) is trained to generate super-resolution DEMs in HMA areas. It uses freely available DEMs from HMA and limited HR DEMs from other regions. A new loss function is

constructed by considering the first-order and second-order terrain parameters in this network. We also compare the accuracies between the proposed method and existing super-resolution methods (i.e., the SRGAN deep learning method and the Bicubic spatial interpolation method) to assess the effectiveness of MSRResNet.

II. MATERIALS AND METHODS

A. Materials

HMA, which is a high-altitude mountain region in Central Asia [11-12], is selected as the study area. The Hengduan Mountains, having treacherous topography conditions in the southeastern HMA, is the test area. The huge differences in elevation of the Hengduan Mountains between river valleys and ridges make it one of the most complex areas of the HMA. The test area and study area are shown in Fig. 1. The detailed information of the experimental data is shown in Table 1. The scale factor is 8 for the super-resolution experiment, which means the experimental results in resolution achieve an eight-fold improvement.

B. Methods

The Flowchart of the DEM super-resolution framework in HMA is shown in Fig. 2. The loss function mainly consists of basic GAN loss, elevation loss, slope loss, curvature loss, and perceptual loss. Among them, elevation loss is the most common loss, and is pixel-based. Slope and curvature are commonly terrain parameters [13], and we transform the two parameters into MSRResNet losses. In addition, perceptual loss has the advantages in extracting high level detailed terrain knowledge. We added perceptual loss to help the network extract overall terrain knowledge.

III. RESULTS

A. Elevation

As shown in Table 2, MSRResNet outperforms the other methods in MAE, RMSE, PSNR, and SSIM from 120 m to 15 m. MSRResNet improves RMSE accuracy by 32.17% and

TABLE I. BASIC INFORMATION OF EXPERIMENTAL DATA

Data	Location	High-res DEM		Low-res DEM	
		Resolution	Data Source	Resolution	Data Source
Training Data	25° - 52.5°N , 70° - 105°E	30 m ^a	ASTER GDEM v3	240 m	90m SRTM DEM
	22° - 29°N , 106° - 117°E	30 m	ASTER GDEM v3	240 m	90m SRTM DEM
	34° - 40°N , 106° - 111°E	5 m	http://www.sxgis.cn/	40 m	30m ASTER GDEM v3
Testing Data	26° - 26.5°N , 98.9° - 99.5°E	15 m	ZY-3	120 m	90m SRTM DEM

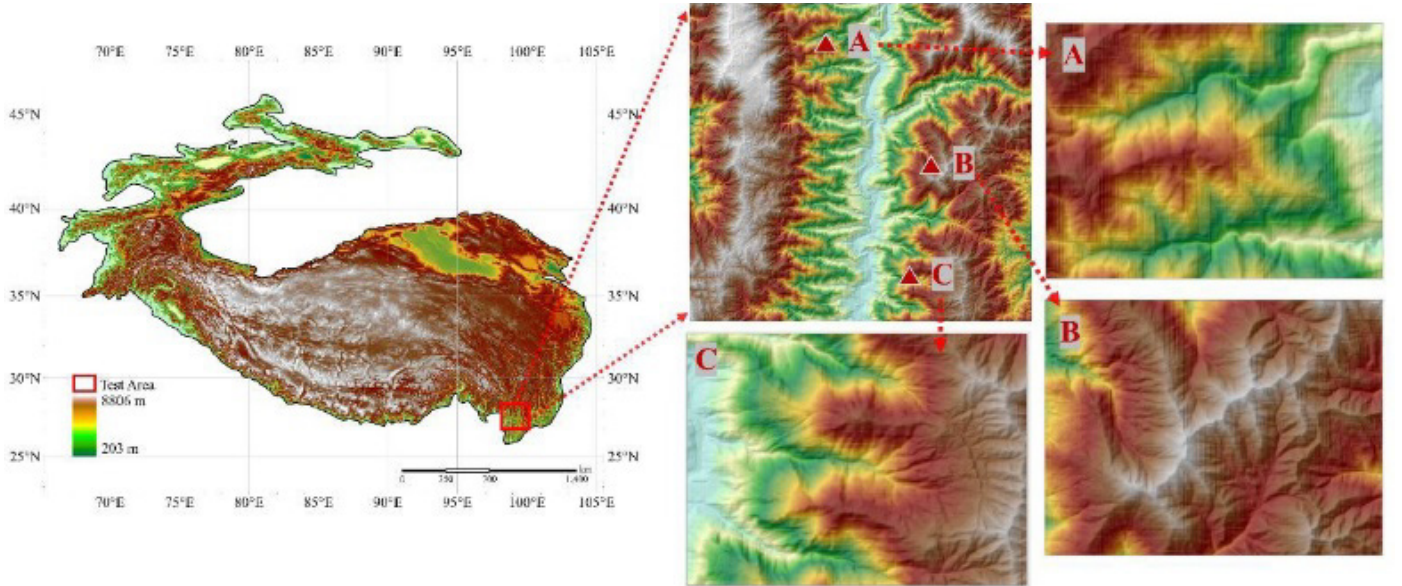


Figure 1. The study area in the Hengduan Mountains in HMA. The small areas represented by A, B, and C are used for evaluation.

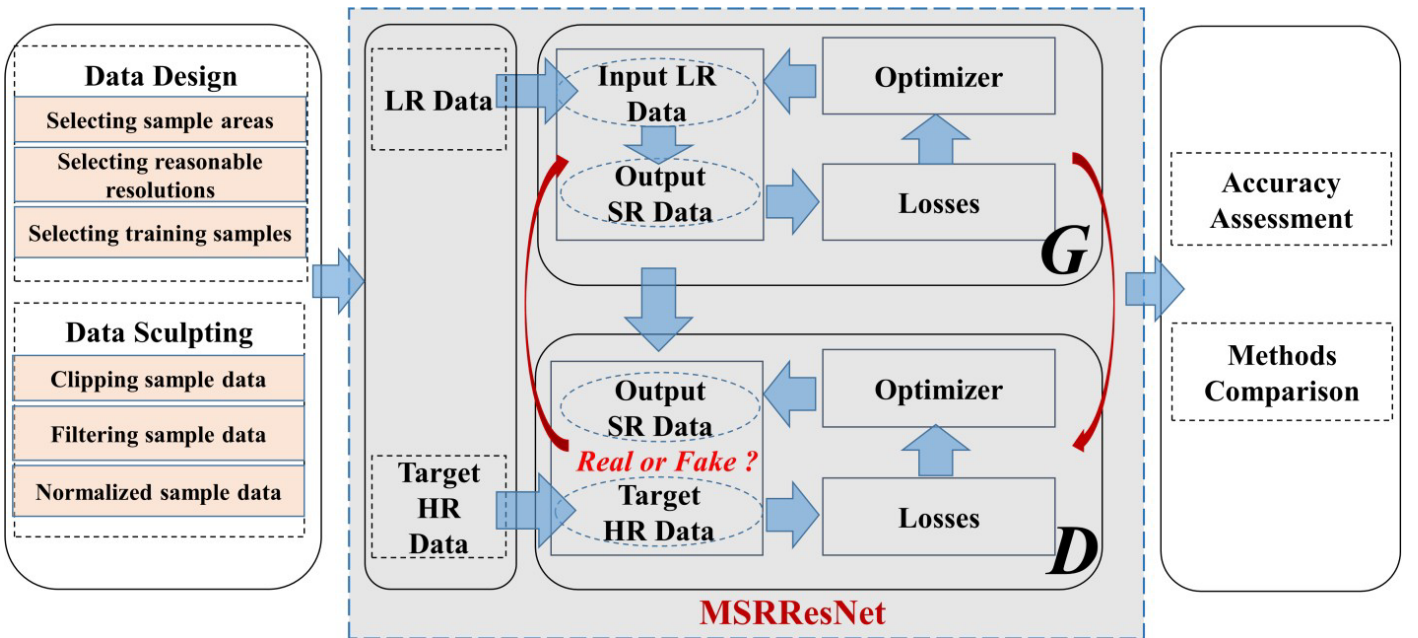


Figure 2. The flowchart for the DEM super resolution framework in HMA.

MAE accuracy by 33.97% compared with Bicubic. And it improves RMSE accuracy by 39.15% and MAE accuracy by 32.47% compared to SRGAN. Fig. 3 shows the DEMs produced by different methods. The results show that MSRResNet network achieves more detailed terrain features. And SRGAN and Bicubic show clear smoothing effects.

B. Slope

As shown in Fig. 4, the slope results by MSRResNet method appear close to those from the reference high resolution DEM. Many detailed terrain information can be found by our method.

C. Stream network

We also compared the stream networks generated by several reconstructed DEMs and experimentally proved that the stream networks generated by MSRResNet is the closest to the stream networks generated by the reference DEM.

TABLE II. ELEVATION ERROR EVALUATION WITH DIFFERENT METHODS.

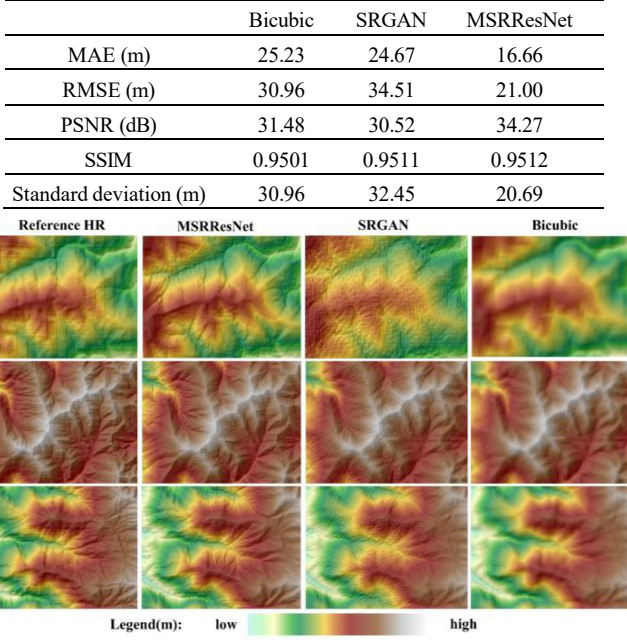


Figure 3. Comparison of reconstructed DEMs in areas A, B and C.

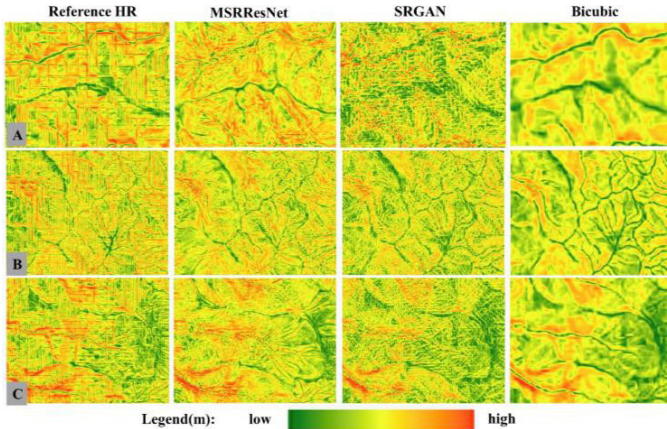


Figure 4. Surface slope by different methods in areas A, B and C.

IV. CONCLUSION

In this paper, a modified super-resolution residual network (MSRResNet) is trained to generate super-resolution DEMs in HMA areas. It uses freely available DEMs from HMA and limited HR DEMs from other regions. A new loss function is constructed by considering the first-order and second-order terrain parameters in this network. We also compare the accuracies between the proposed method and existing super-resolution methods (i.e., the SRGAN deep learning method and the Bicubic spatial interpolation method) to assess the effectiveness of MSRResNet. We can obtain 15m DEMs based on the freely available 30m DEMs in HMA region. In the future, the proposed super-resolution method can be applied to obtain

corresponding HR DEMs for other inaccessible regions to advance scientific researches.

V. ACKNOWLEDGMENT

This work was supported by the National Natural Science Foundation of China [grant number: No. 41971333, No. 41930102] and the Priority Academic Program Development of Jiangsu Higher Education Institutions.

REFERENCES

- [1] Xiong, L., Li, S., Tang, G., Strobl, J., 2022. Geomorphometry and terrain analysis: Data, methods, platforms and applications. *Earth-Science Reviews*. 104191.
- [2] Wang, B., Shi, W., Liu, E., 2015. Robust methods for assessing the accuracy of linear interpolated DEM. *International journal of applied earth observation and geoinformation*. 34, 198-206.
- [3] Lehner, S., Pleskachevsky, A., Velotto, D., Jacobsen, S., 2013. Meteorological Parameters and Their Variability: Observed by High-Resolution Satellite Radar Images. *Oceanography*, 26(2), pp.80-91.
- [4] Mukherjee, S., Joshi, P.K., Mukherjee, S., Ghosh, A., Garg, R.D., Mukhopadhyay, A., 2013. Evaluation of vertical accuracy of open source Digital Elevation Model (DEM). *International Journal of Applied Earth Observation and Geoinformation*. 21, 205-217.
- [5] Atwood, A., West, A.J., 2022. Evaluation of high-resolution DEMs from satellite imagery for geomorphic applications: A case study using the SETSM algorithm. *Earth Surface Processes and Landforms*. 47(3), 706-722.
- [6] Zhou, X., Xue, B., Xue, Y., Xie, X., Yang, J., Qin, K., 2021. An Exploratory Evaluation of Multiscale Data Analysis for Landform Element Detection on High-Resolution DEM. *IEEE Geoscience and Remote Sensing Letters*. 19, 1-5.
- [7] Zhou, A., Chen, Y., Wilson, J.P., Su, H., Xiong, Z., Cheng, Q., 2021. An Enhanced Double-Filter Deep Residual Neural Network for Generating Super Resolution DEMs. *Remote Sensing*. 13(16), 3089.
- [8] Chen, Z., Wang, X., Xu, Z., 2016. Convolutional neural network based DEM super resolution. *International Archives of the Photogrammetry, Remote Sensing & Spatial Information Sciences*. 41.
- [9] Wang, X., Yu, K., Wu, S., Gu, J., Liu, Y., Dong, C., Qiao, Y., Change Loy, C., 2018. Esrgan: Enhanced super-resolution generative adversarial networks, In: Proceedings of the European conference on computer vision (ECCV) workshops. pp. 0-0.
- [10] Shary, P.A., Sharaya, L.S., Mitusov, A.V., 2005. The problem of scale-specific and scale-free approaches in geomorphometry. *Geografia Fisica e Dinamica Quaternaria*. 28(1), 81-101.
- [11] Ding, L., Zhou, J., Zhang, X., Liu, S., Cao, R., 2018. Downscaling of surface air temperature over the Tibetan Plateau based on DEM. *International Journal of Applied Earth Observation and Geoinformation*. 73, 136-147.
- [12] Su, Z., Xiong, D., Zhang, J., Zhou, T., Yang, H., Dong, Y., Fang, H., Shi, L., 2019. Variation in the vertical zonality of erodibility and critical shear stress of rill erosion in China's Hengduan Mountains. *Earth Surface Processes and Landforms*. 44(1), 88-97.
- [13] Deng, Y., Wilson, J.P., Bauer, B.O., 2007. DEM resolution dependencies of terrain attributes across a landscape. *International Journal of Geographical Information Science*. 21(2), 187-213.

A Simply Updatable Cloud-based Ensemble Digital Terrain Model

Yu-Feng Ho, Tomislav Hengl and Leandro Parente

OpenGeoHub

Wageningen, Netherlands

yu-feng.ho@opengeohub.org, tom.hengl@opengeohub.org, leandro.parente@opengeohub.org

Abstract— A wide range of global public topography datasets circulates to service for various purposes. However, the variety of versions, sources, and formats can confuse users and lead to decrease of usage. Users typically require a single terrain model that can be used to produce morphometric and hydrographic terrain variables across borders. An Ensemble Digital Terrain Model (EDTM) by deriving from global public elevation maps and national DTMs, serves as a simply updatable and inclusive map. To further increase the usability, the concept of Analysis-Ready Cloud Optimized (ACRO) on the basis of cloud optimized GeoTIFF (COG) is adopted. ACRO optimizes accessibility by its pyramid structure of overviews and provides data preprocessing and reformatting in an open source, well-documented and reproducible workflow. EDTM aims to reduce the complexity of global elevation datasets and make the data more usable.

I. INTRODUCTION

In recent years a number of global public topography datasets at high spatial resolutions (30 m) have been released including GLO-30 and ALOS AW3D, and that is on top of the existing NASADEM, ASTER DEM, MERIT DEM and similar.

Land-use planners, hydrologists, geomorphologists and a wide range of public and private sectors rely on a digital elevation map in their workflow. However, too many versions, sources, and formats can often confuse users and decrease the usability of each data. In addition, most DEMs produced from remote sensing observations are only surface models requiring removal of canopy and similar objects. Users typically require a single (most current, most accurate, most complete) terrain model that can then be used to produce morphometric and hydrographic terrain variables across borders [1-2].

Accessibility, huge data volume, non-standardized format, too many portals and platforms, and data discovery are five biggest challenges when it comes to open big earth data [3]. Cloud optimized GeoTIFF (COG) targets web-optimized access to raster data, having a pyramid structure of overviews based on tiles. This characteristic allows clients to retrieve the data by allocating to the suitable overview and loading sufficient tiles for visualization [4]. Upon COG, Analysis-Ready Cloud Optimized (ACRO) is the next generation of big earth data, providing data with preprocessing and reformatting, in order to lift the burden of environmental scientists. Furthermore, an open source, well-documented and reproducible workflow is required, so as users evaluate the suitability for their particular analytic task [5].

To help reduce the complexity of global elevation datasets and make the data more usable. We collect global public topography datasets (GLO-30, ALOS AW3D, and MERIT DEM) and nation DTMs (NDTMs), and create a multipurpose Ensemble DTM (EDTM) for the world. Furthermore, the ensemble map is simply updatable, inclusive, and in ACRO.

II. ENSEMBLE TERRAIN MODEL IN 30 M (EDTM30)

A. Concept

Although terrain can be estimated using ICESat / GEDI points as reference training data, we adopt a more simple procedure for building a DTM that allows for faster updates and easy additions of new data: using lower 10% probability quantile. Advantage of having an inexpensive setup to update Ensemble DTM (EDTM30) is that we could possibly run nightly updates, as soon as countries or regions submit locally produced terrain models.

Considering that terrain heights are at the lower part of the distribution, we simply derive a 10% lower quantile from multi source data (Figure 1). We assume that, because canopy is difficult to remove and still remains even in MERIT DEM and FABDEM [6], deriving 10% lower quantile can further help filter out potential canopy remains. The global public datasets and NDTMs are listed in Table I.

B. Methodology

To be computational efficiency, the process is run as the flow chart above, with tile by tile (1,000 x 1,000 pixels). In summary the process works as follows: firstly standard deviation (s.d.) is derived using the list of DEMs (new map). For GLO-30, ALOS, all pixels where s.d. values are greater than 6 m (60 dm) and/or where canopy height is greater than 2m are removed [7]. Subsequently, a lower 10% quantile is derived from GLO-30, ALOS AW3D, MERIT DEM, and NDTMs. Finally, the standard deviation among all maps is derived and used as the uncertainty map.

The process of deriving the estimate is fully documented and automated in Python script (https://github.com/openlandmap/spatial-layers/blob/main/EDTM/ensemble_dtm.ipynb). The generation of an EDTM takes 5 hours running on a fully parallelized high performance computing center (HPC) with Common Component Architecture (CCA) 1050 threads under the

framework of Slurm. However, final mosaic of the world is a massive ~200GB dataset and takes about 3 days to compile a COG using GDAL (<https://gdal.org>).

III. RESULT

Two output layers are produced as ARCO GeoTIFF, which are (1) EDTM in meter, and (2) standard deviation, showing biggest discrepancies between ALOS AW3D, GLO-30, MERIT DEM, and national DTMs.

To access this dataset seamlessly, the global mosaic to COG files are uploaded to S3 repository. Data are hosted accordingly:

- (1) EDTM in meter, (https://s3.eu-central-1.wasabisys.com/openlandmap/dtm/dtm.bareearth_ensemble_p10_30m_s_2018_go_epsg4326_v202_30221.tif), and (2) standard deviation (https://s3.eu-central-1.wasabisys.com/openlandmap/dtm/dtm.bareearth_ensemble_s1d_30m_s_2018_go_epsg4326_v2023_0221.tif).

A demonstration of the maps used and the results obtained (EDTM) is shown in Figure 2. Masked out areas are mainly hills and mountains, and the uncertainty in these areas is also higher. It indicates that the difference in elevation at mountainous regions is significant among DEMs. Figure 3 illustrates the overview of global EDTM.

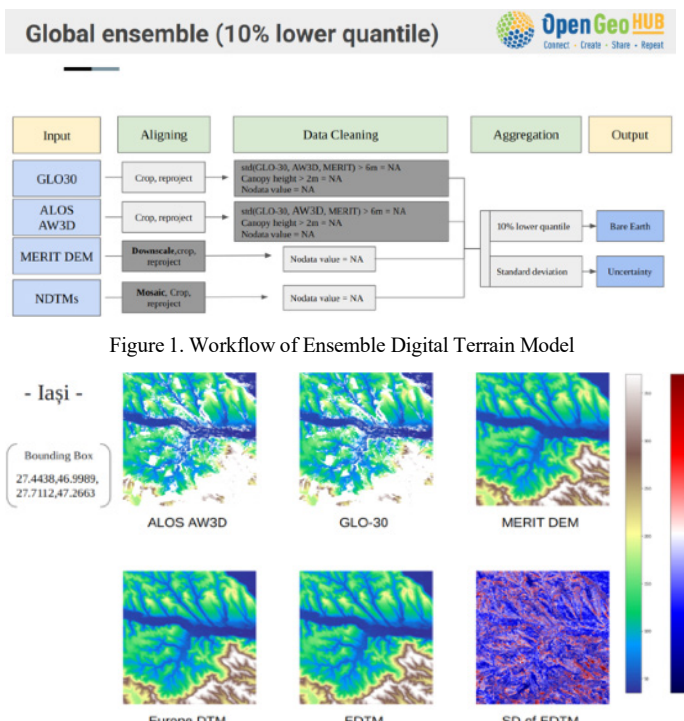


Figure 2. Input maps and EDTM, and the standard deviation (uncertainty) map around Iași

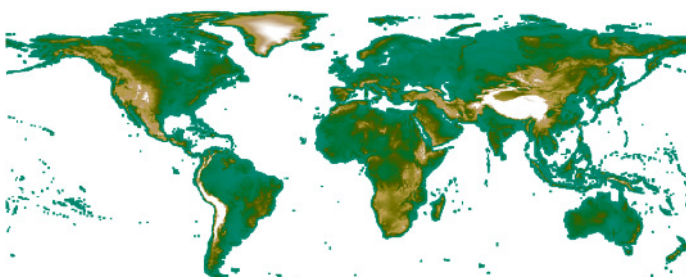


Figure 3. Global EDTM in an overview

TABLE I. LIST OF PUBLIC GLOBAL, REGIONAL, AND NATIONAL MAPS USED FOR MODELING EDTM

Name of map	Type*	Coverage	DOI
GLO-30	DSM	Globe (without Azerbaijan)	https://doi.org/10.5270/E_SA-c5d3d65
ALOS AW3D	DSM	Globe	https://doi.org/10.5194/is_prsannals-II-4-71-2014
MERIT DEM	DTM	Globe	https://doi.org/10.1002/2017GL072874
Dtm_eumap (EcoDataCube)	DTM	Europe	https://doi.org/10.5281/zendo.4724549
Digital Elevation Model (DEM) of Australia, Lidar	DTM	Coastal and Urban area in Australia	https://doi.org/10.26186/89644
Digital Elevation Model (DEM) of USA, Lidar	DTM	United States	https://doi.org/10.3133/fs20193032

*DSM – Digital Surface Model; DTM – Digital Terrain Model

IV. ACKNOWLEDGMENT

This work has been funded by OEMC project The Open-Earth-Monitor Cyberinfrastructure project, which has received funding from the European Union's Horizon Europe research and innovation programme under grant agreement № 101059548.

REFERENCES

- [1] Amatulli, G., Domisch, S., Tuanmu, M. N., Parmentier, B., Ranipeta, A., Malczyk, J., & Jetz, W., 2018. A suite of global, cross-scale topographic variables for environmental and biodiversity modeling. *Scientific data*, 5(1), 1-15. <https://doi.org/10.1038/sdata.2018.40>
- [2] Amatulli, G., Garcia Marquez, J., Sethi, T., Kiesel, J., Grigoropoulou, A., Üblacker, M. M., ... & Domisch, S., 2022. Hydrography90m: A new high-resolution global hydrographic dataset. *Earth System Science Data*, 14(10), 4525-4550. <https://doi.org/10.5194/essd-14-4525-2022>
- [3] Wagemann, J., Siemen, S., Seeger, B., & Bendix, J., 2021. Users of open Big Earth data—An analysis of the current state. *Computers & Geosciences*, 157, 104916. <https://doi.org/10.1016/j.cageo.2021.104916>
- [4] Iosifescu Enescu, I., de Espina, L., Haas-Artho, D., Kurup Buchholz, R., Hanemann, D., Rüetschi, M., ... & Pellissier, L., 2021. Cloud optimized raster encoding (core): A web-native streamable format for large environmental time series. *Geomatics*, 1(3), 369-382. <https://doi.org/10.3390/geomatics1030021>
- [5] Stern, C., Abernathey, R., Hamman, J., Wegener, R., Lepore, C., Harkins, S., & Merose, A., 2022. Pangeo Forge: Crowdsourcing Analysis-Ready, Cloud Optimized Data Production. *Frontiers in Climate*, 3, 179. <https://doi.org/10.3389/fclim.2021.782909>

Integrating terrain knowledge into point cloud simplification for terrain modelling

Jun Chen

School of Geography
 Nanjing Normal University
 Nanjing, China
chenjun@nju.edu.cn

Liyang Xiong

School of Geography
 Nanjing Normal University
 Nanjing, China
xiongliyang@njnu.edu.cn

Guanghui Hu

School of Geography
 Nanjing Normal University
 Nanjing, China
181302065@njnu.edu.cn

Guoan Tang

School of Geography
 Nanjing Normal University
 Nanjing, China
tangguoan@njnu.edu.cn

Abstract— Terrain models are widely used to depict the shape of the Earth's surface. With the development of photogrammetric methods, point cloud data have become one of the most popular data sources for terrain modelling. However, the obtained point clouds are of high density, which often increases redundancy rather than improving accuracy. Therefore, point cloud simplification should be a core component of terrain modelling. This paper proposes a point cloud simplification method by integrating terrain knowledge into terrain modelling (TKPCS). The method contains two steps: (1) terrain knowledge intuition and construction and (2) point cloud simplification using this terrain knowledge for terrain modelling. The proposed approach is benchmarked against improved versions of existing methods to validate its capability and accuracy in digital elevation model construction and terrain derivative extraction. The results show that the simplified points of the TKPCS method can generate finer resolution terrain models with higher accuracy and greater information entropy. The good performance of the TKPCS method is also stable at different scales. This work endeavors to transform perceptive terrain knowledge into a process of point cloud simplification and can benefit future research related to terrain modelling.

I. INTRODUCTION

Earth's surface consists of multiple landforms and a wide range of topographic characteristics [1]. Terrain modelling and subsequent analysis can help recognize and explore the character and formation of the Earth's surface [2]. At present, point cloud data are widely used for terrain modelling [3]. Developments in measurement technology have led to easier acquisition of high-density point cloud data. However, such point clouds introduce new problems concerning postprocessing redundancy for terrain modelling and analysis. Furthermore, terrain data should match the scale of the process mechanism and analysis purpose of geoscience research. Terrain data-related studies do not need to be carried out at decimetre- and millimetre-scale resolutions [4]. For example, accurate slope calculation and water flow simulation can be achieved at the metre level. Therefore, it is necessary to simplify point clouds.

Many studies have focused on point cloud simplification and the methods can be divided into mesh-based and point cloud-based. Mesh-based simplification methods initially build regular meshes based on point clouds and then simplify them using a given rule [5-6]. However, mesh-based methods are limited by

the large computational cost of mesh generation. Point cloud-based methods [7-9], for example cluster-based simplification, directly simplify point clouds without constructing polygonal meshes. The point clouds are first clustered into local point sets which are then simplified based on user defined rules. However, due to the limitations of clustering algorithms, the simplified result points are not suitable for terrain modelling.

Whether the mesh-based or point cloud-based method is used, the point information should always be considered during the simplification process. Normally, the geometric curvature, curvature combined with entropy, and the deviation of the normal vectors were commonly used as indicators to describe the importance of points [7-9]. However, although these indicators can show the significance of points on a local surface from a geometric view, a terrain surface consists of complex topographic characteristics, and traditional indicators are insufficient for the retention of terrain feature points after point cloud simplification.

Previous approaches have produced good simplifications of the point clouds of regular objects. However, a terrain surface is characterized by abrupt change, gradual change, and constant morphology [10] and is so complex that it is beyond the application of existing methods. At present, high-density terrain point cloud data simplification methods mainly include traditional curvature, random, and uniform methods. However, complex terrain features such as slope and land surface curvatures are not fully considered in existing simplification methods. Furthermore, terrain information consists of global structural and local detailed features [11], and both should be considered in simplifying terrain point clouds.

The global and local characteristics can be summarized as the understanding and intuition of terrain knowledge, which represents a combination of the perceptive descriptions of topographic characteristics across different environments [1]. It consists of global and local terrain knowledge. In this paper, we propose a point cloud simplification method by integrating terrain knowledge into terrain modelling. This method first intuits and constructs the terrain knowledge of the point cloud, and then, based on the integrated terrain knowledge, we develop a simplification method to retain terrain feature points.

II. METHODS

A. Terrain knowledge institution and construction

In this paper, global terrain knowledge was used as the principle to extract global feature points, which can control the structure of the terrain, and local terrain knowledge was used as a basis to extract local feature points which can help to enrich the details of a terrain surface. Fig. 1(c) shows the simplified points, which consist of the global and local feature points.

1) Global terrain knowledge

The global structure of a terrain surface is constructed using terrain feature points and lines [1]. We recognized the global terrain feature information as global terrain knowledge to preserve global feature points, which can prevent the loss of global terrain feature points during local simplification process. Normally, the feature points and lines of the terrain surface mentioned above are mainly distributed at the locations of abrupt changes in terrain, which can be indicated by the profile curvature that is the curvature along the direction of the maximum slope gradient, and is the rate of change of the terrain slope. In this study, the profile curvature was used to construct global terrain knowledge to efficiently preserve global feature points.

Specifically, the profile curvature values in ascending order were divided into two categories using the Jenks natural breaks classification method. The points with higher curvature values were selected to form a candidate point set of global feature points. Then global terrain feature points can be obtained by uniformly sampling the global candidate point set with a specific reduction ratio (i.e., point cloud reduction ratio). The extracted global terrain feature points can control the basic structure of the terrain surface (Fig. 1(a)).

2) Local terrain knowledge

Local terrain points can enrich terrain details, ensure the relative uniformity of point distribution, and improve the accuracy of terrain modelling. Terrain derivatives can express the morphological features of landforms. In previous studies, terrain derivatives, such as slope, were chosen to optimize terrain features during DEM processing because they are critical to many analyses [11]. Furthermore, the combination of multiple terrain derivatives has been proved to be more suitable to describe the complexity and roughness of a terrain surface [12]. Thus, in this study, we chose multiple terrain derivatives, including the elevation standard deviation, total accumulation curvature, and slope, to construct local terrain knowledge to control the simplification of the point cloud. These terrain derivatives consider both the terrain complexity and the material flow on the surface and ensure that the extracted points are representative of the local terrain surface (Fig. 1(b)).

The local terrain knowledge was constructed using the weighted summation of the terrain derivatives. Since the distribution of landforms often varies considerably at high, medium, and low altitudes (Fig. 1(d)), for weight setting, we divided the test area into three subregions to construct local terrain knowledge, respectively, because we believe that the weights should be different for subregions in different landforms. Specifically, the Jenks natural breaks method, which uses the elevation data of the test area as input, was used to divide the test area into three subregions of high, medium, and low altitudes to construct local terrain knowledge. Then, the weights of the terrain derivatives were determined using the criteria importance

through the intercriteria correlation method (CRITIC) [13] in different subregions.

The terrain derivatives mentioned above were calculated on a local quadratic function fitted using the local point cloud by the moving least squares algorithm [14]. In addition, we used a multiscale method that computes robust geometric features on point clouds to retrieve the optimal neighbourhood size for each point [15] rather than commonly used fixed search radius or number of points.

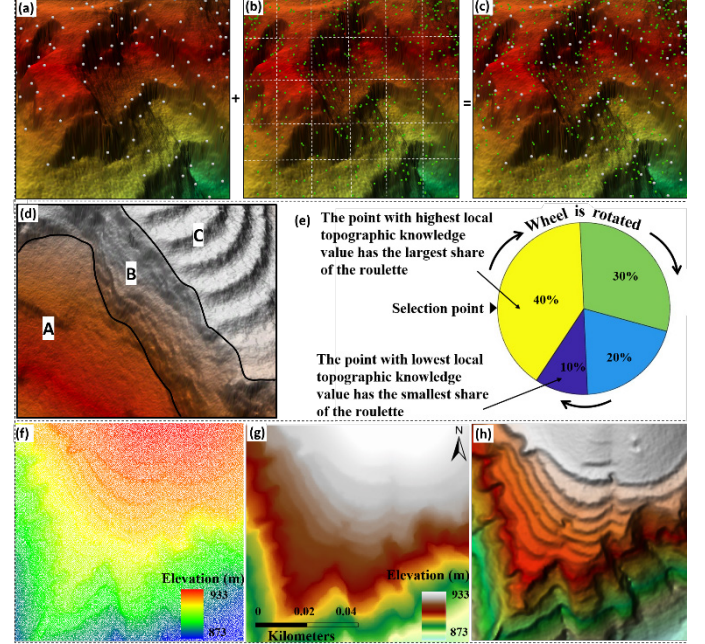


Figure 1. (a) Global feature points. (b) Local feature points. (c) The combination of the global and local feature points. (d) A, B, and C are different landforms in high, middle, and low altitude regions. (e) Diagram of the roulette wheel selection method. (f), (g), and (h) are the raw point clouds, DEM, and rendering map of the test area, respectively.

B. Integrating terrain knowledge into point cloud simplification

The TKPCS method flowchart is shown in Fig. 2. The global terrain feature points were first obtained by uniformly sampling the global candidate point set. Then, the retained global terrain feature points were integrated into the local grid simplification process. The local terrain feature points were extracted using the local terrain knowledge within the grid, which can be divided into two steps. The first step is to grid the point cloud and determine the number of simplified points in each grid based on the number of points and their local terrain knowledge values within the grid relative to all grids. The second step is a grid-by-grid local simplification process controlled by the local terrain knowledge. The test area was first gridded into subregions. In each subregion, points were simplified according to the strength of the local terrain knowledge. The principle is that the greater the local terrain knowledge value of a point is, the greater the probability of retention, and the smaller the probability of being simplified. This is the same as drawing a single sample from a multinomial distribution, which was implemented using the roulette wheel selection method [16]. A proportion of the wheel is assigned to each of the possible selections based on the local terrain knowledge of points within the subregions. Then a random selection is made similar to how the roulette wheel is rotated.

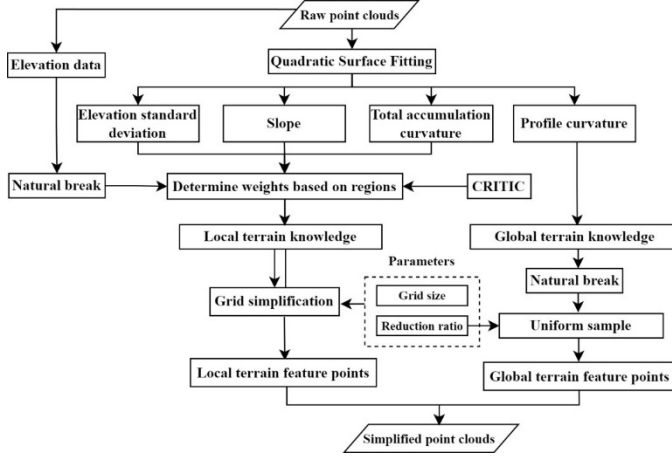


Figure 2. TKPCS algorithm workflow.

C. Evaluation methods and test area

We compared the TKPCS method with the revised random and curvature methods that are also limited by grids. Metrics, including the surface area loss of the modelled terrain based on triangular irregular networks (TINs), the root mean square error (RMSE) and mean absolute error (MAE) of the grid based DEMs (Grid-DEM), and the average slope information entropy of the simplified points, were used for comparing the simplified results. The reference data of the metrics is generated from raw point clouds. Each validation method was carried out at reduction ratios of 90%, 95% and 99% and grid sizes of 1 to 5 m to verify the accuracy and stability of our method. The test area is sampled from a watershed in the Loess Plateau. Point clouds in the test area were generated using photogrammetric methods with approximately 30 points per square metre (Fig. 1(f, g, h)).

III. RESULTS

A. Simplified point clouds using different methods

In contrast to the simplified points of the revised curvature and random methods, the distribution of the TKPCS method's simplified points exhibits two key characteristics (Fig. 4(a)). First, regions with complex terrain are where the TKPCS method's simplified points are most found. Second, the TKPCS method retains a rather uniform distribution of points. Furthermore, our method can retain more terrain feature points from the parts of the test area (Fig. 4(b, c)). In addition, the average slope entropy of the TKPCS method's simplified points is higher than that of the other methods (Fig. 5(a)). This implies a higher slope dispersion of the simplified points of the TKPCS method, indicating that the simplified points of the TKPCS method can retain more terrain information.

B. Terrain modelling with the simplified point clouds

From the perspective of generated Grid-DEM, first, the TKPCS method achieves high frequencies in low difference (0~0.2) with the reference data Fig. 3. Second, the TKPCS method generally achieves smaller MAE values (Fig. 5(b)). In terms of generated TINs, (Fig. 5(c)) shows that the surface area loss of the TKPCS method is smaller overall than that of the other methods. This means that terrain surfaces (e.g., TINs) constructed using the TKPCS method's simplified points are closer to the original terrain surfaces than those of the other methods. The above validation shows that the TKPCS method outperforms the other methods in terrain modelling.

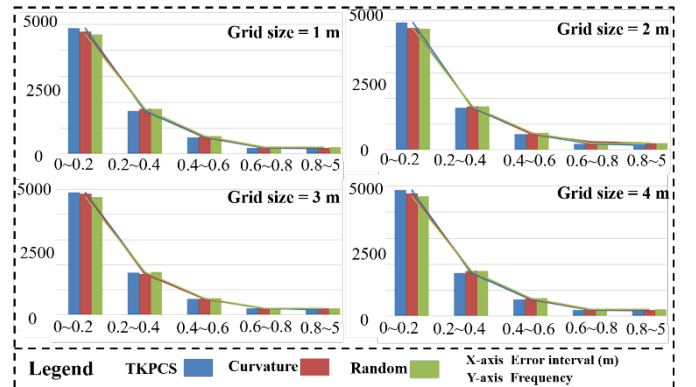


Figure 3. The difference frequency of Grid-DEMSS at 99% reduction ratio.

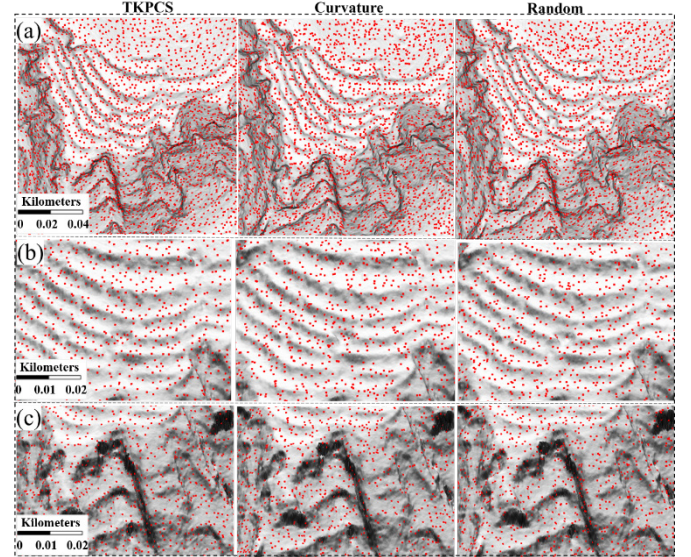


Figure 4. Simplified points and their partial enlargements.

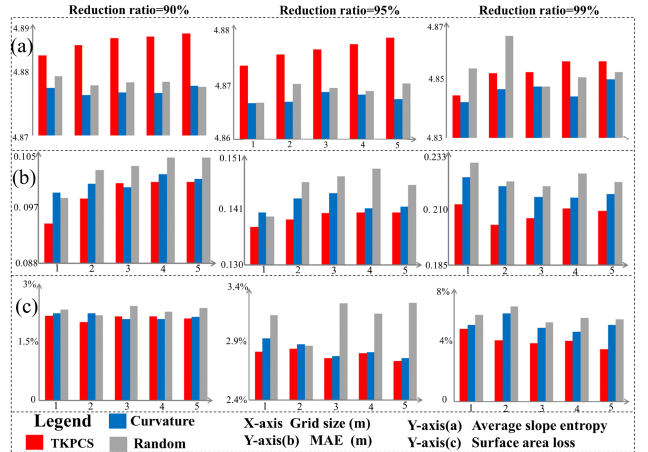


Figure 5. (a), (b), and (c) are average slope entropy, MAE, and surface area loss, respectively, with multiple reduction ratios and grid sizes.

IV. CONCLUSIONS

The comparisons demonstrate the TKPCS method's superior performance in terrain modelling. Furthermore, the simplified points of the TKPCS method are mostly distributed in terrain features and retain more terrain information.

V. ACKNOWLEDGMENTS

This work was supported by the National Science Foundation of China under Grant [41930102]; National Key Research and Development Program of China under Grant

[2021YFB3900901]; Priority Academic Program Development of Jiangsu Higher Education Institutions under Grant [164320H116].

REFERENCES

- [1] Li, S.J., G.H. Hu, X.H. Cheng, L.Y. Xiong, G.A. Tang, and J. Strobl, 2022. “Integrating topographic knowledge into deep learning for the void-filling of digital elevation models” *Remote Sensing of Environment*, 269, 112818. <https://doi.org/10.1016/j.rse.2022.112818>
- [2] Xiong, L.Y., G.A. Tang, F.Y. Li, B.Y. Yuan, and Z.C. Lu, 2014. “Modeling the evolution of loess-covered landforms in the Loess Plateau of China using a DEM of underground bedrock surface” *Geomorphology*, 209, 18–26. <https://doi.org/10.1016/j.geomorph.2014.02.012>
- [3] Podobnikar, T. and A. Vrečko, 2012. “Digital elevation model from the best results of different filtering of a LiDAR point cloud: high quality DEM from LiDAR data” *Transactions in GIS*, 16(5), 603–617. <https://doi.org/10.1111/j.1467-9671.2012.01391.x>
- [4] Wang, Q.L., J. Liu, L.X. Wu, Z.H. Xu, S.T. Fan, and A. Qian, 2016. “Analysis of gully erosion hazard using high resolution terrestrial LiDAR” *IEEE International Geoscience and Remote Sensing Symposium*, 7469–7472. <https://doi.org/10.1109/IGARSS.2016.7730948>
- [5] Luebke, D.P., 2001. “A developer’s survey of polygonal simplification algorithms” *IEEE Computer Graphics and Applications*, 21(3), 24–35. <https://doi.org/10.1109/38.920624>
- [6] Peng, J.L., C.S. Kim, and C.C.J. Kuo, 2005. “Technologies for 3D mesh compression: A survey” *Journal of Visual Communication and Image Representation*, 16(6), 688–733. <https://doi.org/10.1016/j.jvcir.2005.03.001>
- [7] Chen, N. and X. Lu, 2021. “A novel point cloud simplification method with integration of multiple-feature fusion and density uniformity” *Measurement Science and Technology*, 32(12), 125211. <https://doi.org/10.1088/1361-6501/ac2a68>
- [8] Shi, B.Q., J. Liang, and Q. Liu, 2011. “Adaptive simplification of point cloud using k-means clustering” *Computer-Aided Design*, 43(8), 910–922. <https://doi.org/10.1016/j.cad.2011.04.001>
- [9] Zhao, P.C., Y. Wang, and Q.W. Hu, 2016. “A feature preserving algorithm for point cloud simplification based on hierarchical clustering” *IEEE International Geoscience and Remote Sensing Symposium*, 5581–5584 <https://doi.org/10.1109/IGARSS.2016.7730457>
- [10] Hu, G.H., W. Dai, S.J. Li, L. Xiong, and G.A. Tang, 2020. “A vector operation to extract second-order terrain derivatives from digital elevation models” *Remote Sensing*, 12(19), 3134. <https://doi.org/10.3390/rs12193134>
- [11] Zhang, Y.F., W.H. Yu, and D. Zhu, 2022. “Terrain feature-aware deep learning network for digital elevation model superresolution” *ISPRS Journal of Photogrammetry and Remote Sensing*, 189, 143–162. <https://doi.org/10.1016/j.isprsjprs.2022.04.028>
- [12] Mark, D.M., 1975. “Geomorphometric parameters: a review and evaluation” *Geografiska Annaler: Series A, Physical Geography*, 57(3–4), 165–177.
- [13] Diakoulaki, D., G. Mavrotas, and L. Papayannakis, 1995. “Determining objective weights in multiple criteria problems: The critic method” *Computers & Operations Research*, 22(7), 763–770. [https://doi.org/10.1016/0305-0548\(94\)00059-H](https://doi.org/10.1016/0305-0548(94)00059-H)
- [14] Levin, D., 2004. “Mesh-Independent Surface Interpolation” *Geometric Modeling for Scientific Visualization*, 37–49. https://doi.org/10.1007/978-3-662-07443-5_3
- [15] Demantké, J., C. Mallet, N. David, and B. Vallet, 2012. “Dimension-based scaling selection in 3D LiDAR point clouds” *The International Archives of the Photogrammetry, Remote Sensing and Spatial Information Sciences*, XXXVIII-5/W12, 97–102. <https://doi.org/10.5194/isprsarchives-XXXVIII-5-W12-97-2011>
- [16] Bickle, T. and L. Thiele, 1996. “A comparison of selection schemes used in evolutionary algorithms” *Evolutionary Computation*, 4(4), 361–394. <https://doi.org/10.1162/evco.1996.4.4.361>

A method to rank global DEMs quality focused on their horizontal accuracy

Juan F. Reinoso-Gordo

Dept. Expresión Gráfica Arquitectónica y en la Ingeniería
University of Granada
Spain
jreinoso@ugr.es

Francisco J. Ariza-López

Dept. Ingeniería Cartográfica, Geodésica y Fotogrametría
University of Jaén
Spain
fjariza@ujaen.es

Abstract— Currently there are various global digital elevation models (GDEM) and it would be necessary to have measures that help decide which one to use according to the derived product that we need. The DEMIX Project addresses this problem. In this communication we show an automatic measure that assesses the planimetric quality of a DEM product (DEM) and that allows ordering from highest to lowest, according to planimetric quality, any DEM and particularly a set of GDEMs. The planimetric quality of a DEM is assessed by comparing its contours with their homologous ones belonging to a reference DEM (DEMref) of greater accuracy. The area enclosed by homologous contours is an indicator of DEM's accuracy: the smaller the area enclosed by homologous contours, the greater horizontal accuracy. In this study, the area divided by the average length of the contours is used to estimate the DEM horizontal accuracy compared with a DEMref. One of the great advantages of this method is that it is completely automatic (we do not need to identify the homologous curves). Although the method can be used to compare any DEM, in this study we have used 2 GDEMs (ASTER and NASADEM) as DEM which have 30 m of spatial resolution and the DEMref is the Spanish MDT05 (5 m of spatial resolution) generated by the Spanish Instituto Geográfico Nacional (IGN).

I. INTRODUCTION

Digital elevation models (DEM) are used in many branches of knowledge, such as Civil Engineering, Environment, Natural Risk Management, Climate Change, etc. Many products are derived from them, such as slope maps, orientations, basins and hydrographic networks, optimal locations for mobile phone antennas, etc. Due to the large number of DEMs applications, numerous studies of their quality have also been carried out, as shown in [1-3]. In most cases, the DEM vertical accuracy is studied [2,4] and planimetric accuracy is left aside as it is more difficult to compute because the difficulty of identifying homologous points between the DEM and the DEMref or reference control elements [4]. In the DEM vertical accuracy studies, the height values of a sample of points obtained from a DEMref or directly in the field using, for example, GNSS, are compared with their homologous ones in the DEM whose accuracy is to be computed; these studies often use classical statistics (RMSE, μ , σ , MAE, NMAD, etc.) [5-6]. The mentioned above homologous points are selected from the DEM at the same horizontal coordinates that the ground truth points had, but how do we know that these homologous points are really the same in both datasets? Proceeding in this way, we are

considering that DEM has no planimetric error with respect to the ground truth. There are so few studies of planimetric accuracy in DEMs because of the difficulty of identifying homologous points in DEM and DEMref. Some early proposals for planimetric accuracy evaluation measures appear in [7] but do not allow for automation of the process, which makes implementation difficult. And more recently, measures that evaluate the planimetric accuracy of a DEM have been proposed [8-11]; among them, perhaps the best is the one based on the area enclosed by homologous contours that intersect, considering as homologous those contours that represent the same altitude in the DEM and the DEMref respectively [8-9]; this method solves the problem of identifying homologous elements in both the DEMref and DEM, since if no altitudinal bias exists, the homologous contours represent the same planimetric space of the terrain, and the non-coincident part expresses the planimetric discrepancy between the DEM and the DEMref.

In the present communication we develop an application example of the horizontal accuracy method based on contours [9], which could be used to rank GDEMs produced by different sources from best to worst.

II. MATERIAL AND METHODOLOGY

A. Material

In order to illustrate the method, 2 DEM of 10 km x 10 km located in Sierra Nevada, Granada, (Spain) have been used. The source GDEMs are ASTER V003 and NASADEM. Both are open data that we have downloaded from the NASA website <https://search.earthdata.nasa.gov/search>. ASTER and NASADEM have a cell size of 1 arcsecond which is roughly equivalent to 30 m. The DEMref selected was the MDT05 produced by the IGN of Spain, whose cell size is 5 m.

The coordinate reference system (CRS) for ASTER and NASADEM was WGS84 while that of MDT05 was ETRS89 UTM zone 30N. To give the DEM samples (MDT05, NASADEM and ASTER) the same limits and the same cell size, an alignment was carried out, taking MDT05 as a reference and resampling to the nearest neighbor. Finally, the 3 samples were stored in the CRS ETRS89 UTM zone 30N and their respective contours were derived. The contour step had a value of 125 m, beginning the first contour at an altitude of 950 m and ending the last contour at 2825 m height.

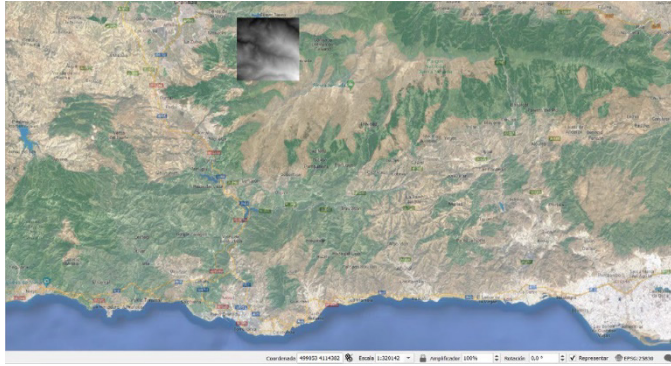


Figure 1: GDEM samples geolocation at Granada (Southern Spain)

B. Methodology

The DEM horizontal accuracy with respect to DEMref is estimated as a function of the area enclosed by homologous contour lines. In Fig. 2 we can see 2 types of homologous contours: suppose that the contours labeled as A belong to DEMref and those labeled as B belong to DEM; the contours are not coincident because DEM lacks accuracy with respect to DEMref and the inaccuracy magnitude is intuited by the amount of enclosed surface (grey color) between homologous contours.

The inaccuracy magnitude of the (Hacc) for a single contour in DEM could be estimated by the equation (1) where LA and LB are the lengths of the contours in DEM and DEMref respectively and Area is the area enclosed by both contours.

$$H_{acc} = \frac{Area}{(L_A + L_B)/2} \quad \text{Eq. 1}$$

An alternative could be to use the LB as denominator, and it would deserve a comparison with our proposal.

In a DEMref, at a particular altitude (h_i) there will be a number of contours m whose total length will be $refLT_i$; in a DEM for the same h_i , there will be a number of curves n whose total length will be $proLT_i$, and the total area enclosed by the homologous contours of DEMref and DEM at altitude h_i will be $AreaTi$. If we only consider the altitude h_i to compute Hacci, then $Hacci = AreaTi/(refLT_i + proLT_i)/2$. Since the number of altitudes for which the contour are calculated is variable $i=1, 2, \dots, k$, the estimate of the total horizontal accuracy (HTacc) of DEM with respect to DEMref will be as shown in equation (2):

$$HT_{acc} = \frac{\sum_i^k AreaTi}{\sum_i^k (refLT_i + proLT_i)/2} \quad \text{Eq. 2}$$

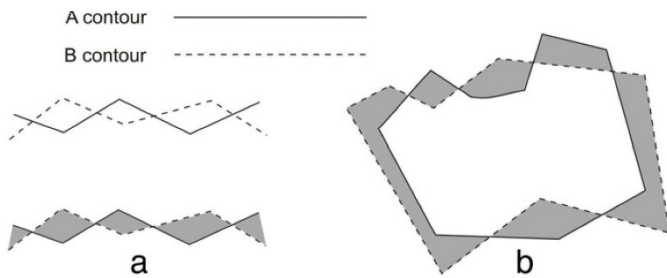


Figure 2: Area between overlapping contours (A and B)

It is difficult to automate the HTacc computation because the correspondence between homologous contours is not a bijective map; *a priori* the correspondence could have any setting, e.g. 1->1, 0->1, 1->n, n->1 and in general manner m->n. To understand all the cases that could happen you can consult [9].

>1, 0->1, 1->n, n->1 and in general manner m->n. To understand all the cases that could happen you can consult [9].

The greatest difficulty to automate the process is to prove the following theorem:

The number of possible different Regions in a DEM (REGk Xs) is exactly 2 and they are complementary.

The regions to which the theorem refers are those that appear in gray in the images f and i respectively of Fig. 3. The correct region will be the one with the smallest surface (image f in Fig. 3). The images a and b in Fig. 3 represent DEMref and DEM respectively, assuming that all contour have the same height. As shown in Fig. 2, the correspondence between homologous contours is not bijective. The images f and i are the 2 complementary regions mentioned in the theorem; f is derived applying the mathematical operation symmetric difference between the d and e images. Similarly is derived this image.

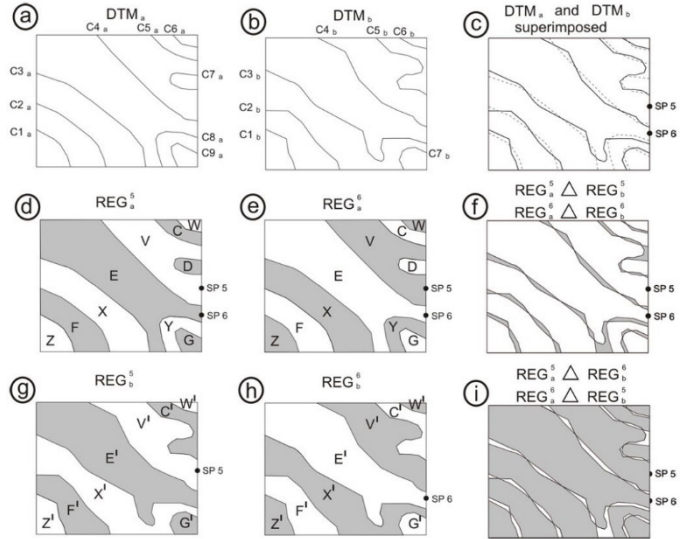


Figure 3: Theorem illustration. Images a and b show homologous contours with no bijective correspondence, and images f and i show the only two possible regions after applying method explained in [9]

III. RESULTS AND DISCUSSION

The algorithm presented in [9] has been applied using MDT05 as a reference and the graphic result is shown in Fig. 4. The images that allow HTacc to be computed are those labeled with NASA vs MDT05 and ASTER vs MDT05. Fig. 4 includes an additional result (ASTER vs NASADEM) that does not measure the horizontal accuracy of the DEM but shows the horizontal discrepancy between ASTER and NASADEM comparing their homologous contours.

In order to have a better understanding of how the algorithm works, in Fig. 4 two examples of each of the three results have been enlarged. These examples have been framed in red and green, giving rise to the left column (red) and the right column (green) respectively. In both examples the area between contour lines of ASTER vs MDT05 is greater than the area NASA vs MDT05, so it is expected that the best value of HTacc belongs to NASADEM.

The HTacc numerical values for ASTER and NASADEM are shown in Table 1, although before performing the HTacc final computation, the horizontal accuracy (Hacci) for each curve elevation (h_i) has been computed: each row corresponds to the values of contours mean length ((refLT $_i$ +proLT $_i$)/2), area between homologous contours (AreaTi) and DEM horizontal accuracy o if only hi (Hacci) is considered. It is observed that for all the hi values the Hacci measure is very similar except for the

value $h_i=950$ m where the horizontal accuracy values are much greater than in the rest. This is because there is a relationship between homologous contours of $1>0$, i.e., both in ASTER and in NASADEM there is a contour that does not appear in MDT05, which produces a very large area (marked with a blue ellipse in Fig. 4).

In this example where we compute the HTacc for ASTER and NASADEM, the best global accuracy is obtained by NASADEM, which has HTacc = 10.7 m compared to ASTER's HTacc=14.0 m, which implies that NASADEM improves ASTER's horizontal accuracy by 23%.

IV. CONCLUSIONS

In this communication we have presented a method that allows ranking a series of GDEMs produced by different sources; the method is based on a measure that can estimate the horizontal accuracy (HTacc). To perform the method requires a DEMref that will be the ground truth to compare the DEM (GDEMs) with. Furthermore, HTacc has the advantage that it can be automated according to the algorithm [9]. We consider that this measure is of interest to the DEMIX project, which aims to compare different GDEMs in order to rank them. A remarkable property from the method is that it can identify homologous elements in DEMs (contours). This ability is hard to find in other methods, even those based on manual processes since there is usually no certainty about which pair of points are homologous in DEMref and DEM.

Finally, the graphic representation capabilities of one of the measurement components (area between homologous contours) demonstrates in which areas the greatest DEM inaccuracies happen (Fig. 4).

TABLE I. HORIZONTAL ACCURACY ESTIMATION FOR ASTER AND NASADEM

h_i Contour height (m)	ASTER vs MDT05		NASA vs MDT05			
	$(refLT_i + proLT_i)/2$ (m)	$AreaT_i$ (m ²)	H_{acci} (m)	$(refLT_i + proLT_i)/2$ (m)	$AreaT_i$ (m ²)	H_{acci} (m)
950	2371,0	276131,3	116,5	1902,2	268245,4	141,0
1075	20908,0	259411,0	12,4	20054,9	227050,7	11,3
1200	31726,1	405635,7	12,8	31429,9	336515,7	10,7
1325	37552,4	465815,1	12,4	36922,7	414114,5	11,2
1450	51316,5	746549,1	14,5	49595,4	554530,1	11,2
1575	46881,6	653031,8	13,9	46079,8	443547,1	9,6
1700	47503,2	675658,8	14,2	46984,4	516096,0	11,0
1825	41267,9	543688,1	13,2	40544,6	389059,7	9,6
1950	32380,7	409800,2	12,7	32211,5	286557,0	8,9
2075	27934,4	358605,1	12,8	27393,5	241606,8	8,8
2200	24431,5	319213,5	13,1	24350,4	223654,3	9,2
2325	19709,6	253086,0	12,8	18886,1	170584,4	9,0
2450	7929,7	100859,4	12,7	7779,4	55654,7	7,2
2575	3619,2	54334,8	15,0	3570,4	29773,6	8,3
2700	2059,8	30973,8	15,0	2023,6	19112,4	9,4
2825	633,4	8220,8	13,0	655,3	5805,7	8,9

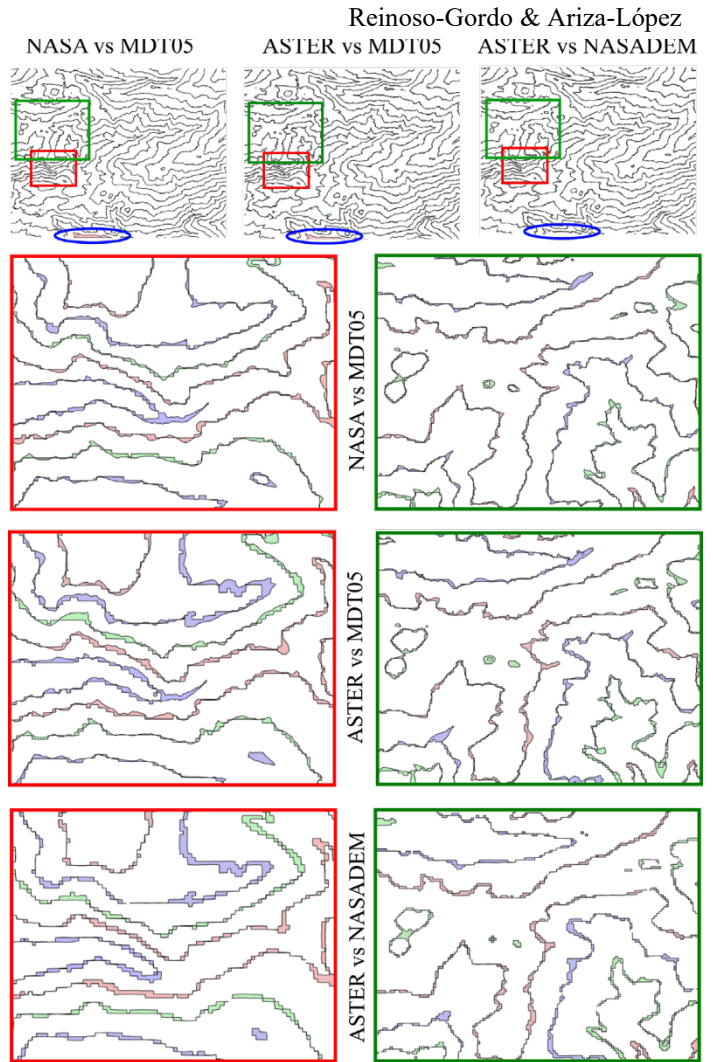


Figure 4: Area inside homologous contours after comparing DEMref and DEM

V. ACKNOWLEDGMENT

This research has been partially funded by the Project: "Functional Quality of Digital Elevation Models in Engineering" of the State Research Agency with code PID2019-106195RB-I00/AEI/10.13039/501100011033, more information at https://coello.ujaen.es/investigacion/web_gic/funquality4dem/.

REFERENCES

- [1] Ariza-López F.J. et al. Analysis of some Positional Accuracy Assessment Methodologies. *Surveying Engineering*, 134(2):45-54, 2008.
- [2] Mesa-Mingorance, J.L., F.J. Ariza-López. (2020). Accuracy Assessment of Digital Elevation Models (DEMs): A Critical Review of Practices of the Past Three Decades. *Remote Sensing* 12, no. 16: 2630. <https://doi.org/10.3390/rs12162630>
- [3] Polidori L., El Hage, M. (2020). "Digital Elevation Model Quality Assessment Methods: A Critical Review" *Remote Sensing* 12, no. 21: 3522. <https://doi.org/10.3390/rs12213522>
- [4] Li, Z., Zhu, Q., Gold, C., 2005. *Digital Terrain Modeling*. CRC Press, Boca Raton. M
- [5] ASPRS. *ASPRS Positional Accuracy Standards for Digital Geospatial Data*, PE&RS, 2015
- [6] Maune D. *Digital elevation model technologies and applications. The DEM user's manual*. ASPRS, 2007
- [7] Ley, R., 1986. Accuracy assessment of digital terrain models. In: Blakemore M. (Ed.), *Proceedings Auto-Carto*, London, pp. 455–464.
- [8] Reinoso-Gordo, J.F. (2010) *A priori horizontal displacement (HD) estimation of hydrological feature H when visioned DEMs are used*. *Journal of Hydrology*, 384: 1–2, pp. 130–141.
- [9] Reinoso-Gordo, J.F. (2011). An algorithm for automatically computing

- the horizontal shift between homologous contours from DTMs, ISPRS Journal of Photogrammetry and Remote Sensing, 66: 3, pp. 272-286.
- [10] Reinoso-Gordo, J.F., León, C., & Mataix, J. (2014). Optical flow algorithm as estimator of horizontal discrepancy between features derived from DEMs: Rivers and creeks as case study. Survey Review, 46(335), 149-154. <https://doi.org/10.1179/1752270613Y.0000000073>
- [11] Reinoso-Gordo, J.F., León, C., & Mataix, J. (2015). Estimating Horizontal Displacement between DEMs by Means of Particle Image Velocimetry Techniques. *Remote Sensing*, 8(1), 14. <https://doi.org/10.3390/rs8010014>
- [12] Strobl, P. A., Bielski, C., Guth, P. L., Grohmann, C. H., Muller, J.-P., López-Vázquez, C., Gesch, D. B., Amatulli, G., Riazanoff, S., & Carabajal, A. (2021). The digital elevation model intercomparison experiment DEMIX, a community-based approach at global DEM benchmarking. The International Archives of the Photogrammetry, Remote Sensing and Spatial Information Sciences, XLIII-B4-2021, 395-400. <https://doi.org/10.5194/isprs-archives-XLIII-B4-2021-395-2021>

The role of geomorphometric predictors in LUCC modeling

Adam Rusinko and Jozef Minár

Department of Physical Geography and Geoinformatics
Comenius University in Bratislava, Slovakia
adam.rusinko@uniba.sk

Abstract—An adequate choice of independent variables poses a basal step to create successful model of Land-Use and Land-Cover Change (LUCC). Spatial predictors derived from digital elevation model (DEM) are a big group of determinants that are relatively easy to obtain. However, the review of more than one hundred articles showed that only basic geomorphometric variables: elevation, slope, partly aspect and characteristics of solar radiation are mostly used. In this study, 21 geomorphometric predictors are tested in LUCC models of 5 distinct changes in Slovakia: urbanisation, intensification, extensification, afforestation, deforestation. The changes were obtained from CORINE Land Cover (CLC) database in the period 1990 – 2018. Logistic regression was used to quantify the association of the predictors and LUCC. In the first step, the relationship of one variable to each change was investigated in univariate logistic regression models. Based on univariate models, insignificant predictors were removed from further analysis. The most important geomorphometric predictors identified by multiple-variable logistic regression models and hierarchical partitioning were elevation, slope, Casorati curvature, duration of solar radiation, relief amplitude, topographic wetness index, terrain ruggedness index, and relief brake force. All have a good energetic interpretation that could be important in land cover formation.

I. INTRODUCTION

Studies investigating Land-Use and Land-Cover Change (LUCC) are a common part of geo-science experiments and applications. Typical mapping of land cover classes and detecting changes over the years has gradually shifted to spatial modeling of it [1]. In general, the modeling of LUCC deals with very traditional geographical issue: the relationship between various geographical factors – spatial predictors and LUCC [2,3]. However, some data (predictors) are difficult to obtain (for example individual motivation of landowners [4]), another data have inappropriate spatial resolution. The modeling is therefore generally limited by availability of the input data [5]. In contrast of it, geomorphometric characteristics derived from digital elevation model (DEM) are a group of spatial predictors that are easily obtainable, thanks to abundance of various, even global DEMs. However, the review of more than one hundred articles showed that most often only basic geomorphometric variables are used: elevation [6,7], slope [8], partly aspect [7,9], and characteristics of solar radiation [6,7]. Resulting from the classification of the fundamental geomorphometric characteristics [10] we assume that there are other geomorphometric characteristics which also could be relevant in LUCC modeling. Moreover, the theory of physical geomorphometry [11] supports better interpretation of these

relationships considering the effect of gravitational force on the land surface processes.

Our aims were to: (1) review research articles and find the most used geomorphometric characteristics used in LUCC models, (2) systematically create the (exhaustive) list of potential geomorphometric predictors, (3) test several geomorphometric predictors in modeling of changes in the area of Slovakia from 1990 – 2018 using logistic regression, (4) find the most important individual variables and quantify their contribution in multiple-variable model with other non-terrain variables which play relevant role in LUCC modeling.

II. MATERIAL AND METHODS

A. Literature review

We searched for LUCC modeling studies in scientific databases (WoS, Scopus, etc.) using keywords such as LUCC modeling, geomorphometric characteristics, topographic variables and we tried to find this information in the articles: DEM product and its spatial resolution, geomorphometric variables derived from it, formulas and tools used in the calculations. Finally, we gathered one hundred LUCC and we made the list of the most frequent geomorphometric predictors used in LUCC modeling (Tab. 1).

TABLE I. THE MOST USED GEOMORPHOMETRIC PREDICTORS IN LUCC MODELING

Variable	Count
Slope	92
Elevation	83
Aspect	36
Solar radiation	20
Topographic Wetness Index	9
Landforms	8
Curvatures	5
Topographic Position Index	5
Relief amplitude	4
Specific Catchment Area	4
Terrain Ruggedness Index	2
Drainage density	1

Variable	Count
Stream Power Index	1

B. LUCC data

Land cover data were obtained from the official CLC dataset for the area of Slovakia. We used data from years 1990, 2000, 2006, 2012, 2018. Changes between 1990 and 2018 were identified by merging the partial layers of change. The changes were categorised by a diagram of land cover flows into six categories [12]: urbanisation, agricultural intensification, agricultural extensification, afforestation, deforestation, and water bodies construction. However, water bodies construction was excluded from the next statistical analysis because of the small area of change.

C. Geomorphometric predictors

Based on our prior knowledge and experience with geomorphometric characteristics, we derived 21 predictors from national DEM (DMR 3.5) with spatial resolution of 10m (Tab. 2). Firstly, we used fundamental local point-based variables, elevation and its changes (first and second derivatives) in the direction of the gravitational field introduced by [13,14]. In addition to basic trio of gravity-specific curvatures [15], field-invariant curvatures [16] (mean, Gaussian, Casorati) were also added. Local area-based variables were represented by relief (amplitude of topographic wave) 'ra', drainage density 'dd' representing length of the wave, and ratio of the wave amplitude and length determining relief brake force 'rbf' [17,18]. Secondly, we calculated characteristics of solar radiation. Thirdly, we added some variables, mostly various terrain indices, which are used in different geo-applications such as hydrology, geomorphology, etc.

TABLE II. LIST OF TESTED GEOMORPHOMETRIC PREDICTORS

Abbrev.	Variable	Notes on tools and sources
elev	Elevation above sea level	10m DEM
slop_deg	Slope [$^{\circ}$, %, rad, sine, tan]	Slope tool ArcGIS Pro
asp	Aspect Sine of aspect Cosine of aspect	Aspect tool ArcGIS Pro
prof_curv	Normal slope line curvature	Surface Parameters tool ArcGIS Pro Enhanced GIS tools proposed by [15]
tang_curv	Normal contour curvature	
torsion_curv	Contour geodesic torsion	
mean_curv	Mean curvature	
caso_curv	Casorati curvature	
gauss_curv	Gaussian curvature	
ra	Relief amplitude	circle, r = 1500m
dd	Drainage density	circle, r = 1500m
solar_glob	Global radiation	Area Solar Radiation tool ArcGIS Pro
solar_dir	Direct radiation	
solar_dur	Duration of direct radiation	
a	Specific catchment area	Raster Calculator [19]
twi	Topographic Wetness Index	Raster Calculator [20]
tpi	Topographic Position Index	Land Facet Corridor tools – Extension for ArcGIS [21]

Abbrev.	Variable	Notes on tools and sources
tri	Terrain Ruggedness Index	TRI tool SAGA GIS [22]
spi	Stream Power Index	SPI tool SAGA GIS [23]
mrn	Melton Ruggedness Number	MRN tool SAGA GIS [24,25]
rbf	Relief Brake Force	Raster Calculator [17,18]

a. Underlined variables recorded the highest overall AUC in univariate regression models.

D. Statistical analysis

We used a regular sampling grid in square net with step of 500m. Values of changes and spatial predictors were assigned to each point of the grid. Univariate logistic regression models revealed eight geomorphometric variables, which are potentially significant for land cover changes in Slovakia (underlined variables in Tab. 2). AUC of ROC curve was used as the indicator of the model's explanatory power. These eight predictors were subsequently added to the multiple-variable model, together with other spatial predictors which play important role in LUCC modeling: mean annual temperature interpolated to 100m grid (temp) from Climate Atlas of Slovakia [26], Euclidean distance to the nearest settlement (dist), and population density (pop_dens) at municipal level [27]. We selected multiple-variable models for the next analyses using the stepwise regression procedure. In each step, the variable with the lowest significance ($p < 0.05$) was excluded from the next step of the procedure until each variable was significant. Lastly, we used hierarchical partitioning as a method for quantifying an individual contribution of the predictors to the overall variance explained by the model [28].

III. RESULTS AND DISCUSSION

Resulting from univariate models, the highest AUC was reached by: 'tri', 'ra', 'rbf', slope, elevation, duration of solar radiation, Casorati curvature, and 'twi'. These variables were used in multiple-variable logistic regression models (Fig. 1).

The explanatory power (AUC) of the models was relatively high for each land cover change, except deforestation: urbanisation 0.81, intensification 0.77, extensification 0.74, afforestation 0.80, and deforestation 0.66. However, the final pool of significant predictors was different for different land cover changes. Individual contribution of variables to the model explanatory power (sum of individual contributions = 100%) was calculated only for the strongest predictors after backward stepwise regression (Fig. 1).

Relative high importance of Casorati curvature (intensification – 17.26%, urbanisation – 13.79%, afforestation – 9.27%) is the most surprising discovery. This curvature is generally used only occasionally, and our review indicates that has never been tested as a predictor in LUCC modeling. It is a measure of general surface non-linearity [15], expressing integral potential energy of surface curvature related to general landforms instability [11]. Investigation of possible relationship between physical specificity of Casorati curvature and its fruitfulness in LUCC modeling is a challenge for the future work.

Another non-trivial result is relative importance of two characteristics describing undulation of topography. 'Ra' (wave amplitude) and 'rbf' (ratio of wave amplitude and length) contributed to explain the model of afforestation (ra – 13.55%, rbf – 9.49%), and extensification (ra – 6.79%, rbf – 6.30%). 'Rbf' recorded almost the highest contribution in the model of intensification (19.34%), together with slope (19.58%). However, it is needed to be aware of parallel use of 'ra' and 'rbf', because of their mutual correlation. If the window for

calculation has size of topographic grain, then ‘rbf’ integrates both, ‘ra’ and ‘dd’ (inverted value of wave length). Multiplication of ‘ra’ and ‘dd’ approximates ‘rbf’ and expresses the average slope of an area [17,18], that is measure of barrier effect of the topography or its brake force.

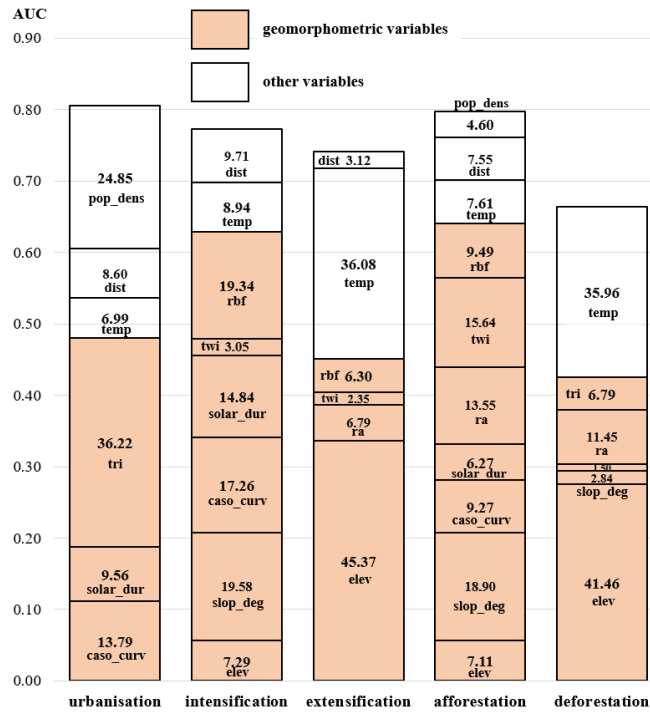


Figure 6. AUC (ROC curve) of the multiple-variable logistic regression models of the land cover changes and independent contribution [%] of single predictors to models' explanatory power.

Positional geomorphometric variables as ‘tpi’ and ‘tri’ are measures of regional difference of potential gravity energy [11] that could also affect the land cover formation. It could be indicated by ‘tri’ with strong result in the model of urbanisation (36.22%) and weaker contribution of deforestation (6.79%).

The last unexpected result is relative importance of duration of solar radiation (intensification – 14.84%, urbanisation – 9.56%, afforestation – 6.27%). It does not use to be used in LUCC modeling, and solar radiation is often represented by global or direct radiation which showed low relevance in our univariate models. Similar to ‘rbf’, also solar radiation can be considered as a combination of another characteristics. In this case, slope and aspect. So, it might express their mutual effect on changes. On the other hand, the commonly used aspect parameter was not important in our analysis.

Non-morphometric predictors (pop_dens, dist, temp), held their stable position in the design of LUCC models. However, geomorphometric characteristics were more important. There are also cases (extensification and deforestation) where elevation and ‘temp’ had high individual contributions. It is well known that in mountainous countries (Slovakia), elevation can be used as a proxy for climatic characteristics [7], however elevation include also influence of gravity energy distribution. It can be a reason of its high individual acquisition to LUCC modeling in these cases.

IV. CONCLUSIONS

This study tested 21 geomorphometric predictors in logistic regression models. Preliminary results (univariate models) revealed the most significant variables: ‘tri’, ‘ra’, ‘rbf’, slope,

elevation, ‘solar_dur’, Casorati curvature, and ‘twi’. Result of traditional variables as elevation or slope is not surprising but success of some newly used variables is very interesting and physically interpretable. Casorati curvature as a measure of energetic disequilibrium of land surface [11]. Relative importance of wave characteristics: ‘rbf’ and ‘ra’ representing regional barrier effect of topography. Priority of duration of solar radiation over global/direct radiation. And notable result of ‘tri’ as a variable of (topographic) position and regional difference of gravity energy. Further research is needed to verify these results. An unsolved question is still the impact of DEM generalisation and changes in the size of computation window and sensitivity of land cover change to such technicalities.

V. ACKNOWLEDGMENTS

This work was supported by the Slovak Research and Development Agency under the contract No. APVV-22-0024.

REFERENCES

- [1] Verburg, P. H., Kok, K., Pontius, R. G., & Veldkamp, A. (2006). Modeling Land-Use and Land-Cover Change. In E. F. Lambin & H. J. Geist (Eds.), *Land-Use and Land-Cover Change* (pp. 117–135). Springer Berlin Heidelberg. https://doi.org/10.1007/3-540-32202-7_5
- [2] Bürgi, M., Hersperger, A. M., & Schneeberger, N. (2004). Driving forces of landscape change – current and new directions. *Landscape Ecology*, 19, 857–868. <https://doi.org/10.5792/ksrr.17.008>
- [3] Plieninger, T., Draux, H., Fagerholm, N., Bieling, C., Bürgi, M., Kizos, T., Kuemmerle, T., Primdahl, J., & Verburg, P. H. (2016). The driving forces of landscape change in Europe: A systematic review of the evidence. *Land Use Policy*, 57, 204–214. <https://doi.org/10.1016/j.landusepol.2016.04.040>
- [4] Lieskovský, J., Bezák, P., Špulerová, J., Lieskovský, T., Koleda, P., Dobrovodská, M., Bürgi, M., & Gimmi, U. (2015). The abandonment of traditional agricultural landscape in Slovakia - Analysis of extent and driving forces. *Journal of Rural Studies*, 37, 75–84. <https://doi.org/10.1016/j.jrurstud.2014.12.007>
- [5] Rindfuss, R. R., Walsh, S. J., Turner, B. L., Fox, J., & Mishra, V. (2004). Developing a science of land change: Challenges and methodological issues. *Proceedings of the National Academy of Sciences of the United States of America*, 101(39), 13976–13981. <https://doi.org/10.1073/pnas.0401545101>
- [6] Álvarez Martínez, J.-M., Suárez-Seoane, S., & De Luis Calabuig, E. (2011). Modelling the risk of land cover change from environmental and socio-economic drivers in heterogeneous and changing landscapes: The role of uncertainty. *Landscape and Urban Planning*, 101(2), 108–119. <https://doi.org/10.1016/j.landurbplan.2011.01.009>
- [7] Rutherford, G. N., Bebi, P., Edwards, P. J., & Zimmermann, N. E. (2008). Assessing land-use statistics to model land cover change in a mountainous landscape in the European Alps. *Ecological Modelling*, 212(3–4), 460–471. <https://doi.org/10.1016/j.ecolmodel.2007.10.050>
- [8] Müller, D., & Munroe, D. K. (2008). Changing rural landscapes in Albania: Cropland abandonment and forest clearing in the postsocialist transition. *Annals of the Association of American Geographers*, 98(4), 855–876. <https://doi.org/10.1080/00045600802262323>
- [9] Schirpke, U., Leitinger, G., Tappeiner, U., & Tasser, E. (2012). SPA-LUCC: Developing land-use/cover scenarios in mountain landscapes. *Ecological Informatics*, 12, 68–76. <https://doi.org/10.1016/j.ecoinf.2012.09.002>
- [10] Minár, J., Krcho, J., & Evans, I. S. (2016). Geomorphometry: Quantitative Land-Surface Analysis. In *Reference Module in Earth Systems and Environmental Sciences*. Elsevier Inc. <https://doi.org/10.1016/b978-0-12-409548-9.10260-x>
- [11] Minár, J., Drăguț, L., Evans, I. S., Feciskanin, R., Gallay, M., & Popov, A. B., in review. Physical geomorphometry for the elementary land surface segmentation and digital geomorphological mapping, *Earth-Science Reviews*.
- [12] Feranec, J., Jaffrain, G., Soukup, T., & Hazeu, G. (2010). Determining changes and flows in European landscapes 1990–2000 using CORINE land cover data. *Applied Geography*, 30(1), 19–35. <https://doi.org/10.1016/j.apgeog.2009.07.003>

- [13] Evans, I. S. (1972). General geomorphometry, derivatives of altitude and descriptive statistics. In R. J. Chorley (Ed.), *Spatial Analysis in Geomorphology* (pp. 17–90). Methuen, London.
- [14] Krcho, J. (1973). Morphometric analysis of relief on the basis of geometric aspect of field theory. *Acta Geographica Universitas Comenianae, Geographico-Physica*, 1, 7–233.
- [15] Minár, J., Evans, I. S., & Jenčo, M. (2020). A comprehensive system of definitions of land surface (topographic) curvatures, with implications for their application in geoscience modelling and prediction. *Earth-Science Reviews*, 211, 103414. <https://doi.org/10.1016/j.earscirev.2020.103414>
- [16] Shary, P. A. (1995). Land surface in gravity points classification by a complete system of curvatures. *Mathematical Geology*, 27(3), 373–390. <https://doi.org/10.1007/BF02084608>
- [17] Minár, J., Bandura, P., Holec, J., Popov, A., Drăguț, L., Gallay, M., Hofierka, J., Kaňuk, J., & Evans, I. S. (2018). Physically-based land surface segmentation: Theoretical background and outline of interpretations. *Geomorphometry*, 1–4. <https://doi.org/10.7287/peerj.preprints.27075v1>
- [18] Bandura, P., Minár, J., & Bielik, M. (2021). Physically based morphostructural land surface segmentation: Case of the Alps and Western Carpathians. *Transactions in GIS*, 25(5), 2394–2418. <https://doi.org/10.1111/tgis.12847>
- [19] Gallant, J. C., & Hutchinson, M. F. (2011). A differential equation for specific catchment area. *Water Resources Research*, 47(5), 1–14. <https://doi.org/10.1029/2009WR008540>
- [20] Beven, K. J., & Kirkby, M. J. (1979). A physically based, variable contributing area model of basin hydrology. *Hydrological Sciences Bulletin*, 24(1), 43–69. <https://doi.org/10.1080/02626667909491834>
- [21] Weiss, A. D. (2001). Topographic position and landforms analysis. *The Nature Conservancy*.
- [22] Riley, S. J., DeGloria, S. D., & Elliot, R. (1999). A Terrain Ruggedness Index that Quantifies Topographic Heterogeneity. *Intermountain Journal of Sciences*, 5(1–4), 23–27.
- [23] Moore, I. D., Grayson, R. B., & Ladson, A. R. (1991). Digital terrain modelling: A review of hydrological, geomorphological, and biological applications. *Hydrological Processes*, 5(1), 3–30. <https://doi.org/10.1002/hyp.3360050103>
- [24] Melton, M. A. (1965). The Geomorphic and Paleoclimatic Significance of Alluvial Deposits in Southern Arizona Author(s): *The Journal of Geology*, 73(1), 1–38. <https://www.jstor.org/stable/30066379>
- [25] Marchi, L., & Dalla Fontana, G. (2005). GIS morphometric indicators for the analysis of sediment dynamics in mountain basins. *Environmental Geology*, 48(2), 218–228. <https://doi.org/10.1007/s00254-005-1292-4>
- [26] Climate Atlas of Slovakia (2015). Slovak Hydrometeorological Institute. <https://klimat.shmu.sk/kas/>
- [27] DATAcube (2020). Statistical office of the Slovak Republic. <http://datacube.statistics.sk/>
- [28] Millington, J. D. A., Perry, G. L. W., & Romero-Calcerrada, R. (2007). Regression techniques for examining land use/cover change: A case study of a mediterranean landscape. *Ecosystems*, 10(4), 562–578. <https://doi.org/10.1007/s10021-007-9020-4>

Mapping gully affected areas based on Sentinel 2 imagery and digital elevation model

XiaoHui Huang

Key laboratory of Virtual Geographic Environment,
 Ministry of Education
 Nanjing Normal University
 Nanjing, China
 xiaohui_wong@njnu.edu.cn

LiYang Xiong

Key laboratory of Virtual Geographic Environment,
 Ministry of Education
 Nanjing Normal University
 Nanjing, China
 xiongliyang@njnu.edu.cn

Abstract—Gully poses a great threat to agricultural production and ecological environment. Mapping accurate gully affected areas plays an important role in regional environmental monitoring and management. In this paper, an object-based image analysis method based on Google Earth Engine (OBIA-GEE) for mapping gully affected areas was proposed by using Sentinel 2 imagery and AW3D 30 DEM data. The method utilized the simple non-iterative clustering (SNIC) segmentation and the random forest (RF) algorithm to segment imagery and map gully affected areas. And terrain skeleton lines were further used to optimize the mapping results. The proposed method was applied to five study areas with different landform types on the Chinese Loess Plateau, and the results showed that the method achieved good performance with the overall accuracy of 86.44%, user's accuracy of 84.97%, and producer's accuracy of 83.90%. The OBIA-GEE method provides the possibility of large-scale gullies mapping, which is beneficial to monitor gullies and manage soil erosion.

I. INTRODUCTION

Gully erosion is a typical form of soil erosion that shapes surface morphology, resulting in development of gullies [1-2]. Accurately mapping gully affected areas not only provides a basis for regional soil and water conservation but also provides important guidance for regional environmental management [3].

There are several gully affected areas mapping methods, including visual interpretation methods (VIM), pixel-based methods (PBM), object-based image analysis (OBIA) methods and deep learning (DL) methods, but the performance of these methods still need to be improved. The VIM method relies on manual visualization, which is labour intensive and time consuming [4]. The PBM based on remote sensing imagery and digital elevation model (DEM) are subject to the phenomena of salt and pepper noise and the topographic features of different study areas [3, 5], while these can be avoided by the OBIA method. The OBIA method can improve the mapping's accuracy to some extent [6, 7], but the accuracy at a large scale still needs to be improved, mainly due to the limitations of image resolution [8]. Studies have used less costly high-resolution Google Earth images with DEM data to map gully affected areas [9], but Google Earth images do not provide a clear enough spectral signal to distinguish gullies with drastic changes in internal morphology [10, 11]. Besides, the DL methods are limited to a large amount of pixel-level or object-level sample data to perform well [12].

Considering gully affected areas have distinct geometric features, textural information, topographic features, and complex dynamic spectral characteristics [13], the OBIA method and spectral information as well as phenological indicators based on temporal patterns, such as normalized difference vegetation index (NDVI), should be used to map gully affected areas. The Google Earth Engine (GEE) platform has gradually become an important platform for large-scale geological analysis [14-16]. And Sentinel-2 images offer the possibility of mapping gully affected areas [17-18]. Therefore, the objective of this paper was to propose an accurate object-based image analysis method based on Google Earth Engine (OBIA-GEE) for large-scale Loess Plateau gully affected areas mapping.

II. MATERIALS AND METHODS

A. Materials

Gully erosion is very serious and the degree of development of loess gullies varied on the Loess Plateau [19, 20]. Hence, five typical Loess Plateau erosion areas representing different landform types were selected as the study area herein (Fig. 1(a-e)). The specific definition of a gully affected area is that the upper boundary is along the gully shoulder line, and the lower boundary is the channel with a flow accumulation threshold area greater than 50 km² according to the boundary of erosion and hydrology [21].

All Sentinel 2 surface reflectance data (https://developers.google.com/earth-engine/datasets/catalog/COPERNICUS_S2_SR) with less than 20% cloudiness in 2020 were selected and masked cloud on GEE. The median images of red, green, blue, NIR bands and NDVI index were obtained every three months as a unit, and a total of 20 images were produced to provide dynamic time series spectral information. In addition, AW3D30 DEM data derived from GEE (https://developers.google.com/earth-engine/datasets/catalog/JAXA_ALOS_AW3D30_V1_1) with 30-meter resolution were used to calculate topographic factors and terrain textural information. A total of 5,150 training samples in point format were generated randomly by the randomPoints function and manually labelled as gully or non-gully on GEE (Fig. 1(a-e)). The validation samples in object format were manually drawn based on high-resolution Google Earth images,

having an 8 km² draw for each study area for a total of 40 km² (Fig. 1(V1-V10)).

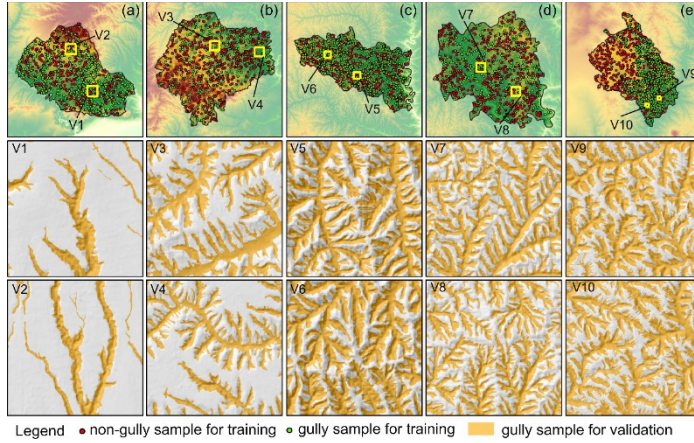


Figure 7. Map of the study area and samples for training and validation. (a) Loess tablelands, SA1; (b) Loess long-ridge fragmented tablelands, SA2; (c) Loess ridge hills and gullies, SA3; (d) Loess hills and gullies, SA4; (e) Loess aeolian and dune transition zones, SA5. The distribution of training samples (a-b) and validation samples (V1-V10) for each study area.

B. Methods

This paper proposed an object-based image analysis method based on Google Earth Engine (OBIA-GEE) for mapping large-scale loess gully affected areas. The main steps were (i) image segmentation, which used SNIC algorithm to create objects based on heterogeneity of each pixel value, (ii) feature selection and random forest, which calculated four types of features selected herein as input data to the RF algorithm to map gully affected areas, and (iii) terrain skeleton utilization for optimization and accuracy assessment, which improved mapping results by removing river areas from gully affected areas and assessed mapping accuracy based on object samples. Fig. 2 shows the techniques flow chart.

C. Image Segmentation

Principal component analysis (PCA) was performed using spectral median images of Sentinel-2 with 10-meter resolution to extract the principal components herein. The top five PCA components were selected for image segmentation. The super-pixel image segmentation method, simple non-iterative clustering (SNIC) algorithm on GEE was used for segmentation due to its superior segmentation performance [22]. Considering the irregular characteristics of gully affected areas and comparing different segmentation results with different parameter sets, the main parameters of SNIC algorithm were set: size = 8, compactness = 0.1, connectivity = 8, and neighbourhood size = 256.

D. Feature Selection and Random Forest

Four types of features with a total of 50 were calculated for each object after image segmentation, including spectral, textural, geometric and topographic features. The spectral median images of red, green, blue, NIR and NDVI were acquired, for a total of 20 images. Topographic factors with slope, surface cut depth (SCD), and positive and negative terrain (PNT) indices were calculated herein to provide terrain information [23]. The terrain textural information was obtained by utilizing the gray level co-occurrence matrix (GLCM) with a 3×3 kernel size for the above three topographic factors, and a total of 24 images of textural information were produced [24].

The geometric features of each object with area, height and width were calculated herein.

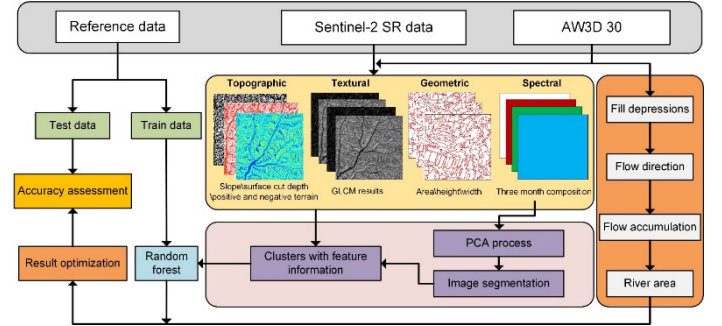


Figure 8. Techniques flow chart.

Random forest (RF) algorithm is one of the most popular predictive classification algorithms due to its simplicity and ease of implementation and superior classification performance [25]. In this paper, the smileRandomForest classifier on GEE was applied to map gully affected areas, with 50 features and 5,150 training samples as input data, and the number of decision trees was set to 100 with other parameters (e.g., bagFraction set to 0.5, maxNodes set to no limit) set to default according to the RF training results.

E. Optimization and Accuracy Assessment

Terrain skeleton lines obtained by the hydrological analysis of AW3D30 DEM data with a flow accumulation threshold of 50 km² were used to optimize the OBIA-GEE mapping results according to the definition of gully affected area herein. Then the distance accumulation was applied to obtain the river area, and the extracted terrain skeleton lines with the slope of DEM data were used as the input data. Finally, river areas were intersected with the gully affected area mapping results to obtain the gully affected areas with the river removed.

To judge the accuracy of the mapping results, the confusion matrix approach was used to perform accuracy assessment herein [26]. The overall accuracy (OA), producer's accuracy (PA) and user's accuracy (UA) were calculated for mapping results after optimization.

III. RESULTS

Table I shows the accuracy assessment of the gully affected area results for each study area and all study areas. The OA of all study areas reached 86.44%, and the PA and UA were 83.90% and 84.97%, indicating that the proposed method was applicable to the various landform types of the Loess Plateau and had good performance. The OA of gully affected areas in each study area was higher than 81%. SA3 (87.15%), SA2 (84.37%), and SA4 (82.68%) had higher UA values, which means that commission error was smaller and the omission error was relatively larger in the area of intense surface erosion. Moreover, SA1 (91.16%) and SA5 (90.34%) had higher PA values, which means that the omission error was smaller and the commission error was relatively larger in the area of less erosion intensity.

TABLE III. THE CONFUSION MATRIX OF THE GULLY AFFECTED AREA RESULTS FOR EACH STUDY AREA AND ALL STUDY AREAS.

Study area	PA (%)	UA (%)	OA (%)
SA1	91.16	83.81	95.67

SA2	76.41	84.37	86.01
SA3	83.32	87.15	83.54
SA4	79.96	82.68	81.90
SA5	90.34	85.46	85.37
All study areas	83.90	84.97	86.44

Fig. 3 shows magnified views of mapping results for each study area with different landform types. The mapping results had reasonable structural characteristics, which reflected the spatial continuity of the gullies and the suitability of the method for different landforms. Magnified views of SA2, SA3 and SA4, where the development of gullies was higher and the area of inter-gully land was smaller, so some inter-gully areas were misclassified as gully affected areas. For the loess tablelands (SA1), the gully affected areas were generally mapped accurately. For the loess-aeolian and dune transition zones (SA5), the erosion degree was relatively small, and the mapping results of the gully affected areas were consistent with the actual distribution.

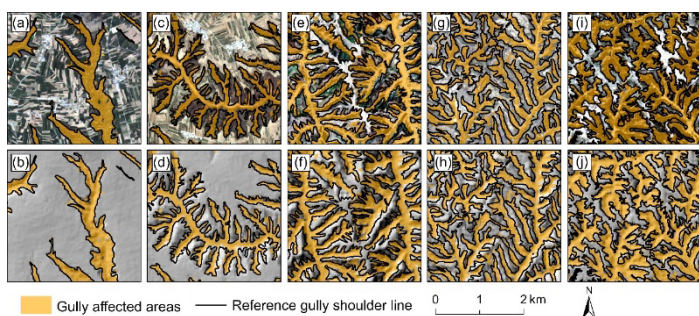


Figure 9. Gully affected area mapping results were overlaid on Sentinel images and DEM images. (a) and (b): SA1; (c) and (d): SA2; (e) and (f): SA3; (g) and (h): SA4; (i) and (j): SA5.

IV. CONCLUSIONS

An OBIA-GEE method was proposed for the rapid mapping of large-scale loess gullies in this paper. By using the SNIC segmentation and RF algorithm with multiple features, the loess gully affected areas with different landform types were mapped. And terrain skeleton lines were used to optimize the gully affected area mapping results. The results showed that the method achieved good performance, with the OA of 86.44% for all study areas, the UA of 84.97%, and the PA of 83.90%. For each landform type, the OA was higher than 81.5%. Moreover, the OBIA-GEE method is convenient due to the advantages of GEE platform. The proposed method will be beneficial for studies related to monitoring gullies and managing soil erosion. This work also provides a new perspective for large-scale landform mapping and the basic idea of this method can be extended to map multiple types of topographic objects.

V. ACKNOWLEDGMENTS

This work was supported by National Natural Science Foundation of China (41930102, 41971333). The authors express their great thanks to everyone who have helped in the writing of this article.

REFERENCES

- [1] Maslov, B. S., 2005. Agricultural Land Improvement: Amelioration and Reclamation. Russian Academy of Agriculture Sciences, Russia, pp. 1–9.
- [2] Valentin, C., Poesen, J., Li, Y., 2005. Gully erosion: Impacts, factors and control. *Catena*. 63(2-3), 132-153. <https://doi.org/10.1016/j.catena.2005.06.001>.
- [3] Liu, K., Ding, H., Tang, G., Song, C., Liu, Y., Jiang, L., Zhao, B., Gao, Y., Ma, R., 2018. Large-scale mapping of gully-affected areas: An approach integrating Google Earth images and terrain skeleton information. *Geomorphology*. 314, 13-26. <https://doi.org/10.1016/j.geomorph.2018.04.011>.
- [4] Singh, B.M., 1977. Interpretation of satellite imagery for delineation of ravines. *J. Indian Soc. Remote Sensing*. 5(1), 31–34. <https://doi.org/10.1007/BF03025387>.
- [5] Whiteside, G. T., Boggs, G. S., Maier, S. W., 2011. Comparing object-based and pixel-based classifications for mapping savannas. *International Journal of Applied Earth Observation and Geoinformation*. 13(6), 884-893. <https://doi.org/10.1016/j.jag.2011.06.008>.
- [6] Blaschke, T., 2010. Object based image analysis for remote sensing. *ISPRS Journal of Photogrammetry and Remote Sensing*. 65(1), 2-16. <https://doi.org/10.1016/j.isprsjprs.2009.06.004>.
- [7] Karami, A., Khoorani, A., Noohegar, A., Shamsi, S. R. F., Moosavi, V., 2015. Gully Erosion Mapping Using Object-Based and Pixel-Based Image Classification Methods. *Environmental & Engineering GeoScience*. 21(2), 101–110. <https://doi.org/10.2113/gseegeosci.21.2.101>.
- [8] D'Oleire-Oltmanns, S., Irene, M., Dirk, T., Thomas, B., 2014. Detection of Gully-Affected Areas by Applying Object-Based Image Analysis (OBIA) in the Region of Taroudannt, Morocco. *Remote Sensing*. 6(9), 8287-8309. <https://doi.org/10.3390/rs6098287>.
- [9] Liu, K., Ding, H., Tang, G., Zhu, A., Yang, X., Jiang, S., Cao, J., 2017. An object-based approach for two-level gully feature mapping using high-resolution DEM and imagery: a case study on hilly loess plateau region. *Chinese Geographical Science*. 27, 415–430. <https://doi.org/10.1007/s11769-017-0874-x>.
- [10] Potere, D., 2008. Horizontal Positional Accuracy of Google Earth's High-Resolution Imagery Archive. *Sensors*. 8(12), 7973-7981. <https://doi.org/10.3390/s8127973>.
- [11] Ortí, M. V., Winiwarter, L., Corral-Pazos-de-Provens, E., Williams, J. G., Bubenzer, O., Höfle, B., 2021. Use of TanDEM-X and Sentinel Products to Derive Gully Activity Maps in Kunene Region (Namibia) Based on Automatic Iterative Random Forest Approach. *IEEE Journal of Selected Topics in Applied Earth Observations and Remote Sensing* 14, 607-623. Doi: 10.1109/JSTARS.2020.3040284.
- [12] Liu, B., Zhang, B., Feng, H., Wu, S., Yang, J., Zou, Y., Siddique, K. H. M., 2021a. Ephemeral gully recognition and accuracy evaluation using deep learning in the hilly and gully region of the Loess Plateau in China. *International Soil and Water Conservation Research*. <https://doi.org/10.1016/j.iswcr.2021.10.004>.
- [13] Nwaogu, C., Okeke, O. J., Assuah Adu, S., Babine, E., Pechanec, V., 2018. Land Use—Land Cover Change and Soil-Gully Erosion Relationships: A Study of Nanka, South-Eastern Nigeria Using Geoinformatics. In: Ivan, I., Horák, J., Inspektor, T. (eds) Dynamics in Glscience. GIS OSTRAVA 2017. Lecture Notes in Geoinformation and Cartography. Springer, Cham. https://doi.org/10.1007/978-3-319-61297-3_22.
- [14] Gorelick, N., Hancher, M., Dixon, M., Ilyushchenko, S., Thau, D., Moore, R., 2017. Google Earth Engine: Planetary-scale geospatial analysis for everyone. *Remote Sensing of Environment*. 202, 18-27. <https://doi.org/10.1016/j.rse.2017.06.031>.
- [15] Huang, H., Chen, Y., Clinton, N., Wang, J., Wang, X., Liu, C., Gong, P., Yang, J., Bai, Y., Zheng, Y., Zhu, Z., 2017. Mapping major land cover dynamics in Beijing using all Landsat images in Google Earth Engine. *Remote Sensing of Environment*. 202, 166-176. <https://doi.org/10.1016/j.rse.2017.02.021>.
- [16] Dong, J., Xiao, X., Menarguez, M. A., Zhang, G., Qin, Y., Thau, D., Biradar, C., Moore, B., 2016. Mapping paddy rice planting area in northeastern Asia with Landsat 8 images, phenology-based algorithm and Google Earth Engine. *Remote Sensing of Environment*. 185, 142-154. <https://doi.org/10.1016/j.rse.2016.02.016>.
- [17] Makaya, N. P., Mutanga, O., Kiala, Z., Dube, T., Seutloali, K. E., 2019. Assessing the potential of Sentinel-2 MSI sensor in detecting and mapping the spatial distribution of gullies in a communal grazing landscape. *Physics and Chemistry of the Earth*. 112, 66-74. <https://doi.org/10.1016/j.pce.2019.02.001>.
- [18] Forkuor, G., Dimobe, K., Serme, I., Tondoh, J. E., 2018. Landsat-8 vs. Sentinel-2: examining the added value of sentinel-2's red-edge bands to land-use and land-cover mapping in Burkina Faso. *GIScience & Remote*

- Sensing. 55(3), 331-354.
<https://doi.org/10.1080/15481603.2017.1370169>.
- [19] Zhang, X., Walling, D. E., Qunie, T. A., Wen, A., 1997. Use of reservoir deposits and caesium-137 measurements to investigate the erosional response of a small drainage basin in the rolling loess plateau region of China. Land Degradation & Development. 8(1), 1-16.
[https://doi.org/10.1002/\(SICI\)1099-145X\(199703\)8:1<1::AID-LDR240>3.0.CO;2-X](https://doi.org/10.1002/(SICI)1099-145X(199703)8:1<1::AID-LDR240>3.0.CO;2-X).
- [20] Zhao, G., Mu, X., Wen, Z., Wang, F., Gao, P., 2013. Soil erosion, conservation, and ecoenvironment changes in the loess plateau of China. Land Degradation & Development. 24(5), 499–510.
<https://doi.org/10.1002/lde.2246>.
- [21] Chen, L., et al., 2017. The First China Census for Water—National Soil and Water Conservation Survey Report.
- [22] Koo, Y., Xie, H., Ackley, S. F., Mestas-Nuñez, A. M., Macdonald, G. J., Hyun, C., 2021. Semi-automated tracking of iceberg B43 using Sentinel-1 SAR images via Google Earth Engine. The Cryosphere 15, 4727–4744.
<https://doi.org/10.5194/tc-15-4727-2021>.
- [23] Li, C., Li, F., Dai, Z., Yang, X., Cui, X., Luo, L., 2020a. Spatial variation of gully development in the loess plateau of China based on the morphological perspective. Earth Sci. Inform. 13, 1103-1117.
<https://doi.org/10.1007/s12145-020-00491-4>.
- [24] Haralick, R. M., 1979. Statistical and structural approaches to texture. Proc. IEEE. 67(5), 786-804. doi: 10.1109/PROC.1979.11328.
- [25] Ding, H., Na, J., Jiang, S., Zhu, J., Liu, K., Fu, Y., Li, F., 2021. Evaluation of Three Different Machine Learning Methods for Object-Based Artificial Terrace Mapping—A Case Study of the Loess Plateau, China. Remote Sensing. 13(5), 1021. <https://doi.org/10.3390/rs13051021>.
- [26] Stehman, S. V., 1997. Selecting and interpreting measures of thematic classification accuracy. Remote Sensing of Environment. 62(1), 77-89.
[https://doi.org/10.1016/S0034-4257\(97\)00083-7](https://doi.org/10.1016/S0034-4257(97)00083-7).

Applicability of longitudinal profiles for glacial cirque classification

Tian Jia², Ping Fu

Department of Geographical Sciences, University of Nottingham Ningbo China
Ningbo, China

Cheng-Zhi Qin

²State Key Laboratory of Resources and Environmental Information System, Institute of Geographic Sciences and Natural Resources Research, CAS, Beijing, China

qincz@lreis.ac.cn

Vladimir Brusic

Department of Computer Science, University of Nottingham Ningbo China
Ningbo, China

Abstract— Accurate classification of cirques is essential for studying paleoglacier activities. Longitudinal-profile-based classification has advantages over other methods such as expert classification and the methods that utilize morphometric parameters. Longitudinal profiles method first deploys exponential function to fit the longitudinal profiles of individual cirque samples and then fits a linear classifier based on the exponential coefficient and the cirque height of the cirque sample set to classify cirque candidates as cirques or non-cirques. However, the existing studies have applied and evaluated longitudinal profile based classification using only small number (i.e., several dozens) of cirque sample-set collected within small study areas. In this study we evaluated the applicability of the longitudinal profile method to a larger number of glacial cirques from a larger area. The cirque sample set (256 cirques and 101 non-cirques) of this study was extracted from the southeastern Tibetan Plateau. The original linear classifier fitted in previous studies, and the linear as well as non-linear classifiers fitted from the new sample set were evaluated. The classification accuracy results reveal that the longitudinal profile based classification method was applicable, and that with the non-linear classifiers shows the improved performance than the refitted linear classifier, when both were better than that with original linear classifier.

I. INTRODUCTION

The cirque is a glacial erosion landform that reflects the glacial imprint on a region as the origin of the mountain glacier. Accurate cirque classification facilitates better understanding and study of the developmental mechanisms of cirques and their coupling with the climate processes [1,2].

Cirque classification methods have slowly evolved from qualitative to quantitative approaches. Qualitative methods, such as expert classification, is based on the experience and knowledge of experts obtained from field observations [3]. However, expert classification is time-consuming, laborious, and difficult to explain and reproduce, making it less suitable for classifying cirques across large areas. Expert classification is descriptive and usually based on qualitative definition, making classification results subjective to different experts' understanding of cirques [4].

Currently there are two types of quantitative cirque classification methods: the morphometric based method, and the longitudinal profile based cirque classification. The former utilizes six morphometric parameters (including length (L), width (W), height (H), L/W, L/H, and area) to cluster cirque candidates. The cluster descriptions are defined by statistics of morphometric parameters that form classification rules [5–7]. However, the morphometric parameters represent insufficiently the spatial structural information of the cirques. The cluster results of the morphometric parameters method do not correspond well to the qualitative expert classification results.

The longitudinal profile based method for cirque classification uses longitudinal profile of cirque to differentiate cirques and non-cirques. Longitudinal profiles of cirques can effectively reflect spatial structures of cirques – that information is useful for understanding the history of development of studied cirques [1,8]. In this classification method, an exponential function shown in Equation (1) is first fitted on the longitudinal profile through the steepest part of the headwall terminated at valley-head point of each individual cirque or non-cirque sample. Then a linear discriminant function based on the fitting parameter of each longitudinal profile, c-value in Equation (1), and the height derived from the profile is built and used to classify cirque candidates into cirques or non-cirques [9].

$$y = (1 - x)e^{cx} \quad (1)$$

Currently, this method has been verified only through classifying a total of 55 samples in the Alps and the High Sudetes, and showed reasonable results (overall accuracy is 92.7% and F1 score is 0.91) [9]. To our best knowledge, this method has not been verified neither with a large sample size, nor within other large regions. This study focuses on the assessment of the performance of longitudinal profile-based cirque classification method on large-amount cirque samples across large area, which conducts a preliminary test with both linear and new non-linear classifiers.

II. EXPERIMENTAL DESIGN

The experiment is designed to evaluate the applicability of the longitudinal profile method for cirque classification on large-number of samples in a large test area (Fig. 1).

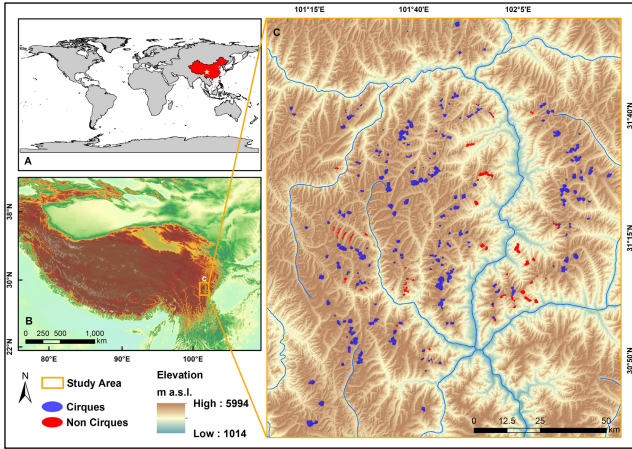


Figure 1. Map of the study area and samples of cirques and non-cirques manually derived in the study area. This area is in the Mt. Daxue and Mt. Qionglai of the Hengduan Range on the southeastern Tibetan Plateau.

A. Study area and data

The study area is in the Mt. Daxue and Mt. Qionglai of the Hengduan Range on the southeastern Tibetan Plateau (Fig. 1). The region is abundant in Quaternary palaeoglacial landforms and has been studied by paleoglacier mapping and reconstruction.

The sample set collected in this area includes 256 typical cirques and 101 non-cirques with cirque-like forms (Fig. 1). It is distinctively larger than the sample set (23 cirques and 32 non-cirques) reported in a related study [9]. The samples were manually delineated based on visual interpretation on Google Earth. ALOS PALSAR RTC (with 12.5-m resolution) was used to derive longitudinal profiles of samples [10].

B. Experimental flow design

The longitudinal profile based cirque classification has two input parameters: the longitudinal profile and the cirque height extracted for each sample or cirque-like object. In this study, the use of longitudinal profile is the median axis of cirque that through the headwall and floor terminated at the cirque threshold. It differs from the Krause et al.'s profile through the steepest part of the headwall terminated at valley-head point that caused by

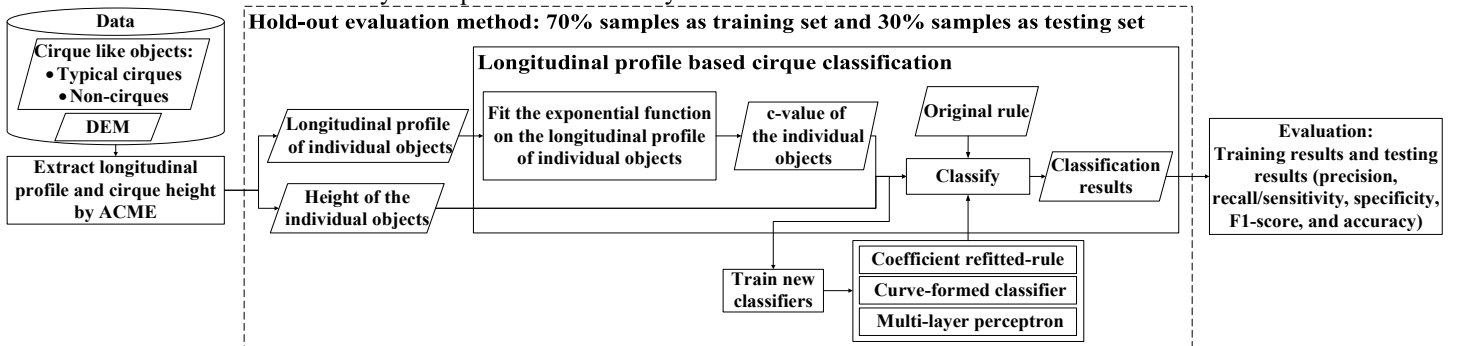


Figure 2. Flow chart for the experiment.

III. RESULTS

Examples of the longitudinal profile of a cirque and a non-cirque corresponding normalized profiles with c-value are shown in Fig. 3a and 3b. The concavity of cirque candidates is decreased with c-value increasing, with a c-value of zero indicating that the cirque candidates consist of a straight slope. Fig. 3c shows fitted curves of cirques and non-cirques, in which

the aims of this study is differentiating cirques and non-cirques rather than differentiating cirque and non-cirque valley head [9]. The longitudinal profile is generated by assigning the elevation of DEM to the median axis of samples that is extracted by an GIS tool in ArcMap named Automated Cirque Metric Extraction (ACME) **Error! Reference source not found.**. The exponential function is fitted to the longitudinal profiles of training samples of cirques. The c-value of the fitted exponential function together with the cirque profile height is used to build rules for classification of cirque candidates into cirques or non-cirques. The original classification rules, built by a linear classifier (or discriminant function), are shown as Equation (2): D1 less than 0 means cirque and D1 larger than 0 means non-cirque) with the fitted c-value and the height of longitudinal profile, based on the study in the Alps and the High Sudetes based on 55 samples [9].

$$D1 = 400 \times (c\text{-value}) - Height + 500 \quad (2)$$

The original classification rules can be directly applied to our study area for testing the extrapolation applicability of these rules. Alternatively, parameter-refitting can be applied whereby the coefficients in the original rules can be first updated with the c-value fitted with the training samples in our study area and then applied to classification. Direct application of the c-value is called “original-rule” while parameter refitting is called “coefficient refitted-rule”. In addition to these two rules based on linear classifier, non-linear classifier can also be explored for this method. This study further tested the adoption of non-linear classifiers, i.e., a curve-formed classifier, and a machine learning classifier (multi-layer perceptron).

The experiment workflow is shown in (Fig. 2). The hold-out method is applied to the sample set for testing the classification method with coefficient refitted-rule and non-linear classifiers. The sample set was randomly separated, with 70% of cirque and non-cirque samples used for training and the remaining 30% for testing. For comparing classification accuracy between application of the original-rule, the coefficient refitted-rule and the two non-linear classifiers, the original-rule was also evaluated by the training set and test set separately.

Classification indices (i.e., precision, recall/sensitivity, specificity, F1-score, and accuracy) were calculated for evaluating the performance of cirque classification methods.

the blue dashed line and red dashed line represent the fitted curve of median c-value in cirques and non-cirques, respectively. The median c-value of cirques is around -1.5 and the median c-value of non-cirques is around -0.2. The actual cirque profile is concave under past glacial erosion, meaning the c-value should be less than zero. However, Fig. 3c shows three c-value of profiles higher than zero, which might be because there are errors between profiles extracted by the median axis and actual profiles of a few cirque candidates.

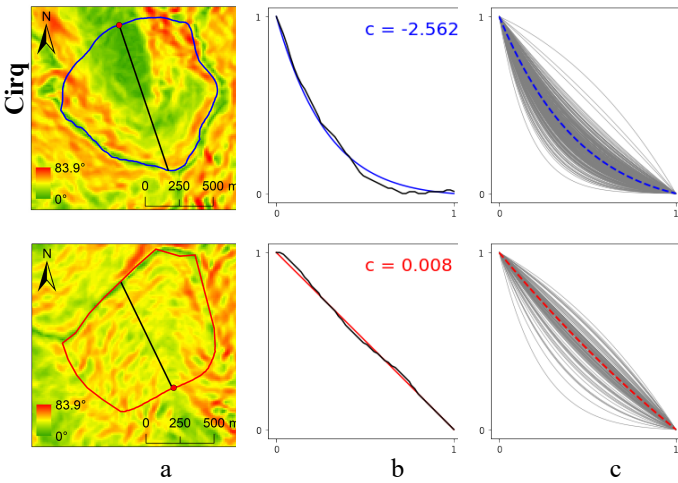


Figure 3. Examples of the longitudinal profiles of cirque and non-cirque based on slope map (a) and corresponding fitted profiles with c-value (b). The fitted curves for the longitudinal profiles of cirques and non-cirques (c).

Fig. 4 shows the distribution of height and c-value of cirque and non-cirques, and the linear discriminant function refitted by the training samples in the study area. The linear discriminant function of the coefficient-refitted rule is shown in Equation (3).

The non-linear curve-formed classifier is shown in Equation (4).

$$D2 = 485.7 \times (c\text{-value}) - Height + 667.7 \quad (3)$$

$$D3 = 666.9 \times (c\text{-value})^3 + 2707.4 \times (c\text{-value})^2 + 3540.3 \times (c\text{-value}) - Height + 1701.7 \quad (4)$$

Table I shows classification accuracy of the longitudinal profile cirque classification method using linear and non-linear

classifiers under test. The results indicate that classification using the original rule ($F1=0.9$ for training set, and $F1=0.92$ for test set) is inferior to all other methods: coefficient-refitted rule ($F1=0.93$ for training set, and $F1=0.96$ for test set), curve-formed rule ($F1=0.95$ for both training and test sets), and multilayer perceptron ($F1=0.96$ for training set, and $F1=0.94$ for test set). The original rule shows very high sensitivity but modest specificity (51.4% and 54.8% for training and test sets, respectively) while other classifiers have higher specificity (74.3%-91.6%) and lower sensitivity (93.4%-98.6%). The original rule will produce more false positives than other rules, while other three classifiers will misclassify 4-6% of true cirques as non-cirques.

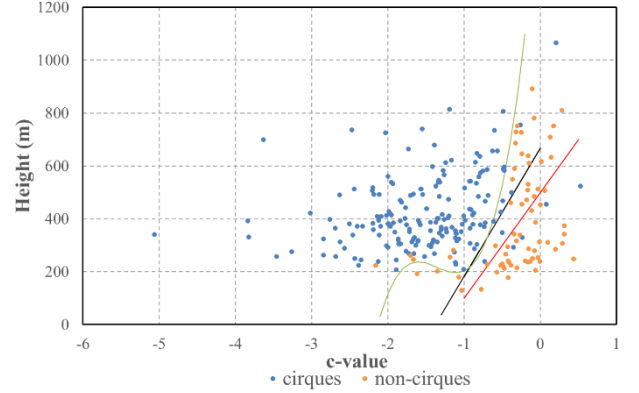


Figure 4. Scatter plot of the c-value and cirque height from training set in this study. Red line is original linear discriminant line (the function $D1$ as Equation (2)). And the coefficient refitted linear discriminant line (the function $D2$ as Equation (3)) is in black color. Green curve is the non-linear, curve-formed classifier (the function $D3$ as Equation (4)).

TABLE I. COMPARISON OF CLASSIFICATION ACCURACY FROM METHODS WITH LINEAR AND NON-LINEAR CLASSIFIERS RESPECTIVELY.

Classification indices	Linear classifier				Non-linear classifier			
	Original rule		Refitted rule		Curve-formed classifier		Multilayer perceptron	
Precision	83.80%	84.40%	90.50%	92.60%	96.60%	94.80%	95.80%	93.90%
Recall/Sensitivity	97.80%	100.00%	95.60%	98.70%	93.40%	96.10%	96.30%	93.90%
Specificity	51.40%	54.80%	74.30%	80.70%	91.60%	87.10%	88.40%	87.50%
F1-score	0.90	0.92	0.93	0.96	0.95	0.95	0.96	0.94
Accuracy	84.80%	86.90%	89.60%	93.50%	92.90%	93.50%	94.20%	91.80%
	CL	CL	DF	CL	DF	CL	DF	CL

a. DF: Data fitting, CL: Classification

on visual interpretation that is not automated. Comparatively, the multi-layer perceptron classifier is automatic, which is convenient for wide applications.

V. CONCLUSION

In this study, the longitudinal profile based classification method shows improved performance in classifying cirques and non-cirques on the southeastern Tibetan Plateau with a large sample size, when the coefficient-refitted linear classifier and the two non-linear classifiers were adopted respectively. Further refinement of classification methods is likely to produce highly accurate cirque classification. In future work, we will also increase the number of manually mapped cirques and non-cirques in other areas on the southeastern Tibetan Plateau and explore other machine learning methods for further improvement of glacial cirque classification.

IV. DISCUSSION

The linear classifier originally used with the longitudinal profile based cirque classification method showed relatively poor performance (besides on the Recall/Sensitivity index) because of low specificity of cirque classification. The overall evaluation of the longitudinal profile classification of cirques using rule-of-thumb shows that all rules under test provide very good classification ($F1 \geq 0.9$) while the refitting and non-linear classifiers further improve classification ($F1 > 0.93$) (Table 1). Note that the curved-formed classifier shown in Fig. 4 is appropriate for differentiating cirque and non-cirques with statistically significant results in this dataset. However, it relied

VI. ACKNOWLEDGEMENTS

This study was supported by the National Natural Science Foundation of China (Grant No. 41971078 and No. 41871362).

REFERENCES

- [1] Barr, I.D., Spagnolo, M., 2015. Glacial cirques as palaeoenvironmental indicators: Their potential and limitations. *Earth-Science Reviews* 151, 48–78. <https://doi.org/10.1016/j.earscirev.2015.10.004>
- [2] Zhang, Q., Fu, P., Yi, C., Wang, N., Wang, Y., Capolongo, D., Zech, R., 2020. Palaeoglacial and palaeoenvironmental conditions of the Gangdise Mountains, southern Tibetan Plateau, as revealed by an ice-free cirque morphology analysis. *Geomorphology* 370, 107391. <https://doi.org/10.1016/j.geomorph.2020.107391>
- [3] Evans, I.S., Cox, N.J., 1995. The form of glacial cirques in the English Lake District, Cumbria. *zfg* 39, 175–202. <https://doi.org/10.1127/zfg/39/1995/175>
- [4] Evans, I.S., Cox, N.J., 2017. Comparability of cirque size and shape measures between regions and between researchers. *Zeitschrift für Geomorphologie*. Supplementary issues. 61, 81–103.
- [5] Gómez-Villar, A., Santos-González, J., González-Gutiérrez, R.B., Redondo-Vega, J.M., 2015. Glacial Cirques in the Southern Side of the Cantabrian Mountains of Southwestern Europe. *Geografiska Annaler: Series A, Physical Geography* 97, 633–651. <https://doi.org/10.1111/geoa.12104>
- [6] Ruiz-Fernández, J., Poblete-Piedrabuena, M.A., Serrano-Muela, M.P., Martí-Bono, C., García-Ruiz, J.M., 2009. Morphometry of glacial cirques in the Cantabrian Range (Northwest Spain). *zfg* 53, 47–68. <https://doi.org/10.1127/0372-8854/2009/0053-0047>
- [7] García-ruiz, J.M., Gómez-villar, A., Ortigosa, L., Martí-bono, C., 2000. Morphometry of glacial cirques in the central spanish pyrenees. *Geografiska Annaler: Series A, Physical Geography* 82, 433–442. <https://doi.org/10.1111/j.0435-3676.2000.00132.x>
- [8] Brook, M.S., Kirkbride, M.P., Brock, B.W., 2006. Cirque development in a steadily uplifting range: rates of erosion and long-term morphometric change in alpine cirques in the Ben Ohau Range, New Zealand. *Earth Surface Processes and Landforms* 31, 1167–1175. <https://doi.org/10.1002/esp.1327>
- [9] Krause, D., Fišer, J., Křížek, M., 2022. Morphological differences of longitudinal profiles between glacial cirques and non-glacial valley heads, described by mathematical fitting. *Geomorphology* 404, 108183. <https://doi.org/10.1016/j.geomorph.2022.108183>
- [10] Dataset: ASF DAAC 2022, ALOS PALSAR Radiometric Terrain Corrected high_res; Includes Material © JAXA/METI 2007. Accessed through ASF DAAC 21 February 2022. DOI: 10.5067/Z97HFCNKR6VA.
- [11] Spagnolo, M., Pellitero, R., Barr, I.D., Ely, J.C., Pellicer, X.M., Rea, B.R., 2017. ACME, a GIS tool for Automated Cirque Metric Extraction. *Geomorphology* 278, 280–286. <https://doi.org/10.1016/j.geomorph.2016.11.018>

Constructing a True 3-D Model of a Karst Cave Using an UAV

Guohua Gou, Haigang Sui, Sheng Wang, Qiming Zhou, Jianya Gong, Deren Li

State Key Laboratory Information Engineering in Surveying, Mapping and Remote Sensing Wuhan University

Wuhan, China

haigang_sui@263.net

Abstract— Karst caves constitute an essential element of natural landforms. Construction of an accurate 3-D model of karst caves is crucial to guide geological exploration, underground space development, and safety in building construction and operation. Karst caves' subterranean location and various challenges such as weak lighting, attenuated satellite positioning signals, texture degradation, and unstructured surface scenes make true 3-D modeling of underground spaces challenging. Current methods of true 3-D modeling rely mostly on expensive and complex lidar scanning combined with ground mobile platforms or supplemented light source photography and multi-view stereo reconstruction. However, these methods are costly for karst cave reconstruction. Our proposed method for reconstructing the true 3-D model of the cave relies on the adaptability of a depth camera to low light environments. It is based on the data captured by an onboard depth camera of a drone for visual autonomous positioning and the surface reconstruction of unstructured scenes. We reconstructed the true 3-D model of Xuansu Cave located in Chibi City, Hubei Province, China. Experimental results demonstrate that the proposed method has the potential to reconstruct the true 3-D model of the underground karst cave surface efficiently and with stability. Furthermore, the use of light and small drones equipped with depth cameras presents a low-cost solution. These drones provide fast and reliable exploration of underground caves and offer true 3-D model reconstruction capabilities.

I. INTRODUCTION

Karst caves are underground spaces formed through the process of karstification in soluble rocks and can differ in scale. The cave can have varying shapes, with some parts resembling squares and others resembling narrow promenades. Karst caves exhibit unique and intricate shapes and contain a complex structure of various features such as stalagmites, stone pillars, and stalactites. The complex composition of these natural features creates peculiar landscapes, as demonstrated in Figure 1. Karst caves are abundant in resources that include water, minerals, tourist attractions, historical and cultural significance, and more. Consequently, conducting an investigation and implementing management practices in underground spaces such as karst caves is vital in enhancing the 3-D monitoring and preservation of natural resources.



Figure 1 Xuansu Cave, located in Chibi City, Hubei Province, China

The traditional digital terrain model (DTM) uses pictures with 3-D effects to map on a flat 2-D base map to create a 3-D visual representation. It is a fundamentally 2-D model, sometimes referred to as a "2.5-D model". The "2.5-D" model only contains prefabricated textures with 3-D effects, making it viewable from only a fixed angle and limiting its ability to meet the observation needs of differing directions and heights of terrain and landforms. Additionally, the analysis function is identical to that of the 2-D model. Another "2.5-D" model renders elevation data from 2-D data to achieve a visual 3-D representation. While a certain level of 3-D analysis can be achieved through elevation data, the reconstruction method is not sophisticated enough to provide a detailed description of natural landforms such as caves with complex structures. A true 3-D model is the most intuitive representation of the real world. It is a digital space that reflects and expresses the ecological space in a certain range in a real, 3-D and time-series manner. It is a standardized product of new basic surveying and mapping and an essential new infrastructure that provides a unified spatial base for economic, social development, and informatization. Consequently, the development of a true 3-D model of the interior surface of a scene like a cave has become one of the most direct and efficient methods for the investigation and monitoring of underground space resources. Generally, the true 3-D model of underground space can be constructed by various methods, including airborne laser scanning (Airborne

Laser Scanner, ALS) [1–3], terrestrial laser scanning (Terrestrial Laser Scanner, TLS) [1,2], Restoring Structure-Motion from Multi View Stereo (SfM-MVS) [4,5], and Simultaneous Localization and Mapping (SLAM) technology. The scanning method typically depends on costly and bulky lidar equipment that requires a high load capacity for the mounting platform, and the material within the cave may cause the laser scanning to deteriorate. However, the SfM-MVS approach necessitates uniform lighting conditions in dark caves, necessitating the use of professional photographic lighting equipment, which can be challenging to acquire in large caves.

We have devised a method for constructing an accurate 3-D model of a cave using depth camera SLAM. We utilize a small quadrotor UAV as a mobile platform to conduct experiments in a cave situated in Chibi City, Hubei Province, China, as depicted in Figure 2. We provide a detailed description of the specific and experimental processes involved in the method, along with the analysis, below.



Figure 2 The UAV scanning the karst cave

II. METHODOLOGY

To mitigate the effects of lighting factors, we utilize only the depth image data obtained from the airborne depth camera to construct a 3-D model of the cave surface. Using a Truncated Signed Distance Field (TSDF) algorithm and a continuous input of depth image frame sequences, 3-D points with sensor uncertainty are fused to create a dense 3-D point cloud model. If a model point \bar{P}_i reappears in the point cloud fusion process and is observed by the depth image I_d again, we re-calculate its vertex coordinates \bar{v}_i and normal \bar{n}_i , as indicated by

Positioning Figures and Tables: Place figures and tables at the top and bottom of columns. Avoid placing them in the middle of columns. Large figures and tables may span across both columns. Figure captions should be below the figures; table heads should appear above the tables. Insert figures and tables after they are cited in the text. Use the abbreviation “Fig. 1”, even at the beginning.

$$\bar{v}_i = \frac{\bar{c}_i \bar{v}_i + \alpha v(u)}{\bar{c}_i + \alpha}, \text{ and } \bar{n}_i = \frac{\bar{c}_i \bar{n}_i + \alpha n(u)}{\bar{c}_i + \alpha}, \quad \text{Eq. 1}$$

where \bar{c}_i represents the weighted number of times the model point is observed, and $v(u)$ and $n(u)$ are the 3-D

points and their normal projected from pixel u in the depth image I_d to the world coordinate system, respectively. Different from the traditional point cloud fusion method [6], we introduce a confidence factor α , so that the number of observed model points \bar{c}_i is weighted average as

$$\bar{c}_i = \bar{c}_{i,pre} + \alpha. \quad \text{Eq. 2}$$

This is based on the assumption that the normalized radial distance γ of the depth camera measurement error from the center of photograph is Gaussian distributed, so α is expressed as

$$\alpha = e^{-\gamma^2/2\sigma^2}, \quad \text{Eq. 3}$$

where $\sigma = 0.6$ is the experience value.

Our point cloud fusion modeling method provides robust denoising results, especially for depth cameras at the consumer level with significant sensor uncertainty. Finally, to obtain the surface of the reconstructed scene, we use ray casting and trilinear interpolation to extract the zero-crossing surfaces that are implicitly stored in the TSDF voxel grid.

The usage of regular voxels to store TSDF data to manage and reconstruct the surface of the scene has the potential to be sparse [7]. However, this sparsity significantly wastes memory resources, increases the computational burden of the algorithm, and negatively affects system performance. To address these issues, we use a simple hashing scheme to compactly store, access, and update the implicit surface in our work. This approach enables us to achieve scalable true 3-D reconstruction in large-volume caves and significantly conserves the limited computing and storage resources. Unlike the practice of pre-setting the reconstruction range of rules [6,8], which is not feasible for unstructured underground caves due to their unknown and ever-changing geometry, our approach is more suitable for this type of environment. Additionally, to accommodate large-scale reconstructions, we employ a bidirectional CPU-GPU data flow scheme [7]. This is achieved by creating an active area, containing the reconstructed surface and a secure zone around the current depth camera perspective, which moves with the camera. To ensure efficient use of resources, when the camera moves beyond a certain distance from the current position, the voxel block data that was initially in the active region is streamed from the GPU and may either be saved to the CPU or to a disk. If the camera returns to the previously reconstructed area, the voxel block data for that region is then streamed from the CPU to the GPU in the same way. This combination of dataflow schema and hashing schema is ideal for the reconstruction of unstructured scenes, as it does not necessitate the reorganization of the hash table for input or output voxel blocks.

Obtaining accurate image poses is crucial before utilizing depth images for surface reconstruction. However, on UAV platforms, traditional pose estimation methods often fail due to the camera's fast movement, which leads to incorrect pose estimation results. To address this issue, we estimate the pose of the airborne depth camera in real-time, using the method of particle swarm template stochastic optimization [8]. However, in contrast to the existing literature [8], we adopt a sparse scene expression in our approach, wherein the number of particles participating in fitness calculations is limited by the active area constructed. Specifically, only the most effective pixels of the current frame can be projected to the sparse scene in the particle

swarm template. The particles that correspond to the surface of the scene and are located in the active region calculate their surface fitness and are processed in parallel on the GPU. The aim of this approach is to estimate the fast-moving camera's pose while also conserving the onboard computer's limited computing and storage resources, thereby expanding the UAV's operating range to a larger area. Our experiments demonstrate a remarkable enhancement in the efficiency of our position estimation method compared to the existing literature [8].

III. PRELIMINARY RESULT

Our mobile platform is the AMOV P450 UAV, which has a wheelbase of 450mm and a 1kg payload capacity. It comes equipped with an Intel RealSense D435i depth camera with an effective measurement distance of 8m. All of our experiments were conducted on the Nvidia Xavier NX embedded computing device, which boasts a six-core ARM Cortex-A57 CPU and a dual-core NVIDIA Denver 2.0 CPU that provide processing capabilities of 1.3 TFLOPS. The device is further equipped with 8GB of LPDDR4x RAM, along with a NVIDIA Volta GPU with 512 CUDA cores, and 16GB of high-speed HBM2 memory, enabling quick and efficient data transfer and processing. Our experiments were conducted in Xuansu Cave, an underground cave located in Chibi City, Hubei Province, China.

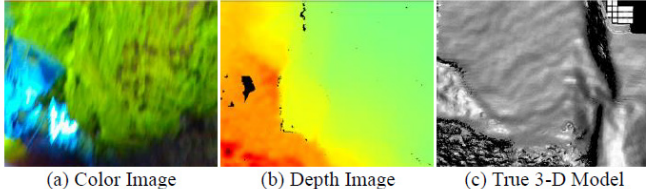


Figure 3 (a) and (b) represent the data acquired by the airborne depth camera, there is motion blur in (a), and (c) represents the real 3-D model reconstructed from its perspective.

Equipped with a depth camera and an onboard computer, the UAV scans the cave's interior. Our use of the path planning algorithm [9] results in a fully autonomous UAV reconstruction task process that requires no manual intervention. The path planning algorithm, proposed SLAM algorithm, and two-way communication channel between the UAV and the ground are all facilitated via the Robot Operating System mechanism on the airborne computer. Our experiments prove the effectiveness of the depth-only positioning method [8] due to the insignificant effect of motion blur on the depth image, as opposed to the color image, which could be affected. This observation is shown in Figure 3. The intel Nvidia Jetson Xavier NX computer processes the 320x240 depth images in real-time for UAV positioning, attitude determination, and scene reconstruction with a processing rate of 40 frames per second, significantly faster than the rate stated in the literature [8]. This speed is due to our method's beneficial usage of scene sparsity and active area constraints to accelerate stochastic optimization of particle swarm templates. Lighting fixtures were installed in the cave to enhance the reconstructed 3-D model's display, allowing for the color of the point cloud to be captured and utilized in rendering a true 3-D model in color. We present a tunnel of the reconstructed 3-D model in Figure 4. Figure 4 illustrates our method's ability to reconstruct the tunnel's basic geometric shape, with clear geometric texturing of the tunnel walls. Our approach largely reconstructs the scene's inherent geometric structure. Our positioning method relies solely on the depth image acquired by the depth camera for autonomous UAV positioning. While the color image obtained by the depth camera

is used only for rendering purposes, our method does not depend on color textures.

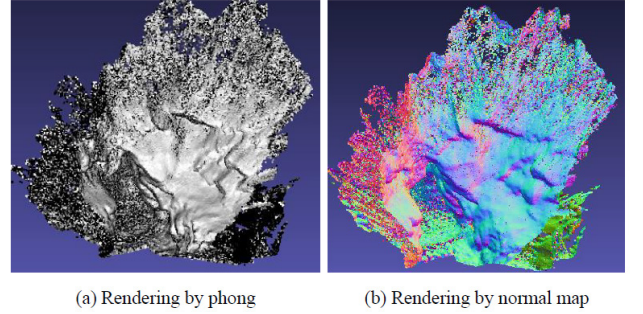


Figure 4 The true 3-D model of Xuansu Cave reconstructed using our method.

IV. DISCUSSION AND CONCLUSION

Despite challenges such as attenuated satellite positioning signals, weak lighting, texture degradation, and unstructured surface scenes, our use of a depth camera enables the UAV's autonomy in obtaining geometric information of the underground natural landforms. This results in successful high-precision real-time scene reconstruction and positioning.

Unfortunately, due to the limited measurement distance of current consumer level depth cameras, resulting in a considerable number of invalid depth values in depth images obtained in too open scenes, which severely impedes the application of autonomous reconstruction in large scenes. Besides enhancing the depth camera to increase its measurement range, constructing a path planning method for drones to scan close to the surface of the scene is a direction deserving researchers' attention.

REFERENCES

- [1] Tranzatto, M.; Mascarich, F.; Bernreiter, L.; Godinho, C.; Camurri, M.; Khattak, S.; Dang, T.; Reijgwart, V.; Loeje, J.; Wisth, D.; et al. CERBERUS: Autonomous Legged and Aerial Robotic Exploration in the Tunnel and Urban Circuits of the DARPA Subterranean Challenge. ArXiv 2022, abs/2201.07067.
- [2] Hudson, N.; Talbot, F.; Cox, M.; Williams, J.L.; Hines, T.; Pitt, A.; Wood, B.; Froushiger, D.; Surdo, K. Lo; Molnar, T.; et al. Heterogeneous Ground and Air Platforms, Homogeneous Sensing: Team CSIRO Data61's Approach to the DARPA Subterranean Challenge. ArXiv 2021, abs/2104.09053.
- [3] Tabib, W.; Goel, K.; Yao, J.W.; Boirum, C.; Michael, N. Autonomous Cave Surveying with an Aerial Robot. IEEE Trans. Robot. 2020, 38, 1016–1032.
- [4] Colón, A. Development of Virtual Cave Exploration Environment Using LiDAR and SfM Photogrammetry. Geological Society of America Annual Meeting. 2019, 51, 5:155-8.
- [5] Moore, A. Integrating 3-D modelling with Unmanned Aerial Vehicles in subterranean environments to aid archaeological stratigraphy. Ph.D. Thesis, Liverpool John Moores University, UK, 2020.
- [6] Newcombe, R.A.; Izadi, S.; Hilliges, O.; Molyneaux, D.; Kim, D.; Davison, A.J.; Kohli, P.; Shotton, J.; Hodges, S.; Fitzgibbon, A.W. KinectFusion: Real-time dense surface mapping and tracking. 2011 10th IEEE Int. Symp. Mix. Augment. Real. 2011, 127–136.
- [7] Nießner, M.; Zollhöfer, M.; Izadi, S.; Stamminger, M. Real-time 3-D reconstruction at scale using voxel hashing. ACM Trans. Graph. 2013, 32, 1–11.
- [8] Zhang, J.; Zhu, C.; Zheng, L.; Xu, K. ROSEFusion: Random Optimization for Online Dense Reconstruction under Fast Camera Motion. ACM Trans. Graph. 2021, 40, 56:1–56:17.
- [9] Zhou, B.; Zhang, Y.; Chen, X.; Shen, S. FUEL: Fast UAV Exploration Using Incremental Frontier Structure and Hierarchical Planning. IEEE Robot. Autom. Lett. 2020, 6, 779–786.

RPA flight pattern and GCP influence on SfM-MVS modeling of a stable landslide in SE Brazil

Carlos H. Grohmann, Helen Cristina Dias

Institute of Energy and Environment, Universidade de São Paulo, São Paulo, Brazil
guano@usp.br, helen.dias@usp.br

Guilherme P.B. Garcia, Camila Duelis Viana, Rebeca Durço Coelho

Institute of Geosciences, Universidade de São Paulo, São Paulo, Brazil
guilherme.pereira.garcia@usp.br, camila.viana@usp.br,
rebeca.coelho@usp.br

Abstract—In this article, we analyze how the flight paths of RPA surveys and the presence/absence of Ground Control Points (GCPs) will impact the surface reconstruction of a stable landslide in southeastern Brazil. We compare the SfM-MVS results from two surveys (2019/2021) in terms of their completeness, georeferencing, and morphometry. The 2019 flight consist of a simple grid pattern, without precise geometric control given by GCPs. In the 2021 campaign, four flight patterns (two simple grids and two cross-grids) were deployed. The data were processed as the individual flights as well as a combination of the two simple grids and two cross-grids. The combination of the simple grids resulted in the most complete DSM, at the expense of a larger processing time. The DSM from the combined cross-grids had fewer voids than those from the simple grids, but with the downside of requiring two flights and longer processing time. Our results indicate that one simple grid flight will be enough to produce a good reconstruction of the surface, with a short processing time.

I. INTRODUCTION

Remotely Piloted Aircrafts (RPAs), or simply “drones”, are essential tools to acquire high-resolution geospatial data in various scientific fields. RPAs offer an easy-to-use, low-cost, and off-the-shelf solution to capture aerial imagery, geophysical data, or collect samples, depending on the payload carried by these platforms.

Digital imagery collected by RPAs can be used to generate high-resolution (i.e., centimeter-level) Digital Elevation Models (DEMs) using Structure from Motion-Multi View Stereo (SfM-MVS) algorithms [1]. Given that the majority of cameras onboard RPAs operate on the visible and near-infrared spectrum, the SfM-MVS process will produce a Digital Surface Model (DSM), that is, a surface that represents the top of canopy and man-made structures [2].

In this article, we analyze how the flight paths of RPA surveys and the presence/absence of Ground Control Points (GCPs) will impact the surface reconstruction of a stable landslide in southeastern Brazil. We compare the SfM-MVS results from two surveys campaigns in terms of their completeness, georeferencing, and morphometry. Based on the results, we discuss their implications in terms of different scenarios, such as multi-temporal monitoring or situations of rapid response to landslide events.

II. STUDY AREA

The area selected is located in the Town of São Sebastião, São Paulo State, southeastern Brazil. It consists of a hillslope vegetated by tall grass with a shallow landslide measuring approximately 250x100m (Fig. 1). Historical satellite imagery shows that the first ruptures of the landslide occurred around 2002 (Fig. 1A).

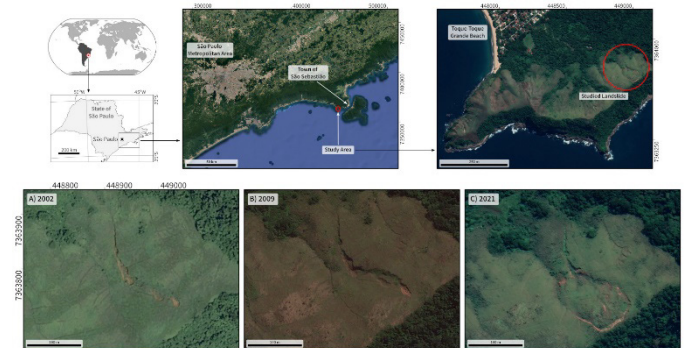


Figure 1. Location of the study area in southeastern Brazil and historical satellite imagery showing the development of the studied landslide.

III. METHODS

Fieldwork for the RPA surveys was carried out in October 2019 and May 2021. Images were acquired by a DJI Phantom 4 Pro V2 RPA, carrying a 1" CMOS 20MP sensor, with global shutter and 8.8 mm focal distance (24 mm at 35 mm equivalent). Flight missions were planned and executed with the MapPilotPro app (<https://www.mapsmadeeasy.com/>) using the “Terrain Aware” option to plan flights with constant height above ground, providing a constant Ground Sampling Distance (GSD) throughout the study area, regardless of elevation differences. The flight height is based on an SRTM DEM [3].

The 2019 campaign had a reconnaissance objective, so the RPA flights were performed without deploying targets to be used as GCPs. Two missions were flown (Flight #1 - Fig. 2B) with height above ground of 100 m, 70% overlap along and across-track, and camera positioned at -85°.

In the 2021 campaign, nine targets were positioned around the landslide area (Fig. 2A) and their coordinates were determined using a Spectra Precision SP60 DGPS in a base-rover static configuration and raw data was post-processed in Survey Office 4.10 software, using the Ubatuba Station of the Brazilian GNSS Network as reference.

The 2021 flight missions were planned to allow a comparison of different flight patterns in the 3D reconstruction. Two simple patterns were flown with height above ground of 100 m, 80% overlap along and across-track, and camera positioned at -85° (Flights #2 and #3 - Figs. 2C,2D). Two “cross-grid” patterns were flown with height above ground of 120 m, 70% overlap along and across-track, and camera positioned at -85° (Flights #4 and #5 - Figs. 2E,2F). Each flight was processed individually as well as the combination of flights #2+#3 and #4+#5.



Figure 2. A) Ground Control Points used for georeferencing the SfM-MVS reconstructions. B-F) Flight missions of the RPA surveys. Dashed lines indicate the RPA path to and from the takeoff point.

The combination of flight lines with different orientations is recommended to mitigate distortions from the camera’s self-calibration [4], while the combination of cross-grid patterns with lower overlap intents to simulate the amount of overlap of the simple pattern flights, but with flight plans that are faster to execute [5].

The SfM-MVS workflow was processed in Agisoft Metashape Pro version 1.7.1 (<https://www.agisoft.com>). In the SfM step, images were aligned with ‘High’ accuracy. Camera alignment optimization was performed considering a marker accuracy of 0.005 m. The MVS step was set to ‘High’ quality and ‘Moderate’ depth filtering.

To evaluate the ‘completeness’ of the reconstructions, the point clouds were imported into GRASS-GIS using the r.in.xyz module as rasters with 10 cm resolution. We set a mask to limit the analysis to the mid and upper portion of the landslide and counted the number of empty (void) pixels.

The subsequent analyses were run using DSMs with 25 cm resolution. The point clouds were imported using the r.in.xyz module, and the voids were filled with bilinear splines. We evaluated the descriptive statistics of each DSM as well as topographic profiles and surface roughness, calculated as the standard deviation of slope [6] using moving-windows with 3x3 pixels.

IV. RESULTS

Processing of the DGPS data resulted in horizontal precision ranging from 0.003-0.005m and vertical precision between 0.007-0.012m. The characteristics of the point clouds from the SfM-MVS workflow are summarized in Table I, including the processing time and the number of voids (i.e., empty 10 cm pixels). Figure 3 shows the distribution of voids for the 2021 flights (2-5 and combinations).

TABLE I. CHARACTERISTICS OF THE POINT CLOUDS

Flight	Photos	Pts.SfM	Pts.MVS	Proc.Time	Voids
1	90	262,691	62,228,877	00:09:59	17094
2	240	701,467	135,262,726	00:36:47	5206
3	208	585,187	136,205,251	00:29:59	5905
2+3	448	1,285,173	164,681,081	01:33:24	1448
4	157	496,613	103,268,426	00:20:48	13710
5	209	572,845	120,873,488	00:35:41	9220

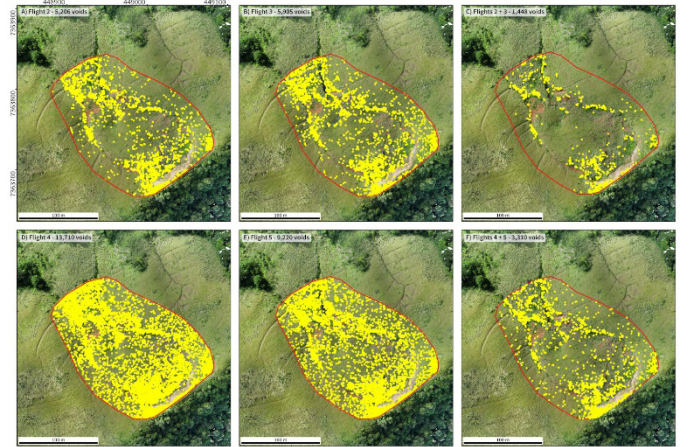


Figure 3. Distribution of voids for the analyzed flight missions. Each dot represents one empty 10 cm pixel.

Processing time varied from ~10' for flight #1 (2019) to ~30' for the single and cross-grid flights (2021), up to ~1:30 for the combined flights. The combination of flights resulted in a significant decrease in the number of voids, both for the simple and the cross-grid flight patterns (Figs. 3C and 3F).

The combination of the cross-grid flights #4 and #5 resulted in a dense point cloud with a similar number of points to the simple flights #2 or #3, despite a longer processing time. The combination of simple flights #2 and #3 resulted in ~3-4x fewer voids than in the simple flights, occurring mainly in areas of shadows or dense vegetation.

Five topographic profiles were extracted from the DSMs with 25 cm resolution. The results from the 2021 flights are all very similar, and no visual differences can be identified (solid lines in Fig.4). Profiles from the 2019 flight (dashed lines in Fig.4), in which no GCPs were used, show only a small difference in the horizontal position compared to the 2021 flights. The vertical position, on the other hand, is almost 60 meters lower than its true value.

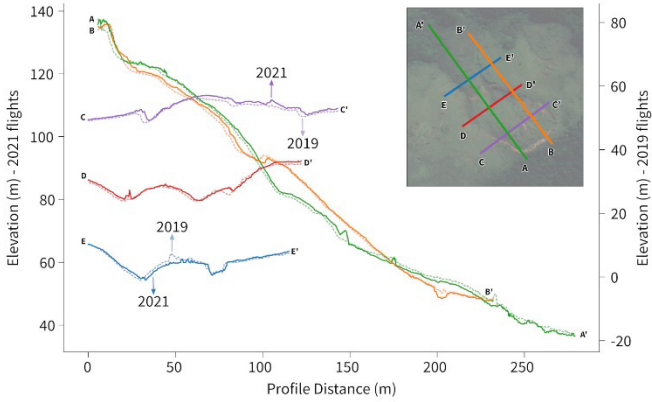


Figure 4. Topographic profiles for the 2019 (dashed lines) and 2021 flights (solid lines).

In the histograms of Fig.5, the curves of the 2021 DSMs overlap almost perfectly, except for the interval between 20 m and 40 m, which corresponds to the densely vegetated area in the NW portion of the surveys. The curve of the 2019 flight shows a similar shape to the 2021 flights, but shifted to the left in the X-axis, as a consequence of the difference of ~60 m in elevation.

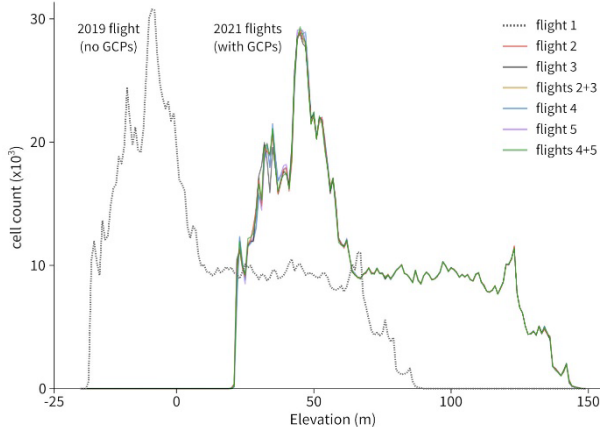


Figure 5. Histograms for the 2019 (dashed line) and 2021 flights (solid lines).

Descriptive statistics of the 25 cm-resolution DSMs are presented in Table II. All DSMs from the 2021 campaign show similar results, with small differences in the minimum and maximum values.

TABLE II. DESCRIPTIVE STATISTICS OF THE DSMs

Flight	min	max	mean	median	std. dev.
1	-35.076	89.981	13.157	3.541	30.311
2	19.877	149.344	68.423	58.758	31.537
3	19.859	147.865	68.413	58.774	31.545
2+3	19.860	148.002	68.387	58.749	31.562
4	20.516	146.984	68.506	58.809	31.456
5	19.514	148.130	68.487	58.806	31.462
4+5	19.127	148.130	68.392	58.741	31.549

V. DISCUSSIONS AND CONCLUSIONS

Visually, all the resulting DSMs are similar. Processing time was around 20-30' for the simple and cross-grids, and 1:30' for the combinations. The DSMs from the simple grid flights had fewer voids than any of the cross-grid flights. The combination of the simple grids resulted in the most complete DSM, at the expense of a larger processing time. The intention of combining cross-grid flights was to simulate the amount of overlap of the simple grid flights. Indeed, the DSM from the combined cross-grids had fewer voids than those from the simple grids, but with the downside of requiring two flights and longer processing time.

Topographic profiles extracted from the DSMs of 2021 are virtually indistinguishable one from another, confirming that the flight patterns did not influence the surface reconstruction. Profiles from the 2019 DSM show small differences in shape that can be attributed to changes in the tall grass vegetation covering the hillside. The main difference is with respect to the Z-axis, where the 2019 DSM is about 60m lower than the 2021 DSMs.

The presence of vegetation cannot be dismissed when interpreting these data, as the SfM-MVS process will generate a DSM and not a DTM. If the area of interest is covered by dense vegetation, one must consider the use of lidar, as the multiple returns of the laser pulse (in the case of airborne lidar) or the very high density of points/m² (in the case of RPA-borne lidar), allow the removal of vegetation and creation of a “bare earth” surface.

In situations of rapid response to landslide events, time is of utmost importance. Our results indicate that one simple grid flight will be enough to produce a good reconstruction of the surface, with a short processing time. In such situations, deploying GCPs and collecting coordinates with DGPS might also not be a feasible task (both in terms of time, accessibility, and safety).

We show that the DSM produced without GCPs had little difference in the XY coordinates from those where GCPs were applied; the main difference was in the Z-axis, which can be easily adjusted in a GIS environment based on other data (such as previous DSMs/DTMs or topographic maps). In this case, it is important to plan the flights to cover a larger area, to capture features that can be used in the georeferencing, and to set the camera position to off-nadir (85° is sufficient), to prevent dome-shaped distortions in the results. Mapping a larger area also allows for monitoring the landslide without GCPs, since point clouds or DSMs from different dates can be aligned based on their stable features.

Given that landslides usually occur in areas of high relief, the flight plans should consider the terrain and be executed with constant height above ground, to provide a consistent pixel size across the region.

VI. ACKNOWLEDGMENTS

This project was supported by FAPESP (grants #2016/06628-0, #2019/26568-0) and CNPq (grant #311209/2021-1). G.P.B.G. and R.D.C. are PhD students financed by CAPES Brasil (Finance Code 001). H.C.D. is a PhD student financed by FAPESP (grant #2019/17261-8).

REFERENCES

- [1] Carrivick, J. L., Smith, M. W., & Quincey, D. J., 2016. Structure from Motion in the Geosciences. In: Analytical Methods in Earth and Environmental Science. Wiley.
- [2] Guth, P.L., Niekerk, A.V., Grohmann, C.H., Muller, J.-P., Hawker, L., Florinsky, I.V., Gesch, D., Reuter, H.I., Herrera-Cruz, V., Riazanoff, S., López-Vázquez, C., Carabajal, C.C., Albinet, C., Strobl, P., 2021 - Digital Elevation Models: Terminology and Definitions. *Remote Sensing*, 13(18):3581. <https://doi.org/10.3390/rs13183581>
- [3] Farr, T. G., Rosen, P. A., Caro, E., Crippen, R., Duren, R., Hensley, S., Kobrick, M., Paller, M., Rodriguez, E., Roth, L., Seal, D., Shaffer, S., Shimada, J., Umland, J., Werner, M., Oskin, M., Burbank, D., & Alsdorf, D., 2007. The Shuttle Radar Topography Mission. *Review of Geophysics*, 45, RG2004. <https://doi.org/10.1029/2005RG000183>
- [4] James, M. R., & Robson, S., 2014. Mitigating systematic error in topographic models derived from UAV and ground-based image networks. *Earth Surface Processes and Landforms*, 39(10), 1413–1420. <https://doi.org/10.1002/esp.3609>
- [5] OpenDroneMap Community, 2020. OpenDroneMap's documentation. <https://docs.opendronemap.org/tutorials.html#calibrating-the-camera>
- Grohmann, C. H., Smith, M. J., & Riccomini, C., 2011. Multiscale Analysis of Topographic Surface Roughness in the Midland Valley, Scotland. *Geoscience and Remote Sensing, IEEE Transactions On*, 49(4), 1200–1213. <https://doi.org/10.1109/TGRS.2010.2053546>

The true 3-D surface reconstruction using a multi-UAV cooperation method

Haigang Sui, Hao Zhang, Qiming Zhou, Jianya Gong, Yixuan Zhu

State Key Laboratory Information Engineering in Surveying, Mapping and Remote Sensing Wuhan University
 Wuhan, China

zhanghao.1003@whu.edu.cn

Abstract—Geomorphometry research largely relies on 3-dimensional land surface models, especially for natural landforms with steep slopes and large complex artificial structures. The traditional Digital Elevation Model (DEM) encounters difficulties in representing detailed features in such scenes. To address this issue, this paper introduces a concept of a “true 3D surface” and proposes a multiple Unmanned Aerial Vehicle (UAV) collaborative method for high-quality reconstruction of a true 3D surface. We established an evaluation model of scene reconstruction based on the Multi-View Stereo (MVS) modeling rules, and utilized the Fibonacci approach to select the optimal viewpoints. We also adopted the method of finding the next-best-view for each UAV in turn to extend the multi-UAV trajectory. This method involved trade-offs between energy consumption and scene reconstruction to enhance the contribution of viewpoints for improved reconstruction quality of the true 3D surface. Real flight experiments were conducted over the Wuhan University Teaching Building and the Fangshiwan Bridge in Chibi, which revealed a significant improvement in the completeness and precision of the true 3D surface constructed by our proposed method when compared to vertical photography techniques.

I. INTRODUCTION

Building a 3D model of large scenes is essential for a better understanding of terrain and geomorphology, especially when repeated observations and analyses are required. Traditional DEMs are widely used in terrain modeling as they can visually display terrain information of the scene. However, DEMs often struggle to depict detailed facade features of certain natural landforms with large drops, such as the Loess Plateau (Fig. 1a), and large-scale artificial structures, such as tower buildings (Fig. 1b); hence, they do not represent a true 3D surface model.

A true 3D surface goes beyond the visualization of topography in large-scale scenes as it captures sufficient surface details from all angles, including elevations. Compared to traditional DEMs, true 3D surfaces contain more information and hence provide greater assistance for topography-related research.

Due to the rapid development of UAV technology, a single high-resolution camera-equipped commercial UAV is now available at a lower cost and has found use in various industries [1-3]. Based on advanced MVS technologies like MVE [4], COLMAP [5], and Pix4D [6], even monocular cameras on UAVs can reconstruct a very detailed true 3D surface.



(a) Loess plateau

(b) Tower buildings

Figure 1. Natural landforms and artificial features with a large drop

Several studies have explored the true 3D surface reconstruction of ground surfaces using a single UAV based on the MVS technique [7, 8]. However, most of these studies relied on the traditional vertical photography method, which fails to adequately collect elevation data. As a result, the reconstructed models did not have sufficient elevation details to represent true 3D surfaces. Alternative studies on collecting elevation data by manually-controlled UAVs have shown the drawbacks of being time-consuming, laborious, and challenging to ensure the model's completeness and precision [9].

This paper introduces a multi-UAV collaborative method capable of reconstructing a true 3D surface. Our proposed method can efficiently devise a collision-free data acquisition path that maximizes scene reconstruction. This allows for autonomous image data acquisition using multiple UAVs which results in a high-quality, precise true 3D surface, based on MVS.

II. METHODS

Our proposed multi-UAV collaborative method consists of three stages. In the first stage, we establish a coarse proxy of the scene through vertical photography and randomly generate sampling points on this proxy. We then employ MVS modeling rules to construct the reconstruction model of the sampling points. In the second stage, multi-UAV trajectories are planned by finding the next-best-view (NBV) in a comprehensive evaluation considering scene reconstruction, flight energy consumption, and distance between the multi-UAV trajectories. By doing so, our method can plan a collision-free data acquisition path that maximizes the scene reconstruction. In the

third stage, the UAVs collaboratively capture images autonomously along the planned trajectories, and a high-fidelity true 3D surface is reconstructed through MVS. Figure 2 provides a general summary of our proposed method.

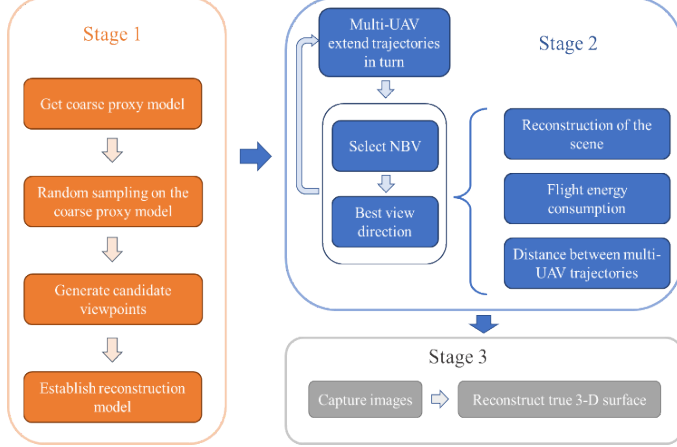


Figure 2. Overview: The first stage: obtain the proxy model and complete the establishment of the reconstruction model. The second stage: multi-UAV extend trajectories in turn. The third stage: multi-UAV collaborative image acquisition, and establish the true 3D surface.

A. Reconstruction Model of 3D Surface

To fully capture the image data of the scene, and reconstruct a fine and complete true 3D surface, we need to avoid planning a wrong trajectory that leads to collision between the UAVs and the ground surface or other obstacles. To achieve this, we can get a coarse proxy of the scene in advance. A DEM can be directly used as the coarse proxy, or we can carry out two-dimensional coverage of the scene by vertical photography of UAV. After that, a coarse proxy of the scene can be quickly established based on MVS.

Given a number of viewpoints $V = \{v_1, v_2, \dots, v_n\}$, we perform Poisson-Disk Sampling on the surface of the coarse proxy to obtain the sampling points $S = \{s_1, s_2, \dots, s_n\}$. According to the reconstruction rules of MVS, we can establish a reconstruction contribution model of viewpoints v_i, v_j to sampling point s_k , which is shown in Figure 3:

$$c(s_k, v_i, v_j) = w_1(\alpha)w_2(d_1, d_2)\cos(\theta_m) \quad \text{Eq. 1}$$

where α is the angle between $\overrightarrow{s_k v_i}$ and $\overrightarrow{s_k v_j}$, d_1 is the further one of the distances between v_i, v_j and s_k , while d_2 is the other distance. θ_m is the largest of the angles between $\overrightarrow{s_k v_i}, \overrightarrow{s_k v_j}$ and the normal vector \mathbf{n}_k . In equation (1), w_1 is used to indicate that if the angle between $\overrightarrow{s_k v_i}$ and $\overrightarrow{s_k v_j}$ is beyond a certain range, the reconstruction will be negatively impacted. w_2 indicates that the reconstruction contribution of the viewpoint to the sample point is negatively related to the distance between them. And $\cos(\theta_m)$ indicates that the greater the angle between the viewpoint and the normal to the plane where the sample point is located, the less significant the reconstruction contribution from the viewpoint. The total reconstruction of the sample point s_k in the viewpoint set V is

$$h_1(s_k, V) = \sum_{\substack{i=1, \dots, |V| \\ j=i+1, \dots, |V|}} \delta(s_k, v_i, \mathbf{p}_i) \delta(s_k, v_j, \mathbf{p}_j) c(s_k, v_i, v_j) \quad \text{Eq. 2}$$

where δ is the visibility function of viewpoint v_i to sampling point s_k under direction \mathbf{p}_i . $\delta(s_k, v_i, \mathbf{p}_i) = 0$ when s_k does not exist in v_i 's field of view or the distance between the two is too large; otherwise $\delta(s_k, v_i, \mathbf{p}_i) = 0$.

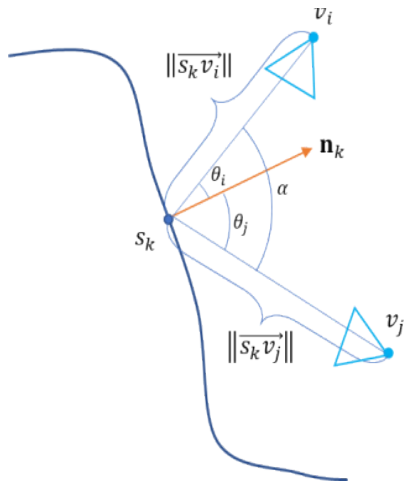


Figure 3. Reconstruction model of the true 3D surface. The figure shows the profile view when viewpoints v_i, v_j are simultaneously observing the model surface sampling point s_k .

B. Selection of Optimal View Direction

To obtain an accurate true 3D surface reconstruction while also minimizing the number of viewpoints, reducing data acquisition time, and improving the modeling speed, it is essential to ensure that the viewpoints at each position observe in the optimal direction.

The optimal viewing direction is determined by discretizing the viewpoint direction and selecting the direction that maximizes the reconstruction of the scene. It is critical at this stage to ensure the uniformity of discretization because uneven discretization can create a considerable gap between the chosen and optimal direction.

Initially, we create a sphere of 1 m radius for each viewpoint using the Fibonacci [10] to generate a uniform point set on its surface. A vector set, $P = \{\mathbf{p}_1, \mathbf{p}_2, \dots, \mathbf{p}_M\}$, is formed by computing the vectors from the center of the sphere to each point on its surface, as shown in Figure 4. Here, M represents the total number of vectors. Given a set of viewpoints, $V = \{v_0, v_1, \dots, v_n\}$, we determine the optimal viewing direction for each viewpoint v :

$$\mathbf{p}^* = \arg \max_{\mathbf{p} \in P} h_2(S, V, \mathbf{p}, v) \quad \text{Eq. 3}$$

where $h_2(S, V, \mathbf{p}, v)$ is the reconstruction contribution of the viewpoint v to the scene in the direction \mathbf{p} :

$$h_2(S, V, \mathbf{p}, v) = \sum_{\substack{i=1, \dots, |V| \\ k=1, \dots, |S|}} \delta(s_k, v_i, \mathbf{p}_i) \delta(s_k, v, \mathbf{p}) c(s_k, v_i, v) \quad \text{Eq. 4}$$

where \mathbf{p}_i is the view direction of viewpoint v_i .

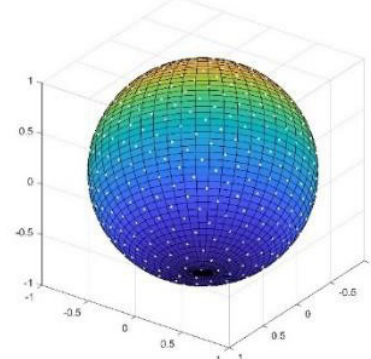


Figure 4. Generate uniform discrete point set based on Fibonacci.

C. Cooperative Path Planning of Multi-UAV

The trajectory planning is carried out in a way that multiple UAVs take turns to gradually extend their trajectories from their respective takeoff points.

Firstly, we generate a uniform, high-density collection of candidate viewpoints in the free space of the scene (see Fig. 5). To ensure UAV flight safety, it is vital to maintain a safe distance f between UAVs and surfaces or other obstacles. Furthermore, any candidate viewpoint located in free space, but whose minimum distance to surfaces or obstacles is less than f , is deemed an invalid candidate viewpoint.

Next, each UAV takes turns selecting the NBV, beginning at their respective takeoff points. The method of Wang et al. [11] is utilized to generate a continuous trajectory $L(t)$ (see Fig. 5), where t represents time. The process then repeats by identifying the NBV and generating a continuous trajectory until the total reconstruction of the scene reaches the target value C .

An evaluation function for the candidate viewpoint v is:

$$H(L, V', S, v) = q_3 H_1(V', S, v) - q_4 H_2(L, V', v) \quad \text{Eq. 5}$$

where L denotes the planned continuous trajectory and V' is the set of selected viewpoints. H_1 in Eq. (5) denotes the total contribution of all the viewpoints in V' to the scene reconstruction together with v . H_2 is the incremental energy consumption of the trajectory after adding v as the trajectory end point, which is used to prevent the UAV from consuming too much unnecessary energy, which is detrimental to the reconstruction of the true 3D surface.

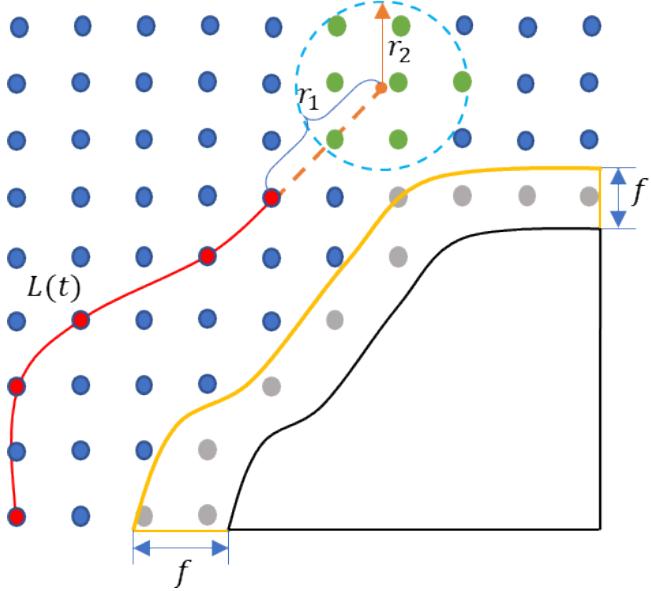


Figure 5. The selection of the NBV. The blue point is the candidate viewpoint position, the gray point is the invalid safety viewpoint, the red point is the selected viewpoint, the NBV will be selected from the green point, and the red curve $L(t)$ is the planned trajectory.

The NBV selection method involves extending each UAV a r_1 distance along the tangent direction of the trajectory endpoint. From there, using the KD-Tree nearest neighbor search, all suitable candidate viewpoints within the r_2 distance and not chosen for selection are identified, and the viewpoint maximizing the function H is chosen as the NBV (see Fig. 5).

To ensure safety, we aim to maintain a suitable distance between UAVs during flight. Therefore, we update the evaluation function of the candidate viewpoint v as follows:

$$H(L, V', S, v, s') = H_3(V', v)(q_3 H_1(V', S, v) - q_4 H_2(L, V', v)) \quad \text{Eq. 6}$$

$$H_3(V', v) = \begin{cases} 1, d^* > d_{min} \\ 0, d^* \leq d_{min} \end{cases}$$

Eq. 7

Where d^* is the maximum closest real-time distance from all other trajectories after v has been added to the end of V' and a new trajectory is planned, and d_{min} is the safe distance between UAVs.

III. RESULT

We conducted real UAV flight and modeling experiments at the teaching building of Wuhan University and the Fangshawan Bridge in Chibi. At these locations, we used three DJI Phantom 4 RTKs to cooperatively capture images. The trajectories were planned by our method, and we built a precise 3D surface on the ground using DasEarth software. For comparison, we used the commercial software DJI-Pilot to plan a trajectory for vertical photography, captured images and built a 3D model on the ground using the same method.

Fig. 6 shows the differences in details between the models built using different methods. In the trajectory planned by DJI-Pilot, the direction of all viewpoints is vertical downward, and the distance between the front and rear viewpoints is the same, which makes it difficult to capture the elevation image of the scene. This problem is particularly obvious for the buildings with eaves and bridges with piers. However, our method avoids the above problems by observing the scene from multiple positions and angles.



(a) Teaching building of Wuhan University

(b) Fangshawan Bridge in Chibi

Figure 6. Detailed display of true 3D surfaces. The first row is a panorama, and the second and third rows are a detailed comparison between the method of this paper and the vertical photography method. The left is vertical photography, and the right is the method of this paper.

In the experimental comparison of Wuhan University's teaching building in Figure 6(a), the traditional vertical photography model lacks numerous details under the eaves, while several areas of the model appear distorted, with fuzzy, unrecognizable text on its surface. In contrast, our method retains far more texture under the eaves, and the building's surface text is crystal clear. Comparably, traditional vertical photography in Figure 6(b) not only agglutinates to render a partial pier structure but also loses the texture of the fence surface. Our method, on the other hand, performs remarkably well regarding the comprehensiveness of the bridge piers and the richness of the surface texture.

IV. CONCLUSION

A method for true 3D surface reconstruction using multi-UAV cooperation is proposed in this paper. This method establishes a mathematical model of scene reconstruction based on MVS, which provides a reasonable evaluation of the contribution of viewpoints to the scene reconstruction. Furthermore, we use the Fibonacci sequence to quickly determine the optimal view direction. Multi-UAV path planning is done using a method where UAVs take turns in finding the NBV and gradually extending the path. Experiments conducted on Wuhan University's teaching building and Fangshawan Bridge in Chibi demonstrate a marked improvement in the fineness and completeness of the true 3D surface when compared to traditional vertical photography.

V. ACKNOWLEDGMENT

This study was supported by the Guangxi Science and Technology Major Project (No. AA22068072), the Natural Science Foundation of China (NSFC) General Program (41971386 and 42271416) and Hong Kong Research Grant Council (RGC) General Research Fund (HKBU 12301820).

REFERENCES

- [1] Mancini, F., Dubbini, M., Gattelli, M., Stecchi, F., Fabbri, S., & Gabbianelli, G. (2013). Using unmanned aerial vehicles (UAV) for high-resolution reconstruction of topography: The structure from motion approach on coastal environments. *Remote sensing*, 5(12), 6880-6898.
- [2] Siebert, S., & Teizer, J. (2014). Mobile 3D mapping for surveying earthwork projects using an Unmanned Aerial Vehicle (UAV) system. *Automation in construction*, 41, 1-14.
- [3] Baiocchi, V., Dominici, D., & Mormile, M. (2013). UAV application in post-seismic environment. *International Archives of the Photogrammetry, Remote Sensing and Spatial Information Sciences*, 1, W2.
- [4] Fuhrmann, S., Langguth, F., & Goesele, M. (2014, October). Mve-a multi-view reconstruction environment. In GCH (pp. 11-18).
- [5] Schonberger, J. L., & Frahm, J. M. (2016). Structure-from-motion revisited. In Proceedings of the IEEE conference on computer vision and pattern recognition (pp. 4104-4113).
- [6] Strecha, C., Von Hansen, W., Van Gool, L., Fua, P., & Thoennessen, U. (2008, June). On benchmarking camera calibration and multi-view stereo for high resolution imagery. In 2008 IEEE conference on computer vision and pattern recognition (pp. 1-8). IEEE.
- [7] Gonçalves, J. A., & Henriques, R. (2015). UAV photogrammetry for topographic monitoring of coastal areas. *ISPRS journal of Photogrammetry and Remote Sensing*, 104, 101-111.
- [8] Uysal, M., Toprak, A. S., & Polat, N. (2015). DEM generation with UAV Photogrammetry and accuracy analysis in Sahitler hill. *Measurement*, 73, 539-543.
- [9] Solazzo, D., Sankey, J. B., Sankey, T. T., & Munson, S. M. (2018). Mapping and measuring aeolian sand dunes with photogrammetry and LiDAR from unmanned aerial vehicles (UAV) and multispectral satellite imagery on the Paria Plateau, AZ, USA. *Geomorphology*, 319, 174-185.
- [10] González, Á. (2010). Measurement of areas on a sphere using Fibonacci and latitude-longitude lattices. *Mathematical Geosciences*, 42, 49-64.
- [11] Wang, Z., Ye, H., Xu, C., & Gao, F. (2021, May). Generating large-scale trajectories efficiently using double descriptions of polynomials. In 2021 IEEE International Conference on Robotics and Automation (ICRA) (pp. 7436-7442). IEEE.

Dependence of statistical results on definitions and extents of study area: examples from cirques and glaciers

Ian S. Evans

Department of Geography
 Durham University
 Durham, UK
 i.s.evans@durham.ac.uk

Yingkui Li

Dep. of Geography & Sustainability
 University of Tennessee
 Knoxville, U.S.A.
 yli32@utk.edu

Zhibin Zhao

College of Geographical Sciences
 Hebei Normal University
 Shijiazhuang, China

Abstract— The boundaries of geographic study areas are mostly defined at an early stage of research, and rarely investigated further. Yet statistical results are critically dependent on the extent of the study area and the way in which its boundaries are defined. The dilemma is that a small study area may lack the number of features required for significant results, whereas a large study area may include sub-areas with different relationships between variables, so that the averaged values or trends obscure relationships. Results for regional trends and mean azimuths of aspect are especially likely to be affected. Examples here are from mountain glaciation (cirques and glaciers), but the conclusions apply to many fields of physical geography and earth science.

I. INTRODUCTION

The advancement of Geographic Information Systems (GIS) and the availability of high-resolution satellite imagery and digital elevation models (DEM) enable the analyses of a large population of geographic data for regional and global trends. However, such analysis may be affected by the Modifiable Areal Unit Problem (MAUP), which has been discussed extensively by human geographers and cartographers (Openshaw and Taylor, 1981; Evans, 1981; Goodchild, 2011). Many MAUP-related studies concern the cases for which data are available or analysed, for example, the data collected for various administrative areal divisions. In comparison, few studies have been investigated similar issues in physical geography. Dark and Bram (2007) considered MAUP in physical geography, mainly in relation to scale effects in remote sensing (pixels) and in drainage tracing on DEMs (grid mesh) – both involving equal units. The impacts of data aggregation to varied shapes and sizes of geographic areas are seldom investigated. Here, we use three examples to demonstrate the impacts of analysing trends and directions in cirque datasets for different extents of investigated area. We suggest that results vary with the size, shape and uniformity of study area.

II. EXAMPLE 2: GLACIATION OF THE CENTRAL HIMALAYAS

Empty cirques were measured in an area of 224 x 134 km between 79.6 and 82.1°E and 29.8 and 30.9°N in central Himalayas (Fig. 1, best enlarged; Li et al., 2023). This is a large and diverse area, with enough cirques to give highly significant statistical results. The cirques (Fig. 1) are in groups with different climates: the Nanda Devi, Byasrikh and Saipal Himal are exposed to the monsoon from the south, while the Gurla Mandhata (Naimon'anyi) and Chandi Himal mountains are in their rain shadow and therefore much drier and with a higher snowline,

past and present. We first test the impact of data aggregation in different spatial divisions on regional easting and northing trends in cirque floor altitudes, then biases in cirque aspect (local asymmetry of glaciation). Both have been used to make inferences about former climates.

The regressions in Table 1 show the relationship between cirque floor altitudes and UTM east and north coordinates (in km). Such trends are used to infer former glacier ELA trends related to precipitation and temperature. The data obey assumptions about uniform distribution of deviations. The regional trend across the central Himalayas is strong, rising mainly northward but also eastward. For the whole study area the rise is at 14 m/km toward an azimuth of 020°, compatible with the 5.8 mm/km decline in precipitation toward 038° (from 1 km resolution data in WorldClim v2.1).

We made a twofold split around approximately 81.2°E, through the pass at Baling La: this would be a West-East split except that in the south six cirques just west of this are closer to cirques in, and therefore are allocated to, the East region, so the terms Northwest and Southeast are used. This confirms the northward rise, especially in Southeast (from Saipal Himal to Chandi Himal). The eastward rise, however, is confined to Northwest.

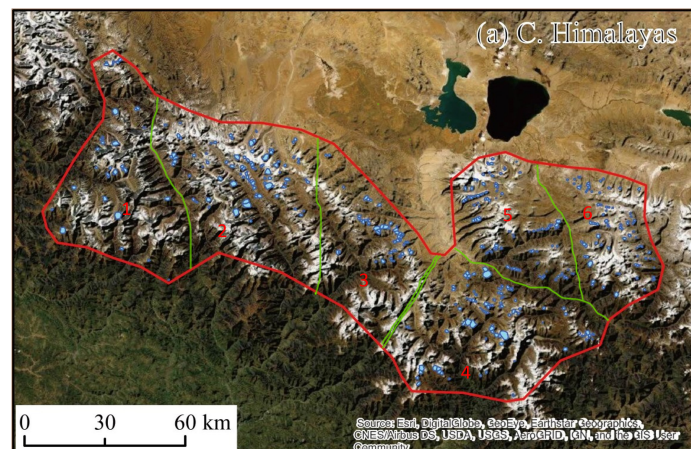


Fig. 1. The central Himalayas study area. Empty cirques are blue polygons.

The cirques cluster in separate mountain ranges and further subdivisions can be made to define more compact, uniform areas separated by valleys and passes. The Northwest region is elongated and oriented WNW-ESE: it can be further split into three subsections by UTM eastings 336 km and 395 km. The westmost is dominated by Nanda Devi, although the empty cirques are on lower peripheral mountains. The central subsection includes Panch Chuli. The eastern is around Gunji, from UTM 395 km to 463 km and north of 3350 km.

Regional trends for these three consistently show a northward rise greater than an eastward: floors are higher toward north of northeast. Two are highly significant with R^2 of 42% and 56%, but the Nanda Devi subsection has only 32 empty cirques, giving completely insignificant results.

TABLE 1. TWO-CONTROL REGRESSIONS PREDICTING CIRQUE FLOOR ALTITUDE (m) from UTM coordinates (in km) for the whole C. Himalayas area, for a twofold division into regions, and for the six subdivisions. The east and north coefficients give component gradients in m/km. $p = 0.0868$ for Nanda Devi, 0.0000 for all others.

area	east	north	R^2 (%)	rmse (m)	n
C. Himalayas	4.743	13.179	46.7	287	455
<i>Regions</i>					
Northwest	6.410	14.315	30.6	273	173
Southeast	-1.955	16.851	65.8	241	282
<i>Subdivisions</i>					
1. Nanda Devi	6.479	7.030	9.7	408	32
2. Panch Chuli	12.698	28.023	55.6	229	86
3. Gunji	15.956	19.771	42.1	156	55
4. Saipal Himal	0.106	17.045	26.7	98	98
5. G. Mandhata	-6.871	20.096	84.6	146	100
6. Chandi Him.	4.343	18.748	52.8	207	84

The Southeast region divides naturally into three blocks or massifs. The eastmost is Chandi Himal, straddling the Nepal – Tibet border east of Labtse La: the north slope is the source of the Brahmaputra R. (Trak Tsangpo, Yarlung Tsangpo). Immediately west is Gurla Mandhata (Naimon’anyi), east of the town of Purang in Tibet but extending into Nepal. South of that, across the Changla La, is Saipal Himal with Jethi Bahurani, mainly in Nepal. The regressions are highly significant, with R^2 between 27% and 85%. In all three subsections the northing coefficient is consistently strong, while the easting coefficient varies from negative to positive. This is where the monsoon rain shadow effect is strongest, with higher cirque floors in the dry north. All trends are more northward than those in the Northwest region. The regional trends in cirque floor altitudes confirm that precipitation providing snowfall came from the south, in the past as today.

Results for cirque aspect are used to infer the relative importance of shade, wind and other effects, moderated by topographic trends. For Central Himalayas these are less interesting. For the whole study area, vector mean aspect is 038.5° and strength is 7.5%, but $p = 0.075$ (using Rayleigh’s test for unimodal bias) and the 95% confidence limits are estimated as 341° to 096°, disappointingly broad. The two regions give consistent means (033.3° and 044.2°) but contrasting strengths (13.3% and 4.0%). Subsections have varied mean aspects of 000°, 168°, 003°, 010°, 095° and 055°. It seems that the degree of symmetry is sufficiently high that this further subdivision produces capricious results, with local topography more effective than slope climates. The Gunji subsection, however, has a due north mean with a strength of 33.8%.

In summary, the C. Himalayas cirque aspect distribution is symmetrical, with a weak tendency to favour northeast aspects in the Northwest region. This is somewhat different to that of the 1535 modern glaciers, downloaded from Randolph Glacier Inventory 6.0., with a vector mean of 017.8° and strength 24.2%. The 1175 glaciers smaller than 1 km² likewise have mean 013.3°, strength 21.8%. Compared with 038.5 for cirques, there is a (weak) hint of greater influence from westerly winds in the past.

III EXAMPLE 2: GLACIATION OF THE EASTERN TIAN SHAN

The E. Tian Shan study area (also from Li et al., 2023) extends over 134 km north-south and 302 km east-west, between 83.7–87.5°E and 42.9–44.2°N (Fig. 2). As it is clearly in the west-wind belt, with precipitation from the west, we expect cirque floors and modern glacier ELAs to rise eastward as precipitation declines. This decline, calculated from estimates of precipitation at roughly 1 km resolution from WorldClim v.2.1, is however at only 0.2 mm/km: much less than the 5.8 mm/km northward decline in the C. Himalayas. The decline

is toward 100°, i.e. close to eastward as expected. Median altitudes of modern glaciers rise at 1.0 m/km toward 065°.

Cirque floor altitudes, however, rise southward: at 2.5 m/km toward 182° (Table 2). As the study area is elongated east-west, an initial threefold division into West, Centre and East is used. Significant results are produced in each region, with declines more northward than eastward in Centre and East. In West, however, floor altitudes decline westward as expected and the northward coefficient is insignificant.

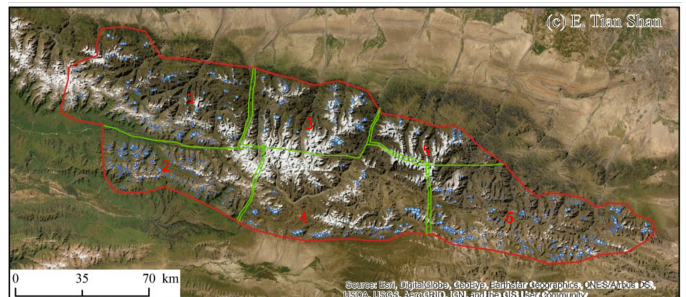


Fig. 2. E. Tian Shan cirques: blue: empty cirques; green: subdivisions. (Best enlarged)

As each of these regions was split by major valleys, and by a central area with large glaciers where cirques could not be measured, a further division into six subdivisions was defined, each having a more compact cluster of cirques. The results (Table 2) are varied. The Northwest and South-central subdivisions show no significant trends: in fact, the R^2 values are negligible, even negative after adjustment for the degrees of freedom lost, and the rmse are close to the standard deviations of floor lowest altitudes. The other four subdivisions show northward declines (southward rises), much steeper than for the whole study area. It is to be expected that small areas show steeper trends: in fact, the steepest is for Northeast, a small cluster of 24 cirques. In each the eastward decline is much less than the northward, and in Southwest it is reversed and insignificant.

TABLE 2. ANALYSES OF CIRQUE FLOOR ALTITUDE trends for the whole E. Tian Shan area, for three regions and for six subdivisions. Cirque floor altitude (m) is regressed on UTM eastings and northings (km): east and north coefficients are in m/km. Coefficients statistically insignificant at the 0.05 level are left blank.

area	east	north	R^2 (%)	rmse	p	n
E. Tian Shan		-2.517	10.5	220	0.0000	675
<i>Regions</i>						
West	1.550		1.9	202	0.0139	343
Centre	-3.087	-5.399	29.4	236	0.0000	137
East	-2.258	-7.230	27.3	186	0.0000	195
<i>Subdivisions</i>						
1. Northwest			0.0	233	0.8035	146
2. Southwest		-4.300	8.7	169	0.0001	188
3. N-central	-6.788	-16.014	30.3	234	0.0000	63
4. S-central			0.0	230	0.6360	78
5. Northeast	-13.787	-44.087	25.9	192	0.0165	24
6. Southeast	-2.391	-10.272	26.2	180	0.0000	176

In this case the more detailed division does not explain the lack of an eastward rise in cirque floor altitudes to match the reduced precipitation. It does, however, confirm the robustness of a southward rise. Although not apparent in the modern precipitation, the implication is that around the maxima of past glaciations precipitation (snow) was brought from more northerly sources than today: the plains of Xinjiang to the south were the more arid then as now. The situation is complicated by the numerous cirques filled by modern glaciers, as these could not be measured.

The steepest trend component is the northward decline of 44 m/km over 22 km in Northeast. This, however, is not supported by the regression of cirque floor altitudes on northing alone, which is

insignificant. We conclude that, despite the p value of 0.0165, the set of 24 cirques is too small to support a two-control regression. The 95% confidence interval on the -44 m/km gradient is from -73 to -15 m/km. On the other hand, the sets of 137 and 195 cirques in Centre and East sections, similarly tested, show a robust northward decline, as does the E. Tian Shan study area as a whole.

The favoured direction in which glacial cirques face has also been used as evidence of palaeoclimate (Mindrescu et al., 2010). The E. Tian Shan is in an arid, sunny region, so glaciers are likely to form and survive more on north-facing than on south-facing slopes. The WNW-ESE orientation of the whole area, and of most component mountain ranges (Fig. 2), militates against east- and west-facing cirques. The vector mean of the 675 empty cirques is 019.5°, north-northeast, which suggests a dominant shade effect moderated by some morning-afternoon differences, probably in cloudiness. Division into three regions shows some reduction in the eastward component in the West and the East regions, but an insignificant ($p = 0.129$) directional bias in the 137 cirques of the Central section.

The six-fold subdivision shows significant results only in two subdivisions, Southwest and Southeast, with greater vector strengths (22 and 28%) and a dominantly northward tendency (Table 3). For North-central $p = 0.066$ and 95% confidence limits are 352 and 094°. The other three subsections give completely insignificant results, to the extent that confidence limits cannot be calculated for Northwest and Northeast. Again there may be problems from exclusion of glacier-filled cirques.

TABLE 3. VECTOR ANALYSES OF CIRQUE ASPECTS in E. Tian Shan. Only significant results are shown: all p values are 0.000.

Area	Mean (°)	Strength (%)	Number	95% conf. (°)
E. Tian Shan	019.5	14	675	358-041
W. region	010.2	15	343	341-039
E. region	008.5	22	195	342-034
Southwest	002.7	28	188	341-024
Southeast	013.2	22	176	346-041

Assuming that almost all the 2997 modern glaciers have sources in cirques, the glacier mean aspect of 356.9° with a strength of 52.7% would shift the overall mean for cirques very close to north (taking only the 2677 glaciers smaller than 1 km², the mean of 355.1° and strength of 53.0% produce the same result). The conclusion is that, like modern glaciers, the glaciers that eroded E. Tian Shan cirques faced north, uninfluenced by wind or by morning: afternoon asymmetry.

IV. EXAMPLE 3: CIRQUES OF THE ENGLISH LAKE DISTRICT

Cirque aspects for the whole Lake District massif (Fig. 3) show a clear climatic signal, with shade favouring poleward aspects, and shelter from westerly winds favouring eastward (Evans and Cox, 1995). Results for 8 individual mountain ranges, separated by passes, show considerable variation (Table 4). The numbers of cirques in each are small, but this is not a random variation: it shows the effects of topographic lineation. The Western Fells are oriented east-west, with few possible east-facing sites: shade gives a north-facing dominance. The Central Fells, Coniston – Black Combe and the Eastern Fells (Helvellyn – Fairfield range) are elongated north-south, favouring east-facing cirque sites and providing few suitable north-facing sites: shelter from westerly winds encouraged glacier formation on east-facing sites. The Far Eastern Fells (High Street range) have north-south and east-west ridges: they and the compact Sca Fell – Bow Fell massif come closest to the overall Lake District cirque vector mean. The Northwestern Fells are oriented northwest-southeast and give a NNE vector mean. The 95% confidence limits on vector means vary between ±15° and ±34° for the divisions, in comparison to ±10° for the whole Lake District.

Implications of numbers of cases are even greater for correlations between morphometric variables. Whereas for the whole District all correlations of ±0.16 or stronger are significant at the $p = 0.05$ level, the number of significant correlations within each division is greatly

reduced by the small numbers. For the two areas with 10 cirques each, correlations need to be over ±0.64; for that with 33 cirques, ±0.35.

The eight mountain ranges are too small to define trends in floor altitude. Even for the whole Lake District, spatial trends are weak.

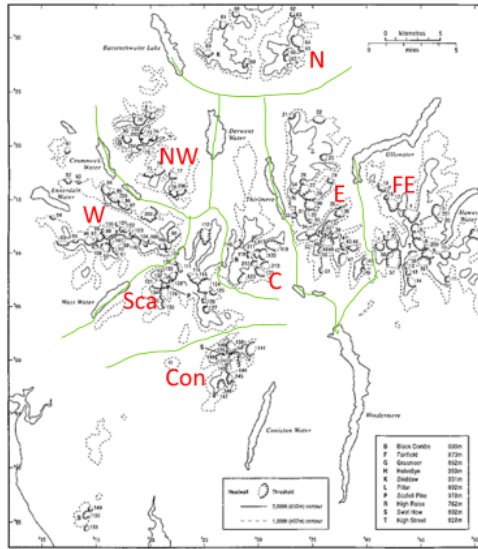


Fig.3. Cirques of the English Lake District, with contours at 457 and 610 m. Green lines follow valleys and passes to divide the District into 8 mountain ranges, named in Table 4.

TABLE 4. VECTOR MEAN AND STRENGTH OF HEADWALL ASPECTS in divisions (mountain ranges) of the English Lake District, ordered by vector mean. All have Rayleigh's $p < 0.001$ except for Central, where $p = 0.001$.

Name (range)	Mean (°)	Strength (%)	Number
Western	015.3	62.2	33
Northwestern	022.8	76.2	16
Northern	036.4	82.1	10
Sca Fell-Bow Fell	048.7	59.0	18
Far Eastern	055.2	69.0	25
Eastern	063.1	59.0	32
Coniston-Black Combe	087.7	83.9	14
Central	102.8	64.9	10
LAKE DISTRICT TOTAL	049.3	60.2	158

V. DISCUSSIONS AND CONCLUSIONS

The regional trends for subdivisions, as well as for a complete study area, are varied and can be inconsistent. Analyses of subdivisions help test the robustness of generalizations and identify which subdivisions dominate the overall statistical results. For correlations, datasets here smaller than 25 tend to give excessively broad confidence intervals: more than 50 is desirable and 100 – 200 can give significant correlations for the weakest correlations likely to be of interest. For larger datasets the homogeneity of the study area should be considered.

The regional trends derived from small areas can give misleading results. With large areas, analysing subdivisions tests the robustness of overall trends. The possibility of non-linear trends should be investigated although high-order polynomials are likely to be unstable and certainly should not be extrapolated. For directional statistics, as for cirque and glacier aspects, small datasets can give significant results if asymmetry is strong (i.e. high vector strengths, high consistency). These results may, however, relate to either topography or climate. High strengths can be produced if one side of a mountain range is studied, but that is of no climatic significance. If a drainage basin is analysed there will be a bias to the direction of the trunk stream. For datasets with more symmetry, mean directions may vary capriciously.

Evans (2012) considered the importance of mountain ranges (as opposed to drainage basins or geometric outlines) as relevant study areas with meaningful boundaries. Compactness (spatial proximity), however, is also important for climatic interpretations: clustering needs to be respected and isolated cirques or glaciers should be allocated to the nearest cluster, i.e. compactness of study areas is important, as well as size and uniformity. Here we advocate multi-

scale analysis in terms of study areas. Results can vary considerably even between adjacent areas. Analysis of nested study areas complicates interpretation; but it can increase confidence in results that are resilient.

REFERENCES

- Dark, S.J., Bram, D., 2007. The modifiable areal unit problem (MAUP) in physical geography. *Progress in Physical Geography* 31 (5), 471-479.
<https://doi.org/10.1177/0309133307083294>
- Evans, I.S., 1981. Census data handling. In: Wrigley, N., Bennett, R.J. (Eds.) *Quantitative Geography: A British View*. London: Routledge & Kegan Paul, pp. 46-59.
- Evans, I.S., 2012. Geomorphometry and landform mapping: what is a landform? *Geomorphology*, 137 (1), 94-106.
- Evans, I.S., Cox, N.J., 1995. The form of glacial cirques in the English Lake District, Cumbria. *Zeitschrift für Geomorphologie*, N.F. 39 (2), 175-202.
- Flowerdew, R., 2011. How serious is the Modifiable Areal Unit Problem for analysis of English census data? *Population Trends* 145, 106-118.
- Goodchild, M.F., 2022. The Openshaw effect. *International Journal of Geographical Information Science*, 36:9, 1697-1698.
<https://doi.org/10.1080/13658816.2022.2102637>
- Li, Y., Zhao, Z., Evans, I.S., 2023. Cirque morphology and palaeo-climate indications along a south-north transect in High Mountain Asia. *Geomorphology* 431, 24 pp.
<https://doi.org/10.1016/j.geomorph.2023.108688>
- Mîndrescu, M., Evans, I.S., Cox, N.J., 2010. Climatic implications of cirque distribution in the Romanian Carpathians: palaeowind directions during glacial periods. *Journal of Quaternary Research*, 25 (6) 875–888.
<https://doi.org/10.1002/jqs.1363>
- Openshaw, S., Taylor, P.J., 1981. The modifiable areal unit problem. In: Wrigley, N., Bennett, R.J. (Eds.) *Quantitative Geography: A British View*. London: Routledge & Kegan Paul, pp. 60-69.

Applying Terrain analysis to human population?

Hannes I. Reuter
 gisxperts
 Trier, Germany
hannes@gisxperts.de

Abstract—Terrain analysis methods are suitable to analysis datasets from a wide variety of statistical domains – not only digital elevation models. We applied a range of these to the total population dataset for Europe for the year 2011 to see the feasibility of identifying outliers, artefacts in the dataset as well as compare against more traditionally generated population derived datasets. The methods applied proved feasible and viable to identify corresponding regions for statistical purposes.

I. INTRODUCTION

The Geomorphometry community applies their methods mainly on surfaces derived from elevation measurements [1]. However the author argues that the quantitative and qualitative methods can be applied to any surface derived from any measurement. In the traditional Geomorphometry sense it would be an elevation surface, however it could be any sparse or complete matrix covering a given area.

Outside the Geomorphometry domain examples observed are human brain images recorded in 3D using Magnetic Resonance Tomography (MRT) [2], shell morphometry [3], charcoal morphometry [4] or dairy cow lameness [5] to name a few. The author observes on a non statistical sound sample from the research literature ($n=20$) that simple methods (e.g. like length/width) are often used to describe and analyse the respective aspect under consideration. We postulate that it seems the more advanced methods developed in the Geomorphometry community have not reached the main stream research as a tool of choice for specific research areas outside the direct Geomorphometry / environmental domain.

We argue that the primary (e.g. based on elevation like focal mean), secondary (based on first derivative like slope) or tertiary (landform classification based on slope and curvature) methods applied can be used for a variety of purposes. Examples could be simply a hill shade for error detection, a landform classifications applied for generating feature objects in the feature space for future statistical aggregation or analysis. The objective of this abstract is to showcase the application of terrain analysis methods to a population distribution surface and to encourage the Geomorphometry community to reach out to other domains so the more “advanced” methods become part of the standard toolset for scientist.

II. DATA & METHODS

A. Dataset

Every 10 years the Census is executed in the statistical world. A census is the periodic enumeration of a population containing quite often a variety of demographic information. In 2011 the European Statistical System (ESS) headed by Eurostat together with the European Forum for Geography and Statistics (EFGS) compiled a 1km total population (e.g. count of people) grid.

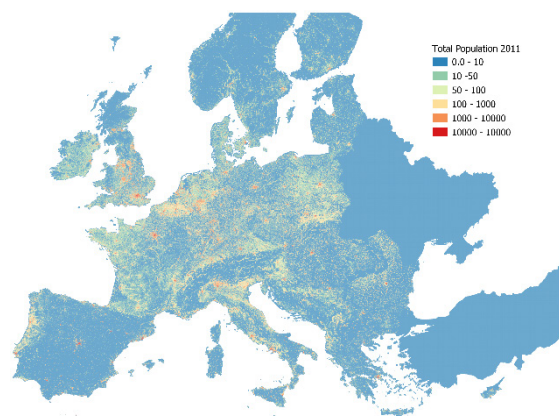


Figure 11 Total Population distribution for 2011

The data were aggregated from point observations or using a hybrid approach for 16 countries, while the rest of the submission from the Countries used a downscaling approach. Reporting data on a grid allows studying causes and effects of many socioeconomic and environmental phenomena.

Additional advantages on reporting on a grid compared to a traditional reporting on statistical/administrative areas are:

- grid cells all have the same size allowing for easy comparison;
- grids are stable over time;
- grids integrate easily with other scientific data (e.g. meteorological information);

- grid systems can be constructed hierarchically in terms of cell size thus matching the study area; and
- grid cells can be assembled to form areas reflecting a specific purpose and study area (mountain regions, water catchments).

The full dataset of total population for the year 2011 is shown in Figure 1. The dataset is available for the years 2011 and 2021 at <https://ec.europa.eu/eurostat/web/gisco/geodata/reference-data/population-distribution-demography/geostat>.

A new dataset has been created for the reference year 2021 containing preliminary and final data.

B. Software

The WhiteboxTools Software Suite, an open-source geospatial data analysis platform was used to perform a variety of analytical tests on the above mentioned dataset.

III. RESULTS

We deployed various terrain measures which are known to highlight inconsistencies in classical terrain analysis. No significant errors could be identified visually using hill shades as seen in Figure 2 and Figure 3. Similar results could be observed for Circular Variance of Aspects which highlighted clearly the stream network type distribution where people are living in Figure 4.

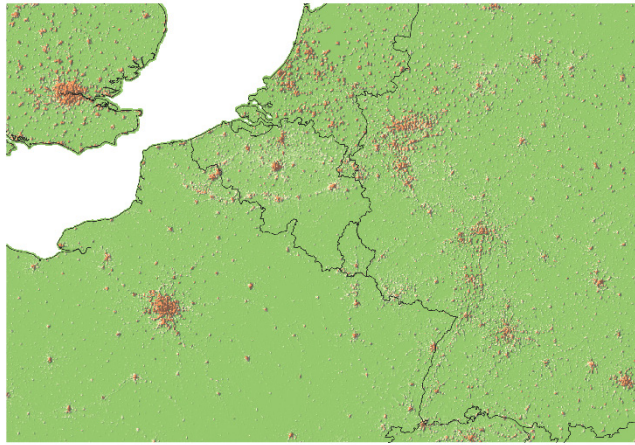


Figure 12 Hypsometric tinted hill shade encompassing some of the Benelux states.

Profile curvature however showed single cells consistently distributed across the city centres plus around the city boundaries of unclear origin as seen in Figure 5 below. Negative profile curvatures could be attributed to unpopulated areas (e.g. graveyards, railway infrastructures) while positive curvatures are of unknown origin. The authors postulates from the metadata that these could be due to allocation of populations of specific nature e.g. foreign duty personal, homeless people. Edges of cities could also be observed with city centres as well. The identified cells can be used as input for further quality control as these could be indications of possible errors in the dataset compared to their surroundings. Further research need

to be performed to see if any valuable information can be extracted –e.g. possible together with land use datasets.

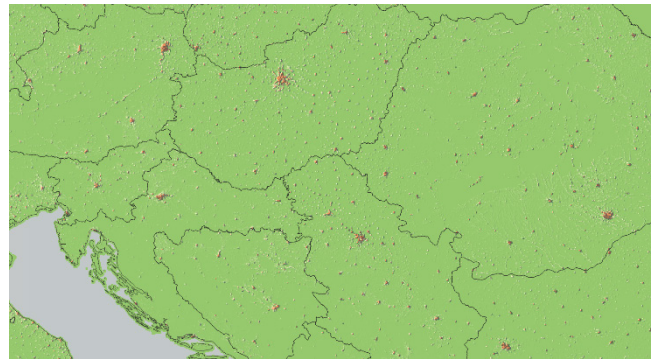


Figure 13 Hypsometric tinted hill shade encompassing some Eastern Europe countries

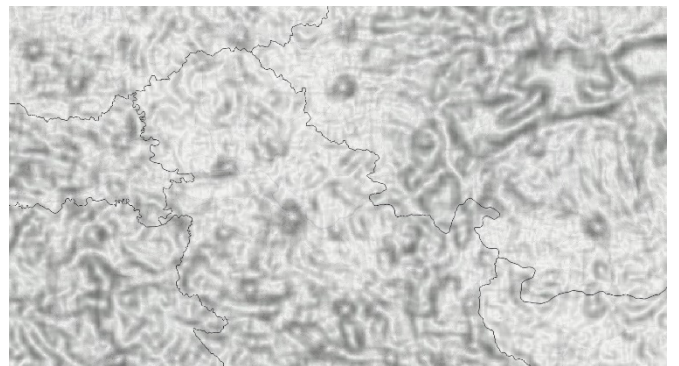


Figure 14 Circular Variance of Aspect for some Eastern European Countries.

The dataset is generated for each Member states separately, than merged into a pan-European dataset. One could expect to see edge artefacts across country boundaries due to different methodologies. However no effects were observed for the 2011 dataset.

Landform classification based on Geomorphons and k-means clustering delivered similar results for populated areas/non populated areas as well for urban/regional classifications.

IV. CONCLUSIONS

The application of terrain analysis methods usually applied to Digital elevation models allowed a quantitative and qualitative assessment of the population grid from 2011 and the upcoming grid from the 2021 exercise. The same methods can be applied elsewhere in the world for the validation of the population grids. While execution times were exceptionally fast, some difficulties were encountered as the sparse data matrices (e.g. large areas set to Zero due to unpopulated areas) need to reasonably treated as edge effects were sometimes polluting the results.



Figure 15 Profile Curvature across Berlin and Potsdam (top) and Madrid (bottom) draped over an OSM background map. Note the location of the dark pixels in the city centers and the white areas surrounding the city boundaries.

REFERENCES

- [1] T. Hengl and H.I. Reuter, Geomorphometry: concepts, software, applications. *Developments in Soil Science*, 33, [https://doi.org/10.1016/S0166-2481\(08\)00001-9](https://doi.org/10.1016/S0166-2481(08)00001-9).
- [2] S. Gerber, M. Niethammer, E. Ebrahim, J. Piven, S.R. Dager, M. Styner, S. Aylward, A. Enquobahrie, Optimal transport features for morphometric population analysis, *Medical Image Analysis*, Volume 84, 2023, <https://doi.org/10.1016/j.media.2022.102696>.
- [3] P. Poitevin, V. Roy, G. Cervello, F. Olivier, R. Tremblay, Spatiotemporal variations of *Chlamys islandica* larval shell morphometry between 2000 and 2018 in a depleted coastal scallop fishing area, *Estuarine, Coastal and Shelf Science*, 286, 2023, <https://doi.org/10.1016/j.ecss.2023.108322>.
- [4] R.S. Vachula, J. Sae-Lim, R. Li, A critical appraisal of charcoal morphometry as a paleofire fuel type proxy, *Quaternary Science Reviews*, 262, 2021, <https://doi.org/10.1016/j.quascirev.2021.106979>.
- [5] B. Jiang, H. Song, H. Wang, C. Li, Dairy cow lameness detection using a back curvature feature, *Computers and Electronics in Agriculture*, 194, 2022. <https://doi.org/10.1016/j.compag.2022.106729>

Functional Quality for GDEM Assessment

Francisco Javier Ariza-López

Dpto. Ingeniería Cartográfica, Geodésica y Fotogrametría.
 Universidad de Jaén
 Jaén, España
fjariza@ujaen.es

Juan Francisco Reinoso-Gordo

Dpto. Expresión Gráfica Arquitectónica y en la Ingeniería
 Universidad de Granada
 Granada, España
jreinoso@ugr.es

Abstract— The current paradigm in geospatial data quality assessment is datacentric (internal quality) and the evaluation of the GDEM does not escape this situation. Data quality should be evaluated as fitness for use, but this perspective is unapproachable. A new paradigm is proposed to overcome this situation by considering generic use cases that link geospatial data with its processing (algorithms). The new approach proposed by the functional quality supposes an intermediate situation between the user's and producer's perspectives (external and internal quality). This paper defines the functional quality, explains the need for this new perspective and shows an example.

I. INTRODUCTION

The concept of quality is close to everyone, it is used in colloquial language and is universally understood and intuitively accepted. In general, it can be said that a well-done work has quality. The term quality is defined in [1] as the degree to which a set of inherent characteristics of an object fulfills requirements. This definition clarifies that quality does not have to be limited to a single property of the object under consideration, but that several factors may come into play to define quality. On the other hand, what is inherent is what is proper or inseparable from things, and it is worth clarifying that here are factors that are more evident, or explicit, than others that have a more implicit character. Another interesting aspect of this definition is the one that quality refers to the fulfillment of requirements.

In this way, it is interesting to define what fitness for use is. The American Association for Quality glossary on quality [2] tells us that fitness for purpose is a «term sometimes used to define the term "quality", to indicate the degree to which a product or service meets the requirements for its intended use». Thus, we consider that term “fitness for use” implies having: i) a well-determined purpose of use and ii) the ability to evaluate the performance level. In relation to the first component, use cases can be considered. Basically, a use case is nothing more than the description of an action or process with a certain level of formalization (e.g., using Unified Modeling Language diagrams, or any other language). Focused on a specific user requirement, the documentation of a use case must include the actors, actions, inputs, outputs and decisions necessary to achieve the proposed goal. The fitness for use approach supposes the loss of the most transcendent, abstract and general vision of quality to focus on specific use cases. For example, in the automobile sector, there are many possible users, uses and ways of driving a specific vehicle model. Considering that for a user the fuel consumption is a relevant aspect of the quality of a

car model, and that it is impossible to adequately inform for all possible situations, standards, such as the New European Driving Cycle (NEDC) [3], and more recently the World Harmonized Light-duty Vehicle Test Procedure (WLTP) [4], have been adopted for dealing in this complex scenario. In the latter, a driving dynamic is adopted that tries to reproduce much better how people drive in the real world [5]. Closer to the geospatial world, there is experience in performing functional tests on web services (semantic services [6], geospatial services [7] such as WFS, WCS, etc.). And, more generally, the OASIS model [8] for web services establishes several quality dimensions on functional aspects.

For all these reasons, we consider that proposing the perspective of functional quality applied to the case of geospatial data is in line with what is already a reality in more advanced fields.

The objective of this paper is to develop a new perspective of the quality of geospatial data, in which we are guided by the example previously exposed for the automobile sector. We propose that quality be defined and evaluated in specific use cases, which means linking data and processes (algorithms). In this way we get much better approximation to the fitness for use. We call this new perspective functional quality.

The structure of the paper is as follows: Section 2 defines functional quality in more detail. Section III shows an application example for the use case of basin delineation. Finally, Section IV presents a brief conclusion.

II. DEFINING THE FUNCTIONAL QUALITY

This paper proposes the adoption of a new level of analysis and information on the quality of geospatial data, which we call functional quality. We describe quality with the adjective functional since we propose evaluate how well the data “works/permits” in specific use cases.

Since geospatial data is used in processes, this new level of quality assessment and reporting picks up on this, linking data with algorithms, or chains of processes, to more fully consider the quality of outputs, which most directly affects to users. Thus, we define functional quality as the consistency, against a reference, of the results generated by a given algorithm (process) when applied to a given geospatial data set (e.g., a given digital elevation model —DEM— dataset that is used for the determination of a hydrographic network).

We understand the functional quality as a new perspective that can be complex and must be defined by various indices (quality measures). For example, for the case of a drainage network determined on a DEM dataset and a given algorithm, some aspects that can help to inform about the functional quality of the DEM are: displacements of the resulting network, completeness of the obtained network, topological problems present in the network, etc. That is to say, aspects that may be of interest to a user who will use that drainage network in their production processes or decision making.

Therefore, functional quality approximates the “fitness for use”, but focused on a use case defined as generic and not considering particular requirements of some users or others (for example, for an engineering project, resolution requirements are different for the phases of feasibility study, preliminary design and project). With all this, a certain component of particularity is eliminated, as occurs when applying the NEDC and WLTP methods for assessing the fuel consumption in specific driving scenarios.

So, functional quality can be considered as the middle layer of a three-layer system, each of which brings us closer to quality from a different perspective: internal quality (the data-centric traditional producer's perspective), functional (use-case-centric perspective) and external quality (fitness for use perspective). In this way, a more general approach to use cases can be made without going into the problem of countless users and specific conditions of their applications, which supposes a context that is too rich and broad to be addressed. Basically, we are following the same scheme that has been mentioned previously for the case of the automobile sector with respect to the information on vehicle consumption.

III. EXAMPLE

The first step in addressing functional quality is to define the use case to be considered. We call “base use case” the use case without being linked to a specific algorithm or process, and “specified use case” the base use case when it is linked to an algorithm or processing. In this example we consider a “basin delineation” as the base use case, which is a use case of some relevance [9]. The definition of the use case should be as detailed as possible. In our case, the proposal made by [10] will be followed. Table 1 presents the use case definition schema for this example. Key aspects are: i) the explanation of the intended use of the data, this explanation must convey an interpretative context of high value for the base use case, ii) the requirements that are established on the data from a functional perspective, they are called key performance indicators (KPI), in this example we consider three KPI based on five measures, iii) the algorithm that is considered, in such a way that the evaluation is linked to that algorithm (specified use case). We want to indicate that the KPIs are the basis of the “functional” evaluation. Therefore, KPIs must be carefully proposed by users or user communities. The international standard ISO 19157 [11] proposes several data quality measures that can be considered

(e.g. six measures for the absolute or external accuracy that can be applied to 1D, 2D and 3D data, and nine measures that are specific for the vertical positional uncertainties). These measures are well defined since the ISO 19157 standard establishes a schema with twelve elements that characterize them (name, definition, description, basic measurement, etc., see annex D "List of standardized data quality measures" of ISO 19157 for details), however they present an excessively data-centric perspective typical of official geospatial data producers.

In addition to the KPIs, you also need a model that allows you to integrate the KPI's individual values into a single final or global result (a single value or an accept/reject). This model may require considerable effort from user communities to agree. The international standard ISO 19157 offers some models that can serve as an example when generating a value for the global result of the assessment (e.g. 100% pass/fail, weighted pass/fail maximum/minimum value, see annex J "Aggregation od data quality results" of ISO 19157 for details). In this case, based on user surveys, a model with five requirements has been established (see Table 1). The five KPIs and the proposed model aim to ensure three aspects (“facts” in Table 1): adequate positional accuracy, adequate statistics of the areas, and adequate spatial overlapping of the areas. This model is equivalent to the “100% pass/fail” insofar as the five KPIs are required to have acceptable values simultaneously.

TABLE I. EXAMPLE OF USE CASE DEFINITION

<i>Use case element</i>	<i>Explanation</i>	
Use case name	Determination of a hydrographic basin.	
Abstract	The user wishes to generate the planimetric delineation of a basin or set of (sub-)basins from a DEM data set.	
Algorithm	Multiple flow direction.	
Use	The result of the processing is a polygonal enclosure(s) that is(are) used to establish areas of interest for further spatial analysis.	
Requirements	Fidelity of the results:	
	Facts:	Measures:
	2D Positional accuracy of boundaries	<ul style="list-style-type: none"> • Buffer width (95%) (m)
	Accuracy of area estimation	<ul style="list-style-type: none"> • Limited bias in the area estimation (ha) • Maximum standard deviation (ha)
Level of area overlay		<ul style="list-style-type: none"> • Minimum mean value of overlay agreement (%) • Maximum standard deviation of the mean overlay agreement (%)

Functional quality can be used to compare data (a product vs. a reference data set), but also to compare algorithms (results of a given algorithm vs. the results of a reference algorithm) using

the same data set. The latter case is the one that will be presented here.

For the example case, we will consider the comparison of the results of two algorithms for watershed delineation (D8 [12] and multiple flow direction [13]) on the same data set. The data set correspond to the SRTM v3 [14] of a small area ($\approx 13 \text{ Km}^2$) in the surroundings of Allo (Navarra, Spain) (Fig. 1). This figure shows the data considered as reference (in blue) and the “product” (in red). The mean watershed size is 0.64 km^2 .

In this example the data will be considered to have adequate functional quality if:

- 1º) the positional accuracy of the boundaries of the basins is less than 50 m in 95% of the cases AND
- 2º) the bias in determining the area is less than 1000 m^2 AND
- 3º) the standard deviation of the estimation of the areas is less than 2,5 hectares AND
- 4º) the degree of agreement in the overlapping of the areas is greater than 95% AND
- 5º) the standard deviation of the average degree of overlap is less than 1%.

It should be noted that the values established for the KPIs are dependent on the scale/resolution of the geospatial data but also on the set of individuals of interest itself (the watersheds in this case). It should be noted that although the determination of the KPIs and their associated measures is complex, the determination of the values to be considered for each measure is no less complex. This is a process in which the voice of the user (model and KPIs) must be considered, but also the voice of the processes (what can be obtained from imperfect data, algorithms and models).

Going back to the example, the results for the measures considered is $\{40 \text{ m}, 990 \text{ m}, 2.29 \text{ ha}, 95.54 \%, 0.033 \%\}$ respectively, therefore, it can be considered that the result of the analyzed algorithm adequately meet the required functional quality.

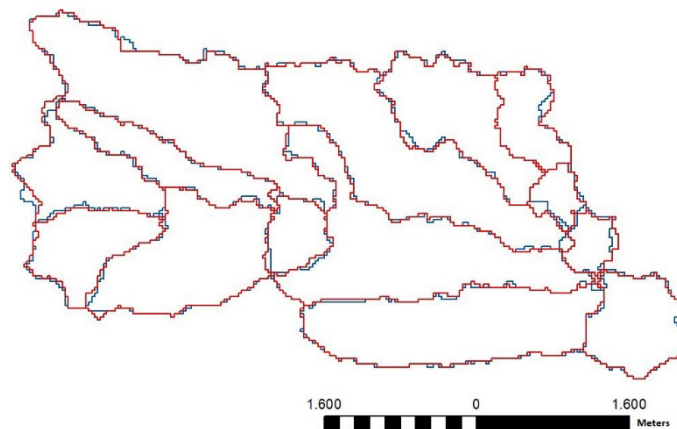


Figure 6. Delineation of basins used in the example

IV. CONCLUSION

The main contribution of this work is conceptual and has focused on justifying the need to introduce a new level of quality assessment (functional quality), which is more informative for users but, at the same time, can be applied by producers. Based on what is already being done in other fields (e.g., vehicles and web services), we consider that adopting the perspective of functional quality is a natural evolution for the case of data and its processes.

This new level of evaluation is intermediate between quality, as it is currently understood and materialized by producers, and quality in the sense of “fitness for use”. Functional quality links geospatial data with its processes, so it offers a way that is much closer to users and can help producers to be more attentive to user’s needs.

There are many use cases that can be considered for GDEM data. In this paper, a fairly simple but usual use case has been presented as an example with the aim of facilitating the understanding of the new evaluation paradigm that is proposed. The most critical issues of this new framework are the need to formalize the use cases, establish the KPIs and the model to integrate the KPI's individual values into a single final or global result (a single value or an accept/reject). We believe that all of this should be the result of consensus among users, and that standards or guides should be established for their homogeneous application.

V. ACKNOWLEDGMENT

This work has been founded by the research project "Functional Quality of Digital Elevation Models in Engineering" of the State Agency Research of Spain. PID2019-106195RB-I00/AEI/10.13039/501100011033 (https://coello.ujaen.es/investigacion/web_giic/funquality4dem/).

REFERENCES

- [6] International Standardization Association, ISO 9000:2015 Quality management systems — Fundamentals and vocabulary, ISO, 2015.
- [7] <https://asq.org/quality-resources/quality-glossary/f>
- [8] European Union, Regulation (EC) No 715/2007. Official Journal L 171, 29.6.2007. <https://eur-lex.europa.eu/eli/reg/2017/1347/oj>
- [9] European Union, Regulation (EU) 2017/1347. Official Journal L 192, 27.2017.
- [10] Dirección General de Tráfico, Nuevas mediciones, consumos más reales. <https://revista.dgt.es/es/motor/reportajes/2020/1217-WLTP.shtml>
- [11] A. Tahir, D. Tosi, S. Morasca, “A systematic review on the functional testing of semantic web services”, Journal of Systems and Software, Volume 86, Issue 11, Pages 2877-2889, 2013, <https://doi.org/10.1016/j.jss.2013.06.064>.
- [12] G. Giuliani, A. Dubois, P. Lacroix, “Testing OGC Web Feature and Coverage Service performance: Towards efficient delivery of geospatial

- data”, Journal of Spatial Information Science, No. 7, 1-23, 2013, <http://dx.doi.org/10.5311/JOSIS.2013.7.112>
- [13] OASIS, Quality Model for Web Services September 2005 <http://cliplab.org/Projects/S-CUBE/papers/oasis05:WSQM-2.0.pdf>
- [14] Ariza-López F.J., E.G. Chicaiza-Mora, J. L. Mesa-Mingorance, J. Cai, and J. F. Reinoso-Gordo, “DEMs: An Approach to Users and Uses from the Quality Perspective,” Int. J. Spat. Data Infrastruct. vol 13, pp. 131–171, 2018. <https://ijkdir.sadl.kuleuven.be/index.php/ijkdir/article/download/469/430>
- [15] Reinoso-Gordo, J.F. (2020). Casos de uso. En proyecto: “Calidad funcional de modelos digitales de elevaciones del terreno en ingeniería”, Programa Estatal, Ministerio de Ciencia, Innovación y Universidades, Convocatoria 2019.
- [16] International Standardization Association, ISO 19157:2013 Geographic information — Data quality. ISO, 2013.
- [17] Susan K. Jenson and Julia O. Domingue (1988). Extracting topographic structure from digital elevation data for geographic information-system analysis. Photogrammetric Engineering and Remote Sensing vol 54. pp: 1593-1600.
- [18] Qin, C., Zhu, A. X., Pei, T., Li, B., Zhou, C., & Yang, L. 2007. "An adaptive approach to selecting a flow partition exponent for a multiple flow direction algorithm." International Journal of Geographical Information Science 21(4): 443-458.
- [19] <https://www.earthdata.nasa.gov/news/nasa-shuttle-radar-topography-mission-srtm-version-3-0-global-1-arc-second-data-released-over-asia-and-australia>



Ariza-López, Reinoso-Gordo & Nero

Proposal for a Collaborative Data Infrastructure for Control of DEMs

Francisco Javier Ariza-López,
Manuel A. Ureña-Cámara
Dpto. Ingeniería Cartográfica,
Geodésica y Fotogrametría
Universidad de Jaén, España
fjariza@ujaen.es, maurena@ujaen.es

Juan Francisco Reinoso-Gordo
Dpto. Expresión Gráfica Arquitectónica
y en la Ingeniería
Universidad de Granada
Granada, España
jreinoso@ugr.es

Marcelo Antonio Nero
Centro de Geociências
Universidade Federal de Minas Gerais
Belo Horizonte, Brasília
marcelo.nero@gmail.com

Abstract— Global digital elevation models are well suited for many applications and therefore their quality needs to be evaluated. However, the evaluation of this type of data is expensive and efforts are often repeated. In addition, in certain global applications, the possibility of accessing local control data is missing. This paper proposes the design of a collaborative data infrastructure for the control of digital elevation models. Specifically, the data model related to the control part is established and, in addition, it must support the collaborative web application. The data may be of point type (e.g. points surveyed by Global Navigation Satellite Systems), transect (e.g. altimetric profiles or paths), or surface (e.g. a high density and accuracy patches). It is a flexible design that incorporates metadata for subsequent filtering. Along with the spatial and temporal aspects of the data, metadata attributes related to accuracy, instrumentation, operator, etc., are also included. All of these attributes must allow content to be properly filtered to provide adequate reference data for Digital Terrain Models (DTM) and Digital Surface Models (DSM) assessments.

I. INTRODUCTION

Digital Elevation Models (DEMs) are a typology of geospatial data product included in the Global Fundamental Geospatial Data Themes defined by the United Nations Committee of Experts for Global Geospatial Information Management [1]. DEMs have a significant role on numerous sustainable development goals of the United Nations (e.g. the 1st, 2nd, 3rd, 6th, 7th, 11th, 13th, 14th and 15th goals). For this reason, the quality of the DEM data is relevant and its control is required, especially at this time in which numerous applications are being developed on the so-called Global Digital Elevation Models (GDEM). Quality in DEM is mostly understood as an assessment of positional accuracy [2, 3], that is vertical accuracy; and the most critical aspect is usually having adequate reference data to be able to carry out the subsequent statistical analysis (e.g.

an estimate of error), with sufficient statistical representativeness.

Traditionally, in the case of geodetic and topographic surveys, the existing infrastructures, both in its physical part (monumentalized), and in its documental part, allowed the development of new and interoperable surveys with those already existing. Our idea is to offer an infrastructure that minimizes the cost of evaluating the accuracy of new GDEMs. This infrastructure will allow the reuse of existing evaluation work. In addition, it will allow collaboration between users and producers.

The objective of this document is to present the design of the proposed data infrastructure, justify some of the decisions made and explain its synergy between this infrastructure and the DEMIX project (Digital Elevation Model Intercomparison eXperiment).

II. GDEM ASSESSMENT, CONTROL INFRASTRUCTURES AND THE DEMIX PROJECT

A. Control infrastructures

Geospatial data refers to a changing reality such as the real world. For this reason, there is a need to update the geospatial data of a specific area, more frequently when greater dynamics of that area (e.g., new urban developments, etc.). So that, it is usual for the same area to have products from different times, depending on the update strategies adopted by the data producers.

Some elements of geospatial data quality (in the sense of ISO 19157) [4] require that quality be assessed against a reference, usually ground-truthing data. An adequate reference requires independence with respect to the data to be evaluated and also greater accuracy. This makes generating the references

costly and therefore it is usual to work with processes based on statistical sampling. It is also common to try to reuse reference data from previous evaluation processes, as long as they remain valid. This is the main justification for a control data infrastructure. There are several examples of geospatial data producers that have created their own control infrastructures (e.g. the Lucas facility by the European Environment Agency) [5]. In the case of GDEM, Bęcek et al. 2022 [6] proposed the Global Elevation Data Testing Facility (GEDTF). It is defined as “a database of anthropogenic and natural features found around the world that are flat (or nearly flat) and large (longer than 500m and wider than 15m)” (<https://zasobynauki.pl/zasoby/global-elevation-data-testing-facility-gedtf.49859/>)

B. GDEM assessment

GDEMs are commonly used for global studies by international user communities or organization. GDEMs are a type of data widely used today due to the interest in the analysis of various processes on a global scale (e.g. climate change). As indicated by [7] there is a need for a high-accuracy, open-access GDEMs. For this reason, there exists a great interest in knowing the quality of the various offered products, many of them available under a free and open data policy (e.g., NASADEM 1”, SRTM 3” and 1”, ASTER-GDEM v3, AW3D30 1”, TanDEM-X90, Copernicus DEM 3” and 1”, MERIT). Some analyses are:

- Iwao et al. [8] compared elevation values of GTOPO30 and SRTM 30 arc second datasets globally at degree confluences by means of GNSS data.
 - Xinchuan et al. [9] used five GDEMs (ASTER GDEM2, SRTM V4.1, GMTED2010, EarthEnv-DEM90, and GTOPO30) and compare them with ICESat/GLA14 data to assess the accuracy.
 - Acharya el at. [10] develop a comparison of the AW3D30 (Advanced Land Observing Satellite World 3D 30m) and SRTM30 (Shuttle Radar Topography Mission Global 30m) using as reference a 30m resampled LiDAR DEM.
 - Uuemaa et al. [11] examined the accuracy of six freely available global DEMs (ASTER, AW3D30, MERIT, TanDEM-X, SRTM, and NASADEM) in four geographic regions with different topographic and land use conditions. They used local high-precision LiDAR and Pleiades-1A data as reference.
 - Geoffroy and Guth [12] used high-resolution ICESat-2 point clouds to evaluate several GDEM (SRTM (V3), ASTER GDEM and ALOS World 3D AW3D30).
- and many others.

A general conclusion of these works is the lack of a common analysis method, and the lack of a common reference data set for the GDEM quality assessments.

C. The DEMIX project and the control infrastructures

The DEMIX project focuses on being able to suggest the best GDEM for a use case in a given area, and for this, reference data on a global scale is required. To date, the DEMIX project has focused on the development of definitions, use cases, the proposal of functional quality measures and the development of a statistical method for decision making based on qualitative and quantitative judgments.

According to [13], developing a test protocol and several comparison criteria is proposed to compare different GDEMs. In the comparison they will use a number of independent test sites (tiles), where in each of them must exist a reference dataset, deemed to be of higher accuracy. The reference data of a tile has an owner (“tile-owner”). It is desired to find a number of tiles, spread over the world that are representative of varying landforms and landscapes. The idea is to declare that a particular global DEM is better than the others, there is no reason to expect that it will be better in all the tiles.

Based on the evaluations for each GDEM and the typologies of the tiles, DEMIX proposes to create a web tool that guides the users of the GDEM so that they themselves choose the product (e.g., STRM, ASTER, TanDEM-X90, etc.) that performs best in areas equivalent to those of their interest.

We consider that there is a high degree of synergy and complementarity between the DEMIX project and the proposal of a control infrastructure. Having a collaborative and global control infrastructure will make it possible to have control data on a global scale, such as the GDEMs. This will allow for more comprehensive assessments. In addition, it will allow researchers to access the same set of reference data, and this will allow more interoperable results between different evaluation analyses. Having control data on a global scale in an open infrastructure does not limit the possible measures to be applied, it is only necessary to include the appropriate types of reference data for each use case (for example, altimetric points for vertical accuracy control and a drainage network for an evaluation on this use case).

III. THE CONTROL DATA INFRASTRUCTURE FOR GDEMS

A. Control infrastructures

The control-data infrastructure for DEM is a facility developed under the following criteria:

- Data Openness. Legal and technical openness by means of open data licenses and non-proprietary formats and access.
- Open contribution and cooperation. The infrastructure is open to receiving contributions from any interested party, with the only restriction of accepting the opening of the data and the technical supervision of their contributions.
- Web application. It is a web-accessible application.

The goal of this infrastructure is to provide reference data sets (points, profiles, surfaces and other data types) that can be used to evaluate the quality of DTMs (digital terrain models) and DSMs (digital surface models) (see [12] for a definition on DTM and DSM). The basic elements constituting the infrastructure are a database that houses the reference data and all the relevant metadata around them (e.g. authorship, accuracy, dates, methods, etc.), and the Web application that offers the service and interfaces with administrators and users. To achieve this purpose, the following bases are required:

- Data with adequate characteristics to serve as a reference data in quality assessment processes.
- Metadata that allows knowing key aspects of the reference data and being able to filter them based on their characteristics and user needs.
- Web system for collaboration and consultation.
- A data model that allows managing data, metadata, collaborations and access.

Our vision about the use of the infrastructure is as follows: this infrastructure should allow the user to filter their content considering time (e.g., date range), space (e.g., introducing a geographic window), type of application (e.g., DTM or DSM), resolution of the data to be controlled (e.g., 1", 3", etc.), and any other criteria that is considered relevant for a quality assessment and that is present in the metadata.

The database that has been designed contains two branches of interest (Figure 1):

- The branch of the responsible party (red branch of Figure 1). This branch is intended to store data relevant to those users who provide the control data (control-data owners) (e.g. name, address, phone, etc.).
- The branch of the control data set (blue branch of Figure 1). This branch is intended to store the control data in a structured way and with its appropriate metadata.

The participation of an individual or organization is done by means of one or several control datasets (*Ctr_DataSet*). Each control dataset must contain at least one control entity (*Ctr_Entity*). The control entities can be of the type point (*Points*), profile (*Profiles*) or surface (*Surfaces*) (Figure 2). Finally, the coordinates of the control structures are stored as triplets of X, Y and Z values (*Coordinates*). The control data sets, the control entities, the points, profiles and coordinates, are objects that have properties (e.g., minimum bounding box, date, accuracy, CRS, etc.), which allow the appropriate selection of the control data.

From the users' perspective, the main use cases considered are the following:

- Users (all): Register/deregister in the system.
- Users providing control data: Create control data sets, along with their metadata.

- Users providing control data: Upload control entities that are included in control data sets, along with their metadata.
- Data infrastructure users: Perform queries.
- Data infrastructure users: Download control data to perform their analysis.

Currently, the database for the infrastructure is in the final design phase. Tests are being carried out with the data corresponding to the geodetic network of Spain (points), road axes (3D profiles) and patches (surfaces) from surveys using laser techniques (aerial and terrestrial). It is now being tested in single user mode. The phase is scheduled to be completed by the end of Summer 2023. It is planned to develop a user management system with adequate capabilities (e.g. registration, log, etc.). It is scheduled to put the system into production at the end of 2023. All the development is done with open software tools and the database manager is PostGIS.

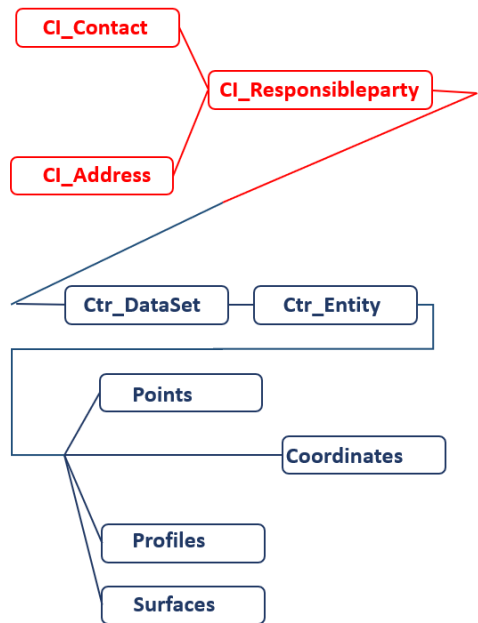


Figure 1. Database model schema, main object classes of the two branches: the responsible of the data (in red) and the data for the DEM control (in blue).



Figure 2. Example of control entities: geodetic monument, football pitch, parking zone, flat roof, pitched roof, airfield runway and a road

We consider that there is a high degree of synergy and complementarity between the DEMIX project and our proposal.

The DEMIX project focuses on being able to suggest the best DEM for a use case in a given area, and for this, reference data on a global scale is required. To date, the DEMIX project has focused on the development of definitions, use cases, the proposal of functional quality measures, and the development of a statistical method for decision making based on qualitative and quantitative judgments.

With a global perspective, our proposed infrastructure allows hosting control elements of a very diverse nature in a structured and use-oriented manner. Thanks to the considered metadata, it will be possible to filter control elements appropriate to the accuracy and space-time requirements of the DEM (or DSM) data to be controlled. For all these reasons, our infrastructure allows hosting the control tiles considered in the DEMIX project.

The development of the infrastructure is mature but not closed, which allows some modifications to be included in the data model, such that they could be relevant for the DEMIX project. The infrastructure is currently in the testing phase regarding the design of the database and the web service component is starting. It is expected to be operational by the beginning of 2024.

IV. ACKNOWLEDGMENTS

This research has been partially funded by the Project: "Functional Quality of Digital Elevation Models in Engineering" of the State Research Agency with code PID2019-106195RB-I00/AEI/10.13039/501100011033, more information at https://coello.ujaen.es/investigacion/web_giic/funquality4dem/.

REFERENCES

- [1] UN-GGIM (2019). The Global Fundamental Geospatial Data Themes. U.N. Committee of Experts on Global Geospatial Information Management. United Nations, New York.
- [2] Polidori L., El Hage, M. (2020). "Digital Elevation Model Quality Assessment Methods: A Critical Review" *Remote Sensing* 12, no. 21: 3522. <https://doi.org/10.3390/rs12213522>
- [3] Mesa-Mingorance, J.L., Ariza-López F.J. (2020). Accuracy Assessment of Digital Elevation Models (DEMs): A Critical Review of Practices of the Past Three Decades. *Remote Sensing* 12, no. 16: 2630. <https://doi.org/10.3390/rs12162630>
- [4] ISO (2013). ISO 19157:2013 Geographic information — Data quality-
- [5] European Environment Agency (2006). The thematic accuracy of Corine land cover 2000. Assessment using LUCAS. EEA Technical report No 7/2006
- [6] Bęćek K, Monika Stepnowska, Jakub Łuczak (2022). Global Elevation Data Testing Facility (GEDTF). Available in Atlas of Open Science Resources, <https://zasobynauki.pl/zasoby/global-elevation-data-testing-facility-gedtf/49859/>. License: CC BY-SA 4.0, <https://creativecommons.org/licenses/by-sa/4.0/legalcode.pl> .
- [7] Schumann Guy J-P. and Paul D. Bates (2018). The Need for a High-Accuracy, Open-Access Global DEM. *Front. Earth Sci.*, 04 December 2018, <https://doi.org/10.3389/feart.2018.00225>
- [8] Iwao K., N. Yamamoto, D. Patton, S. Kodama, R.Nakamura, M.Matsuoka, Tsuchida, S. Sekiguchi, E. Tsukud (2009). Validating global digital elevation models with degree confluence project information and aster-dem on geo grid. The Int. A. Photogrammetry, Remote Sensing and Spatial Information Sciences. Vol. XXXVII. Part B4. Beijing 2008.
- [9] Xinchuan Li, Youjing Zhang, Xiuliang Jin, Qiaoning He, Xiuping Zhang (2017). Comparison of digital elevation models and relevant derived attributes. *J. Appl. Remote Sens.* 11(4), 046027 (2017), <https://doi.org/10.1117/1.JRS.11.046027>
- [10] Acharya, T. D., Yang, J. T., & Lee, D. H. (2018). Comparative Analysis of Digital Elevation Models between AW3D30, SRTM30 and Airborne LiDAR: A Case of Chuncheon, South Korea. *J. of the Korean Society of Surveying, Geodesy, Photo. and Cartography*, 36(1), 17–24. <https://doi.org/10.7848/KSGPC.2018.36.1.17>
- [11] Uuemaa, Evelyn, Sander Ahi, Bruno Montibeller, Merle Muru, and Alexander Kmoch (2020). Vertical Accuracy of Freely Available Global Digital Elevation Models (ASTER, AW3D30, MERIT, TanDEM-X, SRTM, and NASADEM). *Remote Sensing* 12, no. 21: 3482. <https://doi.org/10.3390/rs12213482>
- [12] Geoffroy T., and Peter Guth (2020) Using high-resolution ICESat-2 point clouds to evaluate 1-3 arc second global digital elevation models: in Massimiliano Alvioli, Ivan Marchesini, Laura Melelli & Peter Guth, eds., Proceedings of the Geomorphometry 2020 Conference, https://doi.org/10.30437/GEOGRAPHOMETRY2020_29 .
- [13] Strobl P.A., Bielski C, Guth P, Grohmann C, Muller JP, López-Vázquez C, Gesch D, Amatulli G, Riazanoff S, Carabajal C (2021). The Digital Elevation Model Intercomparison eXperiment DEMIX, a community-based approach at global DEM benchmarking. In The International Archives of the Photogrammetry, Remote Sensing and Spatial Information Sciences, Volume XLIII-B4-2021. XXIV ISPRS Congress (2021 edition)

The DEMIX Wine Contest: a summary

Carlos H. Grohmann

Institute of Energy and
Environment Universidade de
São Paulo
São Paulo 05508-010, Brazil
guano@usp.br

Carlos López-Vázquez

LatinGEO Lab IGM+ORT
Universidad ORT URUGUAY
Montevideo, 11100, Uruguay
carloslopez@uni.ort.edu.uv

Peter L. Guth

Ocean & Atmospheric
Sciences Dept
United States Naval Academy
Annapolis, MD, 21402 USA
pguth@usna.edu

Conrad Bielski

EOXPLORER, Gaugrafenstr. 8,
Oberhaching, 8204,
Bavaria, Germany
conrad.bielski@eoxplore.com

Abstract— The DEMIX ‘wine contest’ is a novel framework for a practical approach to inter-compare a range of candidate digital elevation models (DEMs) based on pre-defined criteria and a statistically sound ranking approach, known as the randomized complete block design (RCBD). The application of the ‘wine contest’ to six 1 arc-second global DEMs, considering a wide set of study sites, covering different morphological and landcover settings, highlights the potentialities of the approach. Results confirmed significant superiority of COPDEM and FABDEM over ALOS AW3D30, NASADEM, SRTM and ASTER GDEM.

I. INTRODUCTION

Over the past two decades, several Earth observation missions have resulted in finer than 100m resolution global Digital Elevation Models (DEMs), most of which are shared freely and openly worldwide.

At this time, at least six different global medium resolution (i.e., 10-100m) DEMs have been produced using a variety of techniques. We expect more to come in the near future as new technologies and methods are developed. However, most users do not have the resources and expertise to perform an in-depth comparison of different DEMs. Therefore, expert advice that provides information pertinent to the user's need will benefit the community to identify the most appropriate dataset.

As a major step towards this goal, this paper presents the wine contest, a novel and flexible tool to provide geospatial data users with a practical approach to inter-compare a set of candidate global DEMs based on pre-defined criteria and a statistically sound ranking approach. The framework provides the wider geospatial community tailored recommendations regarding available DEM products that are not limited to one domain, geographic area, or landscape type. The method is flexible and customizable in relation to the specific needs and requirements of users in their particular application.

II. METHODS

Ranking a collection of wines or a set of DEMs from a given set of candidates leads to a mathematically similar problem. The method can also be applied to comparisons of other geospatial products and is in no way limited to ranking of global DEMs.

In a real wine contest, each expert or connoisseur judges the wine on its own merits which can be based on a set of criteria

such as taste, colour, bouquet, price, etc. The judge(s) evaluate and build an opinion based on their experience and taste without knowing the origins of the wine. The overall winner is thus declared after considering all the opinions, with equal weight.

For the inter-comparison of global DEMs, it is necessary to produce the contest ranking based on evaluations of the DEMs against high accuracy data (high-resolution lidar DEMs, geodetic benchmarks etc). The evaluations can be qualitative (subjective based on the opinion of an expert) or quantitative, based on some objective method that can produce a numerical result, which is amenable to be sorted.

The DEMIX wine contest is prepared as an evaluations table of k columns and N rows recording the assessment outcomes for each of the candidate DEMs and an opinions table, which translates the evaluations table to ranked opinions. A hypothetical example of these tables is presented in Figure 1.

Criteria that in general cannot be ranked, i.e., whose results cannot be interpreted in the sense of better or worse, are not applicable to the wine contest. Ties, individual results which are considered equally good (or equally bad), can be considered by applying the mid-rank procedure.

Tolerances should account for measurement uncertainty to identify minor differences in the evaluations table that will have an impact in the opinions table but are not really different. For example, many of the global DEMs only record elevation to the nearest meter and thus differences of centimeters or even decimeters would not record a significant difference among them.

The null hypothesis in the context of this ‘wine contest’ means that there is no difference among the DEMs, and a consensus based on the opinions cannot be achieved. However, if the null hypothesis is rejected, then the contest ranking is not based on chance (given a chosen confidence level) and some conclusions can be obtained.

A statistical confidence must be associated to the final wine contest rankings because it is imperative that the outcomes produced are not due entirely to chance (as might happen if the opinions table rankings are taken naively).

One of the strengths of the wine contest is that both quantitative and qualitative evaluations can be integrated into the contest. Therefore, a non-parametric test should be used

Assessments	Evaluations			Opinions		
	DEM-1	DEM-2	DEM-3	DEM-1	DEM-2	DEM-3
Visual assessment of the hillshade (by Expert 1)	1	2	3	1	2	3
Visual analysis of fine scale morphology (by Expert 2)	Fair	Very good	Bad	2	1	3
ELVD_RMSE (tol=0.5m)	17.12	16.96	23.94	1.5	1.5	3
ELVD_LE90 (tol=0.5m)	25.95	21.81	36.06	2	1	3
ELVD_MAE (tol=0.5m)	10.47	12.89	16.77	1	2	3
SLPD_RMSE (tol=0.5%)	17.27	14.17	20.73	2	1	3
SLPD_LE90 (tol=0.5%)	23.11	16.34	30.34	2	1	3
SLPD_MAE (tol=0.5%)	9.35	6.95	12.34	2	1	3
				R_i	13.5	10.5
				R_j^2	182.25	110.25
					576.0	sum=868.5

Figure 1. A wine contest example applied to the inter-comparison of DEMs - the evaluations table (left side) records the assessment outcomes for each of the candidate DEMs. The opinions table (right side) translates the evaluations table to ranked opinions.

which can operate over both types of rank results. The chosen non-parametric test for the wine contest is the Friedman Test [1], because among the non-parametric choices at hand, it is the best alternative for minimizing the risk of paradoxical results.

The general Friedman's statistic χ_f , is presented in Eq.1, valid with or without ties (N =number of opinions/assessments, k =number of DEMs).

$$\chi_f^2 = \frac{N(k-1)}{\sum_{i=1}^N \sum_{j=1}^k r_{ij}^2} \left[\sum_{j=1}^k \frac{R_j^2}{N} - C_F \right]; C_F = \frac{Nk(k+1)^2}{4} \quad \text{Eq. 1}$$

To apply the Friedman Test the entries in the opinions table (Fig.1) are denoted as the elements r_{ij} , and the final row presents the column sums by R_j . The remaining values to compute the Friedman statistic (χ_f) can be extracted from the same table: with $C_F=96$, sum of $r^2=111.5$, and sum of $R^2=868.5$, then $\chi_f=12.968$.

For a given k , N and confidence level alpha, the Friedman's statistic value χ_f^2 is compared to the critical value; if χ_f^2 is larger, the null hypothesis is rejected, and the conclusion is that we cannot accept that the DEMs are equivalent. Since we are willing to accept ties, the standard critical values tables from the Friedman Test are not suitable. From the table for $k=3$ provided by [2], and at the 95% confidence level, the row $N=8$ offers a critical value to compare of $\chi_{f\text{crit}}=5.793$. Compared to the χ_f result of 12.968 which is larger, one should reject the null hypothesis that the opinions table entries are purely at random, implying that the DEMs are equivalent.

The null hypothesis has been rejected based on the Friedman Test, so there are statistically significant differences among the set of DEMs under consideration. The lower the values of R_j , the better, but it is still necessary to assess whether the difference between the pairs of ranked candidate DEMs are statistically significant, or otherwise conclude that the pair is tied. The process is denoted as post-hoc analysis and there exist different options to carry out such an analysis. In this case and following [3], we propose to use the test by [4] applying the Bonferroni correction.

A pair of DEMs is considered significantly different if

$$|R_i - R_j| \geq z_{1-\alpha/k/(k-1)} \sqrt{\frac{Nk(k+1)}{6}} \quad \text{Eq. 2}$$

In this example, the critical value for the post-hoc analysis will be 4.005. To conclude whether there is a significant difference between ranked pairs the absolute difference between R_i and R_j should be greater than 4.005:

DEM3 vs. DEM2: $\text{abs}(24.0-10.5) = 13.5 \rightarrow$ significant

DEM3 vs. DEM1: $\text{abs}(24.0-13.5) = 10.5 \rightarrow$ significant

DEM1 vs. DEM2: $\text{abs}(13.5-10.5) = 3.0 \rightarrow$ not significant

From a DEM user perspective, the above wine contest results say that for the given assessment, either DEM1 or DEM2 could be equally recommended because there is no significant difference between them and they both ranked significantly better than DEM3 in the overall comparison. The conclusion is valid at the 95% confidence level.

III. GLOBAL DEMs COMPARISON

The wine contest approach was applied for the comparison of the six global DEMs that are available at a spatial resolution of 1" (ALOS AW3D30, ASTER GDEM, COPDEM, FABDEM,

NASADEM, SRTM) using a variety of criteria. The method is based on four overall steps:

Step 1: Obtain high quality reference elevation data (data with significantly higher accuracy elevation measures and much smaller sampling spacing than the DEMs to be tested);

Step 2: Prepare reference DEMs from the reference data. If required, adjust the vertical datum of reference DEMs;

Step 3: Evaluate the reference and global DEM data, for every test area and for every criterion to produce the evaluations table (Fig.2);

Step 4: Rank the global DEMs according to the wine contest rules to produce the opinions table. Produce final rankings based on chosen statistical confidence levels.

For each test area where reference DEMs were available, one or more DEMIX sampling tiles were extracted. A DEMIX tile is an area covering approximately 10 km x 10 km in size and defined on a geographic latitude/longitude grid [5].

The preparation of the reference DEMs was performed in MICRODEM version 2023.2.5 [6]. Of the global DEMs under consideration, only FABDEM claims to be a DTM. The rest of the candidate global DEMs are closer to DSMs but most likely

fall somewhere between a true DTM and DSM [7]. Due to this ambiguity, all the global DEMs considered were compared against both reference DTMs and DSMs when available. MICRODEM was used to produce a wine contest GIS database, combining the tile characteristics, the evaluations table, and an opinions table with an initial set of tolerances. The implemented DEMIX wine contest database [8] includes 39785 opinions which are rows found within the database.

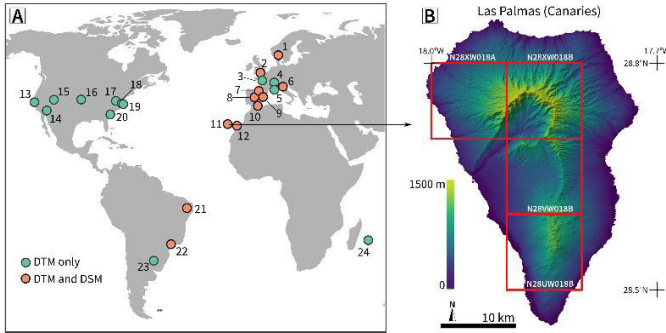


Figure 2. A) Location of the 124 test areas. B) Distribution of DEMIX tiles over Las Palmas Island. The names of the test areas shown on the map A: 01 - Norway, 02 - Oxford, 03 - Caen, 04 - Valonne, 05 - Vanoise, 06 - Trentino, 74 - Pyrenees, 08 - Madrid, 09 - Ebro Delta, 10 - Almeria, 11 - Las Palmas, 12 - Canary East, 13 - Redwoods, 14 - State Line, 15 - Canyon Range, 16 - Republican River, 17 - Shenandoah, 18 - Blackwater, 19 - Chincoteague, 20 - Charleston, 21 - Pernambuco, 22 - São Paulo, 23 - Uruguay, 24 - La reunion.

For all DEMIX tiles the following parameters were computed: Elevation Differences (ELVD), Slope Differences (SLPD), Roughness Differences (RUFD). The differences between the reference DEM and global DEM were always computed in the same manner:

$$\text{difference} = \text{global}_{\text{DEM}} - \text{reference}_{\text{DEM}}$$

where positive values indicate that the global DEM has a higher value than the reference DEM at a specific pixel.

For each parameter, the quantitative assessments were based on the following criteria: Standard Deviation (STD), Average Deviation (AVD), RMSE, MAE, LE90.

These quantitative assessments can be refined based on different slope and land cover classes:

- Cliff – pixels having a slope > 50%;
- Steep – pixels having a slope > 25% and < 50%;
- Gentle – pixels having a slope < 25% and > 12.5%;
- Flat – pixels having a slope < 12.5%.

The land cover classification used was the Copernicus Global Land Cover Layers – Collection 2 [9].

The final step in the DEMIX wine contest ranks of the candidate global DEMs. The functionality to read the database and implement the statistical procedures required to produce the final rankings was made available through a Jupyter notebook [10].

The information provided in the database allows the user to directly select opinions most appropriate to their requirements. For each run, the Jupyter notebook computes the final rankings based on the chosen opinions including the required confidence levels to support the outcomes. Furthermore, the DEMIX wine contest Jupyter notebook provides tools to analyse outputs by creating graphics and figures to help understand the final, wine contest rankings.

IV. RESULTS

Figure 3 summarizes the results of wine contests applied to subsets of the database. The top rows show the overall ranking using all tiles and criteria based on the DTM and DSM reference DEMs. For this set of evaluations (ALL land type), the DTM winner is FABDEM and the DSM is COPDEM, both at the 95% confidence level.

The DEMIX wine contest also associates statistical significance to the ranking and this is presented in Figure 3 by drawing a box around those global DEMs whose rank cannot be differentiated from a random result, i.e., the pairwise rank outcome does not pass the significance test.

The subsequent rows have been grouped by DTM or DSM, land type filter (FLAT, GENTLE, FOREST, etc), and criterion (ELVD_RMSE, SLPD_LE90, RUFD_MAE, etc). Not only the order can change but also the number of ties and between which candidate DEMs the ties have occurred. This illustrates the power of the wine contest procedure in the context of the inter-comparison of global DEMs because depending on the user requirements, the ‘best’ DEM will emerge based on the set of chosen criteria, far from a situation of one-option-fits-all.

To try and visualize the final ranking outcomes with a bit of context, Figure 3, columns B/D presents the same outcomes with the goal of showing how many times a DEM ranks higher/lower over the number of opinions. The output is the sum of the ranks for any particular DEM for each row in the opinions table divided by the number of opinions. The more times a DEM is ranked higher in the opinions table, the higher the ranking. In this case, lower is better.

To demonstrate the effects that changing tolerances can have on the final rankings, Figure 3B/D presents the outcomes based on higher tolerances: 0.5 → 1.0 and 0.2 → 0.4. The increasing of the tolerances has had the effect of producing more ties between the different global DEMs. This is an important result for the inter- comparison of global DEMs..

V. CONCLUSIONS

This paper presents the novel ‘DEMIX wine contest’, for the inter-comparison of digital elevation models which produces a final ranking with prescribed confidence levels based on given criteria. We applied the method to six global 1” DEMs: ALOS, ASTER, COPDEM, FABDEM, NASADEM, and SRTM. The

inter-comparison was done using 15 criteria related to elevation, slope and roughness measures derived from reference 1” DEMs. The wine contest provides final rankings with confidence level based on the choice of criteria and land type which demonstrates the powerful features of this method including the ability for the user to choose the most relevant criteria and areas.

From an overall final ranking of the global 1” DEM inter-comparison, COPDEM, ALOS and FABDEM are clearly the frontrunners based on the chosen criteria and test areas.

SRTM and NASADEM are distinctly in the lower half of the wine contest rankings indicating lower quality than the top three. If we limit ourselves to the tested criteria, the conclusion is that these global DEMs should no longer be used except perhaps to create composite DEMs or where elevations acquired around February 2000 are required.

As many prior studies have shown, the ASTER DEM is clearly the lowest performer and should only be used with great care when no alternatives exist.

VI. ACKNOWLEDGMENT

Support to the DEMIX project is performed by the European Space Agency (ESA) in the framework of the EDAP+ project. CHG is supported by CNPq (grant #311209/2021-1) and FAPESP (grant #2019/26568-0).

REFERENCES

- [1] Friedman, M. 1937. The Use of Ranks to Avoid the Assumption of Normality Implicit in the Analysis of Variance. *Journal of the American Statistical Association* 32, 675–701. <https://doi.org/10.2307/2279372>
- [2] López-Vázquez, C., Tasistro, A., Hochsztain, E., 2021. Exact tables for the Friedman rank test: Case with ties. *Chilean Journal of Statistics (ChJS)* 12(1). <http://soche.cl/chjs/volumes/12/ChJS-12-01-02.pdf>
- [3] Pereira, D. G., Afonso, A., Medeiros, F. M., aug 2014. Overview of Friedman's Test and Post-hoc Analysis. *Communications in Statistics Simulation and Computation* 44 (10), 2636–2653.
- [4] Dunn, O.J. 1961. Multiple Comparisons among Means. *Jour. of the Am.Statistical Association* 56,52-64. <https://doi.org/10.2307/2282330>
- [5] Guth, P. L., Strobl, P., Gross, K., Riazenoff, S., 2023b. DEMIX 10k Tile Data Set (1.0). Dataset on Zenodo.
- [6] Guth, P.L., 2023. MICRODEM. https://github.com/prof-pguth/git_microdem
- [7] Guth, P. L., Geffroy, T. M., aug 2021. LiDAR point cloud and ICESat-2 evaluation of 1 second global digital elevation models: Copernicus wins. *Transactions in GIS*, 2245–2261.
- [8] Guth, P.L. 2022. DEMIX GIS Database (1.0) [Data set]. Zenodo. <https://doi.org/10.5281/zenodo.7402618>
- [9] Buchhorn, M., Lesiv, M., Tsendbazar, N.-E., Herold, M., Bertels, L., Smets, B., mar 2020. Copernicus Global Land Cover Layers—Collection 2. *Remote Sensing* 12 (6), 1044.
- [10] Grohmann, C.H. 2023. DEMIX Wine Contest Jupyter Notebook. URL: https://github.com/CarlosGrohmann/DEMIX_wine_contest

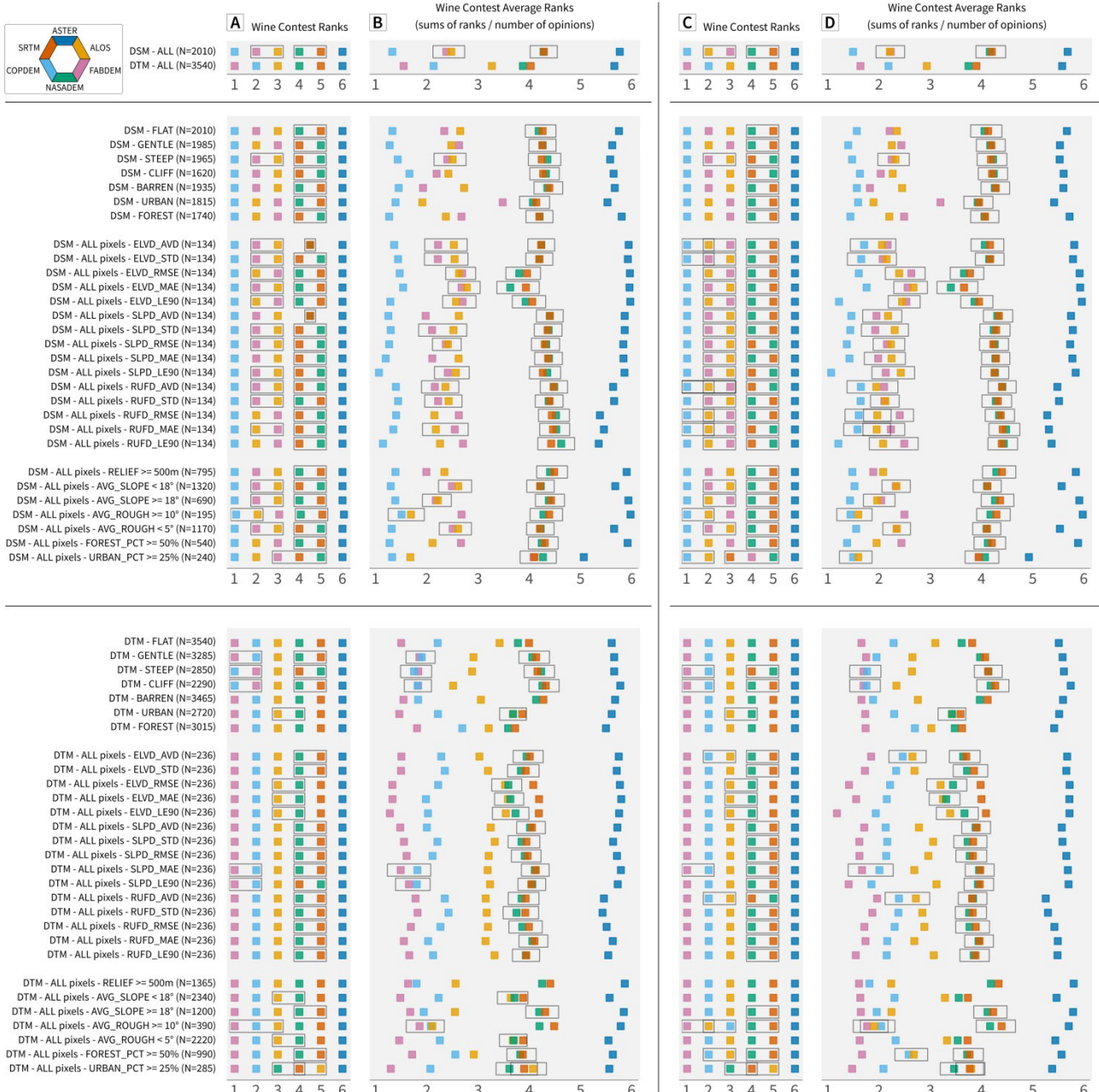


Figure 3. A) The final rankings of the DEMIX wine contest based on the inter-comparison of six 1'' global DEMs. The different outcomes are based on the chosen land types, the 15 contest criteria and filters for tiles with specific characteristics. Tolerances for A/B: ELVD=0.5, SLPD=0.5, RUFD=0.2. Tolerances for C/D: ELVD=1.0, SLPD=1.0, RUFD=0.4; the increase in tolerances led to a greater number of ties in C/D compared to the rankings shown in A/B.

The DEMIX Wine Contest Jupyter notebook

Carlos Henrique Grohmann

Universidade de São Paulo, Institute of Energy and Environment

Av. Prof. Luciano Gualberto, 1289, 05508-010

São Paulo, SP, Brazil

guano@usp.br

Abstract— Jupyter Notebooks are the most widely used system for shareable and reproducible research. Within the DEMIX Working Group, a Python Jupyter Notebook was developed for the analysis and visualization of the DEMIX Wine Contest. It can be run on a user's local machine or in the cloud using the Google Colab platform. The notebook, as well as auxiliary files, are available in GitHub. This article briefly describes its characteristics and usage.

I. INTRODUCTION

Jupyter Notebooks have become the most widely used system for shareable and reproducible research [1-3]. It supports a variety of programming languages, such as Julia, R, JavaScript, and C, allowing the user to create literate programming [4] documents combining code, text, and results with visualizations and other rich media [5].

Within the DEMIX Working Group [6], a Jupyter Notebook was developed for the analysis and visualization of the DEMIX Wine Contest. This article briefly describes its characteristics and usage. The reader is referred to [7] for the details of the DEMIX Wine Contest. In summary, the contest is designed to rank a set of Global DEMs based on a number of objective criteria (although subjective criteria could be used as well). Each criterion (such as RMSE) is used to rank the Global DEMs against a reference DEM. Then, a set of criteria is defined and the Friedman Test [8] is used to determine if the DEMs can or cannot be considered statistically different. If there are statistically significant differences among the set of DEMs, they are compared pairwise using the test by Dunn with Bonferroni correction [9] (a step called post-hoc analysis) and a final ranking is produced.

The notebook, as well as auxiliary files, are available in GitHub [10].

II. CHARACTERISTICS

The DEMIX Jupyter Notebook was developed based on Python version 3.10.x and the Pandas, qgrid, Numpy, Matplotlib, and Seaborn libraries [11-16].

As the idea behind the notebook was to provide a simple “interface” to analyze the DEMIX Wine Contest data, the statistical and plotting functions were implemented in the demix_wine_functions.py file, although the user can alter some plotting options, such as colors or symbols.

The notebook can be run on a user's local machine or in the cloud using the Google Colaboratory (Colab) platform. While running locally requires setting up a working python/jupyter environment, it allows for more flexibility in terms of files' location. Running it in Colab requires installing a specific version of qgrid, and downloading external files from GitHub and Zenodo. All the instructions necessary for the user to run the notebook are included as comments within code cells or as rich text.

III. USAGE

As input the Jupyter notebook takes the Wine Contest GIS database [17] produced by MICRODEM [18]. The GIS database contains signed (mean, median) and unsigned values (RMSE, LE90, MAE) of the differences of elevation, slope and roughness between the Global DEMs and reference DEMs, but only the unsigned values are read for the Wine Contest. The signed values are used to produce plots that help the user to explore and understand the set of data being analyzed.

Before exploring the database, the user can define the values for tolerances, which will impact the occurrence of ties between the DEMs in the rankings.

A pandas dataframe will be created from the GIS database, and the qgrid library will provide an interactive spreadsheet widget (Fig.1). This widget allows the user to query the database by various properties, such as selecting between DTM and DSM, filtering by DEMIX tile, area or difference metric.

It is imperative to select at least between DTM and DSM, as the analysis will not provide meaningful results if these two surface references are mixed.

A new dataframe is created based on the selection in the spreadsheet widget. This new dataframe will then be passed to the function responsible for the Friedman Test. This function will return information about the tolerances, which filters were applied to the database and the initial result, stating if the DEMs have statistically significant differences among them, and if the user can proceed to the post-hoc analysis (Fig.2).

The next step is the post-hoc analysis, and the function will return a table (Fig.3), where each row corresponds to one DEM, and the columns are:

- rank – the final ranking, where lower is better;

Display Database with qgrid

Any filtering/selection made here will propagate to the next step

	AREK	DEMIX	LATT	LONG	AVG _T	AVG _C	AVG _F	RELIE	FORE	URBK	BART	REI	LAN _T	LAN _C	TOL _F	DEMIX	COP _T	FABDE	COP _C	ALOS	NASA	SRTM	ASTER	REC _T	CRIT _T	FABDE	COP _C	ALOS	NASA	SRTM	ASTER	
0	la_p...	N28...	28.55	-17.85	952.47	37.05	7.39	1940...	61.6	1.14	0.83	DSM	Filter by REF_TYPE			x	3	1	3	3	5.5	0	ELV...	6.2	5.26	3.31	5.5	5.53	6.34			
1	la_p...	N28...	28.55	-17.85	952.47	37.05	7.39	1940...	61.6	1.14	0.83	DSM					3	1	3	3	6	1	ELV...	8.24	7.25	4.53	7.61	7.74	8.88			
2	la_p...	N28...	28.55	-17.85	952.47	37.05	7.39	1940...	61.6	1.14	0.83	DSM					2	1	4	5	6	2	ELV...	8.43	7.38	5.74	9.19	10.67	12.51			
3	la_p...	N28...	28.55	-17.85	952.47	37.05	7.39	1940...	61.6	1.14	0.83	DSM	<input type="checkbox"/>	DSM			2	1	4	5	6	3	ELV...	6.35	5.36	4.5	7.09	8.56	9.94			
4	la_p...	N28...	28.55	-17.85	952.47	37.05	7.39	1940...	61.6	1.14	0.83	DSM	<input type="checkbox"/>	DTM			2	1	4	5	6	4	ELV...	13.54	11.57	8.49	14.16	15.98	19.02			
5	la_p...	N28...	28.55	-17.85	952.47	37.05	7.39	1940...	61.6	1.14	0.83	DSM	Select All				1	3	4	5	6	5	ELV...	-1.8	1.36	3.52	5.16	7.34	8.81			
6	la_p...	N28...	28.55	-17.85	952.47	37.05	7.39	1940...	61.6	1.14	0.83	DSM	All	100	0.3		COP	cop	2	1	3	4	5	6	6	ELV...	-1.58	1.18	3.57	5.06	7.26	8.26
7	la_p...	N28...	28.55	-17.85	952.47	37.05	7.39	1940...	61.6	1.14	0.83	DSM	CLIFF	20.31	0.5		ALOS	alos	5.5	3	1	3	3	5.5	7	ELV...	9.07	8.3	4.12	8.36	8.41	8.99
8	la_p...	N28...	28.55	-17.85	952.47	37.05	7.39	1940...	61.6	1.14	0.83	DSM	CLIFF	20.31	0.5		ALOS	alos	4.5	2.5	1	2.5	4.5	6	8	ELV...	11.91	11.04	5.35	11.35	11.67	12.25
9	la_p...	N28...	28.55	-17.85	952.47	37.05	7.39	1940...	61.6	1.14	0.83	DSM	CLIFF	20.31	0.5		ALOS	alos	2.5	2.5	1	4	5	6	9	ELV...	12.06	12.02	7.03	13.56	15.45	17.23
10	la_p...	N28...	28.55	-17.85	952.47	37.05	7.39	1940...	61.6	1.14	0.83	DSM	CLIFF	20.31	0.5		ALOS	alos	2.5	2.5	1	4	5	6	10	ELV...	9.28	9.42	5.77	10.48	12.24	13.68
11	la_p...	N28...	28.55	-17.85	952.47	37.05	7.39	1940...	61.6	1.14	0.83	DSM	CLIFF	20.31	0.5		ALOS	alos	3	2	1	4	5	6	11	ELV...	19.27	18.58	10.36	20.62	22.99	26.54
12	la_p...	N28...	28.55	-17.85	952.47	37.05	7.39	1940...	61.6	1.14	0.83	DSM	CLIFF	20.31	0.3		FAB...	tie	1	2.5	2.5	4	5	6	12	ELV...	1.92	4.74	4.56	7.42	10.19	12.11
13	la_p...	N28...	28.55	-17.85	952.47	37.05	7.39	1940...	61.6	1.14	0.83	DSM	CLIFF	20.31	0.3		FAB...	alos	1	3	2	4	5	6	13	ELV...	2.33	5.33	5	7.36	10.09	11.34
14	la_p...	N28...	28.55	-17.85	952.47	37.05	7.39	1940...	61.6	1.14	0.83	DSM	STEEP	54.26	0.5		ALOS	alos	5.5	3	1	3	3	5.5	14	ELV...	5.72	4.81	3.06	5.15	5.07	5.79
15	la_p...	N28...	28.55	-17.85	952.47	37.05	7.39	1940...	61.6	1.14	0.83	DSM	STEEP	54.26	0.5		ALOS	alos	5	3	1	3	3	6	15	ELV...	7.12	6.16	4.03	6.66	6.56	7.71

Figure 1. GIS database rendered as a spreadsheet by qgrid. The selection between DTM and DSM is shown.

Ranking with user-defined tolerances (might take a while...)

Filter settings for column REF_TYPE:[‘DSM’]
Filter settings for column LAND_TYPE:[‘CLIFF’, ‘STEEP’]

Results of the DEMIX Wine Contest

For k=6, CL=0.05, and N=1770, the critical value to compare is chi_crit=11.038
And since chi_r (5965.160) is greater than chi_crit (11.038)...
Yay!! We can reject the null hypothesis and go to the Post-Hoc analysis!!

Figure 2. Example of results of the Friedman Test. Filters include a selection of DTM as surface type, CLIFF and STEEP as land types.

- sum of ranks – numerical value of the sum of all ranks for the DEM;
- sum of ranks divided by number of opinions – this value might be used for comparing ranks made with different sets of criteria;
- ties with – with which DEM there is a ‘tie’, that is, these DEMs don’t have a statistically significant difference.

Rank	Sum of ranks	Sum of ranks divided by number of opinions	Ties with
FABDEM	3.0	5958.0	3.366
COP	2.0	4471.0	2.526
ALOS	1.0	2372.5	1.340
NASA	5.0	7194.0	4.064 5.0
SRTM	4.0	7182.0	4.058 4.0
ASTER	6.0	9992.5	5.645

Figure 3 Example of the post-hoc analysis results, using the same filters as in Fig.3. Here SRTM and ASTER GDEM are tied in 4th place.

The notebook also provides tools to analyze outputs by creating graphics and figures. The plots included in the notebook were intended to illustrate the publication [7], and the choice of predefined parameters of colors, symbols, and text annotations reflect this.

Included in the notebook are a plot of correlation matrices, a customized scatterplot (Fig.4) of 60 wine contest ranks (including database filters on surface type, land type, land cover, geomorphometric indices, and two sets of tolerances), scatterplots of signed metrics (means, medians), unsigned metrics (RMSE, standard deviation), and of selected criteria per selected tiles (chosen as representative of the metrics’ behavior). All figures can be saved in common formats (e.g., .png, .svg). Note that the plots are not produced in ‘publication-ready’ formatting, as the author prefers to finalize the figures’ in an illustration software.

IV. CONCLUSION

This paper presented the DEMIX Wine Contest Jupyter Notebook, an open-source tool developed to provide an interface to explore the DEMIX GIS database and to generate Wine Contest results from several sets of criteria and tolerances. The notebook is available in GitHub. Indications of errors, bugs or suggestions to improve the code are welcome.

V. ACKNOWLEDGMENT

CHG is supported by CNPq (grant #311209/2021-1) and FAPESP (grant #2019/26568-0).

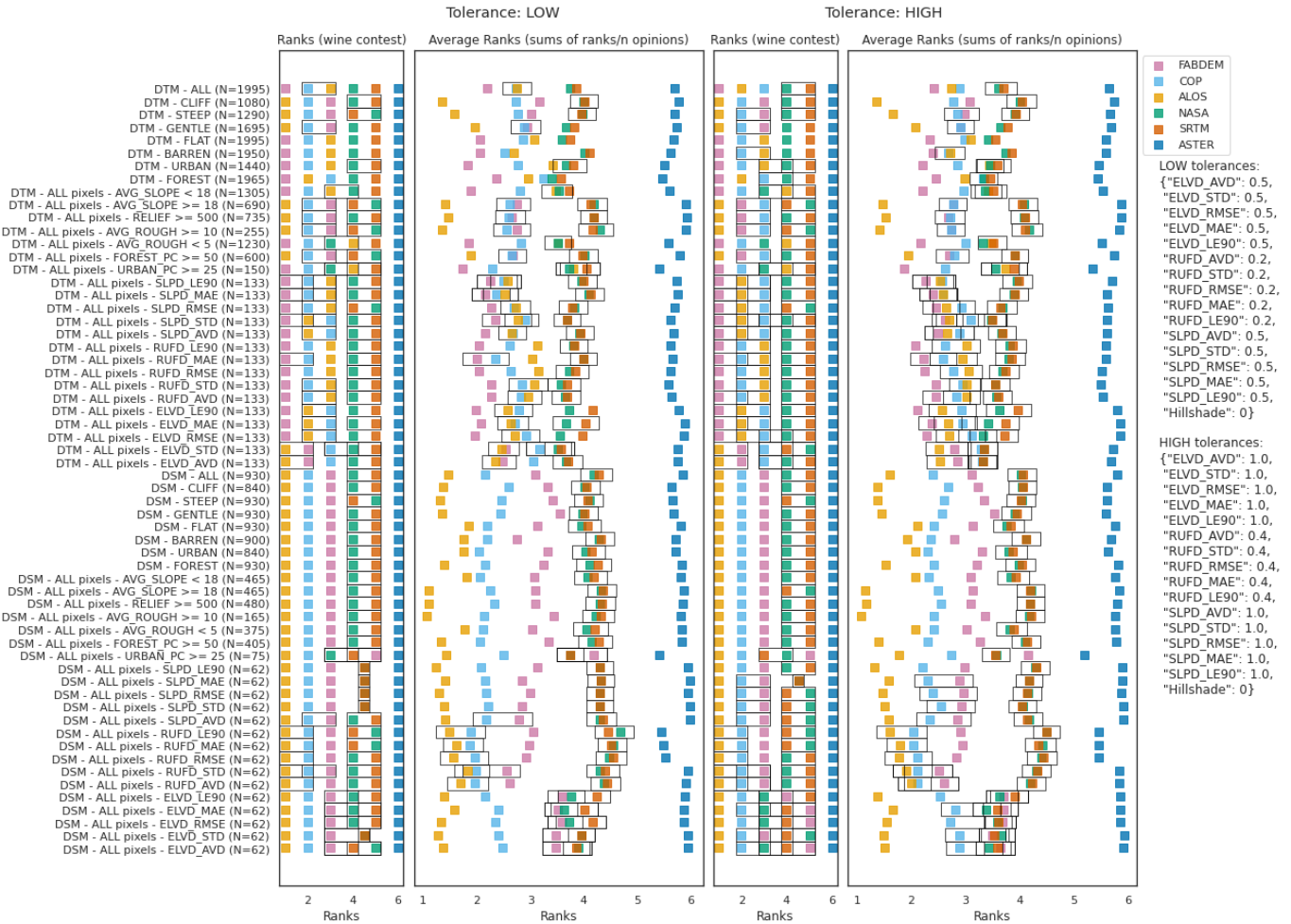


Figure 3. Scatterplot of 60 Wine Contests ran with different sets of criteria and tolerances. Rectangles over DEMs' symbols indicate a tie between them

REFERENCES

- [1] Shen, H. Interactive notebooks: Sharing the code. 2014. *Nature* 515, 151–152. <https://doi.org/10.1038/515151a>
- [2] Rule A, Birmingham A, Zuniga C, Altintas I, Huang S-C, Knight R, et al. (2019) Ten simple rules for writing and sharing computational analyses in Jupyter Notebooks. *PLoS Comput Biol* 15(7): e1007007. <https://doi.org/10.1371/journal.pcbi.1007007>
- [3] Kluyver T., Ragan-Kelley B., Pérez F., Granger B.E., Bussonnier M., Frederic J., Kelley K., Hamrick J.B., Grout J., Corlay S. et al. 2016. Jupyter notebooks - a publishing format for reproducible computational workflows. In: Loizides F., Schmidt B. (eds) Positioning and Power in Academic Publishing: Players, Agents and Agenda. IOS Press, pp 87–90. <http://dx.doi.org/10.3233/978-1-61499-649-1-87>
- [4] Knuth, D.E. 1984. Literate Programming, *The Computer Journal*, 27:2, 97–111, <https://doi.org/10.1093/comjnl/27.2.97>
- [5] Pimentel, J.F., Murta, L., Braganholo, V. et al. 2021. Understanding and improving the quality and reproducibility of Jupyter notebooks. *Empirical Software Engineering* 26:65. <https://doi.org/10.1007/s10664-021-09961-9>
- [6] Strobl, P.A.; Bielski, C.; Guth, P.L.; Grohmann, C.H.; Muller, J.P.; López-Vázquez, C.; Gesch, D.B.; Amatulli, G.; Riazanoff, S.; Carabajal, C. 2021. The Digital Elevation Model Intercomparison eXperiment DEMIX, a community based approach at global DEM benchmarking. *Int. Arch. Photogramm. Remote Sens. Spat. Inf. Sci.* 2021, XLIII-B4-2021, 395–400. <https://doi.org/10.5194/isprs-archives-XLIII-B4-2021-395-2021>
- [7] Bielski, C.; López-Vázquez, C.; Grohmann, C.H.; Guth, P.L.; The TMSG DEMIX Working Group. 2023 (preprint). DEMIX Wine Contest Method Ranks ALOS AW3D30, COPDEM, and FABDEM as Top 1" Global DEMs. ArXiV. <https://arxiv.org/abs/2302.08425>
- [8] Grohmann, C.H. 2023. DEMIX Wine Contest Jupyter Notebook. URL: https://github.com/CarlosGrohmann/DEMIX_wine_contest
- [9] Python Software Foundation, 2021. Python Programming Language, version 3.10.x. <http://www.python.org/>
- [10] Friedman, M. 1937. The Use of Ranks to Avoid the Assumption of Normality Implicit in the Analysis of Variance. *Journal of the American Statistical Association* 32, 675–701. <https://doi.org/10.2307/2279372>
- [11] Dunn, O.J. 1961. Multiple Comparisons among Means. *Jour. of the Am. Statistical Association* 56,52–64. <https://doi.org/10.2307/2282330>
- [12] qgrid python library. 2020. <https://github.com/lukewys/qgrid>
- [13] Harris, C. R., Millman, K. J., van der Walt, S. J., Gommers, R., Virtanen, P., Cournapeau, D., Wieser, E., Taylor, J., Berg, S., Smith, N. J., Kern, R., Picus, M., Hoyer, S., van Kerkwijk, M. H., Brett, M., Haldane, A., del Río, J. F., Wiebe, M., Peterson, P., Gérard-Marchant, P., Sheppard, K., Reddy, T., Weckesser, W., Abbasi, H., Gohlke, C., Oliphant, T. E.. 2020. Array programming with numpy. *Nature* 585 (7825), 357–362. <https://doi.org/10.1038/s41586-020-2649-2>
- [14] McKinney, W., 2011. pandas: a Foundational Python Library for Data Analysis and Statistics. In: Python for High Performance and Scientific Computing. https://www.dlr.de/sc/portaldaten/15/resources/dokumente/pyhpc2011/submissions/pyhpc2011_submission_9.pdf
- [15] Hunter, J.D., 2007. Matplotlib: A 2D graphics environment. *Computing Science & Engineering* 9(3), 90–95. <https://doi.org/10.1109/MCSE.2007.55>
- [16] Waskom, M.L., 2021. seaborn: statistical data visualization. *Journal of Open Source Software*, 6(60), 3021, <https://doi.org/10.21105/joss.03021>
- [17] Guth, P.L. 2022. DEMIX GIS Database (1.0) [Data set]. Zenodo. <https://doi.org/10.5281/zenodo.7402618>
- [18] Guth, P.L., 2023. MICRODEM. https://github.com/prof-pguth/git_microdem

Subjective Criterion for the DEMIX Wine Contest: Hillshade Maps

Peter L. Guth

Ocean & Atmospheric Sciences Dept
United States Naval Academy
Annapolis, MD, 21402 USA
pguth@usna.edu

Carlos H. Grohmann

Institute of Energy and Environment
Universidade de São Paulo
São Paulo 05508-010, Brazil
guano@usp.br

Sebastiano Trevisani

Culture del Progetto Dept
University IUAV of Venice
Venice 30123, Italy
strevisani@iuav.it

Abstract— Evaluation of the hillshade map provides a significant tool for evaluating the quality of digital elevation models. The DEMIX wine contest provides a statistically rigorous way to compare and rank DEMs, and applies the method to evaluate 6 global 1 arc second DEMs. The wine contest used only quantitative criteria; we present an example using the qualitative hillshade map to verify that the wine contest works with either quantitative or qualitative criteria as DEMIX proposed. Our results verify the COPDEM and ALOS are much better than SRTM, NASADEM, and ASTER, and that those three should be retired with the advent of much better technology. We also highlight the challenges in getting enough judges to look at enough DEMs to approach the number of opinions possible with quantitative criteria. Qualitative test will probably remain a useful adjunct to much more numerous quantitative tests.

I. INTRODUCTION

Digital elevation models (DEMs) represent a fundamental building block for work in science, engineering, social science, government, and the military. DEMs at 1" (arc second, about 30 m) provide the best resolution freely available globally. The DEMIX group is working to compare and rank 6 of those DEMs, and created a database to support their work [1-4]. The DEMIX wine contest provides a framework for ranking DEMs and providing statistical significance for the results. An oenological wine contest frequently involves subjective assessments from experts, and the DEMIX group noted the ability to use subjective assessments for a DEM wine contest, but did not include any subjective criteria in their initial results. We will use a subjective, visual criterion, show the challenges in applying it to a large number of test areas, and demonstrate that our application of the subjective criterion validates the DEMIX group findings [3] that COPDEM, ALOS, and FABDEM are demonstrably much better than SRTM, NASADEM, and ASTER.

II. METHODS

Nothing in the wine contest precludes subjective criteria tests; for demonstration purposes, during spring 2022 we experimented with showing 16 “experts” hillshades of the DTM from DEMIX tile [5] N28VW018B covering part of La Palma

in the Canary Islands (Figure 1). The DTM was created by aggregating a source DTM from the national mapping agency, using the 2 m DTM to create a 1 second DTM to match the global DEMs. Using a Google form [6], we asked the “experts” to rank the subjective visual quality of the maps. In addition to the images, they had an animation cycling through the hillshades which highlights differences. They were not allowed to have ties in their rankings.

During spring 2023 we repeated the contest with a larger number of “experts”, several different test areas (two in the western US, and one in the Italian Alps), and improved methodology. Our initial assumption was the students who constituted the bulk of our “experts” did not know anything about the 6 DEMs, and the original test included the DEM names (as Figure 1). The revised test removed the animation and the DEM names, and presented the DEMs in a different random order for each test areas. We will also run the contest during Geomorphometry 2023 in Iasi, both to demonstrate the method and to collect additional data.

III. RESULTS

The Google Form [6] provides the test administrator a figure online (Figure 2) showing a quick visualization of the results, as well as individual results from each judge which we do not need. The Form program downloads the results in a CSV file for import into a spreadsheet. We rearranged the results to get the alternative graphic (Figure 1) which we feel more closely shows the results. We also ran statistics (Figure 3), using the wine contest Jupyter Notebook [7,8]. Table 1 summarizes the scoring for each iteration of the contest, and Figure 4 shows the overall evaluation of the overall results.

IV. DISCUSSION

The results show a clear preference for COPDEM, FABDEM and ALOS; the results are quantitatively confirmed when using the wine contest statistics. The top three DEMs, and the bottom three significantly lower in the opinion of the judges, are the same as those from the DEMIX results [3] which relied

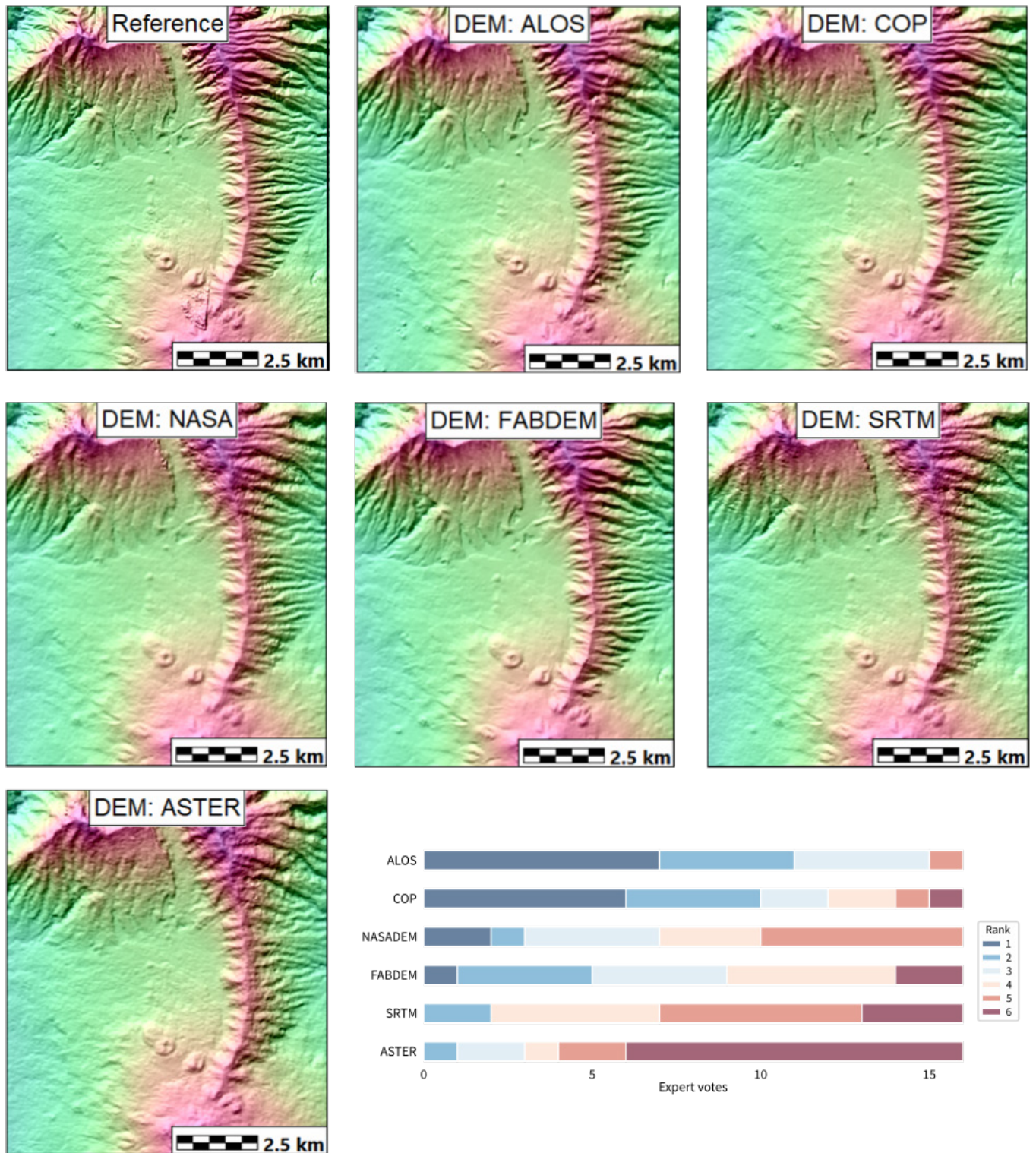


Figure 1. Hillshades of DEMIX tile N28VW018B, and the distribution of expert opinions for each of the 6 ranks. Low score in best.

Judge's Ranking

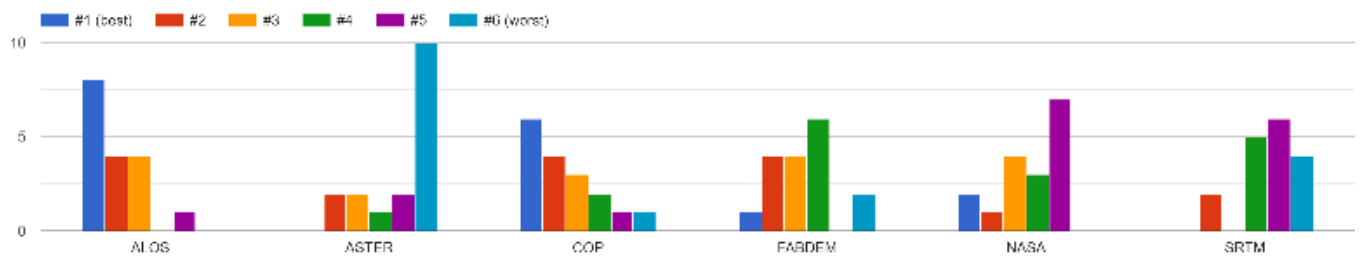


Figure 2. Google Forms automatic display of survey results.

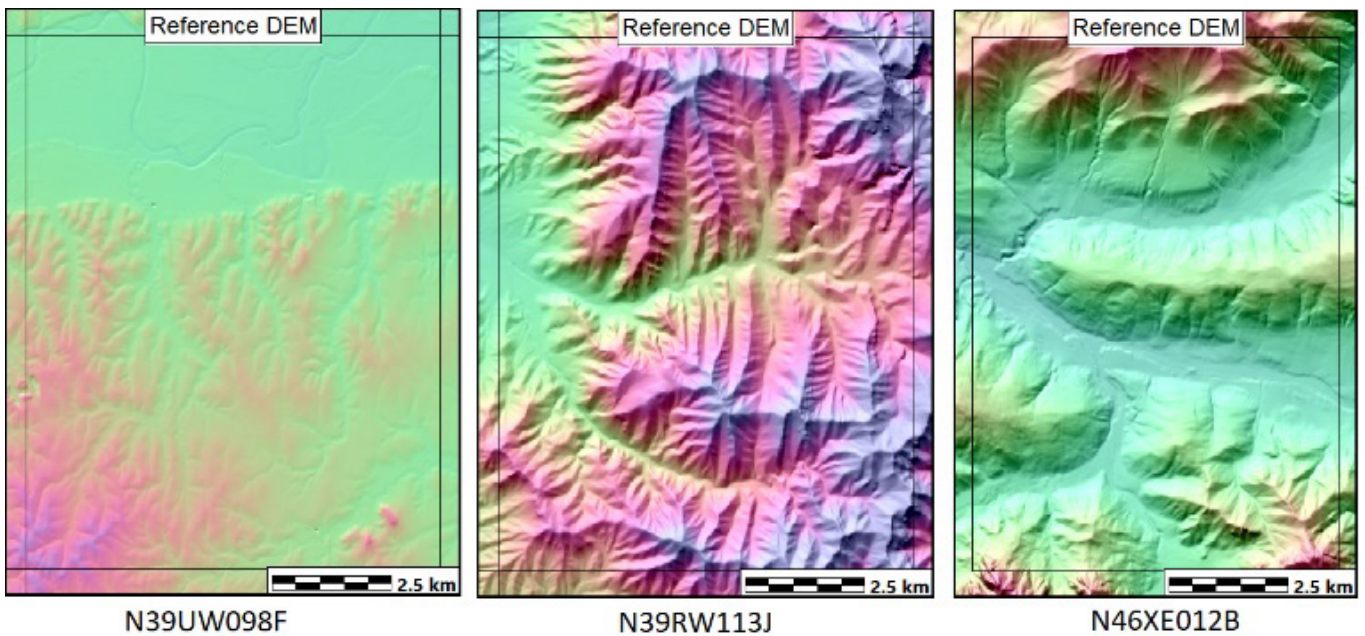


Figure 3. Hillshades for the three additional DEMs used for the second iteration of the contest.

Table 1. Wine contest average rankings for the 6 DEMs. Low score wins.

Area	DEMIX_TILE	JUDGES	NUMBER JUDGES	COPDEM	ALOS	FABDEM	NASA	SRTM	ASTER
La Palma	N28VW018B	USNA 2022	17	2.47	1.94	3.35	3.71	4.59	4.94
Canyon Range	N39RW113J	USNA 2023	24	2.13	2.71	1.92	4.67	4.63	4.96
Canyon Range	N39RW113J	IUAV 2023	36	2.06	2.11	2.06	4.47	4.64	5.08
Bolzano	N46XE012B	IUAV 2023	36	2.78	2.53	2.14	4.42	4.00	4.97
Republican River	N39UW098F	São Paulo 2023	41	2.24	2.76	2.20	4.24	4.05	5.54
Average all tests				2.27	2.39	2.51	4.27	4.61	4.95

Ranking without tolerance

No filters applied

Results of the DEMIX Wine Contest

For k=6, CL=0.05, and N=188, the critical value to compare is chi_crit=11.038
 And since chi_r (430.675) is greater than chi_crit (11.038)...
 Yay!! We can reject the null hypothesis and go to the Post-Hoc analysis!!

	Rank	Sum of ranks	Sum of ranks divided by number of opinions	Ties with
FABDEM	1.0	422.5	2.247	ALOS, COP
COP	2.0	457.5	2.434	ALOS, FABDEM
ALOS	3.0	465.0	2.473	COP, FABDEM
NASA	4.0	815.5	4.338	SRTM
SRTM	5.0	818.5	4.354	NASA
ASTER	6.0	969.0	5.154	

Figure 4. Wine contest ranking and statistical significance matrix. “Ties with” means the DEMs are not statistically different in this test

on over 20,000 quantitative opinions for 15 criteria using 133 100 km² tiles from 19 areas spread over three continents.

While the hillshade maps show elevation with color, slope and surface roughness, derivatives of elevation, dominate the visual display. For many users these are more important characteristics of the DEM, but as emphasized by the DEMIX group, users must select the comparison criteria that most closely match their requirements.

For these areas, the difference between FABDEM and COPDEM are minimal and would be very hard to differentiate in a hillshade map, verified by the similarity in their contest scores. While NASADEM improved on SRTM for the elevation differences compared to the reference DEM, it generally has very little effect on the slope and roughness differences [3,4]. Since slope and roughness determine the hillshade, the judges did not clearly differentiate NASADEM and SRTM.

V. CONCLUSIONS

Other potential subjective assessments for DEMs include topographic profiles [9,10] or elevation-slope plots [9,12,13]. DEM quality varies with land cover, land forms, and the slope of the terrain, so the test areas should cover a wide range of conditions.

The design and implementation of an expert-based approach to criteria evaluation is not a trivial task. The approach requires a considerable effort to collect this data and does not easily scale to multiple test regions. The demands on the judges to evaluate multiple DEMs mean that we could never reach the hundreds of test areas, and over a dozen criteria, which are possible with automated quantitative criteria. In our first iteration the DEMs were always in the same order; for the second iteration, we used multiple test areas which always had the DEMs in the same order, but varied in not showing the same DEM first or last in every test area. This was the best we could do using Google forms. It would require custom programming to make an ideal survey, and an effort to collect multiple experts willing to judge a number of tiles. Custom programming would also allow judges to give ties.

Despite the challenges, the test shows the power of the wine contest to evaluate DEMs, and that subjective criteria can be used. While the statistical validity of qualitative criteria may have caveats due to relatively small sample sizes, it provides another metric that users can evaluate in deciding which DEM they prefer to use, which in the end comes down to a value judgment. The mean of the differences to terrain parameters cannot be used in the wine contest, but means also provide information about where the candidate DEMs are low or high,

too steep or too flat, and too rough or too smooth. SRTM, NASADEM, and ASTER should be retired, and users should choose among COP, ALOS, or FABDEM, all of which are very similar to the reference DTM.

VI. ACKNOWLEDGMENT

We thank the students serving as wine experts for this work, and our colleagues in DEMIX for many helpful discussions.

REFERENCES

- [1] Guth, P.L.; Van Niekerk, A.; Grohmann, C.H.; Muller, J.-P.; Hawker, L.; Florinsky, I.V.; Gesch, D.; Reuter, H.I.; Herrera-Cruz, V.; Riazanoff, S.; López-Vázquez, C.; Carabajal, C.C.; Albinet, C.; Strobl, P. Digital Elevation Models: Terminology and Definitions. *Remote Sens.* 2021, 13, 3581. <https://doi.org/10.3390/rs13183581out>
- [2] Strobl, P.A.; Bielski, C.; Guth, P.L.; Grohmann, C.H.; Muller, J.P.; López-Vázquez, C.; Gesch, D.B.; Amatulli, G.; Riazanoff, S.; Carabajal, C. The Digital Elevation Model Intercomparison eXperiment DEMIX, a community based approach at global DEM benchmarking. *Int. Arch. Photogramm. Remote Sens. Spat. Inf. Sci.* 2021, XLIII-B4-2021, 395–400. <https://doi.org/10.5194/isprs-archives-XLIII-B4-2021-395-2021>
- [3] Bielski, C.; López-Vázquez, C.; Guth, P.L.; Grohmann, C.H. and the TMSG DEMIX Working Group. 2023. DEMIX Wine Contest Method Ranks ALOS AW3D30, COPDEM, and FABDEM as Top 1" Global DEMs: <https://arxiv.org/pdf/2302.08425.pdf>
- [4] Guth, Peter L. (2022). DEMIX GIS Database (1.0) [Data set]. Zenodo. <https://doi.org/10.5281/zenodo.7402618> Version 2 will soon be out.
- [5] Guth, Peter L., Peter Strobl, Kevin Gross, & Serge Riazanoff. (2023). DEMIX 10k Tile Data Set (1.0) [Data set]. Zenodo. <https://doi.org/10.5281/zenodo.7504791>
- [6] Google, 2023, Get insights quickly, with Google Forms: <https://www.google.com/forms/about/> Accessed 12 June 2023,
- [7] Grohmann, C.H., 2023. DEMIX Wine Contest Jupyter Notebook. URL: https://github.com/CarlosGrohmann/DEMIX_wine_contest last access 12 June 2023:
- [8] Grohmann, C.H., . (2023). The DEMIX Wine Contest Jupyter notebook. Geomorphometry2023, Iasi, Romania. <https://doi.org/10.5281/zenodo.77792562023-02-12>.
- [9] Guth, P.L., 2010, Geomorphometric Comparison of ASTER GDEM and SRTM: ASPRS/CaGIS 2010 Fall Specialty Conference, Orlando, FL, November 15-19, 10 p. <http://www.asprs.org/a/publications/proceedings/orlando2010/files/Guth.pdf>
- [10] Grohmann, C.H., 2018. Evaluation of TanDEM-X DEMs on selected Brazilian sites: comparison with SRTM, ASTER GDEM and ALOS AW3D30. *Remote Sensing of Environment*, 212C:121-133
- [11] Alganci, U.; Besol, B.; Sertel, E. Accuracy Assessment of Different Digital Surface Models. *ISPRS Int. J. Geo-Inf.* 2018, 7, 114. <https://doi.org/10.3390/ijgi7030114>
- [12] Guth, P.L., 2006, Geomorphometry from SRTM: Comparison to NED: Photogrammetric Engineering & Remote Sensing, special issue based on Shuttle Radar Topography Mission—Data Validation and Applications Workshop, Reston, VA, 14 June 2005, vol.72, no.3, p.269-277. https://www.asprs.org/wp-content/uploads/pers/2006journal/march/2006_mar_269-277.pdf
- [13] Grohmann, C.H., & Steiner, S.S. (2008) SRTM resample with short distance - low nugget kriging, International Journal of Geographical Information Science, 22:8, 895-906, DOI: 10.1080/13658810701730152

Going Forward: Extending and Exploiting the DEMIX Database With MICRODEM

Peter L. Guth
 Ocean & Atmospheric Sciences Dept
 US Naval Academy
 Annapolis, MD, 21402 USA
pguth@usna.edu

Carlos H. Grohmann
 Institute of Energy and Environment
 Universidade de São Paulo
 São Paulo 05508-010, Brazil
guano@usp.br

Sebastiano Trevisani
 Culture del Progetto Dept
 University IUAV of Venice
 Venice 30123, Italy
strevisani@iuav.it

Conrad Bielski
 EOXPLORE, Gaugrafenstr. 8,
 Oberhaching, 8204, Bavaria,
 Germany
conrad.bielski@eoxplore.com

Abstract— We show the power of the DEMIX database and the reference DEMs created to support it to analyze the properties and characteristics of 1 arc second global DEMs. This allows us to see why COPDEM and FABDEM are best, and how they improve on the others. The distributions of the differences from the reference DEMs in terms of elevation, slope, and roughness show that COPDEM and FABDEM consistently have the least bias compared the reference DEM, and the smallest standard deviations.

I. INTRODUCTION

DEMs provide a critical base layer for almost all earth science studies. The DEMIX group is working to compare and rank 6 global DEMs: COPDEM, FABDEM, ALOS, NASADEM, SRTM, AND ASTER [1,2]. We use their database [3] and reference DEMs [4] to demonstrate preliminary results of the rich potential to mine those datasets. Two other papers at this conference have examined the ability to use qualitative evaluation of hillshade maps to rank DEMs [5], and to look at the difference maps to study the spatial patterns where ALOS and COPDEM differ [6].

II. RESULTS

The wine contest [1] cannot use signed results because their choice of statistics requires that the values be ranked from low score (best) to high score. They commented that signed values like the mean and median provide additional context, which we will explore with Figure 1 which shows the mean, median, mode, and standard deviations of the difference distributions of elevation, slope, and roughness for all 236 tiles in the database. This summarizes the individual difference histograms for each tile. It allows the following generalizations:

- The difference distributions for COPDEM and FABDEM, and to a lesser extent ALOS, have a very sharp peak close to 0, indicating very little bias compared to the reference DTM. The other DEMs have much smaller and flatter peaks; for many it is hard to find a mode.
- NASADEM has little bias from the reference DTM only for elevation differences, where it is much better than SRTM.

- NASADEM does not improve on slope and roughness compared to SRTM.

- ASTER is clearly the worst performer.

Overall Figure 1 supports the DEM ranking from the wine contest [1], but provides insight into how the DEMs differ.

Figure 2 shows where each of 6 DEMs is tied for best, with the tiles sorted by average slope and percent forest, using three criteria of the 15 used in the wine contest [1]. Supplementary figures on Zenodo show 7 land characteristics with 6 criteria. There are 236 opinions, one per tile for each criterion with the DTM as reference and 134 opinions for the DSM as reference. There can be 1 to 6 DEMs tied, and the figure suggests where each is best:

- Fewer tiles have a DSM, which must be factored into looking at the figure.
- COPDEM and FABDEM are almost always at the top, FABDEM more often when compared to a DTM and COPDEM when compared to a DSM.
- Based on a limited number of very steep and very rough (shown on a supplementary figure) tiles, ALOS may out perform the other DEMs in that type of topography.
- NASADEM and SRTM perform best in low slope tiles, and in unforested tiles and some tiles with about 70% forests.
- ASTER is tied for first for only 6 tiles, two of which are very flat coastal DEMs in which none of the 1 arc second DEMs performs very well.

Inspection of the difference maps reveals aspects of the DEMs that do not always show up in the statistics. For example, Figure 3 shows linear anomalies with the ALOS DEM showing where images were merged; we have seen the same patterns elsewhere with ALOS and notably have not seen similar artefacts with COPDEM. The scale of these anomalies makes them hard to see on individual DEMIX tiles, and is one reason we prefer to work with larger areas with many DEMIX tiles. The other, and perhaps bigger reason, is that the geographic tile boundaries do not line up well with the UTM boundaries of the source DEMs used to aggregate the reference DEMs, and it is

much easier to get data for an area and then extract the individual tiles on the fly.

IV. CONCLUSIONS

We foresee several ways that the DEMIX wine contest and its associated database will be extended (1) adding more tiles, particularly in mountainous areas, (2) adding new criteria, and (3) looking beyond the numerical rankings to understand what causes the differences, and when each DEM performs best. We do not expect that the relative rankings of the DEMs will change much, but that understanding where ALOS performs best could lead to improved DEMs in areas where COPDEM

underperforms; understanding the difference between optical and radar sensors might lead to better composite DEMs. All of these DEMs are composites, using additional data to fill voids, and FABDEM removed trees and buildings from COPDEM very well in creating the best (and only) DTM in the group.

V. ACKNOWLEDGMENT

All work done in the open source MICRODEM [8], which has source code and a 64 bit Windows executable. Larger figures and Supplementary figures available on zenodo with this paper. We thank our collaborators on the DEMIX group for stimulating discussions.

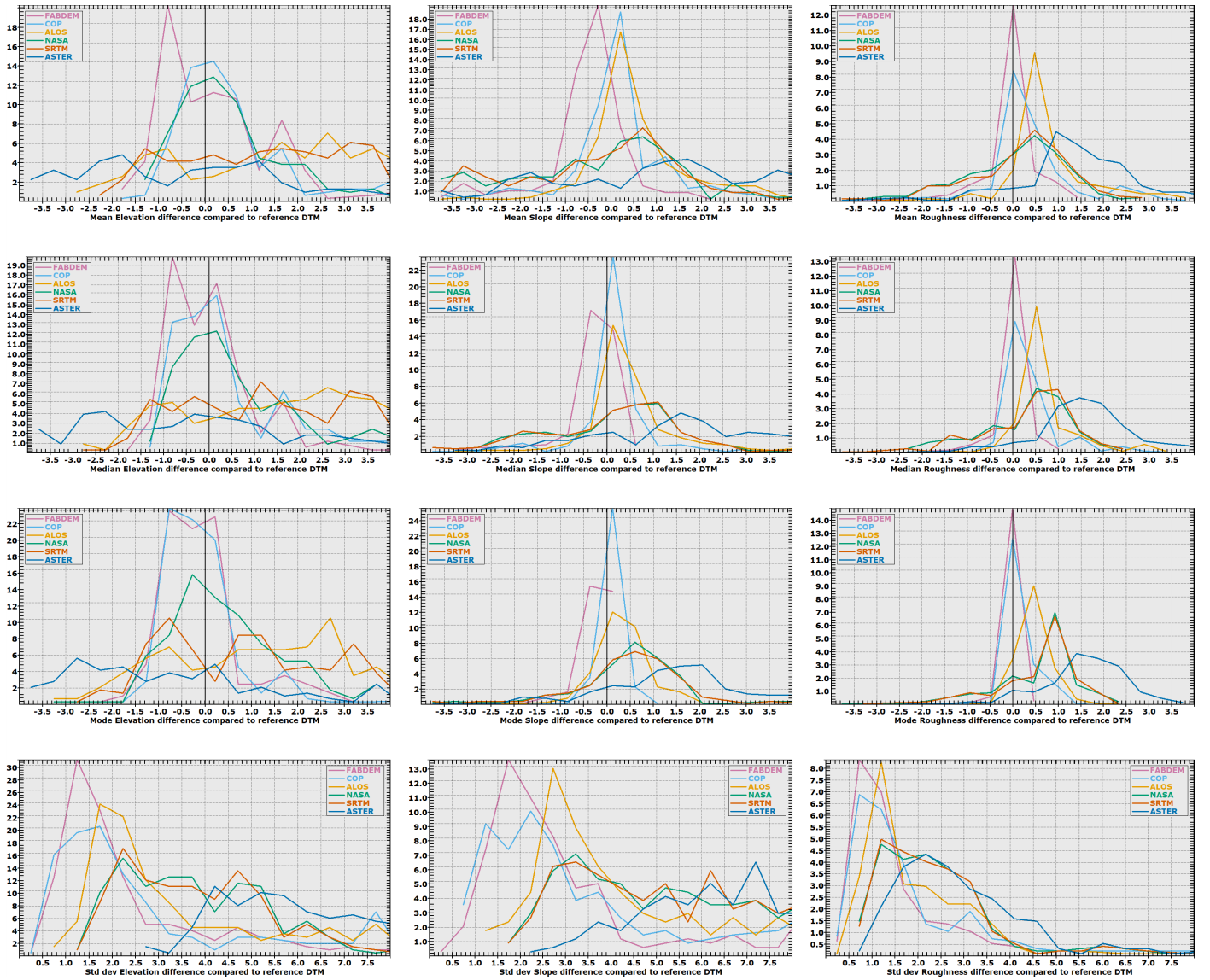


Figure 1. Summary statistics (mean, median, mode, and standard deviation) for the difference distribution compared to the reference DTM for 6 global DEMs and 236 DEMIX tiles. Graphs of the difference distributions are available online [7].

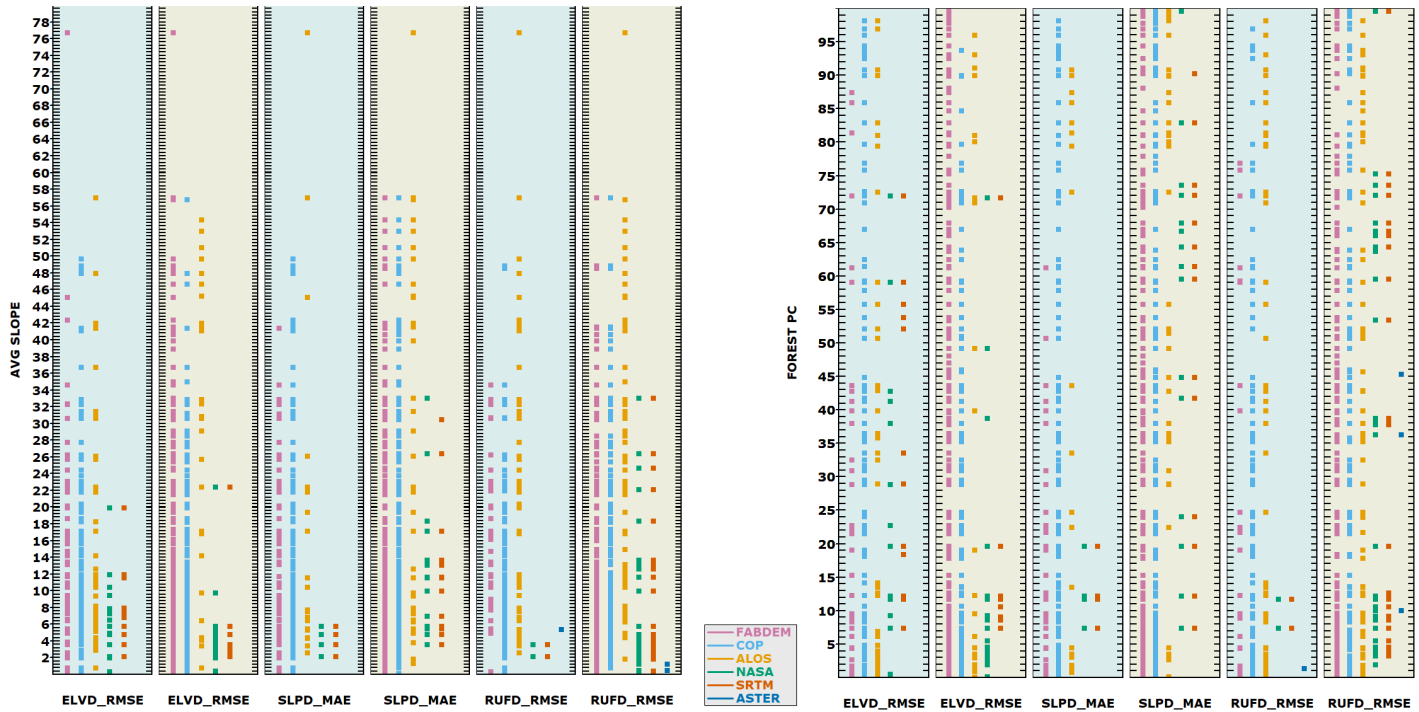


Figure 2. Tile by tile results where each DEM is ranked best within tolerance, for three parameter and both DSM (blue background) and DTM (brown background). On the left side the tiles are sorted by average slope of the tile in percent, and on the right by how much of the tile is forested. Additional results are with the paper online.

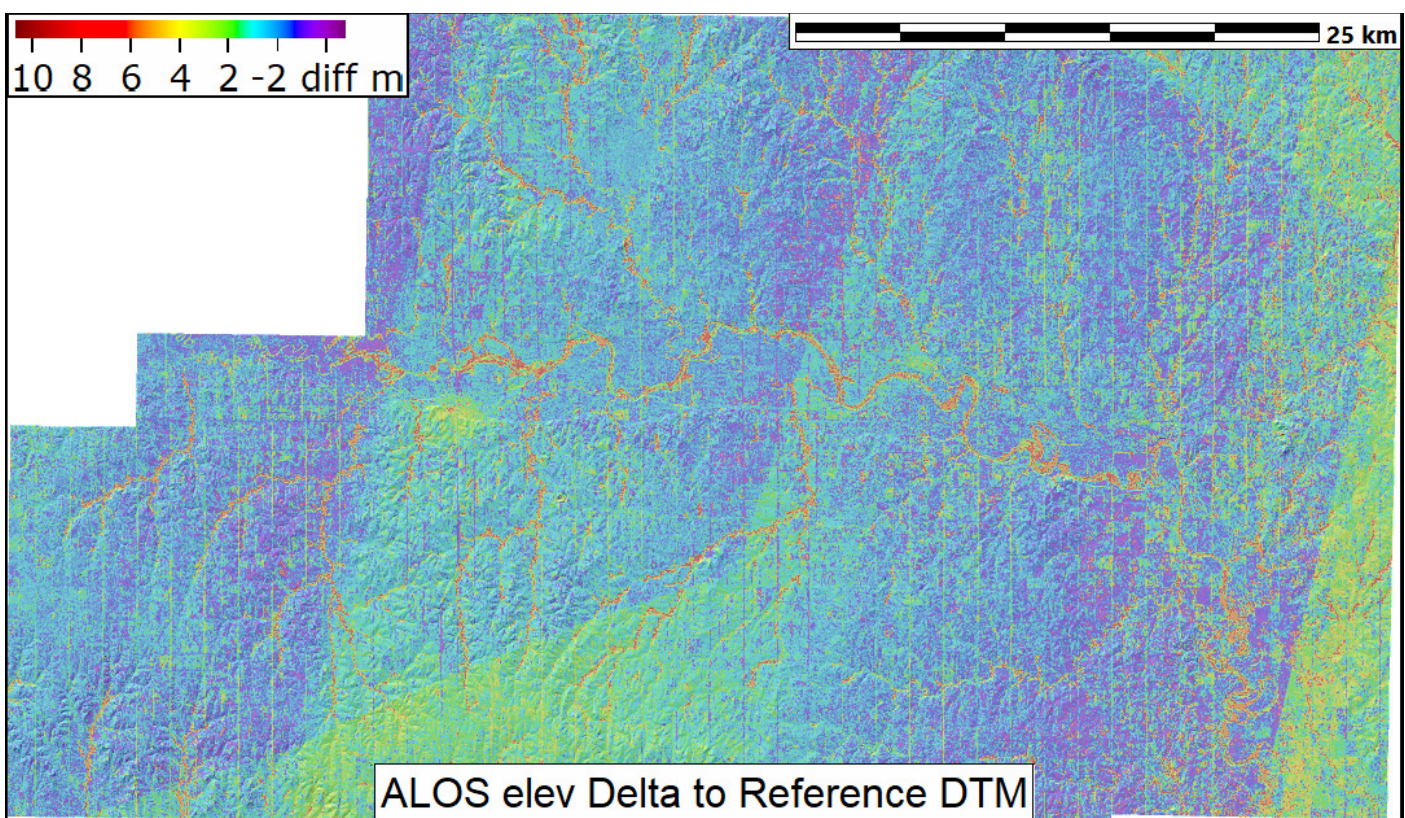


Figure 3. Elevation differences, ALOS minus reference DTM for the Republican River test area in Kansas.

REFERENCES

- [1] Bielski, C.; López-Vázquez, C.; Guth, P.L.; Grohmann, C.H. and the TMSG DEMIX Working Group, 2023. DEMIX Wine Contest Method Ranks ALOS AW3D30, COPDEM, and FABDEM as Top 1" Global DEMs: <https://arxiv.org/pdf/2302.08425.pdf>
- [2] Grohmann, C.H., López-Vázquez, C., Guth, P.L., & Bielski, C., 2023, The DEMIX Wine Contest: a summary. Geomorphometry 2023, Iasi, Romania.<https://doi.org/10.5281/zenodo.8066531>
- [3] Guth, P. L., 2023. DEMIX GIS Database Version 2 (2.0) [Data set]. Zenodo. <https://doi.org/10.5281/zenodo.8062008>.
- [4] Guth, P.L., Grohmann, C., Trevisani, S., & López-Vázquez, Cs, 2023. DEMIX 1" Reference DEMs version 1.0 (1.0) [Data set]. Zenodo. <https://doi.org/10.5281/zenodo.7600699>.
- [5] Guth, P.L., Grohmann, C.H., & Trevisani, S., 2023, Subjective Criterion for the DEMIX Wine Contest: Hillshade Maps. <https://doi.org/10.5281/zenodo.8030735>
- [6] Guth, P.L., Grohmann, C.H., & Trevisani, S., 2023, Geomorphometric and Geospatial Patterns in Differences Between ALOS and COPDEM: Geomorphometry2023. <https://doi.org/10.5281/zenodo.8057703>
- [7] Guth, Peter L. (2023). DEMIX Difference Distribution Histograms (1.0) [Data set]. Zenodo. <https://doi.org/10.5281/zenodo.8087804>
- [8] Guth, P.L., 2023, git-microdem: https://github.com/prof-pguth/git_microdem, accessed 5 Feb 2023.

Sponsors



www.tehnopress.ro



9 786066 875172